

Advancing EDL Technologies for Future Space Missions: From Ground Testing Facilities to Ablative Heatshields

Thesis by

Jason Rabinovitch

In Partial Fulfillment of the Requirements

for the Degree of

Doctor of Philosophy



California Institute of Technology

Pasadena, California

2014

(Defended May 16, 2014)

© 2014

Jason Rabinovitch

All Rights Reserved

Acknowledgments

First and foremost, I would like to thank my advisor, Guillaume Blanquart, for working with me over the past several years. In addition, I would like to thank my committee members, Tim Colonius, Beverley McKeon, and Joe Shepherd, for taking the time to review my work, and for offering many insightful comments about this thesis. It has been a privilege to be surrounded by so many intelligent people throughout my entire time at Caltech.

In addition, I would like to thank all members of The FORCE and Joe Shepherd's research group; this work would not have been possible without the help and support of all of students in these groups. In particular, I would like to thank Nick Parziale for the time we spent working together on the Vertical Expansion Tunnel and organizing the Caltech Space Challenge, for many years of softball, and for his friendship throughout my time at Caltech.

I have had the privilege of being a graduate student fellow of the Keck Institute for Space Studies since coming to Caltech. I would like to thank KISS for funding me during my first year at Caltech, and for allowing me to interact with so many leaders in the aerospace industry over the past several years. In particular, I would like to thank Michele Judd for making all of these amazing events possible, and for acting as a professional mentor to me.

The work on ablative heatshields has benefited greatly from collaborations with Vanessa Marx and Rémy Mevel. To all of my friends from home, from Yale, and from California, thank you for supporting me all of these years, and for listening to me talk about my research.

Finally, without the endless support of my parents, Marsha and Jed Rabinovitch, and my brother, Marty Rabinovitch, none of this would have been possible. Thank you.

Funding for this work was provided by the U.S. Air Force Office of Scientific Research (Award FA9550-12-1-0472) under the supervision of Dr. Chiping Li.

Abstract

Motivated by recent MSL results where the ablation rate of the PICA heatshield was over-predicted, and staying true to the objectives outlined in the NASA Space Technology Roadmaps and Priorities report, this work focuses on advancing EDL technologies for future space missions.

Due to the difficulties in performing flight tests in the hypervelocity regime, a new ground testing facility called the vertical expansion tunnel is proposed. The adverse effects from secondary diaphragm rupture in an expansion tunnel may be reduced or eliminated by orienting the tunnel vertically, matching the test gas pressure and the accelerator gas pressure, and initially separating the test gas from the accelerator gas by density stratification. If some sacrifice of the reservoir conditions can be made, the VET can be utilized in hypervelocity ground testing, without the problems associated with secondary diaphragm rupture.

The performance of different constraints for the Rate-Controlled Constrained-Equilibrium (RCCE) method is investigated in the context of modeling reacting flows characteristic to ground testing facilities, and re-entry conditions. The effectiveness of different constraints are isolated, and new constraints previously unmentioned in the literature are introduced. Three main benefits from the RCCE method were determined: 1) the reduction in number of equations that need to be solved to model a reacting flow; 2) the reduction in stiffness of the system of equations needed to be solved; and 3) the ability to tabulate chemical properties as a function of a constraint once, prior to running a simulation, along with the ability to use the same table for multiple simulations.

Finally, published physical properties of PICA are compiled, and the composition of the pyrolysis gases that form at high temperatures internal to a heatshield is investigated. A necessary link between the composition of the solid resin, and the composition of the pyrolysis gases created is provided. This link, combined with a detailed investigation into a reacting pyrolysis gas mixture, allows a much needed consistent, and thorough description of many of the physical phenomena occurring in a PICA heatshield, and their implications, to be presented.

Through the use of computational fluid mechanics and computational chemistry methods, significant contributions have been made to advancing ground testing facilities, computational methods for reacting flows, and ablation modeling.

Contents

Acknowledgments	iii
Abstract	iv
1 Introduction	1
1.1 Overview of Successful Mars Landings	2
1.2 MSL—Design Considerations and Flight Data	4
1.3 Organization and Objectives of Thesis	5
1.3.1 Ground Testing Facilities	6
1.3.2 Reacting Flows	8
1.3.3 Ablative Heat Shields	10
2 Vertical Expansion Tunnel	13
2.1 Motivation	13
2.2 Available Conditions	16
2.3 Test Time Calculation for the RST and ET	19
2.4 Ideal Test Time Calculation for the VET	20
2.4.1 The Compressible Euler Equations with Area Change	21
2.4.2 Roe Solver	23
2.4.3 Treatment of Fluid Interfaces	25
2.4.4 Higher-Order Corrections	26
2.4.5 Entropy Fix	27
2.4.6 Numerical Results: Verification	27
2.4.7 Numerical Results: VET with Nozzle	29
2.5 Real Facility Effects	33
2.5.1 Initial Test Gas/Accelerator Gas Separation	34

2.5.2	Ideal <i>vs.</i> Experimental Test Conditions	34
2.6	Discussions	36
3	Rate-Controlled Constrained-Equilibrium	38
3.1	Motivation	38
3.2	Previous Work	39
3.3	Reacting Euler Equations	40
3.4	RCCE Overview	43
3.5	Methodology for Constraint Selection	47
3.5.1	Timescale Analysis	47
3.5.2	Degree of Disequilibrium	49
3.5.3	Effect of Elemental Conservation	50
3.6	Air Test Cases—Overview	51
3.6.1	Case #1: Shocked Gas	52
3.6.2	Case #2: Steady Expansion	53
3.7	Air Test Cases—Constraint Selection	54
3.7.1	Species Constraints	55
3.7.2	Global Quantities	55
3.7.3	Constraints based on Timescale Analysis	56
3.7.4	Constraints Based on DOD Analysis	59
3.8	Constraint Performance	60
3.8.1	Comparison Methodology	61
3.8.2	Constraint: Individual Species	61
3.8.3	Constraint: Major and Radical Species	68
3.8.4	Constraint: Global Quantities	71
3.8.5	Constraint: Timescale Analysis and <i>DOD</i>	75
3.8.6	Analysis of Constraint Performance	78
3.9	Integrated RCCE Simulation	83
3.9.1	Methodology for RCCE Simulations	83
3.9.2	Tabulated Approach	84
3.9.3	Integrated Simulation Results - Shock	85
3.9.4	Integrated Simulation Results - Nozzle	86
3.9.5	Integrated Simulation Results - Discussion	88

3.10 Extension to the Martian Atmosphere	89
3.11 Discussion	97
4 Pyrolysis Gas Composition in PICA Heatshields	99
4.1 Motivation	99
4.2 Ablation Overview	101
4.3 PICA Composition	103
4.3.1 Expected Fiber Properties	104
4.3.2 Expected Resin Properties	105
4.3.2.1 Types and Production	105
4.3.2.2 Curing and Thermal Decomposition	107
4.3.2.3 Presence of Impurities	108
4.3.3 Expected Char Composition	109
4.4 Pyrolysis Gas Composition	110
4.4.1 Equilibrium Pyrolysis Gas Composition	111
4.4.1.1 Gas Model	111
4.4.1.2 Elemental Composition of Pyrolysis Gases	113
4.4.1.3 Equilibrium Results—PAH Species	114
4.4.1.4 Equilibrium Results—Varying Mixture Composition	115
4.4.1.5 Equilibrium Results—Discussion	118
4.4.2 Kinetic Evolution of Pyrolysis Gas Composition	119
4.5 Pyrolysis Gas Flow Regime	124
4.5.1 Continuum Flow Assumption	124
4.5.2 PAH Collisions	126
4.5.3 PAH and Fiber Collisions	128
4.6 Effect of Carbon Deposition	130
4.6.1 Model #1	131
4.6.2 Model #2	132
4.6.3 Results	133
4.7 Analysis of Experimental Results	135
4.8 Constrained Equilibrium Calculations	139
4.9 Summary and Discussion	145

5 Conclusions and Future Work	147
5.1 Vertical Expansion Tunnel	147
5.2 Rate-Controlled Constrained-Equilibrium	148
5.3 Pyrolysis Gas Composition in PICA Heatshields	149
Appendices	167
A Constrained Thermodynamic Equilibrium Calculations	168
B RCCE Table Sensitivity	169
C Resin Synthesis	172
C.1 General	172
C.2 Curing and Decomposition Characteristics	173
C.3 Synthesis of Novolac Resins	174
C.3.1 Brønsted Acid Catalysts—Novolac Resins	176
C.3.2 Lewis (Neutral) Acid Catalysts—High Ortho Novolac Resins	176
C.4 Synthesis of Resole Resins	177
C.5 Byproducts formed in synthesis of resins	179
D Pyrolysis Gas Model	182

List of Figures

1.1	Three Generations of Mars Rovers	4
1.2	MSL Flight Data	6
1.3	Secondary Diaphragm Impacts in an Expansion Tube	8
1.4	Avcoat and PICA Pyrolysis Gas Compositions	11
2.1	Expansion Tunnel Schematic	13
2.2	Pressure-Velocity Diagram for a Conventional Expansion Tube	17
2.3	Pressure-Velocity Diagram for a Vertical Expansion Tunnel	17
2.4	Schematic x-t Diagram for a Conventional ET	20
2.5	Numerical Flux Correction for Fluid Interfaces	25
2.6	1D Numerical x-t Diagram	28
2.7	Analytic and Numerical Test Time Comparison	29
2.8	Numerical x-t Diagram for an Expansion Tunnel	30
2.9	x-t Diagram for Accelerator and Nozzle Sections	31
2.10	Test Time Calculations for the VET	32
2.11	VET Normalized Flow conditions	33
3.1	Overview of RCCE Method	44
3.2	Species Evolution for Shocked Air	53
3.3	Species Evolution for Expanding Air	54
3.4	Reaction Mode Time Scales for Air	57
3.5	Reaction Coefficients for Air—Fast Mode	58
3.6	Degree of Disequilibrium for Air	59
3.7	Shocked Air—Constraining O ₂	62
3.8	Shocked Air—Constraining N ₂	62
3.9	Shocked Air—Constraining NO	63

3.10	Shocked Air—Constraining O	64
3.11	Expanding Air—Constraining O ₂	65
3.12	Expanding Air—Constraining N ₂	65
3.13	Expanding Air—Constraining O	66
3.14	Expanding Air—Constraining NO	67
3.15	Shocked Air—Constraining Major Species	68
3.16	Shocked Air—Constraining Radical Species	69
3.17	Expanding Air—Constraining Major Species	69
3.18	Expanding Air—Constraining Radical Species	70
3.19	Shocked Air—Constraining Molecular Weight	71
3.20	Shocked Air—Constraining Standard Enthalpy of Formation (by Mass)	72
3.21	Expanding Air—Constraining Molecular Weight	74
3.22	Expanding Air—Constraining Standard Enthalpy of Formation (by Mass)	74
3.23	Shocked Air—Constraining Using Fast Reaction Mode	75
3.24	Shocked Air—Constraint Based on DOD Analysis and Elemental Conservation	76
3.25	Expanding Air—Constraining Using Fast Reaction Mode	76
3.26	Expanding Air—Constraint Based on DOD Analysis and Elemental Conservation	77
3.27	L2 Error Plot Air— $h(T_o)$ and γ	79
3.28	Weighted L2 Error Plot Air— $h(T_o)$ and γ	80
3.29	L2 Error Plot Air— $ \partial\phi/\partial t $	80
3.30	Reconstruction of ϕ —Constraining Enthalpy of Formation	82
3.31	RCCE Simulation for a Shocked Gas (Mass Fractions)	86
3.32	RCCE Simulation for a Shocked Gas (Constraint)	87
3.33	RCCE Simulation for a Diverging Nozzle (Mass Fractions)	87
3.34	RCCE Simulation for a Diverging Nozzle (Constraint)	88
3.35	Species Evolution for Martian Atmosphere Processed by a Normal Shock	90
3.36	Species Evolution for Martian Atmosphere Undergoing a Steady Expansion	91
3.37	Shocked Mars Atmosphere—Constraining Enthalpy of Formation (by Mass)	92
3.38	Expanding Mars Atmosphere—Constraining Enthalpy of Formation (by Mass)	92
3.39	L2 Norm Comparisons for Mars Atmosphere	93
3.40	Reconstruction of ϕ (Mars Atmosphere)	94
3.41	RCCE Simulation for a Shocked Flow—Mars (Mass Fractions)	95

3.42	RCCE Simulation for a Shocked Flow—Mars (Constraint)	95
3.43	RCCE Simulation for a Diverging Nozzle—Mars (Mass Fractions)	96
3.44	RCCE Simulation for a Diverging Nozzle—Mars (Constraint)	96
4.1	Ablation Schematic Diagram	102
4.2	PICA Material	104
4.3	Idealized Resin Structure	107
4.4	Equilibrium Mixture—Resin Composition	114
4.5	Coronene Molecule	115
4.6	Equilibrium Composition—Varying Char Yields	116
4.7	Equilibrium Enthalpy Comparisons	117
4.8	Maximum C ₂₄ H ₁₂ Mass Fraction Over a Range of Char Yields and Pressures	119
4.9	Kinetic Evolution of Pyrolysis Gas	121
4.10	Equilibrium Composition of Pyrolysis Gas	122
4.11	Enthalpy Comparison for Equilibrium and Finite-Rate Kinetics	123
4.12	Schematic for Carbon Fiber Arrangements	125
4.13	Fiber/PAH Collision Schematic	129
4.14	Effect of Solid Carbon Deposition (0% Char Yield)	134
4.15	Effect of Solid Carbon Deposition (35% Char Yield)	134
4.16	Effect of Solid Carbon Deposition (60% Char Yield)	135
4.17	Experimental Data Compared to Thermodynamic Equilibrium Calculations	138
4.18	Comparison of Elemental Composition of Pyrolysis Gas	139
4.19	Comparison of Elemental Composition of Pyrolysis Gas—Integrated	140
4.20	Experimental Data Compared to Constrained Equilibrium Calculations	141
4.21	Mixture Enthalpy Comparison—Sykes	141
4.22	Constrained Equilibrium Composition—A ₁ OH	142
4.23	Constrained Equilibrium Composition—8 Species	143
4.24	Constrained Equilibrium Composition—Summation of PAH Species	144
4.25	Enthalpy Comparison for Different Constrained Equilibrium Calculations	144
B.1	RCCE Results for Varying Table Resolution—Shock Mass Fractions	169
B.2	RCCE Results for Varying Table Resolution—Shock ϕ	170
B.3	RCCE Results for Varying Table Resolution—Nozzle Mass Fractions	170

B.4	RCCE Results for Varying Table Resolution—Nozzle ϕ	171
C.1	General Synthesis of a Phenolic Resin	173
C.2	Conversion of Ether to Methylene Linkages Upon Curing	173
C.3	General Synthetic Scheme for the Production of a Novolac Resin	175
C.4	Hexamethylenetetramine as a Source of Formaldehyde	175
C.5	Brønsted Acid-Catalyzed Reaction of Phenol with Formaldehyde	177
C.6	Lewis Acid Catalyzed Reaction of Phenol with Formaldehyde	178
C.7	General Synthetic Scheme for the Production of a Resole Resin	179
C.8	Base-Catalyzed Reaction of Phenol with Formaldehyde	180
C.9	Byproducts Formed in Resin Synthesis	181

List of Tables

1.1	Summary of Successful NASA Mars Landers and Rovers	3
2.1	Run Condition Comparison for RST, ET, and VET	18
2.2	VET Conditions for Varying Run Conditions	33
3.1	Test Case #1 Conditions	52
3.2	Test Case #2 Conditions	54
3.3	Summary of Constraints	55
3.4	Global Constraint Examples	56
3.5	Calculated Constraints Based on DOD Analysis	60
3.6	Sensitivity of $ \partial\phi/\partial t $	73
3.7	Sensitivity of Reaction Rates	73
4.1	Summary of Phenolic Resins	106
4.2	Summary of Pyrolysis Gas Compositions	114
4.3	Calculated Elemental Composition of Pyrolysis Gas Reported by Sykes.	137
4.4	Elemental Composition of Pyrolysis Gas Reported by Trick <i>et al.</i> (1995)	138
D.1	Species Model for Pyrolysis Gas Mixture	182
D.2	Additional Three Species for Experimental Comparison	183

Chapter 1

Introduction

The goal of this thesis is to use computational methods to advance entry, descent, and landing (EDL) technologies for future space missions. The motivation stems from a recent NASA report which identified key mission enabling technologies in order to ensure that NASA remains a world leader in technology and science.

In 2010, NASA’s Office of the Chief Technologist (OCT) drafted a set of 14 Space Technology Area Roadmaps (STARS) to identify key technologies for NASA to invest in. The Aeronautics and Space Engineering Board of the National Research Council (NRC) then appointed a steering committee to solicit external inputs and to evaluate the roadmaps. This led to the release of the report: “NASA Space Technology Roadmaps and Priorities: Restoring NASA’s Technological Edge and Paving the Way for New Era in Space” [39]. The 14 technical areas identified covered many engineering and scientific disciplines, while remaining consistent with the three overall technical objectives for NASA:

- Objective A: Extend and sustain human activities beyond low Earth orbit (LEO)
- Objective B: Explore the evolution of the solar system and the potential for life elsewhere (in situ measurements)
- Objective C: Expand our understanding of Earth and the universe in which we live (remote measurements)

This work will focus on technology development related to Technical Area 09 (TA09) “Entry, Descent, and Landing Systems”. NASA’s justification for the inclusion of EDL technologies in STARS is found in [39]:

NASA’s future missions will require ever greater mass delivery capability in order to place scientifically significant instrument packages on distant bodies of interest, to

facilitate sample returns from bodies of interest, and to enable human exploration of planets such as Mars. As the maximum mass that can be delivered to an entry interface is fixed for a given launch system and trajectory design, the mass delivered to the surface will require reductions in spacecraft structural mass; more efficient, lighter thermal protection systems; more efficient lighter propulsion systems; and lighter, more efficient deceleration systems.

EDL systems are mission critical technologies. The primary goal of EDL technology development is to extend the ability to deliver more payload safely to the destination. Two specific technologies needed to achieve this goal were identified to be the development of rigid thermal protection systems, and advancing EDL modeling and simulation.

Related to TA09, is TA14 “Thermal Management Systems”, where the over-arching goal is to [39]:

Develop a range of rigid ablative and inflatable/flexible/deployable thermal protection systems (TPS) for both human and robotic advanced high-velocity return missions, either novel or reconstituted legacy systems.

TPS is mission-critical for all future human and robotic missions that require planetary entry or reentry. The current availability of high-TRL rigid ablative TPS is adequate for LEO re-entry but is inadequate for high-energy re-entries to Earth or planetary missions. Ablative materials are enabling for all NASA, military, and commercial missions that require high-Mach-number re-entry, such as near-Earth asteroid visits and Mars missions, whether human or robotic.

Advancing these technologies requires a combination of theoretical, experimental, and numerical work. The report asserts that:

Adequate ground-test facilities are required to validate analytical models, to benchmark complex computer simulations such as computational fluid dynamics models, and to examine new designs and concepts ...

Large contributions have been made to this field in the past half-century; it is important to outline some of NASA’s recent successful landings on Mars in order to understand the current state of the art in EDL technologies.

1.1 Overview of Successful Mars Landings

“Von Braun got the astronauts into space. Lester Lees got them down.” - Apollo project manager [1]

During the re-entry flight of a spacecraft returning from lower earth orbit, speeds greater than 6 km/s can be realized; for potential Mars return missions, speeds between 11 km/s and 14 km/s

could be reached by the earth re-entry vehicle [15, 30, 120]. The aeroshell component of a re-entry vehicle is designed to both dissipate the re-entry vehicle’s high speeds, and to protect the payload from the extremely harsh aerothermal environment experienced during re-entry. The interaction between the vehicle’s heatshield and the atmosphere generally dissipates more than 90% of the vehicle’s kinetic energy, which is largely converted into thermal loads that the vehicle must endure [82, 94]. An accurate understanding of the aerodynamics and aerothermodynamics at high enthalpies is crucial for the success of any space mission that includes a re-entry phase.

The pioneering work performed by Lester Lees investigating heat transfer over blunt bodies at hypersonic speeds [82] aided the Mercury, Gemini, and Apollo astronauts safe return to the Earth. Since then, great advances have been in this field that have allowed for the design of more advanced re-entry vehicles. At the fundamental level, these advances have contributed to NASA’s ability to land larger, and more complex missions on different planets with a greater level of precision and control. Table 1.1 summarizes NASA’s different missions that have landed rovers or landers successfully on Mars. Advances in hypersonics have allowed each missions’ respective landing ellipse (expected landing site range) to continue to decrease, and for larger payloads to be landed on the surface of Mars. The recent successful landing of the Mars Science Laboratory (MSL) mission is a true testament to advances in hypersonics, as the entry mass of the MSL spacecraft into the Martian atmosphere was ~ 3300 kg, nearly three times more massive than any previous mission. This spacecraft also endured the highest heating and stress on the heatshield compared to any previous Mars mission [4]. Figure 1.1 shows a comparison of three generations of Mars rovers, showing the large size increase of the recent Curiosity rover. Not only has MSL enhanced our knowledge of Mars since its successful landing, but the flight data it recorded during atmospheric entry allows initial predictions to be compared to the actual flight conditions experienced in the Martian atmosphere. Some of the design considerations and flight data from the MSL mission are discussed in the following section.

Table 1.1: Summary of successful NASA Mars landers and rovers. Data taken from [37] and NASA-JPL press releases made available to the public [2, 3, 4, 5, 6].

Mission	Landing Date	Entry Mass (kg)	Landing Ellipse (km)
Viking 1 & 2	June 19/August 7 1976	930	420 x 200
Pathfinder	July 4 1997	585	100 x 50
Mars Exploration Rovers	January 4/25 2004	840	80 x 20
Phoenix	May 25 2008	602	75 x 20
Mars Science Laboratory	August 5 2012	3300	20 x 7

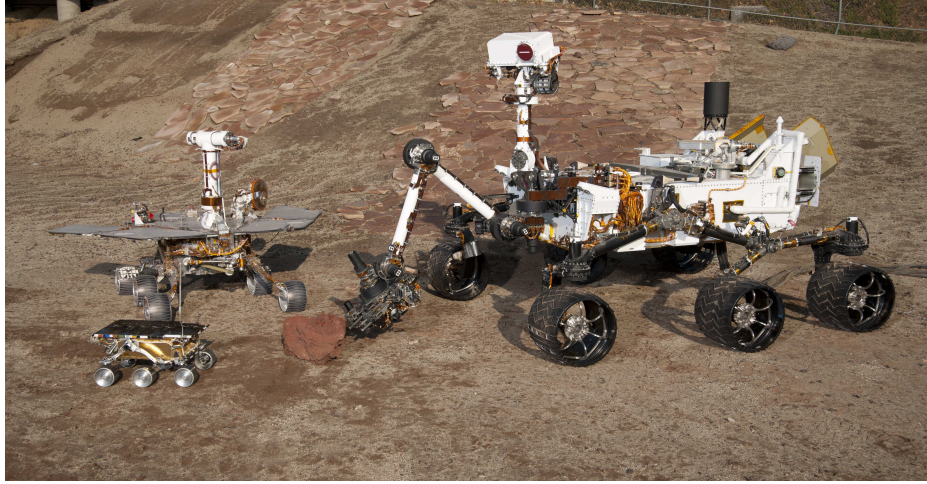


Figure 1.1: Scale models of three generations of Mars Rovers. From bottom left, and moving clockwise: Pathfinder, Mars Exploration Rover, and Mars Science Laboratory (Sojourner, Spirit/Opportunity, and Curiosity). Photo-credit NASA-JPL <http://photojournal.jpl.nasa.gov/> [retrieved 21 April 2014].

1.2 MSL—Design Considerations and Flight Data

In order to continue to decrease the size of the landing ellipse (Table 1.1) for future missions, understanding the hypersonic flight characteristics of a vehicle is vital. As a reference point, the Apollo capsules required an entry flight path angle guidance accuracy of $\pm 0.4^\circ$ [30], while late trajectory corrections for the recent MSL mission used a flight path angle guidance accuracy of $\pm 0.05^\circ$ [97]. In addition, a better understanding of the aerothermal properties of a vehicle’s thermal protection system allows design margins to be reduced, ultimately resulting in a lighter system. This allows mass on the spacecraft to be used for other payloads, such as additional science instruments. Bose *et al.* [21] noted that “an under prediction of stagnation point heating is also seen when comparisons are made with wind tunnel data, especially at turbulent conditions [36]. In MSL TPS sizing, a stagnation point heating margin of about 50% was implemented to account for this under prediction”. There is a stark lack of predictive capability.

A quote from the MSL press release [4] summarizes some of the factors involved in the design process for MSL, and explains the motivation for the MSL Entry, Descent and Landing Instrumentation (MEDLI) scientific instrument which took data as MSL entered the Martian atmosphere:

Models of the Martian atmosphere, heating environments, vehicle aerodynamics, and heat-shield performance, among other factors, were employed in designing the Mars Science Laboratory entry vehicle. Uncertainties in these parameters must also be modeled. To account for those uncertainties, the design incorporates large margins for success. The margin comes at a cost of additional mass. The goal of MEDLI is to better quantify

these atmospheric entry characteristics and possibly reduce unnecessary mass on future Mars missions, by collecting data on the performance of the Mars Science Laboratory entry vehicle during its atmospheric entry and descent.

The heatshield for the recent MSL mission was outfitted with a series of pressure and temperature sensors called MEDLI [43]. The specific subsystem containing thermocouples is referred to as the MEDLI Integrated Sensor Plug (MISP), and this system provided temperature information for the heatshield at a variety of locations and depths.

This is illustrated in Fig. 1.2, which shows the reconstructed flight data taken from MISP. The flight data was taken from early entry into the Martian atmosphere until the heatshield was jettisoned as part of the EDL sequence. Each of the seven plugs installed contained four thermocouples at varying depths. TC1 was closest to the surface of the heatshield, while TC4 was farthest away from the surface. Prior to launch, modeling efforts predicted that the thermocouples closest to the surface of the heatshield (~ 0.25 cm depth, TC1) at the leeward shoulder of the capsule would be destroyed due to the recession of the heatshield surface. This was not the case, as data was gathered throughout the entire EDL sequence from all of the thermocouples. For MISP 3, MISP 6, and MISP 2, it is possible to see when TC 1 was predicted to burn out (vertical dashed line), and how the solid line (flight data) shows that the thermal couple survived. Among other reasons, it is believed that errors in the predicted transition point along the capsule and models used for the gas/surface interactions led to these large over-predictions in the recession rate [94]. This over-prediction translates into an over designed and more massive heatshield that must be carried from the Earth all the way to Mars. A more detailed discussion of the MSL heatshield will be presented in Chapter 4.

Despite the ongoing great success of this mission, these discrepancies show the need for improvement of modeling capabilities, and how fundamental knowledge gaps have large implications on the uncertainties that need to be incorporated into the design process. These technologies are developed through a combination of theoretical, numerical, and experimental work, which leaves a wide range of topics which could be studied. In order to ensure the relevance of this work, it is important to align the subjects investigated with NASA's view for future technology development, along with advancing fundamental scientific research.

1.3 Organization and Objectives of Thesis

Motivated by the recent MSL results, and staying true to the objectives outlined in the NASA Space Technology Roadmaps and Priorities report, this thesis specifically focuses on advancing

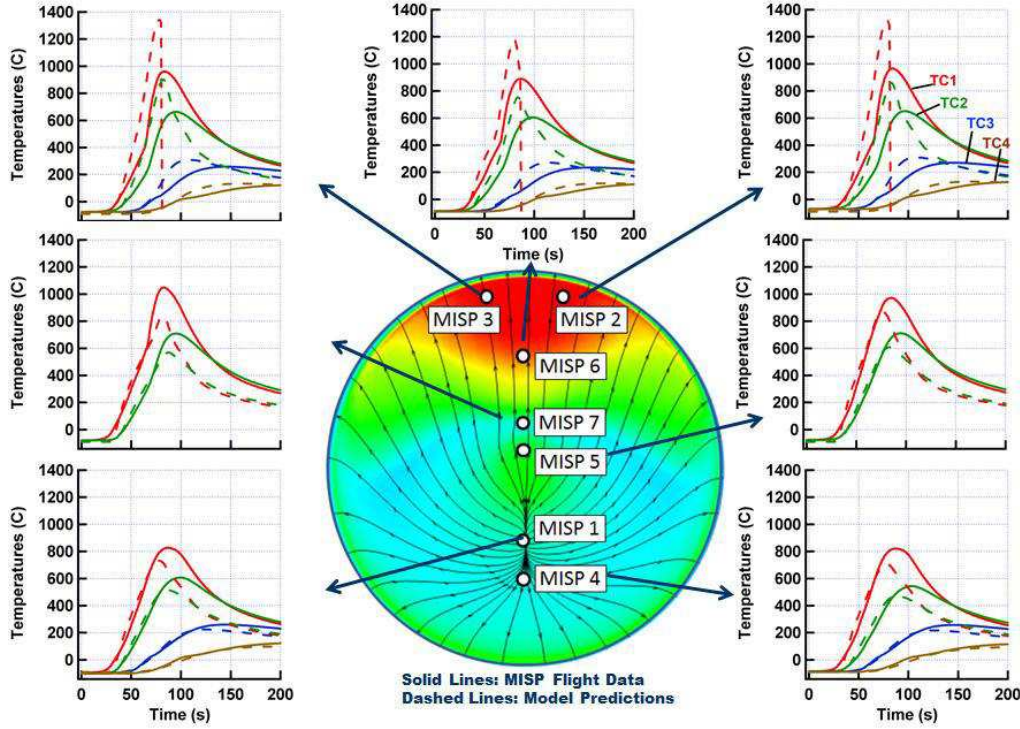


Figure 1.2: Reconstructed data taken from the MEDLI Integrated Sensor Plug (MISP) instrument incorporated into the MSL heatshield. Each plot contains temperature data *vs.* time for thermocouples at varying depths in the heatshield (TC1—TC4), with the dashed lines showing model predictions, and the solid lines showing actual flight data. Image taken from Bose *et al.* [21], reproduced with permission from the author.

ground testing facilities, computational methods for reacting flows, and computational models for ablative heatshields; all subjects which are highly relevant to EDL technologies. Chapter 2 proposes a new ground testing facility for hypervelocity flows; Chapter 3 investigates a novel, computationally efficient numerical method for modeling hypervelocity reacting flows; and Chapter 4 focuses on ablative heatshields.

1.3.1 Ground Testing Facilities

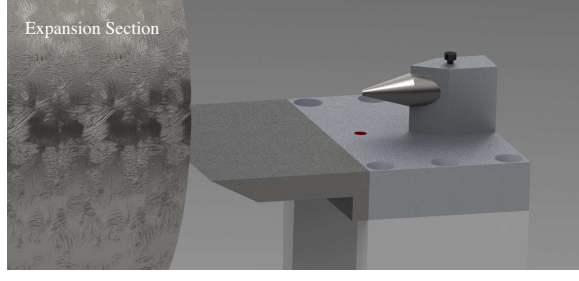
Due to the difficulties in performing flight tests in the hypervelocity regime, large efforts have been put into developing facilities on the ground that can be used to re-create re-entry-like flows. The two most widely used hypervelocity ground test facilities are the reflected shock tunnel (RST) and the expansion tube (ET). A detailed explanation of the design and operation of these ground testing facilities is provided by Lukasiewicz [90].

In brief, to generate hypersonic flow, the RST processes the test gas with two normal shocks (primary and reflected shock). This high temperature and pressure gas is stagnated, and then

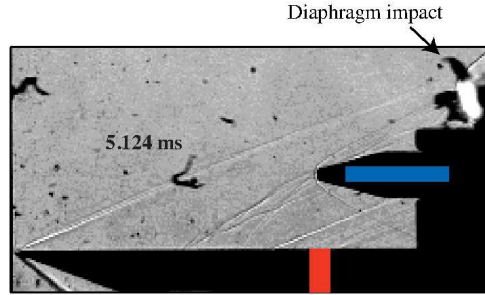
undergoes a steady expansion through a diverging nozzle to generate the desired test conditions. In an ET, a primary shock is generated, similar to the RST, but then the test gas is processed by an unsteady expansion (instead of a reflected shock). This allows the test gas to never be fully brought to rest, contrary to the RST. Hornung [60] provides an overview for the requirements needed for ground simulation of hypervelocity flows, and identifies the general advantages and disadvantages of different facilities. Lukasiewicz [90] and Ben-Yakar and Hanson [13] provide a more detailed description of the advantages and disadvantages of using a reflected shock tunnel *vs.* an expansion tunnel. Due to the different operating modes of these two facilities, reflected shock tunnels are able to produce longer test times than expansion tubes (excluding very high enthalpy conditions), but are limited by the fact that the flow is stagnated during operation of the facility. The high pressure and temperature of the stagnated (reservoir) flow imparts many structural and thermal requirements on the facility, and may also lead to a test gas that is partially dissociated. While expansion tubes benefit from the fact that the flow is never brought to rest (*i.e.* structural and thermal requirements are generally not the main design driver), they are limited by a relatively short test time [60].

The appeal of an ET is that a higher maximum reservoir mass specific enthalpy (h_R) and reservoir pressure (p_R) can be realized than in a RST. The expanded parameter space in an ET is due to the unsteady manner in which the test gas is processed. Unfortunately, successful operation of an expansion tube or tunnel is often hampered by excessive perturbations in the test gas; efforts to reduce these perturbations are critical. Recent work performed by Miller *et al.* [104] in the Stanford Expansion Tube Facility [13, 55] highlights the fact that in addition to noise associated with non-ideal secondary diaphragm rupture, noise in pressure measurements can also correspond to physical impacts of secondary diaphragm particulates with the objects being tested. This is shown in Fig. 1.3, where the effect of secondary diaphragm particulates impacting the structure can be seen in the pressure trace.

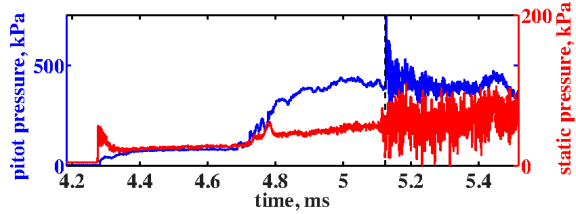
In an attempt to remedy these problems, Chapter 2 proposes a new ground testing facility, named the vertical expansion tunnel, or VET. In this facility, the adverse effects from secondary diaphragm rupture in an expansion tunnel may be reduced or eliminated by orienting the tunnel vertically, matching the test gas pressure and the accelerator gas pressure, and initially separating the test gas from the accelerator gas by density stratification.



(a) Schematic of Pitot-Plate Set Up



(b) Schlieren Image



(c) Pressure Trace

Figure 1.3: Effect of secondary diaphragm particulate impact on pressure traces in an expansion tube. An impact is shown (b) that correlates to large pressure fluctuations measured (c). Figure reproduced from Miller *et al.* [104], with permission from the author.

1.3.2 Reacting Flows

At the high speeds reached by re-entry vehicles entering an atmosphere, not only is the vehicle traveling in a hypersonic regime (Mach number $\gtrsim 5$), but the ordered kinetic energy per unit mass of the gas (which for a body moving at U_∞ can be approximated as $U_\infty^2/2$), is of the same order of the relevant thermo-chemical energy scales in the flow [60]. In this regime, the velocity is so large that the conditions behind a bow shock on a re-entry vehicle would cause the molecular components of the gas to dissociate. The perfect gas assumption breaks down, and the chemical composition and properties of the flow can no longer be assumed to be constant; thermo-chemical effects must be accounted for. These effects must be taken into account when modeling re-entry flight conditions and when used to simulate high enthalpy flows in ground testing facilities. As outlined by Hornung [60],

nozzle freezing in a RST (due to the highly dissociated gas mixture in the reservoir) can produce a test gas which varies greatly from the desired free-flight conditions. In addition, not accounting for the finite amount of recombination reactions during the unsteady-expansion in an ET (radical species present due to dissociation reactions caused by the primary shock) can under-predict facility performance [60]. These effects cannot be predicted analytically, and must be modeled numerically.

A simulation that models reacting flows by using a detailed chemistry model generally requires two additional considerations when compared to a similar non-reacting simulation: a transport equation for each species considered, and a chemical source term for each species considered. When the reacting 3D Navier-Stokes or Euler equations are considered, requiring a transport equation for each chemical species increases the number of simultaneous equations that must be solved from 5 to $5+ns$, where ns is the number of chemical species considered. The inclusion of chemical source terms also has significant consequences when solving these equations: an increase in the computational cost at every time step if a non-linear implicit solver is used, or a decrease in magnitude of the allowable time step if explicit integration methods are used. These complications are due to the stiff nature of chemical source terms. The added complexity dramatically increases the computational cost of performing reacting simulations compared to non-reacting simulations.

One possible solution to reduce the computational complexity of reacting flow problems is to reduce the chemical model used to a more manageable size. This involves choosing kr species that are believed to be most important, where (ideally) $kr \ll ns$, and $ns - kr$ species are eliminated. This decreases the number of species from ns to kr , and therefore reduces the number of equations that need be solved. However, for gases traditionally used in ground testing facilities, or gases considered for Earth or Mars entry (air and CO_2 respectively), gas models have already been significantly reduced [53, 157].

Another solution that has been used in order to continue to reduce the computational time needed for reacting flow problems is to introduce tabulated chemistry. A tabulated chemistry approach generally solves for a small number (one or two) of transported quantities, potentially with or without source terms. All mixture properties are then mapped onto this quantity. One common method to implement tabulated chemistry for simulations involving combustion applications is to create a table based on a laminar diffusion flamelet approach [44, 127, 174]. However, this method generally requires a low Mach number assumption, and only recently have attempts been made to extend this method to compressible flows [175]. In addition, tabulations geared towards combustion applications are generally created based on 1D flame calculations, assuming that the flame structure

in multi-dimensions is unchanged from the 1D problem.

An additional model reduction method that has successfully been applied to combustion applications is a one-step chemistry model [11]. With this method, reactants go directly to products (one reaction), at a finite rate; intermediate species are not considered. In addition, this method has been successfully applied to compressible flows to numerically model reacting detonation waves [35, 61]. However, this method is geared towards systems where there are well defined reactants and products, which is generally not the case for ground testing facilities or re-entry flows, as no flames are being considered. Due to these issues, a different efficient computational method is sought to handle reacting compressible flows.

With these considerations in mind, the Rate-Controlled Constrained-Equilibrium (RCCE) method, first proposed by Keck [70], is chosen. RCCE relies largely on the thermodynamic properties of individual species, rather than solely on reaction rates. This method can be used to greatly reduce the computational complexity of a given problem and does not require knowledge of the reaction zone structure, nor is it limited to flames. This could be especially useful when considering the complicated gas mixtures that are the product of ablative heatshields undergoing thermal decomposition. Rate-Controlled Constrained-Equilibrium tracks one or several constraints through a reacting system, and reconstructs the composition of the gas mixture as a function of the chosen constraint(s). This reconstruction is based on a constrained thermodynamic equilibrium calculation. To date, RCCE has largely been applied to flames in the incompressible regime [56, 63, 65, 71, 70, 80, 163, 164], but there are no fundamental issues limiting the RCCE method only to incompressible flows. Furthermore, to the author's best knowledge, there has only been one previous work applying RCCE to compressible flows [94]. Finally, RCCE has never been previously considered for ablation modeling.

The goal of Chapter 3 is to perform a fundamental investigation of the RCCE method in the context of flows characteristic to ground testing facilities, and re-entry conditions. The effectiveness of different constraints are isolated, and new constraints previously unmentioned in the literature are introduced. The intuition and insight gained from this investigation is later applied to the pyrolysis gas products from an ablative heat shield in Chapter 4.

1.3.3 Ablative Heat Shields

Ablative heatshields, like the one recently used on the successful MSL mission, are designed to dissipate the high heat fluxes experienced during atmospheric entry through material degradation. The heatshield is designed to undergo a phase change so that some of the thermal energy is dissipated

by the ablation of specific components in the heatshield. This translates into a heatshield that is designed to recess upon entry into an atmosphere at hypervelocity speeds. Due to the many complicated physical phenomena occurring when a heat shield starts to ablate, it is difficult to accurately predict the performance of the heatshield (Fig. 1.2). This thesis focuses on phenolic impregnated carbon ablators (PICA) heatshields, as this material is currently being studied and used by NASA, SpaceX, and ESA. This material was first used as the forebody heat shield on the Stardust mission launched in 1999 [159], and was more recently used as the heatshield material for MSL [21]. PICA is a composite material that is formed by combining a porous carbon fiber matrix with a phenolic-resin. As the composite material is heated, the resin begins to thermally degrade at a lower temperature than the fibers. Pyrolysis gases are created as the resin undergoes a thermal decomposition, and these gases flow internal to the heatshield before being injected into the boundary layer above the heatshield. The properties of these pyrolysis gases play a prime role in determining the overall thermal response of the heatshield.

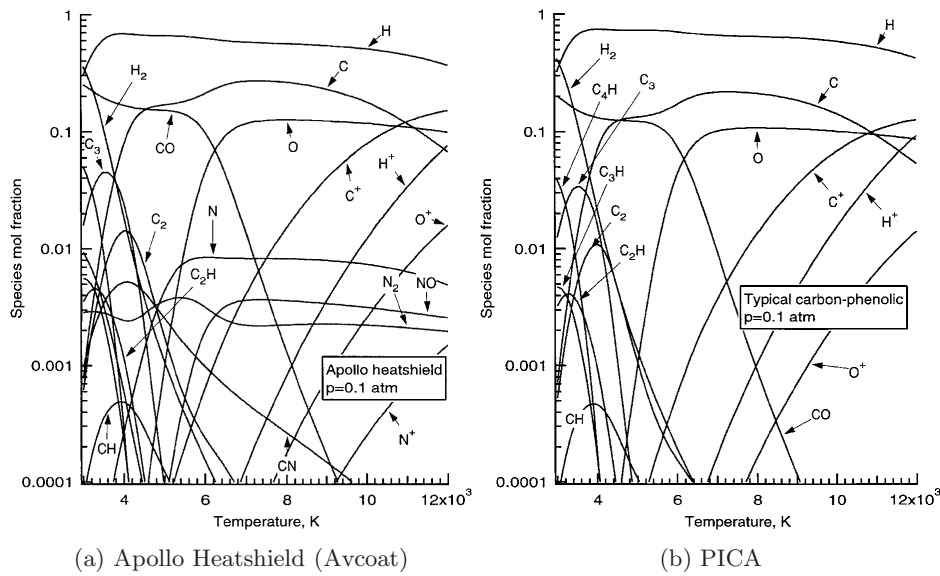


Figure 1.4: Example thermodynamic equilibrium gas mixture produced from the Avcoat material used in the Apollo Heatshield (**a**), and from PICA (**b**). Figure reproduced from Park *et al.* [122].

Unfortunately, in the ablation community, there is a large disconnect between the physical and chemical properties of the PICA material, and the pyrolysis gases created. For example, there is little discussion in the published literature pertaining to the choice of elemental composition for the pyrolysis gas mixture, and the elemental composition of the pyrolysis gas mixture is also assumed to be constant [26, 96, 106, 108, 117, 122]. In addition, a constant elemental composition has been used to describe gas mixtures at unrealistically high temperatures, such as in Fig. 1.4, where

equilibrium calculations are shown using the same elemental composition up to 12000 K. The MSL data analysis predicted a maximum surface temperature of the heatshield to be ~ 2000 K [21], and simulations performed on sample Earth re-entry trajectories predict maximum surface temperatures to be ~ 3500 K [108]. Higher temperatures will be found external to the heatshield, but there the gas composition will be a combination of both the pyrolysis gases, and the atmospheric gas. This implies that using a constant elemental composition for all temperatures, as shown in Fig. 1.4, is an over-simplification of what is occurring around a re-entry vehicle. Furthermore, little experimental data exists beyond Sykes' [162] work from the late 1960s, and only recently have preliminary results been shown re-creating these experiments [182].

The goal of Chapter 4 is to address these issues, and to suggest new approaches to model PICA. This chapter compiles published physical properties of PICA, and investigates the composition of the pyrolysis gases that form at high temperatures internal to a heatshield. This work provides the necessary link between the composition of the solid resin, and the composition of the pyrolysis gases created. This link, combined with a detailed investigation into a reacting pyrolysis gas mixture, allows a much needed consistent, and thorough description of the physical phenomena occurring in a PICA heatshield, and their implications, to be presented in Chapter 4.

Chapter 2

Vertical Expansion Tunnel¹

2.1 Motivation

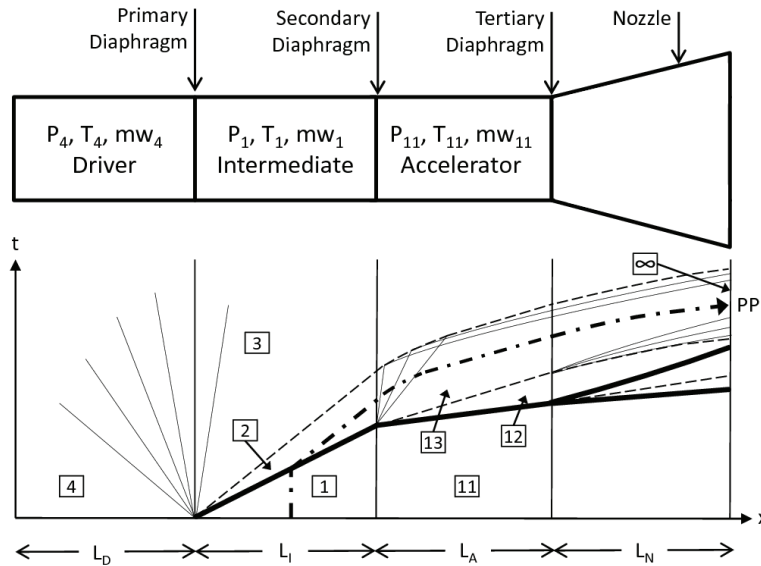


Figure 2.1: Above is a schematic of an expansion tunnel. The states $[4]$, $[1]$ and $[11]$ are the initial (or fill) conditions of the driver, the intermediate and the accelerator sections, respectively. Below is an x - t diagram of expansion tunnel operation. Shock waves are shown as thick solid lines. Expansion characteristics are shown as thinner solid lines. The contact discontinuities are shown as dashed lines. A particle path (PP), representative of the test gas, is shown as a dashed-dot line. L_D , L_I , L_A and L_N are the lengths of the driver tube, the intermediate tube, the accelerator tube, and the nozzle, respectively. The test time is labeled by ∞ .

First proposed by Trimpf and Callis [171, 172], the expansion tube and tunnel (ET) have been developed as hypersonic ground-test facilities for approximately half a century. A schematic for the

¹The work in this chapter was performed in collaboration with N. J. Parziale, and has been published in large part in Parziale, N. P., Rabinovitch, J., Blanquart, G., Hornung, H. G., and Shepherd, J. E. Proposed vertical expansion tunnel. *AIAA Journal*, 51(12):2792–2799, 2013.

operation of a standard expansion tunnel is shown in Fig. 2.1, where each numbered box represents a state in the expansion tunnel. Shock waves are shown as thick solid lines. Expansion characteristics are shown as thinner solid lines. The contact discontinuities are shown as dashed lines. A particle path (PP), representative of the test gas, is shown as a dashed-dot line. L_D , L_I , L_A and L_N are the lengths of the driver tube, the intermediate tube, the accelerator tube, and the nozzle, respectively.

An expansion tunnel operates ideally as follows: a pressure difference between the driver tube and the intermediate tube is prescribed, and the primary diaphragm is instantly ruptured. The primary contact surface impulsively advances from the primary diaphragm station into the intermediate tube. The impulsive advance of the primary contact surface necessitates a pressure discontinuity that processes the test gas (the primary shock wave). Upon arrival of the primary shock wave at the secondary diaphragm station, the secondary diaphragm instantly ruptures, and a secondary contact discontinuity impulsively advances into the accelerator tube. The impulsive advance of the secondary contact surface necessitates a pressure discontinuity that processes the accelerator gas (the secondary shock wave). Concurrent with the secondary diaphragm rupture, an unsteady expansion (centered at the secondary diaphragm station) processes the test gas. The test gas is accelerated, first through this unsteady expansion, and then (in the case of an expansion tunnel) through the diverging nozzle at the end of the accelerator tube. With the addition of a nozzle, a light tertiary diaphragm is required to separate the accelerator section and the nozzle. As shown in Fig. 2.1, the tertiary diaphragm ruptures with the arrival of the secondary shock. This occurs sufficiently far from the test gas that any non-ideal effects associated with this diaphragm rupture will not be a major source of noise during the test time.

In the 1960's and 1970's, several expansion tubes and tunnels were constructed and results were reported with significant perturbations in the test flow [102, 116, 153, 158]. The perturbations were likely the result of acoustic waves in the driver gas being transmitted into the test gas and/or non-ideal rupture of the secondary diaphragm. The disruptive acoustic waves that are transmitted to the test gas from the driver gas occur for certain ratios of sound speed across the primary contact surface, a_3/a_2 [124, 125]. Jacobs [62] used numerical techniques to study the introduction of perturbations from the driver gas to the test gas. Mitigation of these unsteady sources of noise by appropriate design and operation of an expansion tube has been successfully demonstrated at the University of Illinois at Urbana-Champaign by Dufrene *et al.* [34]. The effects of the disruptive acoustic waves were decreased by increasing the ratio of the driver pressure to the intermediate pressure (p_4/p_1), which in turn decreased the value of c_3/c_2 . Dufrene *et al.* [34] measured that a value of $c_3/c_2 \approx 0.55$

corresponded to maximum pressure fluctuations of $\pm 50\%$ of the mean value during the test time, which was deemed acceptable from an experimental standpoint.

The non-ideal rupture of the secondary diaphragm can disturb the test gas in three ways: 1) the reduction in useful test time due to finite secondary diaphragm rupture duration [60], 2) the wave system that arises from the reflection of the primary shock wave off the secondary diaphragm can affect the thermo-chemical properties of the gas [10], and 3) the diaphragm particulates can contaminate the test gas by introduction of foreign matter to the test flow [104], reacting with the test gas if the temperature is sufficiently high.

Since the inception of the simple shock tube, significant efforts have been made to understand and mitigate diaphragm rupture issues [42, 126, 146, 154, 180]. Researchers have extended this basis of knowledge to the problems associated with secondary diaphragm rupture in an expansion tube [41, 104, 144, 179]. Furthermore, models of the secondary diaphragm rupture process have been formulated and can be found in the literature [10, 115]. The particulates, which travel on the order of the test flow velocity, can also impact and damage the test article [104, 179].

A number of expansion tube/tunnel facilities exist, including the X facilities at the University of Queensland [115], the HYPULSE facility at NASA [38], the JX-1 facility at Tohoku University [150], the 6-inch expansion tube at Stanford University [13, 55], the HET facility at University of Illinois at Urbana-Champaign [34], and the LENS X facility at CUBRIC [58]. These facilities have been used successfully for hypersonic aerodynamics and combustion research. Nevertheless, some of the proceedings and articles show results from these facilities with significant test gas perturbations (often conveyed through pressure measurements). In particular, many of these perturbations appear in the vicinity of the test gas/accelerator gas interface; this is evidence of the secondary diaphragm rupture adversely affecting the results. Recent work at Stanford has explicitly shown the effect of impact of secondary diaphragm particulates on pressure measurements [104].

In this chapter, a means of mitigating the effects of secondary diaphragm rupture in an expansion tunnel is proposed by eliminating the need for a secondary diaphragm. The secondary diaphragm is no longer required if the facility is oriented vertically and the intermediate and accelerator tubes are filled to the same initial pressure with gases of different density, light over heavy (e.g., He over Air). The intermediate/accelerator interface would be initially separated by a fast acting sliding valve, allowing the facility to be filled with the accelerator gas and test gas and reducing the diffusion across the interface. The fast acting valve would be removed prior to the bursting of the primary diaphragm, leaving the interface hydrodynamically stable. This facility is termed the vertical expansion tunnel

(VET). In the following sections, an overview of expansion tubes/tunnels is provided, a comparison of the available parameter space in a vertical expansion tunnel (VET), an expansion tunnel (ET), and a reflected shock tunnel (RST) is presented. The comparison is restricted to perfect-gas conditions. Perfect-gas quasi-1D Euler computations are used to calculate the available test time in the VET and the ET; in addition, a referenced method is used to calculate the test time in a RST.

2.2 Available Conditions

In this section, a comparison of the parameter space available in a vertical expansion tunnel (VET), conventional expansion tube (ET), and reflected shock tunnel (RST) is presented. The driver pressure ($p_4 = 8.16$ MPa) is chosen so that it could be filled by conventional research He gas bottles. In all but one case, the test gas temperature is restricted to be below ≈ 2000 K to ensure a fair comparison between facilities and to avoid the detrimental effects of test gas heating [60]. The restriction of maximum test gas temperature permits the perfect-gas assumption. Additionally, at the pressure ratio specified in Table 2.1, ($p_4/p_1 \approx 1000$), the sound speed ratio is $a_3/a_2 \approx 0.57$; at this a_3/a_2 , Dufrene *et al.* [34] observed experimentally that the Paull and Stalker type [125] perturbations in the free-stream were acceptable. To aid in comparison, the test gas in each facility is expanded to a free-stream Mach number of 5.5. In the VET, this necessitates the use of a nozzle at the end of the expansion tube to increase the Mach number, making it an expansion tunnel. Without a nozzle for the VET, useful test conditions cannot be created. A nozzle is not needed at the end of the conventional ET because of the more efficient unsteady expansion.

Pressure-velocity diagrams are used to find the conditions of the test gas as it is processed by the wave systems (for reference, follow the particle path, PP, in Fig. 2.1). The static pressure and velocity must be matched in states $[2]$ and $[3]$ and in states $[12]$ and $[13]$. This is done by plotting the expansion

$$\frac{p_3}{p_4} = \left(1 - \frac{(\gamma_4 - 1)(u_3 - u_4)}{2a_4} \right)^{\frac{2\gamma_4}{\gamma_4 - 1}}, \quad (2.1)$$

and shock relationships

$$\frac{u_2 - u_1}{a_1} = \frac{p_2 - p_1}{\gamma_1 p_1 \sqrt{1 + \frac{(\gamma_1 + 1)(p_2 - p_1)}{2\gamma_1 p_1}}}, \quad (2.2)$$

in pressure - velocity space and finding the point of intersection [87]. Here, γ is the ratio of specific heats, p is the static pressure, u is the velocity, and a is the sound speed. Eq. 2.1 and Eq. 2.2 are annotated for finding the conditions after primary diaphragm rupture and are analogous to the

equations that would be used to evaluate the states [12] and [13]. In the VET, the gas from state [13] is expanded through a nozzle using the usual steady quasi-1D gas-dynamic equations.

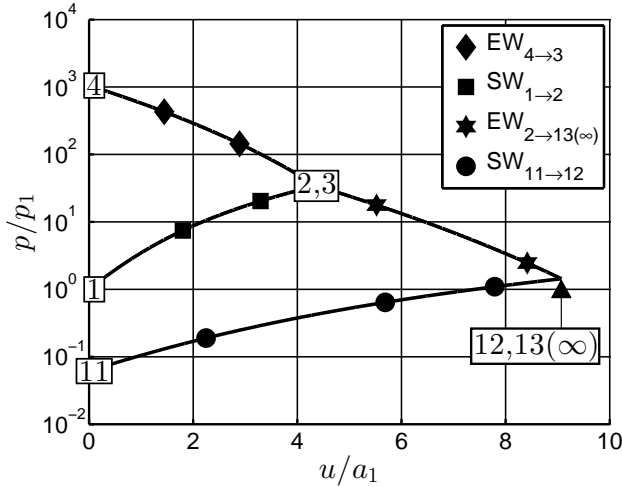


Figure 2.2: Pressure-velocity diagram for a conventional expansion tube. Expansion waves are denoted by EW, and shock waves are denoted by SW. Note that $[13(\infty)]$ denotes the free-stream state.

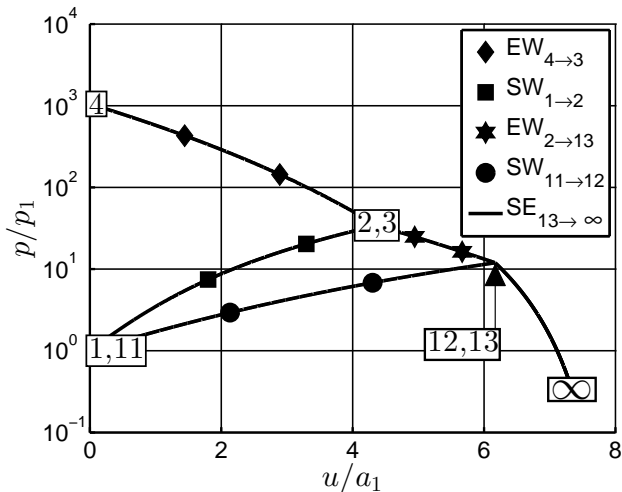


Figure 2.3: Pressure-velocity diagram for a vertical expansion tunnel. Expansion waves are denoted by EW, shock waves are denoted by SW, and the steady expansion is denoted by SE. Note that ∞ denotes the free-stream state.

In a conventional ET, a diaphragm is located between the intermediate and accelerator chambers so that there can be a mismatch of the fill pressures in states [1] and [11] (pressure-velocity diagram in Fig. 2.2). This secondary diaphragm may be eliminated by orienting the tunnel vertically, matching the initial test gas pressure and the accelerator gas pressure, and initially separating the test gas from

the accelerator gas by density stratification (pressure-velocity diagram in Fig. 2.3). The unsteady expansion centered at the secondary diaphragm station is stronger in the ET when compared with the VET; for this reason, the conventional ET is able to reach higher effective reservoir states than the VET. If some sacrifice of the reservoir conditions can be made, the VET can be utilized in hypervelocity ground testing without the problems associated with secondary diaphragm rupture.

The available conditions and test times for a given set of fill pressures are tabulated (Table 2.1) for three types of impulse hypersonic facilities, the VET, the ET, and the RST. The effective reservoir conditions (reservoir pressure and mass specific enthalpy) for the conventional ET and the VET are found by isentropic compression of state [13] to rest. The pressure, p_1 , for the first shock tunnel case (RST-1) is chosen such that it is operated in the tailored mode. The pressure, p_1 , for the second shock tunnel case (RST-2) is chosen so that the temperature in the test gas does not exceed 2000 K. At this pressure ratio (p_4/p_1), the RST will be operated in an over-tailored mode, and the Mach number of the primary shock is 10% higher in RST-2 relative to the tailored condition (RST-1). The pressure, p_1 , for the third shock tunnel case (RST-3) is chosen such that the reservoir mass specific enthalpy is matched to the VET case and requires a 50% increase in the Mach number of the primary shock relative to the tailored condition (RST-1). In this case, the test gas will be reacting, so Cantera [47] with the Shock and Detonation Toolbox [25] is used to evaluate the conditions in the reservoir and through the nozzle. The appropriate thermodynamic data [50, 100] and reaction rates [53] are found in the literature. The test gas is assumed to be in chemical equilibrium in the reservoir and up to the throat of the nozzle. The run conditions at the nozzle exit are found by the integration of a system of coupled ordinary differential equations (accounting for finite-rate chemistry) from the throat to the nozzle exit; the equations are derived in [69]. At matched reservoir mass specific enthalpy, the VET has a higher effective reservoir pressure than in the RST-3 case. This performance advantage of the VET relative to the RST would become increasingly apparent by increasing the local Mach number in state [2] because the total temperature and pressure gain in an unsteady expansion varies strongly with Mach number. In the RST-3 case there is 3.5% NO (by

Table 2.1: Comparison of run conditions available for a reflected shock tunnel (RST), conventional expansion tunnel (ET), and a vertical expansion tunnel (VET).²

	p_4 [He] (MPa)	p_1 [Air] (kPa)	p_{11} [He] (kPa)	h_R (MJ/kg)	p_R (MPa)	T_{Max} (K)	u_∞ (km/s)	p_∞ (kPa)	ρ_∞ (kg/m ³)	T_∞ (K)	M_∞ (-)	τ (μs)
ET	8.16	7.75	0.47	5.7	11	1980	3.1	11	0.048	800	5.5	56
VET	8.16	7.75	7.75	3.8	2.4	1980	2.5	2.6	0.017	534	5.5	82
RST-1	8.16	106	NA	1.8	7.8	1780	1.8	8.4	0.116	252	5.5	6400
RST-2	8.16	77.0	NA	2.0	6.7	2010	1.9	7.3	0.089	285	5.5	5700
RST-3	8.16	7.10	NA	3.8	2.0	3110	2.5	0.9	0.008	553	5.5	920

mole) in the free-stream (calculated using Cantera [47] with the Shock and Detonation Toolbox [25]); all other cases in all facilities produce a negligible amount of NO.

If the quantity of interest in ground-test facilities is effective reservoir conditions, then the capability of the VET is above the RST, but below the ET. One advantage of the ET or VET over the shock tunnel is a lower maximum test gas temperature for a given reservoir mass specific enthalpy, so the detrimental effects of the test gas being partially dissociated and partially vibrationally excited are less severe. To increase test time one can scale the facility size up; however, in the case of a RST nozzle throat heating will become a problem long before the problem would become apparent in the ET or VET [60].

2.3 Test Time Calculation for the RST and ET

Test time calculations for the facilities shown in Table 2.1 require facility sizing choices to be made. An L/d (1.27 m/25.4 mm) ratio of 50 is chosen to minimize the effects of the boundary layer on the walls of the shock tube [109]; and is held constant for the RST, ET, and VET for comparison. The overall length is chosen so that it may fit into a single story lab as a demonstrator-type facility.

In the RST, a 10° half angle nozzle of throat diameter 8.46 mm (1/3 in), length 175 mm, and area ratio 70 is chosen so that the test section is of similar size to the VET. The test time (listed in Table 2.1) was considered to begin after the nozzle startup time (estimate formulated by Smith [156]) and end after the driver gas contaminates the test gas (estimate formulated by Wilson and Davies [32]). This methodology to estimate the test time has been successfully demonstrated by Sudani and Hornung [161].

When calculating the maximum test time for a given total tube length in a conventional ET, the lengths for the intermediate and accelerator sections must be optimized. The sum of their lengths is subject to the L/d constraint given above. Following [34, 181], the calculated test time is the time between the secondary contact discontinuity and intersection of the tail and the reflected head of the secondary expansion wave (Fig. 2.4), which can be solved for using the method of characteristics. If the test section is not located at the ideal spatial location, the test time will be limited by the arrival of the head or reflected tail of the secondary expansion wave. With L/d limited to 50, the ideal lengths for the intermediate and accelerator tubes are determined to be 0.86 m and 0.41 m, respectively, for the conditions given in Table 2.1. In this case, the test time is estimated to be 106 μ s. It is important to note that this is an idealized test time calculation based on 1D inviscid gasdynamic calculations; a discussion of viscous effects (among others) in relation to experimentally

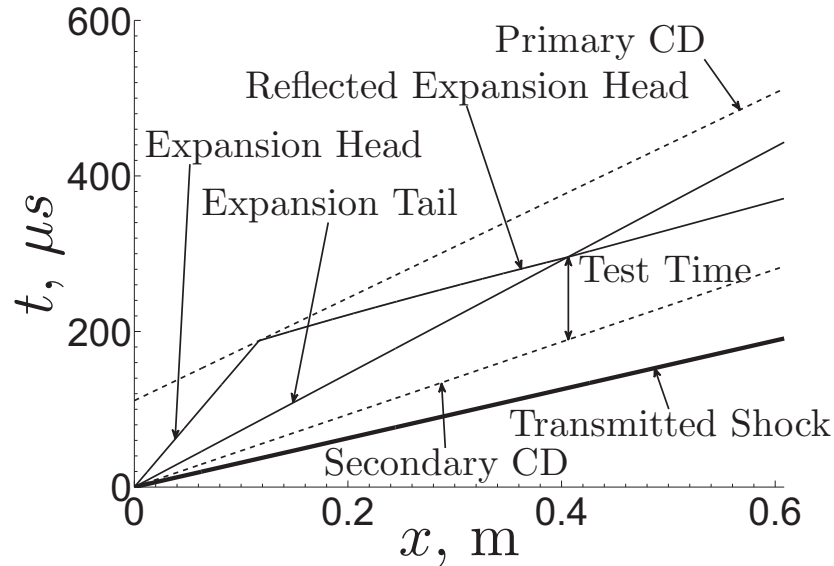


Figure 2.4: Schematic x-t diagram for a conventional ET, focusing on the accelerator tube, and the ideal test time.

observed test times in expansion tunnels will be provided in Sec. 2.5.2. Within the framework of these idealized calculations, increasing the test time of the facility simply requires an increase in the facility length, as the test time scales linearly with combined length of the intermediate and accelerator sections.

Calculation of the ideal test time in the VET requires the consideration of the location and length of the nozzle, both of which significantly affect the test time. Unfortunately, no analytical results are available when a nozzle is present. To explore a large parameter space at a relatively low computational cost, quasi-1D Euler computations are performed based on a method suggested by Glaister [45]. A summary of this method is presented in the following section, followed by the results.

2.4 Ideal Test Time Calculation for the VET

While it is possible to solve the 1D problem analytically as shown previously, the problem becomes inherently 2D or 3D once a nozzle is added. The problem can still be cast in a 1D configuration, but analytical solutions no longer exist to describe the test time after the nozzle has expanded the flow. In this case, numerical simulations are very useful when trying to estimate the duration of the test time. The present analysis is performed assuming that all the gases behave as ideal gases, and that no chemical reactions occur throughout the experiment. Due to the relatively low static

temperatures reached by the gases throughout the different states, this is a valid assumption. In addition, it is assumed that there is no mixing between any of the gases at the fluid interfaces as a result of the short run time. A discussion of non-idealized effects associated with expansion tunnels will be provided in Sec. 2.5.

2.4.1 The Compressible Euler Equations with Area Change

Following the method of Glaister [45], in three dimensions, and in a general orthogonal coordinate system given by (x_1, x_2, x_3) , the Euler equations are given by Eqs. 2.3—2.5.

$$\rho_t + \nabla \cdot (\rho \mathbf{u}) = 0 \quad (2.3)$$

$$(\rho \mathbf{u})_t + \nabla \cdot (\rho \mathbf{u} \mathbf{u}) = -\nabla p \quad (2.4)$$

$$e_t + \nabla \cdot [\mathbf{u}(e + p)] = 0 \quad (2.5)$$

Combining these with Eq. 2.6, the equation of state for an ideal gas, allows the flow of an unsteady compressible inviscid fluid to be solved for.

$$e = \frac{p}{\gamma - 1} + \frac{1}{2} \rho \mathbf{u} \cdot \mathbf{u} \quad (2.6)$$

Here, $\rho = \rho(\mathbf{x}, t)$, $p = p(\mathbf{x}, t)$, $e = e(\mathbf{x}, t)$, and $\mathbf{u} = \mathbf{u}(\mathbf{x}, t) = [u_1(\mathbf{x}, t), u_2(\mathbf{x}, t), u_3(\mathbf{x}, t)]^T$ represent the density, pressure, total energy, and the three components of velocity, respectively, at a general position in space given by $\mathbf{x} = (x_1, x_2, x_3)^T$ and at time t . The divergence and gradient operators are left in a general form, and to evaluate these equations, the appropriate operator must be used based on the chosen coordinate system.

In a general 3D orthogonal coordinate system, a line element $d\mathbf{s}$ can be written as

$$d\mathbf{s} = \xi_1 dx_1 \hat{\mathbf{x}}_1 + \xi_2 dx_2 \hat{\mathbf{x}}_2 + \xi_3 dx_3 \hat{\mathbf{x}}_3, \quad (2.7)$$

where ξ_1 , ξ_2 , and ξ_3 are scalar lengths. In Eq. 2.7, $\hat{\mathbf{x}}_1$, $\hat{\mathbf{x}}_2$, and $\hat{\mathbf{x}}_3$ are the unit vectors parallel to their specific coordinate lines. Assuming an ideal nozzle, all changes in the flow depend only on one coordinate direction. In this case, it is assumed that all variables are a function of only x_1 and t , where the x_1 coordinate corresponds to the location along the centerline of the nozzle. It is now possible to write $\mathbf{u} = [u(x_1, t), 0, 0]^T = u$, which is a parallel flow assumption, and is only valid for nozzles where the nozzle area varies relatively slowly. With this simplifying assumption, Eq. 2.3—2.5

can be re-written as follows

$$(\xi_1 \xi_2 \xi_3 \rho)_t + (\xi_2 \xi_3 \rho u)_{x_1} = 0 \quad (2.8)$$

$$(\xi_1 \xi_2 \xi_3 \rho u)_t + (\xi_2 \xi_3 \rho u^2)_{x_1} = -\xi_2 \xi_3 \frac{\partial p}{\partial x_1} \quad (2.9)$$

$$(\xi_1 \xi_2 \xi_3 e)_t + [\xi_2 \xi_3 u(e + p)]_{x_1} = 0 \quad (2.10)$$

In order to describe compressible fluid flow through a duct of smoothly varying cross section, ξ_1 can be an arbitrary constant, and here it is assumed that $\xi_1 = 1$. Using this assumption, it is now possible to once again rewrite the Euler equations as

$$(\xi_2 \xi_3 \rho)_t + (\xi_2 \xi_3 \rho u)_{x_1} = 0 \quad (2.11)$$

$$(\xi_2 \xi_3 \rho u)_t + [\xi_2 \xi_3 (p + \rho u^2)]_{x_1} = p \frac{\partial}{\partial x_1} (\xi_2 \xi_3) \quad (2.12)$$

$$(\xi_2 \xi_3 e)_t + [\xi_2 \xi_3 u(e + p)]_{x_1} = 0 \quad (2.13)$$

In the above equations, the left hand side is similar to the 1D compressible Euler equations in conservative form, while there is an additional source term added to the right hand side that is not present in the classic 1D Euler equations. In order to simplify these equations further, Glaister uses the notation $S(r) = \xi_1 \xi_2$, so that $S(r)$ represents the cross-sectional area of the duct at a point r , where r is the distance in the x_1 direction. This system of equations can then be written as

$$[S(r)\mathbf{w}]_t + [S(r)\mathbf{f}(\mathbf{w})]_r = \mathbf{g}(\mathbf{w}), \quad (2.14)$$

where

$$\mathbf{w} = \begin{pmatrix} \rho \\ \rho u \\ e \end{pmatrix}, \quad \mathbf{f}(\mathbf{w}) = \begin{pmatrix} \rho u \\ p + \rho u^2 \\ u(e + p) \end{pmatrix} \quad \text{and} \quad \mathbf{g}(\mathbf{w}) = \begin{pmatrix} 0 \\ p S'(r) \\ 0 \end{pmatrix}. \quad (2.15)$$

Note that it is also possible to obtain Eq. 2.15 by integrating the Euler equations (Eqs. 2.3—2.5) over a cross section at a given point in space. It can be shown that $S(r)\mathbf{f}(\mathbf{w}) = \mathbf{f}[S(r)\mathbf{w}]$, which will be called $\mathbf{F}(\mathbf{W})$, and that $S(r)\mathbf{w}_t = [S(r)\mathbf{w}]_t$, assuming that the geometry of the domain does not change with time. This allows Eq. 2.14 to be re-written as,

$$\mathbf{W}_t + [\mathbf{F}(\mathbf{W})]_r = \mathbf{g}(\mathbf{w}), \quad (2.16)$$

where $\mathbf{W} = S(r)\mathbf{w}$. Following the terminology used by Glaister, this gives rise to a new set of “conserved” variables; \mathcal{R} , E , and \mathcal{P} . $\mathcal{R} = S(r)\rho$, $E = S(r)e$ and $\mathcal{P} = S(r)p$. It is important to note that with these new conserved variables, the gas velocity, speed of sound, and enthalpy remain the same: $U = u$, $a = \sqrt{\gamma p/\rho} = \sqrt{\gamma \mathcal{P}/\mathcal{R}}$, and $h = (e + p)/\rho = (E + \mathcal{P})/\mathcal{R} = H$. In addition, the Jacobian remains unchanged:

$$\mathbf{A} = \frac{\partial \mathbf{F}(\mathbf{W})}{\partial \mathbf{W}} = \frac{\partial \mathbf{f}(\mathbf{w})}{\partial \mathbf{w}}. \quad (2.17)$$

Finally, the Euler equations for duct flow are written as

$$\begin{pmatrix} \mathcal{R} \\ \mathcal{R}U \\ E \end{pmatrix}_t + \begin{pmatrix} \mathcal{R}U \\ \mathcal{P} + \mathcal{R}U^2 \\ U(E + \mathcal{P}) \end{pmatrix} = \begin{pmatrix} 0 \\ \mathcal{P} \frac{S'(r)}{S(r)} \\ 0 \end{pmatrix}. \quad (2.18)$$

with

$$E = \frac{\mathcal{P}}{\gamma - 1} + \frac{1}{2}\mathcal{R}U^2. \quad (2.19)$$

2.4.2 Roe Solver

A standard Roe Riemann Solver [145] is used to solve these equations. To denote Roe averaged values, the notation \tilde{Y} is used, where

$$\tilde{Y} = \frac{\sqrt{\mathcal{R}_L}Y_L + \sqrt{\mathcal{R}_R}Y_R}{\sqrt{\mathcal{R}_R} + \sqrt{\mathcal{R}_L}}. \quad (2.20)$$

L and R refer to the left and right cell values, as the averaged quantities are calculated at cell interfaces. The eigenvalues of $\tilde{\mathbf{A}}$ can be calculated to be

$$\tilde{\lambda}^{(1)} = \tilde{U} - \tilde{a}, \quad \tilde{\lambda}^{(2)} = \tilde{U}, \quad \tilde{\lambda}^{(3)} = \tilde{U} + \tilde{a} \quad (2.21)$$

with corresponding eigenvectors of

$$\tilde{\mathbf{e}}^{(1)} = \begin{pmatrix} 1 \\ \tilde{U} - \tilde{a} \\ \tilde{H} - \tilde{U}\tilde{a} \end{pmatrix}, \quad \tilde{\mathbf{e}}^{(2)} = \begin{pmatrix} 1 \\ \tilde{U} \\ \frac{1}{2}\tilde{U}^2 \end{pmatrix} \quad \text{and} \quad \tilde{\mathbf{e}}^{(3)} = \begin{pmatrix} 1 \\ \tilde{U} + \tilde{a} \\ \tilde{H} + \tilde{U}\tilde{a} \end{pmatrix}, \quad (2.22)$$

where $\tilde{a} = (\gamma - 1)(\tilde{H} - \frac{1}{2}\tilde{U}^2)$.

A numerical approximation for $\tilde{\mathbf{g}}(\mathbf{w})$ must be used, and Glaister proposed that

$$\tilde{g}_2(\mathbf{w}^n) = \frac{S_j - S_{j-1}}{\Delta r} \frac{\tilde{\rho}\tilde{a}^2}{\gamma} \quad (2.23)$$

is a natural choice for this approximation. Here, S_j represents the average cross sectional area over cell j . With this notation, it is easy to see that to go from this new set of conserved variables to the more traditional set of conserved variables, the simple relation of $\mathbf{w}_j^n = \frac{\mathbf{W}_j^n}{S_j}$ must be used.

The fluxes are projected onto the eigenvectors of the system so that a standard explicit update step can be employed. In addition to the standard wave strengths being obtained for the Euler equations, $\tilde{\mathbf{g}}(\mathbf{w}^n)$ is also projected onto the eigenvectors which modifies the standard wave strengths that result from the Euler equations. Cell values are updated using a flux difference splitting method which is outlined in Eq. 2.24.

$$\mathbf{W}_j^{n+1} = \mathbf{W}_j^n - \frac{\Delta t}{\Delta r} \left(\sum_{\tilde{\lambda}_{j+\frac{1}{2}}^{(i)} \leq 0} \tilde{\lambda}_{j+\frac{1}{2}}^{(i)} \tilde{\gamma}_{j+\frac{1}{2}}^{(i)} \tilde{\mathbf{e}}_{j+\frac{1}{2}}^{(i)} + \sum_{\tilde{\lambda}_{j-\frac{1}{2}}^{(i)} \geq 0} \tilde{\lambda}_{j-\frac{1}{2}}^{(i)} \tilde{\gamma}_{j-\frac{1}{2}}^{(i)} \tilde{\mathbf{e}}_{j-\frac{1}{2}}^{(i)} \right) \quad (2.24)$$

Here, the summations are performed over i , where $i = 1, 2, 3$. The subscripts refer to the cell interface ($j \pm 1/2$) where each value is calculated, the regular superscripts (n) correspond to a time step, and the superscripts in brackets (i) correspond to a component ($i \in 1, 2, 3$).

Additionally, $\tilde{\gamma}^{(i)}$ refers to the modified wave strength, where

$$\tilde{\gamma}^{(i)} = \tilde{\alpha}^{(i)} + \tilde{\beta}^{(i)} / \tilde{\lambda}^{(i)}. \quad (2.25)$$

The $\tilde{\alpha}^{(i)}$ wave strengths are the standard Roe-averaged wave strengths, where

$$\tilde{\alpha}^{(1)} = \frac{1}{2\tilde{a}^2}(\Delta_r \mathcal{P} - \tilde{\mathcal{R}}\tilde{a}\Delta_r U), \quad \tilde{\alpha}^{(2)} = \Delta_r \mathcal{R} - \frac{\Delta_r \mathcal{P}}{\tilde{a}^2} \quad \text{and} \quad \tilde{\alpha}^{(3)} = \frac{1}{2\tilde{a}^2}(\Delta_r \mathcal{P} + \tilde{\mathcal{R}}\tilde{a}\Delta_r U). \quad (2.26)$$

The Δ_r operator is the difference in value between different cells, so that $\Delta_r U_{j+1/2} = U_{j+1} - U_j$. The $\tilde{\beta}^{(i)}$ in Eq. 2.24 takes into account changes in cross sectional area and can be expressed as

$$\tilde{\beta}^{(1)} = \frac{\tilde{\mathcal{R}}\Delta_r S}{2\gamma\tilde{S}}[(\gamma-1)\tilde{U} + \tilde{a}], \quad \tilde{\beta}^{(2)} = -\frac{(\gamma-1)\tilde{\mathcal{R}}\tilde{U}\Delta_r S}{\gamma\tilde{S}}, \quad \text{and} \quad \tilde{\beta}^{(3)} = \frac{\tilde{\mathcal{R}}\Delta_r S}{2\gamma\tilde{S}}[(\gamma-1)\tilde{U} - \tilde{a}], \quad (2.27)$$

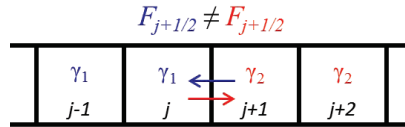


Figure 2.5: Schematic for the flux correction suggested by Abgrall and Karni when dealing with an interface between two different fluids.

where $\tilde{S}_{j+1/2} = \sqrt{S_{j+1}S_j}$.

2.4.3 Treatment of Fluid Interfaces

The above numerical method assumes that γ is constant for every cell in the domain. This is not true for the present investigation. It is possible to create unphysical oscillations at the interface between two different fluids if no special care is taken when calculating values at these fluid interfaces. A modification to the above scheme is used that was originally suggested by Abgrall and Karni [7].

Abgrall and Karni [7] suggested that a way to avoid unphysical oscillations at fluid interfaces is to calculate two separate fluxes between the different fluids. A schematic explaining this method is shown in Fig. 2.5, where the cell face at $j + \frac{1}{2}$ is the interface between two different fluids with two different ratios of specific heats, γ_1 and γ_2 , respectively. When updating cell j , γ_1 is used to calculate the properties needed at $j + \frac{1}{2}$, and when updating cell $j + 1$, γ_2 is used to calculate the values needed at $j + \frac{1}{2}$. In addition, the order in which γ values are updated in the domain based on a scalar transport equation need be performed carefully. A more detailed explanation can be found in Abgrall and Karni's original work [7].

The drawback is that this scheme no longer conserves total energy since two different fluxes are calculated at the same interface. In addition, the scheme uses “frozen” thermodynamics, or γ values from the previous time step to calculate the new values. Abgrall and Karni [7] show that across a material interface where pressure and velocity are constant (a standard contact discontinuity), the errors induced due to the different fluxes used and the lag in updating γ are actually opposite in sign, and very similar in magnitude. In addition, there are only three material interfaces in the current simulations, and these interfaces are the only places where total energy is not conserved. When the number of grid points in the domain is increased, the relative loss of total energy reduces. It has been checked that the loss of total energy in the simulations run for this investigation were negligible ($< 0.001\%$).

In order to accurately describe the location of the different fluids, a method has to be implemented to track the location of the fluid interfaces. A simple advection equation (Eq. 2.28) is solved where

ϕ is a passive scalar.

$$\frac{\partial \phi}{\partial t} + u \frac{\partial \phi}{\partial x} = 0 \quad (2.28)$$

The levelset function, ϕ , is used to determine the location of the different gases. For the case where the driver and accelerator gases are the same and the test gas is different, it is simple to assign ϕ an initial value of 1 in the driver and accelerator sections, and a value of -1 in the intermediate section. If a nozzle is used, it is assumed that the nozzle will be filled with low pressure air, and therefore ϕ in this section is also assigned a value of -1. After advecting ϕ , a hard switch is employed such that if $\phi \geq 0$, the properties of driver/accelerator gas are used; and if $\phi < 0$, the properties of the intermediate gas are used. A modified form of the semi-Lagrangian scalar scheme discussed in [136] is used to solve the scalar advection equation. Traceback of the grid-node particles is achieved using first-order backward Euler time integration. A 5th-order accurate Lagrange polynomial is used for interpolating the scalar at the traced-back location. A switch to monotonicity preserving first-order linear interpolation is triggered if the interpolated scalar value breaches physical bounds.

2.4.4 Higher-Order Corrections

The numerical scheme explained in Section 2.4.2 is at best first order and diffusive, which means shocks and contact discontinuities are unphysically spread over many grid cells. To help alleviate this problem, a higher-order flux correction is added using wave limiters [84]. In order to implement this, an additional term is added to Eq. 2.24, so that it is modified to

$$\mathbf{W}_j^{n+1} = \mathbf{W}_j^n - \frac{\Delta t}{\Delta r} \left(\sum_{\tilde{\lambda}_{j+\frac{1}{2}}^{(i)} \leq 0} \tilde{\lambda}_{j+\frac{1}{2}}^{(i)} \tilde{\gamma}_{j+\frac{1}{2}}^{(i)} \tilde{\mathbf{e}}_{j+\frac{1}{2}}^{(i)} + \sum_{\tilde{\lambda}_{j-\frac{1}{2}}^{(i)} \geq 0} \tilde{\lambda}_{j-\frac{1}{2}}^{(i)} \tilde{\gamma}_{j-\frac{1}{2}}^{(i)} \tilde{\mathbf{e}}_{j-\frac{1}{2}}^{(i)} \right) - \frac{\Delta t}{\Delta r} (\hat{\mathbf{F}}_{j+\frac{1}{2}} - \hat{\mathbf{F}}_{j-\frac{1}{2}}), \quad (2.29)$$

with

$$\hat{\mathbf{F}}_{j-\frac{1}{2}} = \frac{1}{2} \sum_{i=1}^3 |\tilde{\lambda}_{j-\frac{1}{2}}^{(i)}| \left(1 - \frac{\Delta t}{\Delta r} |\tilde{\lambda}_{j-\frac{1}{2}}^{(i)}| \right) \tilde{\mathcal{B}}_{j-\frac{1}{2}}^{(i)}. \quad (2.30)$$

$\tilde{\mathcal{B}}_{j-\frac{1}{2}}^{(i)} = \Phi(\theta_{j-\frac{1}{2}}^{(i)}) \mathcal{B}_{j-\frac{1}{2}}^{(i)}$, where $\Phi(\theta)$ is a limiting function, and $\mathcal{B}_{j-\frac{1}{2}}^{(i)} = \tilde{\alpha}_{j-\frac{1}{2}}^{(i)} \tilde{\mathbf{e}}_{j-\frac{1}{2}}^{(i)}$. A Van Leer limiting function is used [173]:

$$\Phi(\theta) = \frac{\theta + |\theta|}{1 + \theta}. \quad (2.31)$$

A careful choice must be made for θ in order to deal with the relatively large change in properties at the interfaces between the different sections of the expansion tunnel. The initial pressure ratio of

≈ 1000 between the driver gas and intermediate gas creates extremely steep gradients and rapidly changing eigenvectors. Lax and Liu [81] suggested a robust function for θ that is designed to work with systems of non-linear equations. They define

$$\theta_{j-\frac{1}{2}}^{(i)} = \frac{\hat{\mathcal{B}}_{J-\frac{1}{2}}^{(i)} \cdot \mathcal{B}_{j-\frac{1}{2}}^{(i)}}{\mathcal{B}_{j-\frac{1}{2}}^{(i)} \cdot \hat{\mathcal{B}}_{j-\frac{1}{2}}^{(i)}}, \quad (2.32)$$

where

$$\hat{\mathcal{B}}_{J-\frac{1}{2}}^{(i)} = (\tilde{\mathbf{l}}_{j-\frac{1}{2}}^{(i)} \Delta \mathbf{W}_{J-\frac{1}{2}}) \tilde{\mathbf{e}}_{j-\frac{1}{2}}^{(i)}, \quad (2.33)$$

and $\tilde{\mathbf{l}}$ is the appropriate left eigenvector using Roe-averaged quantities. In addition, J changes value based on the sign of the eigenvector, so that the limiting is performed in an upwinded or downwinded manner as necessary, so

$$J = \begin{cases} j - 1 & \text{if } \tilde{\lambda}_{j-\frac{1}{2}}^{(i)} > 0 \\ j + 1 & \text{if } \tilde{\lambda}_{j-\frac{1}{2}}^{(i)} < 0. \end{cases} \quad (2.34)$$

These higher-order corrections do a good job at making both contact discontinuities and shocks sharper in the simulations. The flux limiters are not used in the vicinity of walls, or at the interface between two fluids with different values of γ .

2.4.5 Entropy Fix

Due to the large pressure ratios needed initially in order to achieve relevant test conditions, an entropy fix is required to avoid entropy-violating (expansion) shocks in the solution. The entropy fix proposed by Sanders *et al.* [149] is implemented, and no entropy violating solutions are observed.

2.4.6 Numerical Results: Verification

A 1D perfect-gas Euler computation with the same initial conditions as the proposed VET but *without* a nozzle (see Table 2.1) is performed. Without a nozzle, numerical results can be compared directly to 1D analytical results, and this comparison serves as a verification of the numerical method used. In this simulation, $L_D = 2.0$ m, $L_I = 0.86$ m, and $L_A = 1.0$ m. The subscripts correspond to the driver section, intermediate section, and accelerator section, respectively. The accelerator section is made longer than the theoretical necessary length of 0.41 m (see Section 2.3) to ensure that the tail and reflected head of the secondary expansion intersect inside the computational domain, as sketched in Fig. 2.4. The primary diaphragm is located at $x = 0$ m, and the interface between the

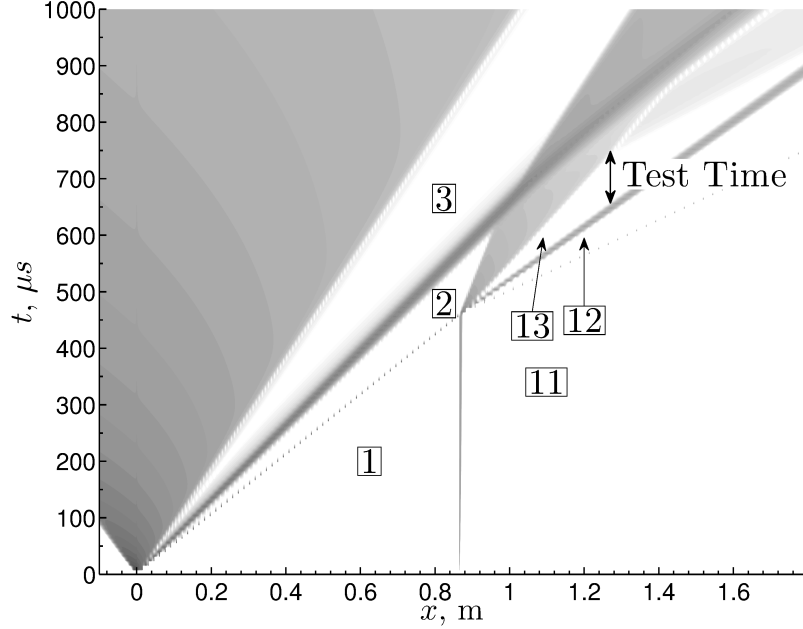


Figure 2.6: Numerical x-t diagram for a 1D perfect gas Euler simulation with the same initial conditions as the proposed VET.

intermediate and accelerator sections is at $x = 0.86$ m.

To visualize the results of the 1D perfect-gas Euler computations, a numerical x-t diagram is made using a numerical schlieren method, where contours of the function $-\log(|\frac{\partial \rho}{\partial x_1}|)$ are plotted (Fig. 2.6). The simulation results capture the theoretical wave system depicted in Fig. 2.1. There is also good quantitative agreement between the numerical results and the analytical solution. The numerical results differ from the analytical results by no more than the third significant digit ($\approx 0.5\%$) for pressure, velocity or density in states [2] and [3] and states [12] and [13]. The numerical values have been averaged over the respective appropriate section, at $t = 450$ μs for states [2] and [3] and at $t = 600$ μs for states [12] and [13].

Comparison of the test time between the 1D perfect gas Euler simulations and the analytic calculations is also necessary to fully validate the numerical technique. The numerical test time is defined to be when the density is within 1% of the average value of density in the constant region, state [13]. Figure 2.7 shows a comparison between the analytic test time and the numerical test time. While fluctuations during the test time in an experimental facility are expected to be much larger than 1%, we note that these analyses are for validation of the numerical technique.

The analytical test time is calculated to be 106 μs ; the numerical test time is found to be 104 μs . Figure 2.7 shows that the test times are also slightly offset in time from each other. This discrepancy is due to the numerical methods used. Contact discontinuities, which are infinitely thin in the ideal

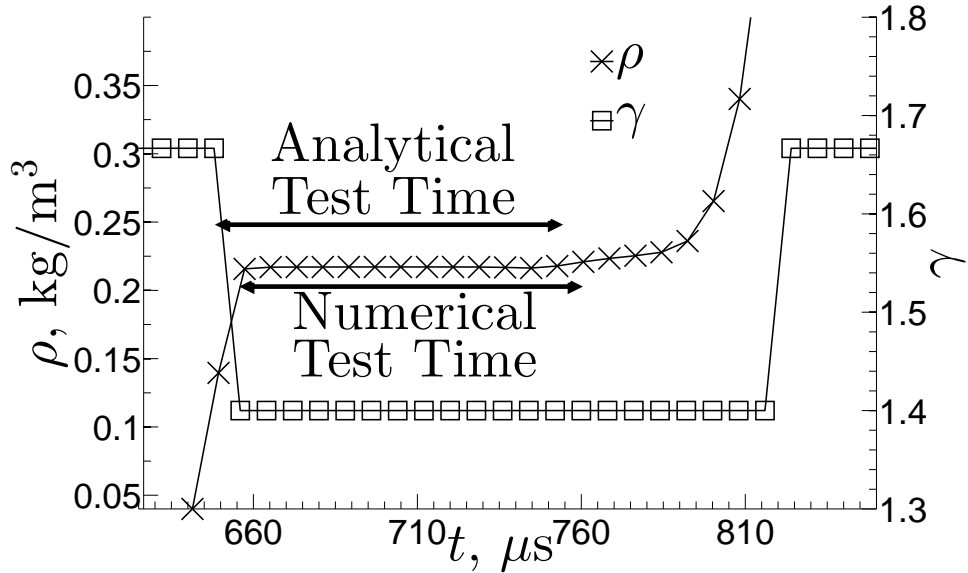


Figure 2.7: Comparison between the analytic test time and the numerical test time for the 1D case.

case, are spread out over a few cells in simulations due to numerical diffusion. In addition, the reflection of waves off of a contact discontinuity of finite thickness may introduce errors in the simulations. Nevertheless, these small differences are acceptable, so quasi-1D Euler simulations are started with the addition of the nozzle at the end of the accelerator tube.

2.4.7 Numerical Results: VET with Nozzle

The addition of a nozzle at the end of the accelerator tube is necessary for useful test conditions to be generated with the VET. The addition of a nozzle also expands the design parameter space that must be investigated. In this analysis, we consider changes to the location of the nozzle and lengths of the intermediate and accelerator sections. The sum of the intermediate and accelerator section lengths is still subject to the constraint $L/d = 50$. The same initial conditions as the proposed VET (Table 2.1) were used. A 10° conical nozzle of length $L_N = 0.16$ m is used (area ratio of 10.7). Prior to the run, the nozzle is considered to be at a state similar to that of a dump tank; air at low pressure ($p_N = 100$ Pa, 750 mTorr). A burst pressure of 30 kPa is specified for the tertiary diaphragm. Until the diaphragm breaks, it acts as a perfectly reflecting, infinitely stiff wall. The primary diaphragm, the interface between the intermediate and accelerator sections, and the tertiary diaphragm are located at 0 m, 0.94 m, and 1.27 m, respectively. The slightly larger length of the intermediate section when compared to a conventional ET (0.94 m vs. 0.86 m) will be justified later.

Figures 2.8 and 2.9 show numerical $x - t$ diagrams with the same fill pressures as the proposed

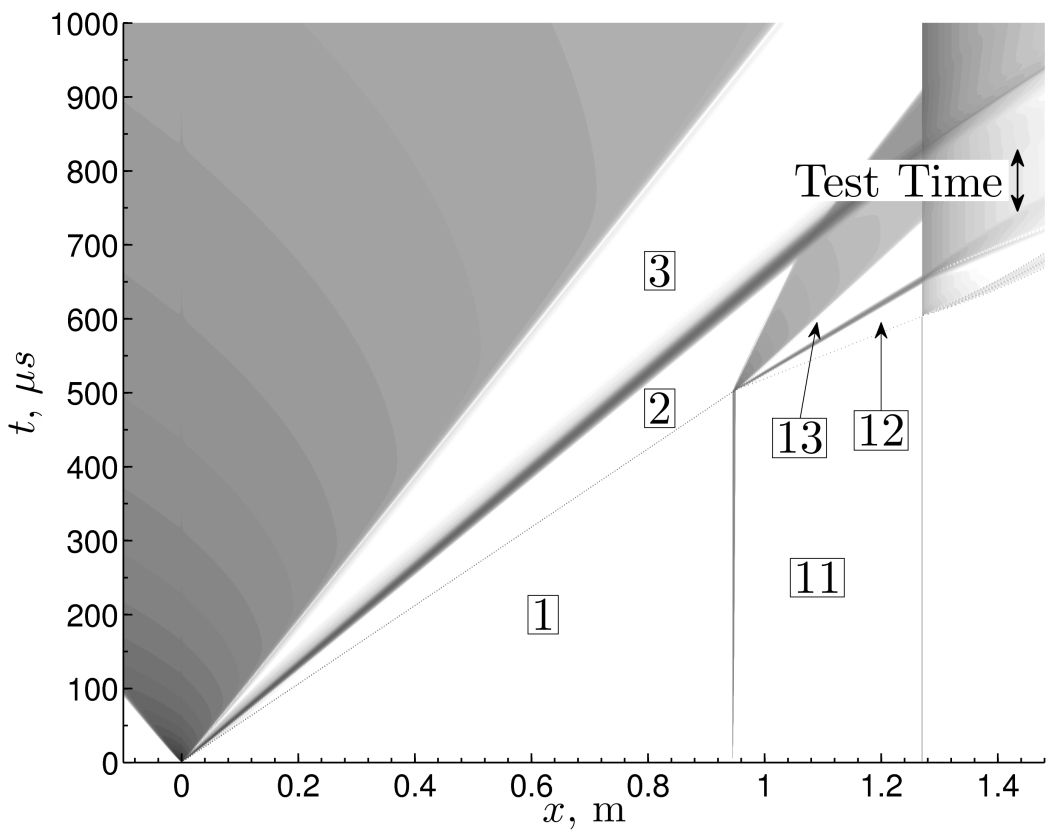


Figure 2.8: Numerical x-t diagram for an expansion tunnel with a 10° half angle diverging conical nozzle.

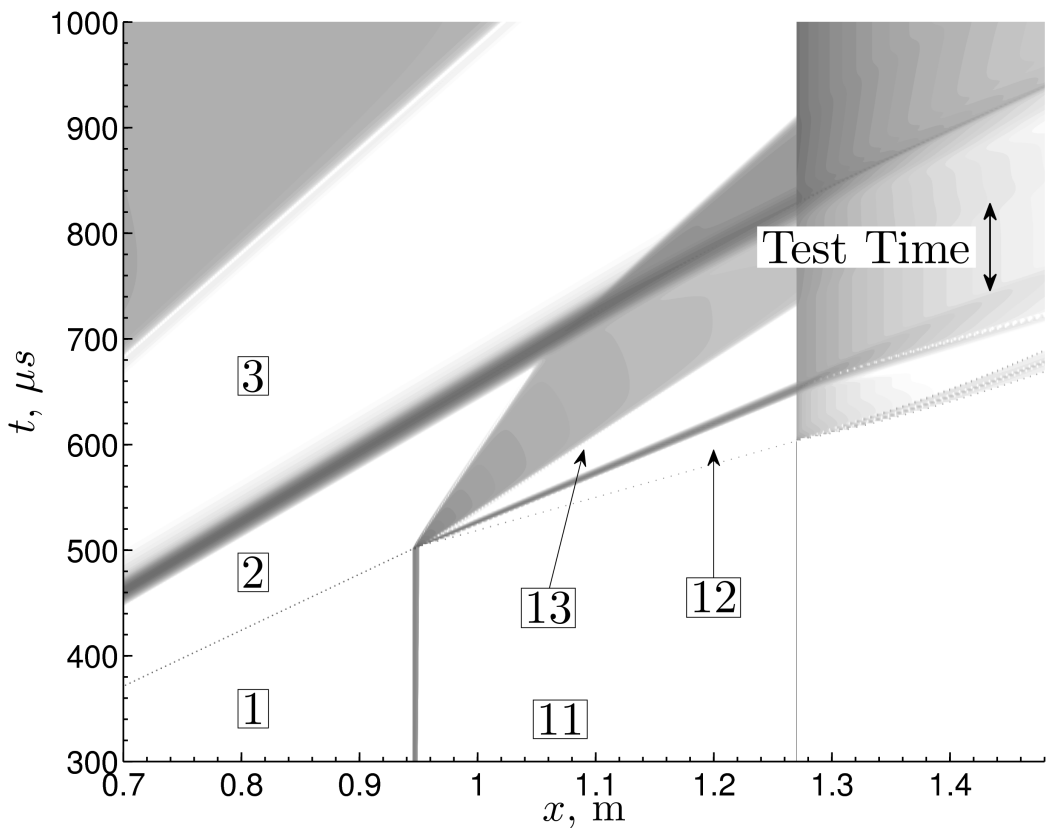


Figure 2.9: A close-up of the accelerator section and nozzle from Fig. 2.8.

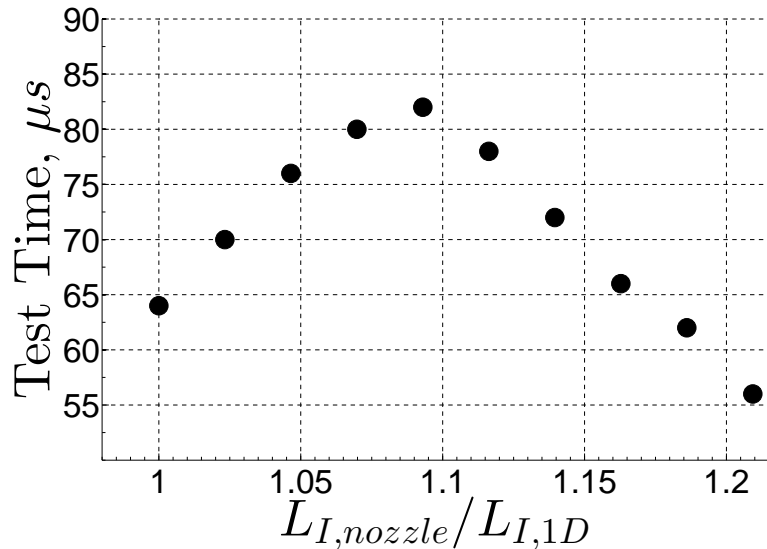


Figure 2.10: Test time for varying lengths of the intermediate and accelerator sections when using a nozzle.

VET (Table 2.1). An unsteady expansion is created when the secondary contact discontinuity enters the nozzle. The trailing characteristic from this unsteady expansion corresponds to the beginning of the test time. The test time is ended when either the tail or reflected head of secondary expansion wave reaches the test location. The qualitative behavior of the nozzle startup processes observed in Fig. 2.9 are consistent with the features seen in previous studies on nozzle start up phenomenon [156].

The predicted test time changes with the intermediate and accelerator lengths (Fig. 2.10). For all cases, the intermediate and accelerator section length sum is held constant at 1.27 m. $L_{I,nozzle}$ refers to the length of the intermediate section when a nozzle is used, and this length is normalized by $L_{I,1D}$, the ideal intermediate section length when no nozzle is used ($L_{I,1D} = 0.86$ m). Increasing the intermediate section length (and reducing the accelerator section length) - with respect to the 1D case - increases the test time. After a certain threshold, the test time starts to decrease. All points to the left of the maximum test time (Fig. 2.10) are limited by the reflected secondary expansion wave head; all points to the right of the maximum test time are limited by the secondary expansion wave tail. The maximum point is where the tail and reflected head of the secondary expansion wave arrive at the test location inside the nozzle at the same time. A maximum test time of 82 μs is found when $L_{I,nozzle} = 0.94$ m and $L_A = 0.33$ m. Traces of γ , ρ , p , u , and M are shown in Fig. 2.11 at the maximum test time. The average flow values (Table 2.2) are calculated during this test time at a downstream location of $x = 1.43$ m, which corresponds to an area ratio of 10.7.

To show that it is possible to have more than one run condition for a given experimental set-up,

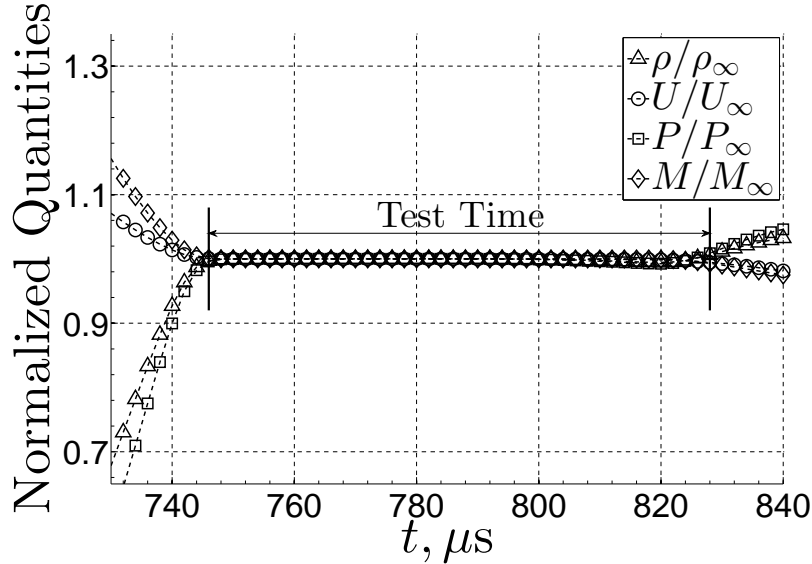


Figure 2.11: Normalized flow conditions at a point ($x = 1.43$ m) corresponding to an area ratio of 10.7.

computations are performed with fill pressures in the intermediate and accelerator tubes doubled and halved from the originally proposed VET conditions (Table 2.2). The data are still sampled at a downstream location corresponding to an area ratio of 10.7 (fixed nozzle length). It is important to note that the maximum static temperature reached in the half pressure trial is approximately 2350 K, which means the perfect-gas assumption will begin to break down, so the calculated properties are presented only as an estimate. Nonetheless, useful test times and test conditions are still generated when the fill conditions of the VET are changed.

2.5 Real Facility Effects

The previous calculations were based on inviscid idealized 1D or quasi-1D gasdynamics. This section outlines some of the physical effects and design considerations that should be accounted for when operating an expansion tunnel or vertical expansion tunnel.

Table 2.2: Comparison of run conditions available for a vertical expansion tunnel (VET) with varying fill pressures.³

	p_4 [He] (MPa)	p_1 [Air] (kPa)	p_{11} [He] (kPa)	h_R (MJ/kg)	p_R (MPa)	T_{Max} (K)	u_∞ (km/s)	p_∞ (kPa)	ρ_∞ (kg/m ³)	T_∞ (K)	M_∞ (-)	τ (μs)
VET-Table 2.1	8.16	7.75	7.75	3.8	2.4	2000	2.5	2.6	0.017	535	5.5	82
VET-halved	8.16	3.88	3.88	4.5	1.5	2330	2.8	1.5	0.009	623	5.6	54
VET-doubled	8.16	15.5	15.5	3.1	3.6	1680	2.3	4.3	0.033	554	5.4	72

2.5.1 Initial Test Gas/Accelerator Gas Separation

For the vertical expansion tunnel, we propose that the intermediate and accelerator chambers are to be initially separated by a fast acting sliding valve. This sliding valve would separate the two tubes during filling, and then be pulled away before the primary diaphragm bursts. The design of such a sliding valve would be similar to one that has been shown to work for detonation-gas interface studies in GALCIT's Detonation Tube [85, 86]. The helium in the accelerator tube is expected to diffuse into the intermediate tube after the sliding valve is pulled away. A characteristic diffusion length scale, L_{diff} , associated with helium and air can be approximated as $L_{diff} \approx \sqrt{Dt_{diff}}$, where D is the binary diffusion coefficient for air and helium, and t_{diff} is a characteristic time. The characteristic diffusion time is chosen to be 50 ms, which is an estimate of the sliding valve opening time. For practical tube fill pressures ($p_1, p_{11} \approx 10$ kPa), $D \approx 0.001$ m²/s [57, 47], which gives a diffusion distance of about $L_{diff} = 7$ mm in $t_{diff} = 50$ ms. This is an acceptable diffusion length and opening time.

2.5.2 Ideal *vs.* Experimental Test Conditions

The application of inviscid 1D gasdynamic calculations has been the basis for expansion tunnel facility design in the past [34]. Some of the discrepancies noted between predicted test conditions and experimental measurements of test conditions will be discussed in this section. Mirels [109] performed a parametric study investigating the effect of boundary layers in shock tubes on the test time. The boundary layer that forms on the tube wall between the shock and contact surface can act as an aerodynamic sink and absorb mass from the core flow of a shock tube, which in turn will cause the contact surface to accelerate, and the shock to decelerate. This can result in the test time in a shock tube to be lower than the test time predicted from an inviscid calculation. Mirels [109] reports that for shock tubes the test time varies as $d^2 P$ and $d^{5/4} P^{1/4}$ for laminar and turbulent boundary layer cases (when viscous forces are considered), respectively. P is the pressure behind the shock, and d is the inner shock tube diameter. An L/d of 50 is chosen for the VET in order to minimize the effect of viscosity in this chapter, though it is important to note that Mirels [109] correlation is based on an absolute value of the diameter and pressure in a shock tube, as the size of the boundary on the tube wall will increase as the Reynolds number decreases behind the primary shock.

The expansion tube at the University of Illinois at Urbana-Champaign [34] used an L/d of 52, with a total facility length of 12 m. Although this expansion tube and the proposed VET vary greatly in

size, the similar L/d ratio permits some comparisons to be drawn. It was found that experimentally measured test times in the expansion tube at the University of Illinois at Urbana-Champaign were significantly ($\sim 50\%$) lower than the test times predicted with 1D gasdynamic calculations [34]. It was originally hypothesized that viscous effects, non-ideal rupture of the secondary diaphragm, and a contact surface with a non-zero width could account for the measured discrepancies [34]. Detailed 2D viscous computations were performed to investigate these discrepancies further [101]. It was found that the effect of the boundary layer growth in the accelerator section was large due to the initially low accelerator fill pressure (26.6 Pa) for the run condition considered. In addition, the low pressure He in the accelerator section was susceptible to air contamination, which also altered the test conditions. Once these effects were accounted for in the 2D simulations, viscous 2D numerical predictions matched well with experimental measurements [101].

Results reported from the 6-inch expansion tube at Stanford University [13] claim that viscous effects actually resulted in test times that were longer than the predicted test times from ideal 1D inviscid calculations. This expansion tube has an L/d of 90, and a facility length of just under 10 m [13]. Ben-Yakar and Hanson [13] stated that the acceleration of the secondary contact surface in the accelerator section lengthened the experimental test time. However, it is unclear if the 1D inviscid calculations performed in this study accounted for the curvature of the reflected expansion head (see Sec. 2.3). The accelerator pressure in the cases analyzed by Ben-Yakar and Hanson [13] were at minimum an order of magnitude higher than the pressure in the accelerator tube analyzed by McGilvray *et al.* [101], so it is possible that viscous effects in the accelerator tube were mitigated.

By construction, the VET maintains a relatively high pressure in the accelerator tube, since the pressure in the accelerator tube must be matched to that of the intermediate tube. This lessens the expected effect of boundary layer growth in the accelerator section, and the susceptibility of the accelerator gas to contamination from air when compared to the facility at the University of Illinois at Urbana-Champaign [34]. In addition, no secondary diaphragm is required in the VET. However, a trade-off is made, as the VET requires a nozzle. Numerical simulations performed by Chue *et al.* [27] highlight some of the difficulties associated with nozzle design for expansion tunnels. Care must be taken to account for the boundary layer that is present at the inlet of the nozzle, among other design considerations.

Due to many discrepancies observed in different experimental facilities, it is clear that experimental measurements or 2D viscous detailed numerical simulations are needed to more accurately predict the expected test conditions for the VET. However, the idealized inviscid quasi-1D gasdy-

namic calculations performed in this chapter for the VET demonstrate that a useful test time can be realized. One possible way to attempt to mitigate the effects that the non-idealized processes will have on the test time is to design an expansion tunnel with a movable secondary diaphragm location, or, in the case of the VET, design the facility with movable sliding valve. Flexibility in the location of the secondary diaphragm/sliding valve allows the facility length optimization calculations previously performed (Fig. 2.10) to be modified based on experimental results. This could help optimize experimental test times for a given run condition, and would allow more flexibility to optimize the test time for different fill conditions.

2.6 Discussions

In this chapter, a test facility configuration termed the vertical expansion tunnel (VET) is proposed. This facility avoids the detrimental effects of secondary diaphragm rupture in a conventional ET by eliminating its necessity. The secondary diaphragm is no longer required if the facility is oriented vertically and the intermediate and accelerator tubes are filled to the same initial pressure with gases of different density, with light gases located over heavy gases (e.g., He over Air) so that the interface is hydrodynamically stable. The intermediate/accelerator interface would be created just before the run by a fast acting sliding valve that would be removed prior to the bursting of the primary diaphragm.

The sliding valve opening time and characteristic diffusion length of the helium into the test gas are shown to be acceptable. The maximum reservoir mass specific enthalpy and pressure of the VET are higher than for a RST, but below the ET values. Perfect-gas quasi-1D Euler computations and performance estimates indicate that the test time in the VET is slightly longer than in the ET, but shorter than in the RST. Increasing the test time of the facility would require an increase in length. In doing so, the machine would not fit into a single story laboratory, and a multi-story design, like that successfully used in vertical shock tubes [9, 24], would be required. If some sacrifice of the reservoir conditions can be made, the VET can be utilized in hypervelocity ground testing to eliminate problems associated with secondary diaphragm rupture while maintaining useful performance.

As previously mentioned, the limited test time in an ET or VET still imposes constraints on possible experiments to be performed. Table 2.2 shows the predicted test time of the VET to be $82 \mu\text{s}$, with $u_\infty = 2.5 \text{ km/s}$. In order to generate steady flow around a test object at these high speeds, a conservative estimate is that the test time is required to be $\tau = 20 \frac{L}{u_\infty}$, where L

is the relevant length scale of the test object [60]. For the VET described in this chapter, with $\tau = 82 \mu\text{s}$, this corresponds to $L = 0.01 \text{ m}$. Even though the diameter of the nozzle at test location is approximately 0.105 cm, not all of this space is usable. This model size will increase linearly with test time, and it is important to note that this is a conservative estimate of the allowable model size.

Throughout this chapter, static temperatures of the gas were kept below 2000 K. In order to generate test conditions relevant to re-entry type flows, the velocity during the test time would have to be increased. As outlined in Sec. 1.3.1, to generate these higher speeds during the test time the chemical composition of the flow throughout the facility can no longer be assumed to be constant. The higher static temperatures of the gases produced would require a computational method to be introduced, to simulate the reacting flow when modeling a test facility. The most common way to model chemical reactions would be to solve transport equations for each species, and to use detailed chemistry. The following chapter introduces a different computational method that is suitable for reacting flows in ground testing facilities, but can also be extended to more complicated mixtures characteristic of ablative heatshields.

Chapter 3

Rate-Controlled Constrained-Equilibrium¹

3.1 Motivation

In order to accurately simulate flows that are highly compressible, viscous, chemically reacting, and possibly in thermal and chemical non-equilibrium, a computational method to handle chemical reactions must be implemented into a CFD solver. There is a large increase in computational cost when moving from non-reacting to reacting flows; a transport equation for each species considered, and a chemical source term for each species must now be included in a computational method. In the past, there has been a significant amount of effort put into reducing chemical models so that a relatively large set of stiff ODEs need not be solved in conjunction with the fluid flow. Many methods are either based on reducing the chemical model used to a manageable size, or to introduce tabulated chemistry.

One class of methods that are geared towards reducing the size of the chemical model are based on separating chemical reactions by time scales [52, 91, 92]. “Slow” reactions (associated with large time scales) are solved, while “fast” reactions (associated with small time scales) are put into local equilibrium. Keck [70] proposed a similar method, except that his method relies more on the thermodynamic properties of the species present, rather than on the chemical reaction rates. This method, referred to as Rate-Controlled Constrained-Equilibrium (RCCE), tracks one or several constraints through the system, and reconstructs the system as a function of the constraint(s), based on constrained thermodynamic equilibrium calculations. Examples of possible constraints include the mass fraction of a single major species, radical species (species with valence electrons), or any

¹The work in this chapter has been presented in part in J. Rabinovitch and G. Blanquart. A computationally efficient approach to hypersonic reacting flows. In *Proceedings of the 29th International Symposium on Shock Waves*, Madison, Wisconsin, 2013.

linear combination of species mass fractions. In general, only the reaction rates associated with the rate of change of the constraint variable need to be known for this method. Both the state of the system and the rate of change of the constraint can be tabulated, and then efficient methods can be used to incorporate this tabulated chemistry into a CFD solver. The computational benefits of RCCE are clearly stated by Keck in his original work: “since in general the number of constraints necessary to determine the state of a complex system to a specified degree of accuracy is very much smaller than the number of degrees of freedom of the system, there are fewer differential equations to integrate” [70].

The RCCE method has already been applied successfully to laminar and turbulent flames under low Mach conditions in the past [56, 63, 65, 70, 71, 80, 163, 164]. Unfortunately, there is little available data detailing the performance of the RCCE method for compressible flows, and virtually none of it pertains to re-entry like conditions. Therefore, the goal of this chapter is to investigate different possible constraints to be used with the RCCE method for reacting compressible flows. The effectiveness of different constraints will be isolated by performing a point-wise comparison of results based on constrained thermodynamic equilibrium calculations, to detailed chemistry results. These results are shown in Sec. 3.8, and are not based on integrated RCCE simulations. The results from this comparison allow an appropriate constraint to be selected for full RCCE simulations, and help one understand the limits of the applicability of the RCCE method for the test cases considered. Results from full RCCE simulations are then shown in Sec. 3.9. It will be seen that while some constraints might perform well for a supersonic flow undergoing a steady expansion, the same kind of constraint will perform poorly behind a shock wave. The analysis performed in this chapter determines when a specific constraint is expected to yield accurate results, and when it is expected to perform poorly. This chapter uses relatively simple gas mixtures, assuming thermal equilibrium throughout, in order to isolate performance of individual constraints.

3.2 Previous Work

The RCCE method has been used in a variety of studies in the past to large degrees of success, and these studies are summarized in this section. In Keck’s work [70], a detailed description of the RCCE method is provided, as well as an overview of RCCE results obtained in other studies. In an earlier study, Keck and Gillespie [71] compared steady state calculations to results obtained using the RCCE method for the formation and removal of NO in an internal combustion engine. Later, Morr and Heywood [111] used the RCCE method to analyze measurements of CO concentrations in a steady

flow cylindrical burner. Law *et al.* [80] investigated the performance of several different constraints when studying the reacting H₂/O₂ system. These studies showed good agreement between the RCCE method and detailed chemical models. More recently, the RCCE method has been used to show good agreement with full detailed mechanisms for complex hydro-carbon fuels [63, 65], and the method has also been extended to allow for non-linear constraints [14].

Keck's work [70] emphasized that only the rate constants for the reactions related to the rate of change of the chosen constraint are needed for this method, and that the benefits gained from using the RCCE method continue to increase as chemical systems become larger and more complex. With more complicated systems in mind, this has motivated investigations of the RCCE method in conjunction with tabulated approaches, such as in [163] and [164]. In addition, Hiremath *et al.* [56] have extended the basic RCCE method to investigate dynamic methods to change the constraint in order to minimize errors, but this was limited to investigating the effect of constraining different combinations of individual species.

While the previously mentioned studies have all been geared towards subsonic combustion problems, Janbozorgi and Metghalchi [64] used a degree of disequilibrium analysis (Sec. 3.5.2) to successfully model a supersonic reacting H/O system expanding through a nozzle. To the authors knowledge, this is the only published work using the RCCE method for compressible reacting flows. The timescale analysis performed in this chapter will build on the work performed in [64], and incorporate other formal timescale analysis techniques that have not been incorporated into the RCCE method previously (Sec. 3.5.1). All of the studies discussed that use the RCCE method have been geared towards combustion applications, where reactants and products can be distinguished. This chapter extends the use of the RCCE method to compressible reacting flows that are not combustion based, where it is more challenging to define specific reactants and products.

3.3 Reacting Euler Equations

When reduced order models are compared to detailed models, it is not always possible to compare the yield of individual species, as some species might only exist in the detailed model. Instead, it is common to compare the bulk properties of the fluid mixture, which a reduced order model should reproduce. In order to determine which properties of the fluid are relevant in reacting supersonic flows, the reacting Euler equations should be considered. The 3D reacting Euler equations in conservative form are shown in Eqs. 3.1–3.3.

$$\frac{\partial \mathbf{w}}{\partial t} + \frac{\partial \mathbf{f}_x}{\partial x} + \frac{\partial \mathbf{f}_y}{\partial y} + \frac{\partial \mathbf{f}_z}{\partial z} = \mathbf{g}, \quad (3.1)$$

where

$$\mathbf{w} = \begin{pmatrix} \rho \\ \rho u \\ \rho v \\ \rho w \\ e \\ \rho Y_1 \\ \vdots \\ \rho Y_{ns} \end{pmatrix}, \quad \mathbf{f}_x = \begin{pmatrix} \rho u \\ \rho u^2 + P \\ \rho uv \\ \rho uw \\ u(E + P) \\ \rho u Y_1 \\ \vdots \\ \rho u Y_{ns} \end{pmatrix}, \quad \mathbf{f}_y = \begin{pmatrix} \rho v \\ \rho uv \\ \rho v^2 + p \\ \rho vw \\ v(E + P) \\ \rho v Y_1 \\ \vdots \\ \rho v Y_{ns} \end{pmatrix}, \quad \mathbf{f}_z = \begin{pmatrix} \rho w \\ \rho uw \\ \rho vw \\ \rho w^2 + P \\ w(E + P) \\ \rho w Y_1 \\ \vdots \\ \rho w Y_{ns} \end{pmatrix}, \quad (3.2)$$

and

$$\mathbf{g} = \begin{pmatrix} 0 \\ 0 \\ 0 \\ 0 \\ 0 \\ \omega_1(T, P, Y_1, \dots, Y_{ns})W_1 \\ \vdots \\ \omega_{ns}(T, P, Y_1, \dots, Y_{ns})W_{ns} \end{pmatrix}. \quad (3.3)$$

E is the total energy, which is given by

$$E = \rho \left(e + \frac{1}{2}|\mathbf{u}|^2 \right), \quad (3.4)$$

where e is the internal energy, $|\mathbf{u}|^2 = u^2 + v^2 + w^2$, and u , v , and w are the velocities in the x , y , and z directions, respectively. The above equations require an equation of state for closure, such as the caloric equation of state, $P = P(\rho, e, Y_1, \dots, Y_{ns})$. T , P , ρ , Y_i , ns , ω_i , and W_i are the temperature, pressure, density, mass fraction of species i , number of total species, net production rate of species i , and the molecular weight of species i , respectively. From a mathematical standpoint, the RCCE method alters the final ns equations given in Eq. 3.2 and Eq. 3.3. This will be shown in more detail in Sec. 3.4 and Sec. 3.9. To limit the scope of this chapter, while still retaining the complexity of

the chemical processes, steady one-dimensional, and quasi-one-dimensional flows are considered.

Following the derivations performed in [69], in the shock-fixed frame, the one-dimensional reacting Euler equations can be re-written as:

$$\frac{d\rho}{dx} = -\frac{\rho \dot{\sigma}}{w \eta} \quad (3.5)$$

$$\frac{dw}{dx} = \frac{\dot{\sigma}}{\eta} \quad (3.6)$$

$$\frac{dP}{dx} = -\rho w \frac{\dot{\sigma}}{\eta} \quad (3.7)$$

$$\frac{dY_i}{dx} = \omega_i(T, P, Y_1, \dots, Y_{ns}) \frac{W_i}{\rho} \frac{1}{w}, \quad (3.8)$$

where w , $\dot{\sigma}$, and η are the velocity in the x direction in the shock-fixed frame, the thermicity, and the sonic parameter ($\eta = 1 - M^2$), respectively. Equations 3.5—3.8 can be generalized to include an area change if desired, as shown by Kao and Shepherd [69]. To simplify notation, a chemical source term, Ω , is introduced such that $\Omega_i = \omega_i \frac{W_i}{\rho}$. The thermicity is defined to be

$$\dot{\sigma} = \sum_{i=1}^{ns} \sigma_i \Omega_i, \quad (3.9)$$

where σ_i takes the form

$$\sigma_i = \frac{\bar{W}}{W_i} - \frac{h_i}{c_P T}, \quad (3.10)$$

assuming an ideal gas. c_P is the specific heat at constant pressure, \bar{W} is the mixture averaged molecular weight, and h_i is the enthalpy of species i . For each individual species, the enthalpy can be calculated by

$$h_i = h_i(T_o) + \int_{T_o}^T c_{p,i}(T') dT', \quad (3.11)$$

where $h_i(T_o)$ is the reference enthalpy at $T_o = 298$ K [25].

While the Ω_i term is sensitive to individual species concentrations, the other bulk properties, \bar{W} and c_p are dominated by species with the largest mole and mass fractions (respectively), as $\bar{W} = \sum_{i=1}^{ns} X_i \cdot W_i$ and $c_p = \sum_{i=1}^{ns} c_{p,i} \cdot Y_i$. Here X_i refers to the mole fraction of species i . While not appearing directly in the reacting Euler equations, the mixture enthalpy, $h = \sum_{i=1}^{ns} h_i \cdot Y_i$, gives an indication as to how much energy is stored in the gas (not including contributions to internal energy from pressure and volume). As a result, the overall evolution of the flow is mainly based on the bulk properties of the mixture (such as \bar{W} , c_p , and h). Because of this, it is believed that errors

made on minor species will have a relatively small effect on the overall evolution of the reactive Euler equations. This is the major concept behind RCCE and allows for the successful application of reduced order models that do not necessarily predict all minor species correctly, but do well predicting bulk properties of a mixture.

3.4 RCCE Overview

The RCCE method is very different than many other chemistry reduction techniques, and this section provides a general overview of RCCE. To quote Keck directly:

In the RCCE method it is assumed that for many practical applications, the evolution of a complex system can be described with acceptable accuracy by a relatively small number of rate-controlling reactions which impose slowly changing constraints on the allowed states of the system. It is also assumed, as in thermodynamics, that fast reactions exist which relax the system to the associated constrained-equilibrium state on a time scale short compared to that on which the constraints are changing. Under these conditions, a non-equilibrium system will relax to its final equilibrium state through a sequence of rate-controlled constrained-equilibrium states which can be determined by maximizing the entropy subject to the instantaneous values of the constraints. Thus only the rate equations for the constraints must be integrated [70].

The fundamental purpose of RCCE (and many other methods) is to reduce the complexity of a given system, yet to retain an “acceptable” level of accuracy. In general, when solving for the flow field of a chemically reacting flow, the bulk (intensive) mixture properties are determined by the chemical composition of the flow, and the macroscopic evolution of the flow is highly coupled to the state of the reacting mixture. The level of accuracy required by a reduced order method is a subjective description, and generally relies on some user-defined threshold. For general engineering purposes, the bulk properties of the fluid (described in more detail in Sec. 3.3) must be compared between the detailed and reduced order models, and this can give a good indication of the fidelity of the reduced order model. It will be shown in Sec. 3.8 and Sec. 3.8.6 that seemingly major errors made on minor species when reconstructing a gas mixture may have relatively little (if any) influence on the bulk properties of the fluid mixture.

The RCCE method relies on the assumption that a limited number of chemical properties of a mixture (constraints) can be used to reconstruct the composition of a mixture through constrained thermodynamic equilibrium calculations. This is illustrated graphically in Fig. 3.1, where the inverse of the molecular weight of a mixture is chosen to be the constraint (ϕ). The reaction begins in the bottom left corner, and ends in the upper right corner of Fig. 3.1. A unique trajectory in T , P ,

and ϕ space is traversed as the reaction goes to completion. With the RCCE method, the mixture composition is calculated using a constrained equilibrium calculation based on the local temperature, pressure, and molecular weight, at every point along this trajectory.

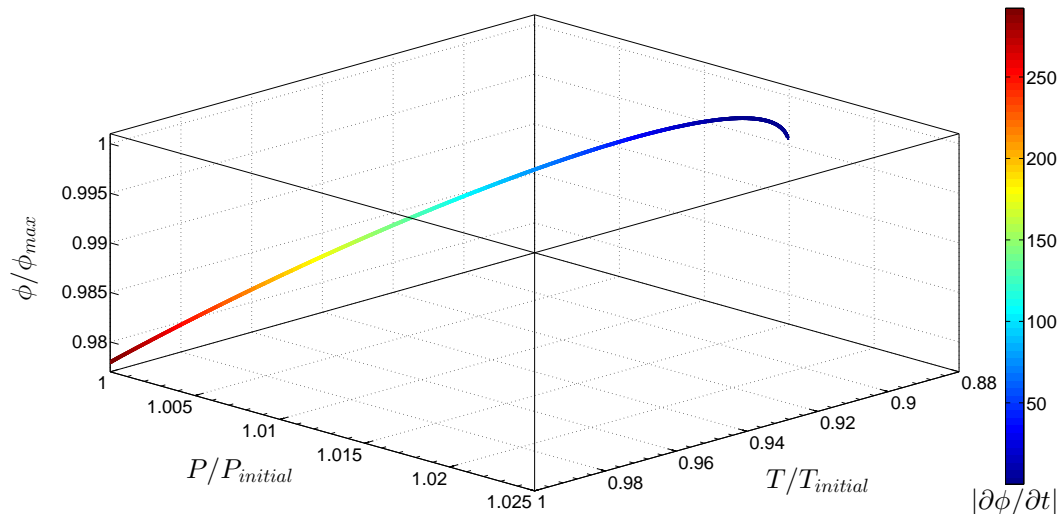


Figure 3.1: Evolution of ϕ as a function of T and P for a shocked air flow where $\phi = 1/\bar{W}$. The color shows the magnitude of the rate of change of the inverse of the molecular weight ($|\partial\phi/\partial t|$), for a given value of T , P , and ϕ .

One challenge associated with successfully applying the RCCE method to a given reacting system is choosing the proper constraint(s). Some possible constraints originally suggested by Keck [70] include tracking individual species, the sum of mass (or mole) fractions of major species, or the sum of mass (or mole) fractions of radical species present in a mixture. Only the chosen constraint(s) now need be solved for throughout the system, and then the rest of the mixture can be reconstructed around this/these value(s).

In order to evaluate the performance of different constraints, comparisons between constrained thermodynamic equilibrium calculations, and detailed chemistry can be calculated, without performing an integrated simulation. An overview of this comparison is presented below and in Sec. 3.8. Details on integrated simulations are shown later in Sec. 3.9.

Mathematically, the constraint variable, ϕ , is often a linear function of all of the chemical species present in a mixture. Assuming ns species present in a mixture,

$$\phi^k = \sum_{i=1}^{ns} C_i^k Y_i, \quad (3.12)$$

where k corresponds to a chosen constraint, and C_i^k is the coefficient associated with the i th species, for the k th constraint. To clarify notation, the superscript k is dropped for the rest of this section, and the following analysis is performed for a single ϕ . It should be understood that the C_i coefficients (constraint coefficients) will change if a different constraint is chosen. Eq. 3.12 is therefore re-written as:

$$\phi = \sum_{i=1}^{ns} C_i Y_i. \quad (3.13)$$

For example, if one were to constrain only the j th species in a mixture, then $C_j = 1$, and $C_{i \neq j} = 0$. The constraint is generally chosen *a priori* for a given simulation, and the same constraint is used throughout the entire simulation, *i.e.*, the C_i 's are constant. If this were not the case, and non-constant constraints were chosen, then $C_i = C_i(\mathbf{Y})$, and Eq. 3.13 is no longer valid, as ϕ is no longer a linear function of the Y_i 's. Non-linear constraints are not considered for this work, though have been used in other studies [14].

A superscript of *CEQ* will be used from this point on in order to distinguish between values calculated through the use of constrained thermodynamic equilibrium calculations (*CEQ* superscript), and values calculated through detailed chemistry calculations (no superscript). In order to evaluate how a constraint performs without running an integrated RCCE simulation (Sec. 3.8), values for T , P , and ϕ (Eq. 3.13) are calculated from detailed chemistry results.

Values for \mathbf{Y}^{CEQ} ($\mathbf{Y}^{\text{CEQ}} = [Y_1^{\text{CEQ}} \dots Y_{ns}^{\text{CEQ}}]^T$) are calculated such that \mathbf{Y}^{CEQ} minimizes Gibbs function, G , while keeping T , P , and ϕ constant for a specific mixture. This implies that

$$Y_i^{\text{CEQ}} = Y_i^{\text{CEQ}}(T, P, \phi). \quad (3.14)$$

All constrained equilibrium calculations performed to evaluate Eq. 3.14 are performed using the CEQ code developed by Professor Stephen B. Pope at Cornell University [129, 131, 132]. An overview of the method used in the CEQ code is provided in Appendix A. Equation 3.14 implies that $\phi = \phi^{\text{CEQ}}$, by definition, where $\phi^{\text{CEQ}} = \sum_{i=1}^{ns} C_i Y_i^{\text{CEQ}}$. However, Eq. 3.17 and Eq. 3.18 will show that $\frac{\partial \phi}{\partial t}$ and $\frac{\partial \phi^{\text{CEQ}}}{\partial t}$ are not necessarily equal.

A chemical source term based on \mathbf{Y}^{CEQ} can now be calculated:

$$\Omega_i^{\text{CEQ}} = \Omega_i^{\text{CEQ}}(T, P, \mathbf{Y}^{\text{CEQ}}) = \Omega_i^{\text{CEQ}}(T, P, \phi). \quad (3.15)$$

This is in contrast to the chemical source term described previously, $\Omega_i = \Omega_i(T, P, \mathbf{Y})$. The difference between Ω_i^{CEQ} and Ω_i is caused by the differences between \mathbf{Y}^{CEQ} and \mathbf{Y} ; the same T and P are used in both calculations.

The rate of change of the constraint must also be calculated, and this is done by differentiating Eq. 3.13 with respect to time:

$$\frac{\partial \phi^{CEQ}}{\partial t} = \sum_{i=1}^{ns} C_i \frac{\partial Y_i^{CEQ}}{\partial t}. \quad (3.16)$$

Using Eq. 3.15 this simplifies to

$$\frac{\partial \phi^{CEQ}}{\partial t} = \sum_{i=1}^{ns} C_i \Omega_i^{CEQ}. \quad (3.17)$$

A rate of change of the constraint can also be calculated solely based on the detailed chemistry results (for comparison purposes), and this is defined to be

$$\frac{\partial \phi}{\partial t} = \sum_{i=1}^{ns} C_i \Omega_i. \quad (3.18)$$

Finally, it is also possible to calculate bulk properties of the mixtures. For example,

$$c_p^{CEQ} = \sum_{i=1}^{ns} c_{p_i}(T) Y_i^{CEQ}, \quad (3.19)$$

while

$$c_p = \sum_{i=1}^{ns} c_{p_i}(T) Y_i. \quad (3.20)$$

Comparisons between the CEQ quantities and quantities calculated from detailed chemistry calculations are shown in Sec. 3.8. The previous analysis was performed assuming only one constraint was chosen, but these calculations can be generalized if multiple constraints are chosen for a specific application.

It is important to recognize that there is no guarantee that the same constraint(s) will work for every problem investigated. This method requires some *a priori* intuition about the system to be investigated, or some simplified analysis to be performed. The fact that constraints must be identified before investigating a specific system can be seen as a disadvantage, yet Keck argues that this is an advantage, as it "... forces one to think before embarking on elaborate calculations!" [70].

3.5 Methodology for Constraint Selection

Inherent to the RCCE method is the necessity of picking constraints to be used. This section outlines the general method for picking constraints based on time scale analysis and a degree of disequilibrium analysis. A full explanation of all constraints considered, and how these constraints can be calculated for specific test cases will be provided later in Sec. 3.7.

3.5.1 Timescale Analysis

Analyzing chemical timescales has been used extensively in the past by the combustion community. The two popular methods that use time scale analysis for reduced order modeling techniques include Computational Singular Perturbation (CSP) [52] and Intrinsic Lower Dimensional Manifolds (ILDM) [91, 92]. These methods advance quasi-steady state and partial equilibrium approximations [79] by systemically reducing a complicated detailed chemical model into a reduced model, without relying on prior intuition about the chemical model being investigated. These methods continue to be updated [51], but only the basic principles are needed in this section. A brief overview of CSP and ILDM is provided below for completeness.

The original work on CSP by Goussis and Lam [52] used CSP to model the homogeneous oxidation of methanol in air at constant pressure. The authors applied a dynamical systems approach that allowed the full 30 species mechanism to be reduced to a minimum set that required only 16 species. The over-arching idea of CSP is to separate the system into “fast” and “slow” reaction subspaces, with a rigorous and repeatable mathematical method. The reactions are divided into an “equilibrated set,” which contains fast reactions that are in a local equilibrium, and a “rate-controlling” set which contains the slower reactions that control the evolution of the system. If a reaction falls into neither of these sets, then it is considered to be “superfluous”. Decoupling the fastest timescales from the slowest timescales removes the stiffness from the system ODEs that needs to be solved, and allows the system of equations to be solved in an explicit manner with high accuracy. The results reported by Goussis and Lam [52] showed good agreement between the reduced order model and the detailed mechanism.

ILDM, a method first proposed by Maas and Pope [91, 92], is also based on a dynamical systems approach. Unlike CSP, which is geared towards reducing the stiffness of the system of ODEs needed to be solved, ILDM is geared towards identifying a lower-dimensional manifold that the reaction is confined to. A full overview and explanation of the applications of ILDM and the numerical issues associated with the implementation of this method are provided by Eckett [35] and Hung [61], though

a brief summary is also provided here. ILDM was originally developed for a spatially homogeneous, adiabatic, and constant pressure system [92].

To begin, a chemical reaction can be described in terms of a state space, where the different chemical species define the different dimensions of the state space. Therefore, a chemical reaction is limited to a specific manifold in this state space, based on the initial conditions, and on mass conservation. As the two state variables, h and P , were originally assumed to be constant by Maas and Pope [92], the reaction space is limited to a manifold of dimension $ns - ne$, where ns is the number of species considered, and ne is the number of elements. The subtraction of ne occurs due to elemental conservation, and limits the dimension of the manifold. With this in mind, a chemical reaction can be interpreted as a trajectory in this state space. Over time, these trajectories all tend towards a point in state space that corresponds to the thermodynamic equilibrium composition, given that enthalpy and pressure are held constant. Maas and Pope found that these reaction trajectories tend to “bunch” and approach one another long before chemical equilibrium was reached. This prompted an investigation that found lower dimensional manifolds which act as attractors in state space, and are governed by slow reactions. Based around the attracting manifolds in state space, the ILDM method can greatly reduce the overall order of the reacting system, while still maintaining a user-defined level of accuracy.

For this work, only the first steps used in the ILDM method need be considered. The timescale analysis performed by Maas and Pope [91, 92] is based on an analysis of the Jacobian matrix of the chemical source term. This analysis is reproduced below.

In general, the rate of change of mass fractions of the species present in a mixture can be written as

$$\frac{d\mathbf{Y}}{dt} = \boldsymbol{\Omega}, \quad (3.21)$$

where $\boldsymbol{\Omega} = [\Omega_1 \ \Omega_2 \ \dots \ \Omega_{ns}]^T$. To analyze the time scales associated with small perturbations from a given chemical state, a small change in mass fraction is considered such that $\mathbf{Y} = \mathbf{Y}_o + \mathbf{Y}'$. Using a Taylor series expansion, and keeping only the linear term in \mathbf{Y}' results in

$$\frac{d\mathbf{Y}'}{dt} = \mathbf{J} \cdot \mathbf{Y}', \quad (3.22)$$

where \mathbf{J} is the time dependent Jacobian matrix for the chemical reaction, with $J_{ij} = \frac{\partial \Omega_i}{\partial Y_j}$. If \mathbf{J} is assumed to be constant during a small time interval (small compared to the relaxation times associated with the perturbations), the decomposition $\mathbf{J} = \mathbf{A}\Lambda\mathbf{B}$ can be used. \mathbf{A} is a matrix of

basis vectors, and $\mathbf{B} = \mathbf{A}^{-1}$. If \mathbf{A} is an ideal basis matrix, then Λ would be a diagonal matrix with ns entries. However, for chemical systems in general, \mathbf{J} is a rank-deficient, non-symmetric, and ill-conditioned matrix. It is at most rank $ns - ne$. This is caused by elemental conservation throughout the system.

The first $ns - ne$ right eigenvectors (columns of \mathbf{A}), $\mathbf{e}_1, \mathbf{e}_2, \dots, \mathbf{e}_{ns-ne}$, are reaction modes for the system. Each reaction mode is associated with a characteristic time scale, which is the inverse of the real component of the corresponding eigenvalue, λ_i . A reaction mode with a small characteristic timescale relaxes to the initial state faster than a mode with a larger characteristic timescale. The eigenvector associated with fastest reaction mode (largest eigenvalue) will be referred to as $\boldsymbol{\nu}^*$, where $\boldsymbol{\nu}^* = [\nu_1^* \dots \nu_{ns}^*]^T$. If the real component of an eigenvector is positive, it means that a perturbation in the direction of its eigenvector will actually increase. This formal timescale analysis has not been combined with RCCE previously; the reaction modes, and their associated timescales will be tested as constraints, and the method used to calculate $\boldsymbol{\nu}^*$ for a specific problem is presented later in Sec. 3.7.3.

3.5.2 Degree of Disequilibrium

Another constraint based on time scale analysis, and also one of the constraints that Keck proposed in his original work [70], is the degree of disequilibrium of an individual chemical reaction. The idea behind this constraint is to evaluate whether or not specific chemical reactions are in a local state of equilibrium. This information can be used to make an informed decision for the constraint selection, and has been applied in previous works showing good agreement with detailed chemical models [64].

In order to evaluate whether or not a specific chemical reaction is in a state of equilibrium, the “degree of disequilibrium” (or degree of equilibrium if preferred) can be calculated. The degree of disequilibrium, DOD , for a specific reaction is defined to be $DOD = \log(\frac{r^-}{r^+})$, where r^- is the backwards reaction rate, and r^+ is the forwards reaction rate. When this value is close to 0, then the reaction is close to equilibrium, as $r^- \approx r^+$, and if this ratio is far from 0, then $r^- \gg r^+$ or $r^- \ll r^+$. As outlined in Sec. 3.4, the chosen constraint should be representative of the rate limiting reactions that are occurring in the system. It can be reasoned that reactions that are close to equilibrium are related to relatively fast time scales, and should therefore not affect the value of the constraint (as the constraint should only be affected by reactions with slow time scales). Keeping this in mind, constraints that are independent of the fast reactions can be chosen.

A simple example is shown below for a five species (O_2, N_2, O, N, NO) air model. It is assumed

that the system can be modeled by the following five reactions:



where M represents any one of the five species. Assuming that Eq. 3.26 has a degree of disequilibrium value close to zero for the entire reaction, and the other four reactions have values far from zero, several different constraints for the RCCE method can be picked. For example, the constraint $\phi = X_{NO} + X_{O_2}$, $\phi = X_O + X_N$, or $\phi = X_{NO} + X_O - X_{O_2} - X_N$ are some of the possibilities that represent summations that are not changed as the reaction $\text{NO} + \text{O} \rightleftharpoons \text{O}_2 + \text{N}$ progresses. X_i refers to the mole fraction of species i . If several reactions have a *DOD* close to zero, then the number of constraints that could be chosen would be reduced.

3.5.3 Effect of Elemental Conservation

The *DOD* constraint can be augmented by the fact that elements are conserved throughout a chemical reaction (assuming no nuclear decay). However, for new information to be added to the system, the *DOD* constraint must be linearly independent of elemental conservation.

A simple example is performed by returning to the five species air model given in Sec. 3.5.2, and again assuming that $\text{NO} + \text{O} \rightleftharpoons \text{O}_2 + \text{N}$ (Eq. 3.26) is in a local equilibrium throughout the system. The following three equations represent the conservation of elemental oxygen, conservation of elemental nitrogen, and a constraint based on *DOD* analysis, respectively.

$$2\Delta X_{\text{O}_2} + \Delta X_{\text{O}} + \Delta X_{\text{NO}} = 0 \quad (3.28)$$

$$2\Delta X_{\text{N}_2} + \Delta X_{\text{N}} + \Delta X_{\text{NO}} = 0 \quad (3.29)$$

$$-\Delta X_{\text{O}_2} - \Delta X_{\text{N}} + \Delta X_{\text{NO}} + \Delta X_{\text{O}} = 0, \quad (3.30)$$

where ΔX_i represents the change in number of moles of species i during some amount of time. Equation 3.30 is generated by taking the stoichiometric coefficients from the reaction (Eq. 3.26) that is in local equilibrium, and re-arranging the coefficients such that they sum to zero.

Solving Eqs. 3.28–3.30 simultaneously results in two free parameters, as there are five equations and three unknowns. For example, $\Delta X_{N_2} = \frac{1}{2}(3\Delta X_{O_2} - \Delta X_{NO})$, $\Delta X_O = -2\Delta X_{O_2} - \Delta X_{NO}$, and $\Delta X_N = -3\Delta X_{O_2}$, if ΔX_{O_2} and ΔX_{NO} are chosen to be the free parameters. This defines an infinite set of constraints that are based on the reaction $NO + O \rightleftharpoons O_2 + N$ having a *DOD* value close to zero throughout the entire reaction, and augmented by considering the effects of elemental conservation. The free parameters can be chosen arbitrarily, and the method used to calculate this constraint for a specific problem is shown in Sec. 3.7.4.

The augmented *DOD* constraint, along with the new time scale constraint can now be applied to actual test problems to see how they perform. These constraints will be compared to more traditional constraints, such as individual species constraints, in the following sections.

3.6 Air Test Cases—Overview

As very few previous studies exist that use the RCCE method to solve problems involving compressible flows, a detailed investigation into the performance of different constraints must be performed in order to understand if RCCE is a viable method for this flow regime. Two model test problems are used to accomplish this. Each case is set up in Cantera [47], using the Shock and Detonation Toolbox [25] to solve the reacting Euler equations. The appropriate thermodynamic data [50, 100] and reaction rates [53] are found in the literature. Temperatures are kept under 6000 K so that there is a negligible concentration of ionized species in the gas mixture. Reactions shown in Eqs. 3.23–3.27 are used to model the air mixture which includes five species: N_2 , O_2 , NO , O , N . The vector of mass fractions of the mixture, \mathbf{Y} , is defined to be $\mathbf{Y} = [Y_{N_2} \ Y_{O_2} \ Y_{NO} \ Y_O \ Y_N]^T$. The parameters for the test cases are chosen so that finite-rate chemical kinetics plays a role in determining the composition of the flow, and that the flow parameters are characteristic of what might be experienced in a hypersonic ground testing facility. One test case involves processing a gas mixture by a normal shock; and the other test case involves looking at the steady expansion of a previously shocked gas. Not only are these two types of flows necessary for the operation of ground testing facilities, but these two genres of flows are also akin to what a blunt body would experience under re-entry conditions; a bow shock over the forebody of the vehicle, and an expansion region as the flow turns around the shoulder of the body. For all of the following work it is assumed that the gas is in thermal equilibrium, *i.e.*, translational/rotational/vibrational temperatures are assumed to be the same.

3.6.1 Case #1: Shocked Gas

For this test case, a gas mixture at 20 kPa and 297 K is processed by a normal shock traveling at 3 km/s. These initial conditions are very similar to Shot 2791 from T5 [123], where a gas mixture at 22 kPa in the shock tube portion of the experimental facility was processed by a normal shock traveling at 3.1 km/s. However, the T5 gas mixture was primarily CO₂, and not air, for Shot 2791.

Across the normal shock, it is assumed that the composition of the flow remains frozen, but the gas behaves as an ideal gas where the relevant gas properties (γ , c_p , c_v , etc.) are a function of temperature. This assumption requires that the post-shock state be solved for in an iterative manner, and Reynolds' iterative method is used for this calculation [25]. After the post-shock properties are calculated, the gas evolves kinetically until changes in the gas composition and thermodynamic properties are negligible. Sample results for air (79% N₂, 21% O₂ by volume) are shown in Fig. 3.2. Quantities are plotted as a function of distance in the shock fixed frame, where the shock is located at $x = 0$ m. In this example, the mixture compositions reaches a relatively constant value at ~ 1 cm which corresponds to $\sim 25 \mu\text{s}$ downstream of the shock. Conditions for Case #1 are summarized in Table 3.1.

Immediately behind the normal shock, the gas is in a state that is far from thermodynamic equilibrium, as it is at a high temperature and pressure, and it is not yet dissociated. Farther downstream from the shock, a thermodynamic equilibrium state is reached, where T , P , and \mathbf{Y} remain constant. There is no imposed length scale on this problem, and the gas will reach a thermodynamic equilibrium state some distance downstream of the shock. The point where thermodynamic equilibrium is reached is therefore only related to the initial condition used for the problem (shock speed, initial pressure, and the gas mixture and model chosen). This test case focuses on testing the RCCE method for a flow which starts far from thermodynamic equilibrium, and should eventually relax to a thermodynamic equilibrium state.

Table 3.1: Initial and final gas properties for Case #1.

	Initial Conditions	Thermodynamic Equilibrium Conditions
T (K)	297	3457
P (kPa)	20	1853
Y_{N_2}	0.77	0.74
Y_{O_2}	0.23	0.17
Y_{NO}	0.00	0.068
Y_O	0.00	0.023
Y_N	0.00	0.000018

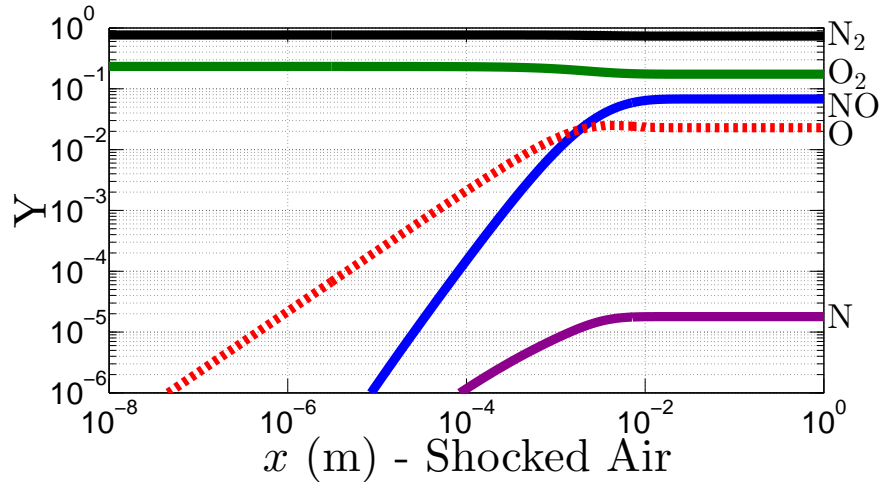


Figure 3.2: Evolution of mass fractions for air at 20 kPa and 297 K processed by a 3 km/s ($M = 8.7$) normal shock. Some of the N_2 and O_2 dissociates at this high temperature and pressure condition.

3.6.2 Case #2: Steady Expansion

For this test case, a gas mixture at high temperature and pressure is expanded through a 20° half angle conical nozzle. The composition of this gas is calculated by taking the same initial conditions as in Sec. 3.6.1, then taking the equilibrium result from the original normal shock, and finally reprocessing the gas again by a reflected shock. This approximates the conditions that would be seen in the reservoir of a reflected shock tunnel. In order to exaggerate the effect that finite rate kinetics have on the expansion of this gas, this gas mixture is taken to be the composition of the gas at the throat of the nozzle traveling at $M = 1$. In a real facility, the gas would accelerate to the sonic point through the converging aspect of the nozzle, and the temperature and pressure would both decrease as the velocity increases. Sample results for air are shown in Fig. 3.3 where the length is normalized by the nozzle diameter (2.54 cm). Some recombination of the highly dissociated gas occurs before nozzle freezing, and then the composition remains constant after ~ 9 throat diameters downstream, which corresponds to an area ratio (AR) of ~ 17 . Conditions for Case #2 are summarized in Table 3.2.

This test case differs greatly from the previously discussed shock test case. First, the flow at the nozzle throat is in a thermodynamic equilibrium state. As the flow travels downstream, temperature and pressure decrease, which slow down the chemical reactions occurring. Eventually, the chemical reaction rates are so small that the gas composition remains relatively constant. This phenomenon is often referred to as nozzle freezing. From this point on, the flow is in a constant state away from a local equilibrium. In fact, the gas is in a state farther from thermodynamic equilibrium the farther

downstream the nozzle it travels. In addition, and contrary to the shock case (Sec. 3.6.1), a length scale is inherently imposed on this problem by choosing a nozzle geometry. This test case focuses on testing the RCCE method for a flow that should reach a final state where the gas mixture is not in thermodynamic equilibrium, and this transition from equilibrium to non-equilibrium takes place over a finite length, imposed by the user.

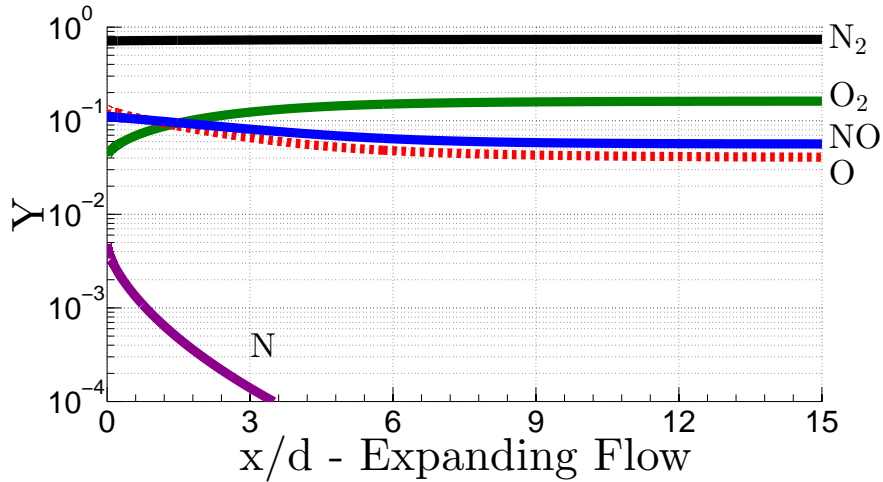


Figure 3.3: Evolution of mass fractions for air originally in thermodynamic equilibrium at 5710 K and 17.3 MPa, undergoing a steady expansion. Recombination reactions dominate this flow until the composition freezes at approximately $x/d = 9$.

Table 3.2: Initial and final gas properties for Case #2.

	Initial Conditions	Conditions at AR = 17
T (K)	5710	2732
P (kPa)	17300	192
Y_{N_2}	0.71	0.74
Y_{O_2}	0.042	0.16
Y_{NO}	0.11	0.058
Y_O	0.0048	0.043
Y_N	0.13	$6.6 \cdot 10^{-6}$

3.7 Air Test Cases—Constraint Selection

With the test cases set-up, it is now possible to calculate the specific constraint coefficients (C_i^k) to be tested with the RCCE method. The constraints fall under three major categories: individual species constraints, global quantities, and constraints based on time scale analysis. The different constraints chosen in each category are outlined in the following sections, and are summarized in Table 3.3.

Table 3.3: Summary of constraints to be investigated in this section. For $k = 8$, the conversion from mole fractions to mass fractions requires that the inverse of molecular weight be used to keep the constraint linear in mass fractions, and for $k = 11$ and $k = 12$, more analysis is needed to determine the appropriate constraint coefficients.

Category	Constraint Name	k	$\phi^k = \sum_{i=1}^{ns} C_i^k Y_i$	Same C_i 's for Shock and Nozzle (Y/N)
Species Constraints	Major Species	1	$C_{N_2, O_2}^1 = 1, C_{NO, O, N}^1 = 0$	Y
	Radical Species	2	$C_{N_2, O_2}^2 = 0, C_{NO, O, N}^2 = 1$	Y
	N_2	3	$C_{N_2}^3 = 1, C_{i \neq N_2}^3 = 0$	Y
	O_2	4	$C_{O_2}^4 = 1, C_{i \neq O_2}^4 = 0$	Y
	NO	5	$C_{NO}^5 = 1, C_{i \neq NO}^5 = 0$	Y
	O	6	$C_O^6 = 1, C_{i \neq O}^6 = 0$	Y
	N	7	$C_N^7 = 1, C_{i \neq N}^7 = 0$	Y
Global Quantities	Molecular Weight	8	See Sec. 3.7.2	Y
	Enthalpy of Formation	9	$C_{N_2, O_2}^9 = 0$ $C_{NO}^9 = \frac{\Delta h_f^\circ_{NO}}{W_{NO}} Y_{NO},$ $C_O^9 = \frac{\Delta h_f^\circ_O}{W_O} Y_O,$ $C_N^9 = \frac{\Delta h_f^\circ_N}{W_N} Y_N$	Y
Timescale Analysis	Fast Mode	10	$C_i^{10} = \bar{\nu}_i^*$	N
	DOD #1	11	See Sec. 3.7.4	N
	DOD #2	12	See Sec. 3.7.4	N

3.7.1 Species Constraints

For simplicity, each of the 5 species, O_2 , N_2 , O , N , and NO , are used as individual constraints. In addition, the linear combination of the mass fractions of the major species ($O_2 + N_2$) and the linear combination of the mass fraction of the radical species ($NO + O + N$) are used as constraints. These are some of the original constraints suggested by Keck [70].

3.7.2 Global Quantities

Several “global quantities” of the gas mixture are also chosen to be used as constraints. This is done by performing a weighted sum of the species mass fractions, in order to keep the desired quantity constant. These quantities include the mixture molecular weight (previously used by Keck [70] and the standard enthalpy of formation (summation of the enthalpy of formation of the species present, by mass), which is a new constraint. The enthalpy of formation is defined to be the change in enthalpy due to the formation of a molecule from its constituent elements at standard conditions. The mathematical formulation for these constraints are shown in Table 3.4, where Δh_f° is its enthalpy of formation (kJ/mol). The calculation of the molecular weight generally takes the

form $\overline{W} = \left(\sum_{i=1}^{ns} \frac{Y_i}{W_i} \right)^{-1}$. However, in order to define a constraint that is linear in mass fractions for the constrained equilibrium calculations, a choice of $\phi^8 = \sum_{i=1}^{ns} C_i^8 Y_i$ is used, where $C_i^8 = 1/W_i$. This results in $\phi^8 = 1/\overline{W}$. The global constraints are shown in Table 3.4.

Table 3.4: Global constraint examples. The enthalpies of formation for O₂ and N₂ are zero, which is why they are not included in the general enthalpy of formation calculation.

Global Property	Constraint
Molecular Weight	$\phi^8 = \frac{Y_{N_2}}{W_{N_2}} + \frac{Y_{O_2}}{W_{O_2}} + \frac{Y_{NO}}{W_{NO}} + \frac{Y_O}{W_O} + \frac{Y_N}{W_N}$
Enthalpy of Formation	$\phi^9 = \frac{\Delta h_{fNO}^\circ}{W_{NO}} Y_{NO} + \frac{\Delta h_{fO}^\circ}{W_O} Y_O + \frac{\Delta h_{fN}^\circ}{W_N} Y_N$ $\Delta h_{fNO}^\circ = 90 \text{ kJ/mol}, \Delta h_{fO}^\circ = 247 \text{ kJ/mol}, \Delta h_{fN}^\circ = 471 \text{ kJ/mol}$

3.7.3 Constraints based on Timescale Analysis

Using the method outlined in Sec. 3.5.1, the different reaction modes and associated time scales are analyzed for the two test cases. For a five species air mixture that contains O₂, N₂, O, N, and NO, $ns = 5$ and $ne = 2$. This results in three ($= ns - ne$) reaction modes and timescales that can be calculated from the Jacobian matrix (Eq. 3.22). The characteristic time associated with mode i is defined to be $t_i^* = -1/\text{Re}(\lambda_i)$. The modes are ordered such that $t_1^* < t_2^* < t_3^*$. Figure 3.4 shows the evolution of the normalized time scales for the two test cases. As a point of reference, at $x/d = 2$, $t_1^* \approx 5 \cdot 10^{-9} \text{ s}$, $t_2^* \approx 5 \cdot 10^{-7} \text{ s}$, and $t_3^* \approx 1.3 \cdot 10^{-6} \text{ s}$. These times should be compared to the relevant fluid mechanical time scales in the flow, and for a nozzle, this can be estimated from² $t_{flow}^* \approx (\frac{U}{P} \frac{dP}{dx})^{-1}$. At $x/d = 2$, $t_{flow}^* \approx 1.5 \cdot 10^{-5}$. The fastest chemical time scales are much smaller than the time scale associated with the flow, while the slowest chemical time scale is similar to that of the flow.

Figure 3.4 shows this graphically; while there is a significant time scale separation between mode one and the other two reaction modes, modes two and three have similar characteristic times. This result holds for both the shocked flow and expanding flow, and suggest that time scale analysis can be combined with the idea outlined in Sec. 3.5.2 to pick a constraint for the RCCE method based on the fastest reaction mode. The fastest reaction mode represents a linear combination of some or all of the original five reactions (Eqs. 3.23—3.27). As this mode equilibrates quicker than the other two modes in the system, this “pseudo” reaction should not affect the value of the chosen constraint.

²Professor Joe Shepherd, Notes of March 9, 2013, “Simplified time scale analysis for reacting flow using Jacobian eigen-analysis.”

This is a similar argument that was used for the *DOD* method, except that the reaction mode is used instead of one individual reaction from the original chemical mechanism.

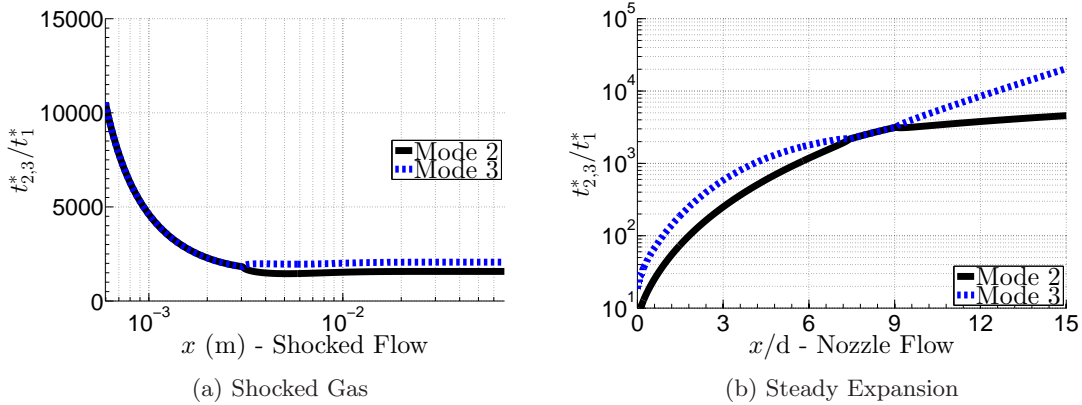


Figure 3.4: Evolution of the normalized reaction mode time scales for both shocked and expanding flow.

Figure 3.5 shows the evolution of the fastest reaction mode (mode one) for each test case, where ν_i^* is the coefficient taken from the eigenvector associated with the fastest reaction mode (molar based), for species i . All coefficients are normalized by $\nu_{O_2}^*$. For both cases, the reaction coefficients remain relatively constant throughout the system. It should be noted that for small distances behind the shock ($x < 10^{-3}$ m, not plotted) in Case #1, eigenvalues with positive real components are calculated. As mentioned previously, this identifies reaction modes where perturbations parallel to this mode will not relax to the initial composition, but instead will move farther away from the initial state. These positive eigenvalues are attributed to the state of the shocked air system immediately downstream of the shock, where the high temperature non-dissociated gas mixture is very far from an equilibrium composition. After a short amount of time, as the mixture begins to become closer to its thermodynamic equilibrium composition, all of the calculated real components of the eigenvalues become negative. The presence of these positive eigenvalues shows that while being an interesting theoretical concept, it is often difficult to apply a time scale analysis used in methods like CSP and ILDM to practical systems.

Some practical issues arise when calculating numerical values for a constraint based on the fastest reaction mode. First, as the solution evolves, neither the reaction modes nor the characteristic time scales remain constant. The separation between the characteristic time associated with the fastest and slower modes is consistent throughout both cases, but the changing value of the reaction mode implies that a non-constant constraint should be used when combined with RCCE. Second, these constraints are not consistent between the shocked flow and expanding flow scenarios, due to the

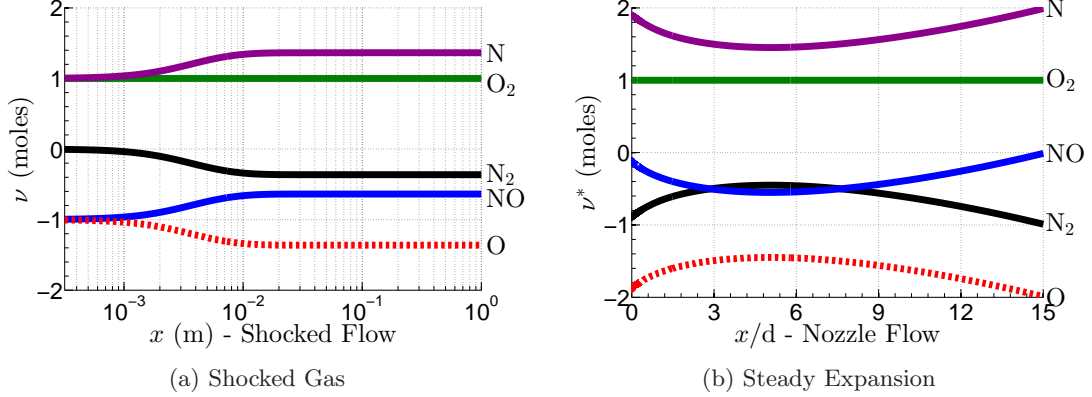


Figure 3.5: Evolution of the reaction coefficients for the fast reaction mode in air, normalized by ν_{O_2} .

fundamentally different physical phenomena that occur in each case. After extensive testing, while the changing reaction coefficients were found to have some effect on the calculated results, an average reaction coefficient value was found to give results characteristic of this constraint.

For the constraint based on the fast reaction mode (ϕ^{10}), the coefficients, C_i^{10} , are chosen to be $C_i^{10} = \overline{\nu}_i^*$, yielding $\phi^{10} = \sum_{i=1}^{ns} \overline{\nu}_i^* Y_i$, where $\overline{\nu}_i^*$ is the average i th reaction coefficient (mass fraction based) for the fastest reaction mode. The average (to calculate $\overline{\nu}_i^*$ from ν^*) is performed over the domain where the eigenvalue associated with the fastest reaction mode is negative, and reactions are still occurring. All values of $\overline{\nu}_i^*$ are normalized such that $\overline{\nu}_{O_2}^* = 1$. For the shocked flow, the average is performed over the range $3.17 * 10^{-4} \text{ m} < x < 10^{-2} \text{ m}$, and for the nozzle flow, the average is performed over $0 < x/d < 9$. The values for $\overline{\nu}^*$ are *not* the same for both the shock and nozzle cases. Calculating these averages results in $\overline{\nu_{\text{Shock}}^*} = [-0.20, 1, -0.72, -0.61, 0.53]^T$, and $\overline{\nu_{\text{Nozzle}}^*} = [-0.46, 1, -0.44, -0.76, 0.67]^T$, for the shocked and nozzle flow, respectively, where $\mathbf{Y} = [Y_{N_2}, Y_{O_2}, Y_{NO}, Y_O, Y_N]^T$. This results in

$$\phi_{\text{Shock}}^{10} = \sum_{i=1}^{ns} \overline{\nu_{\text{Shock},i}^*} Y_i, \quad (3.31)$$

and

$$\phi_{\text{Nozzle}}^{10} = \sum_{i=1}^{ns} \overline{\nu_{\text{Nozzle},i}^*} Y_i. \quad (3.32)$$

3.7.4 Constraints Based on DOD Analysis

Figure 3.6 shows the results when the DOD analysis explained in Sec. 3.5.2 is applied to both test cases. The sign of the value of *DOD* in general switches between the two cases, as dissociation reactions are more prevalent in the shocked flow, while recombination reactions dominate the nozzle flow. In both cases, it can be seen that for at least one of the five reactions (different in each case), the forwards and reverse reaction rates remain essentially equal throughout the system. In the shocked case, it is $N + O + M \rightleftharpoons NO + M$, while in the nozzle flow it is $NO + O \rightleftharpoons O_2 + N$. These are the respective reactions that will be combined with elemental conservation when determining a constraint to be used with RCCE.

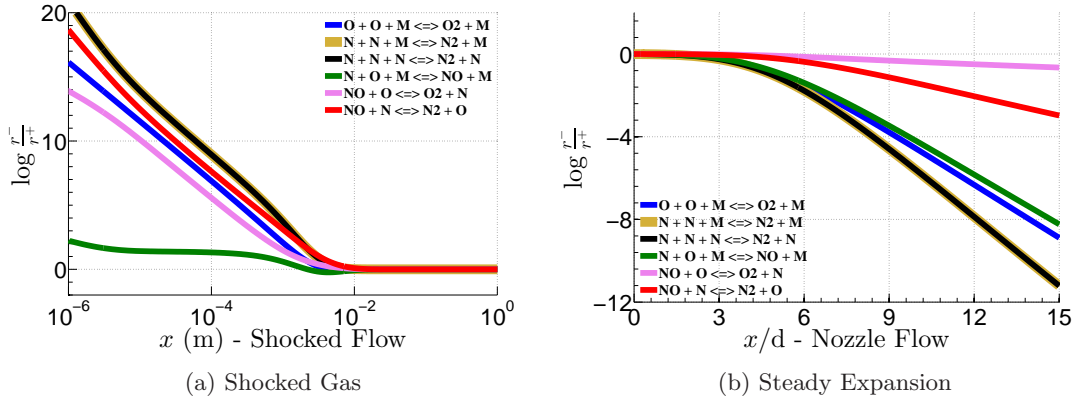


Figure 3.6: Degree of disequilibrium calculation for each reaction considered in the air system.

As discussed previously, equations for the conservation of oxygen and nitrogen can be written as

$$2\Delta X_{O_2} + \Delta X_O + \Delta X_{NO} = 0 \quad (3.33)$$

$$2\Delta X_{N_2} + \Delta X_N + \Delta X_{NO} = 0. \quad (3.34)$$

Re-arranging the stoichiometric coefficients for the reactions identified with a value of *DOD* close to zero yields

$$-\Delta X_{NO} + \Delta X_N + \Delta X_O = 0, \quad (3.35)$$

for the shock case (reaction 3.25), and

$$-\Delta X_{O_2} - \Delta X_N + \Delta X_{NO} + \Delta X_O = 0, \quad (3.36)$$

for the nozzle case (reaction 3.26). Equations 3.33, 3.34, and 3.35 are solved simultaneously for

the shock case. As shown in Sec. 3.5.3, there are three equations with five unknowns, so two free parameters can be picked arbitrarily. One solution is $\Delta X_{N_2} = \frac{1}{4}(2\Delta X_{O_2} - 3\Delta X_N)$, $\Delta X_{NO} = \frac{1}{2}(-2\Delta X_{O_2} + \Delta X_N)$, and $\Delta X_O = -(\Delta X_{O_2} + \frac{\Delta X_N}{2})$, where ΔX_{O_2} and ΔX_N are chosen to be the free parameters.

For the nozzle case, Eqs. 3.33, 3.34, and 3.36 are solved simultaneously. One solution is $\Delta X_{N_2} = \frac{1}{2}(3\Delta X_{O_2} - \Delta X_{NO})$, $\Delta X_O = -2\Delta X_{O_2} - \Delta X_{NO}$, and $\Delta X_N = -3\Delta X_{O_2}$, where ΔX_{O_2} and ΔX_{NO} are chosen to be the free parameters.

The constraints calculated through the degree of disequilibrium analysis combined with element conservation are summarized in Table 3.5. Two possible constraints are shown for each test case, as it is possible to vary the free parameters and create a different constraint. $k = 11$ is named *DOD #1*, and $k = 12$ is named *DOD #2*. The arbitrariness involved with picking free parameters is not desirable when trying to pick a constraint in a rigorous manner. Values for the free parameters are chosen to be of order 1, in order to stay consistent with the other constraints described in this section. It will be shown that this subjectivity in constraint selection does have an impact on the performance of the constraint, and hence, reduces the applicability and generality of DOD-based constraints.

Table 3.5: Calculated constraints based on degree of disequilibrium analysis. Two possible constraints (*DOD #1* and *DOD #2*) are shown for each test case.

Test Case	Chosen Reaction	k	Chosen Free Parameters	Constraint
Expanding Flow	$NO + O \rightleftharpoons O_2 + N$	11	$X_{O_2} = 2, X_{NO} = 1$	$\phi_{Nozzle}^{11} = \frac{5}{2} \frac{Y_{N_2}}{W_{N_2}} + 2 \frac{Y_{O_2}}{W_{O_2}} + \frac{Y_{NO}}{W_{NO}} - 5 \frac{Y_O}{W_O} - 6 \frac{Y_N}{W_N}$
		12	$X_{O_2} = 3, X_{NO} = 2$	$\phi_{Nozzle}^{12} = \frac{7}{2} \frac{Y_{N_2}}{W_{N_2}} + 3 \frac{Y_{O_2}}{W_{O_2}} + 2 \frac{Y_{NO}}{W_{NO}} - 8 \frac{Y_O}{W_O} - 9 \frac{Y_N}{W_N}$
Shocked Flow	$N + O \rightleftharpoons NO$	11	$X_{O_2} = 1, X_N = 0$	$\phi_{Shock}^{11} = \frac{1}{2} \frac{Y_{N_2}}{W_{N_2}} + \frac{Y_{O_2}}{W_{O_2}} - \frac{Y_{NO}}{W_{NO}} - \frac{Y_O}{W_O}$
		12	$X_{O_2} = 2, X_N = 1$	$\phi_{Shock}^{12} = \frac{1}{4} \frac{Y_{N_2}}{W_{N_2}} + 2 \frac{Y_{O_2}}{W_{O_2}} - \frac{3}{2} \frac{Y_{NO}}{W_{NO}} - \frac{5}{2} \frac{Y_O}{W_O} + \frac{Y_N}{W_N}$

3.8 Constraint Performance

The different aforementioned constraints are implemented and compared to the results from the Cantera simulations obtained with detailed chemistry. In order to gain insight into the effectiveness of each constraint, the effect of error propagation that would be present in a fully-coupled simulation is removed by comparing the detailed chemistry simulation results to RCCE results at every point in the flow. Results pertaining to fully-integrated simulations will be shown later, in Sec. 3.9.

3.8.1 Comparison Methodology

For each test problem, four basic plots are used to reveal how the constraint behaves through the system (see, for example, Fig. 3.7). First, the constraint, ϕ , is plotted as a function of a spatial coordinate, showing how the constraint evolves through the reacting system (top left). The shock case consists primarily of dissociation reactions, while the expansion case consists primarily of recombination reactions. This difference will cause the evolution of the constraint to vary greatly between the two test cases. For the remaining three plots, quantities are plotted as a function of ϕ (Eq. 3.12). This represents a shift from physical space into a “reaction space” (or phase space). As the RCCE method requires the system to be reconstructed as a function of ϕ , this is the appropriate space to visualize and evaluate the efficacy of the constraints.

The second plot (top right) shows the species mass fractions as a function of ϕ . Values calculated from the detailed chemistry simulations, \mathbf{Y} , are labeled as “Cantera”, and are compared to values calculated from constrained thermodynamic calculations, \mathbf{Y}^{CEQ} (Eq. 3.14). All discrepancies in the mixture properties between the Cantera results and the CEQ results can be attributed to differences between \mathbf{Y} and \mathbf{Y}^{CEQ} .

As discussed in Sec. 3.4, when coupled with a CFD solver, the bulk properties of the fluid mixture are needed. γ , the ratio of specific heats, is taken to be a characteristic bulk property. Constrained equilibrium calculation results (γ^{CEQ}) are compared to detailed chemistry results (γ) in the third plot (bottom left). Finally, it is necessary to not only transport the value of ϕ in an integrated simulation, but the source term for the constraint, $\partial\phi/\partial t$, must also be known as a function of ϕ . The final plot (bottom right) compares $|\frac{\partial\phi^{CEQ}}{\partial t}|$ (Eq. 3.17) and $|\frac{\partial\phi}{\partial t}|$ (Eq. 3.18). Depending on the choice of constraint, all or only some of the reactions from the full mechanism are used. The absolute value of this function is compared between the two cases (for visualization purposes). Qualitative comparisons are shown first for each constraint, and then quantitative comparisons are shown in Sec. 3.8.6.

3.8.2 Constraint: Individual Species

The results for a constraint based on the mass fraction of each individual species, O₂, N₂, O, and NO, are shown in Figs. 3.7 - 3.13. Comparisons are made both for the shock and nozzle cases, comparing finite rate chemistry results and constrained equilibrium results. Results for N are not shown due to the low concentration of N present. As Y_N tends to 0, the constrained equilibrium holding Y_N constant tends towards the unconstrained equilibrium calculation. In all figures, ϕ is

normalized by the maximum value of ϕ in the domain (ϕ_{max}), and the absolute value of $\partial\phi/\partial t$ is plotted for simplicity.

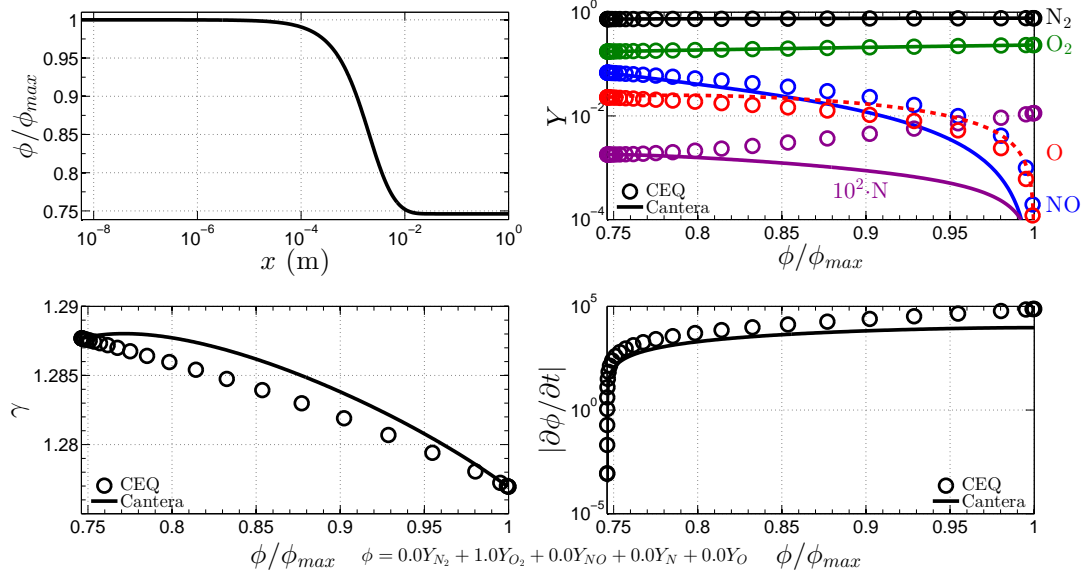


Figure 3.7: Finite rate chemistry and constrained equilibrium calculations for a shocked air flow. Constrained equilibrium calculations are performed constraining the mass fraction of O_2 .

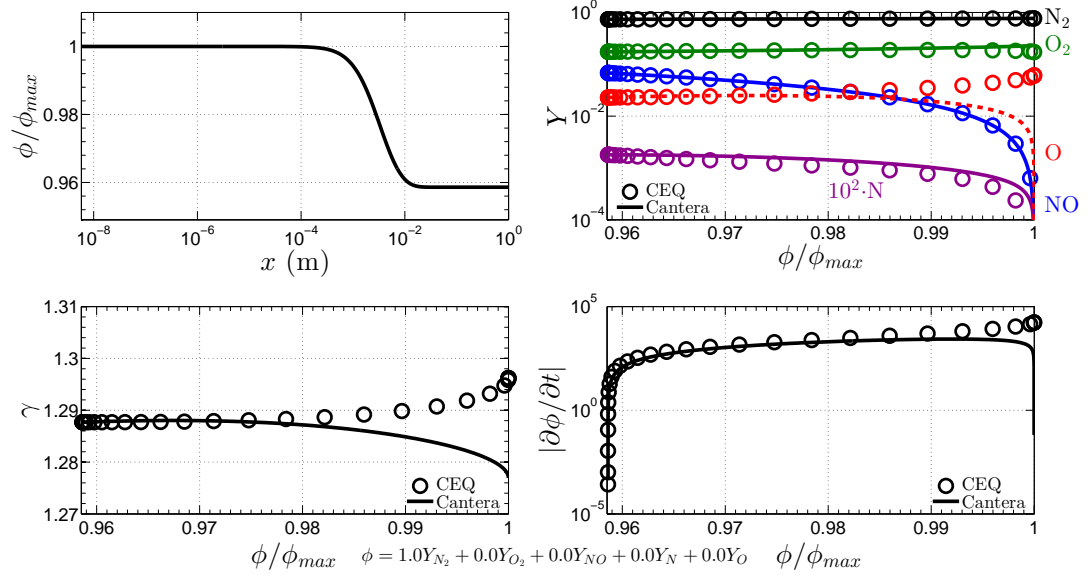


Figure 3.8: Finite rate chemistry and constrained equilibrium calculations for a shocked air flow. Constrained equilibrium calculations are performed constraining the mass fraction of N_2 .

Figures 3.7 and 3.8 show the O_2 and N_2 constraints, respectively, for the shock test case. Both of these constraints decrease monotonically throughout the system, as the O_2 and N_2 undergo dissociation reactions. The mass fraction of O_2 decreases by approximately 25% throughout the

reaction, while the mass fraction of N_2 decreases by approximately 5%. A larger range of the constraint variable throughout the system is seen as desirable, as this allows the entire system to be less sensitive to small errors made in ϕ . The reconstructed gas mixture based on the species constraint on O_2 (Fig. 3.7) over predicts the amount of N present, and the reconstructed gas mixture based on the species constraint on N_2 (Fig. 3.8) over predicts the amount of O present. Errors are seen in both the bulk properties and source term for ϕ , and a more quantitative analysis of the errors observed will be presented in Sec. 3.8.6.

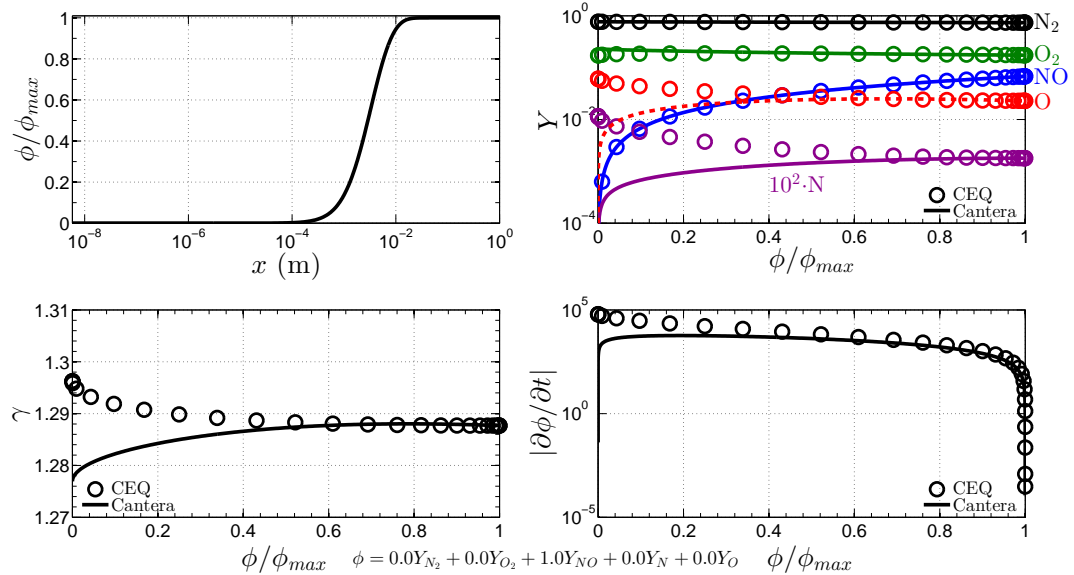


Figure 3.9: Finite rate chemistry and constrained equilibrium calculations for a shocked air flow. Constrained equilibrium calculations are performed constraining the mass fraction of NO.

Figures 3.9 and 3.10 show the O and NO constraints, respectively, for the shock test case. As these radical species are products of the dissociation reactions, their mass fractions increase through the system. However, while NO increases monotonically throughout the system, the mass fraction of O peaks midway through the system, and then decreases again, as shown in Fig. 3.10. This causes properties to appear to be double valued when plotted as a function of ϕ . However, as temperature and pressure are also changing throughout the system, each point is unique in T , P , and ϕ space. A graphical example of a similar case was shown previously in Fig. 3.1. These constraints undergo a relatively large change through the system, as the initial radical concentration is zero.

The increase then decrease in O can be explained by considering the dominant reactions in the

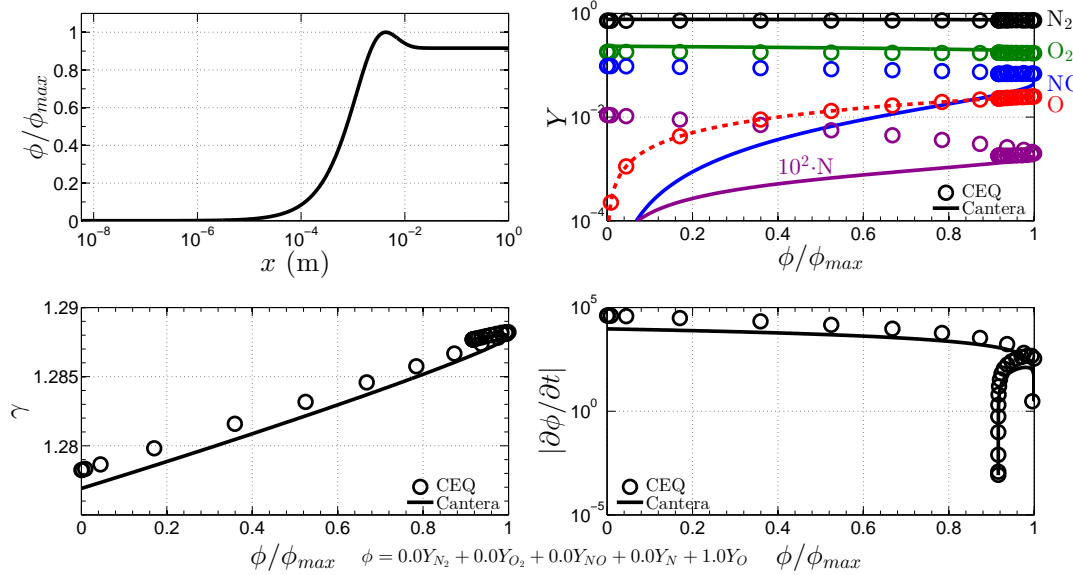
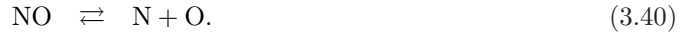
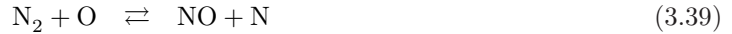


Figure 3.10: Finite rate chemistry and constrained equilibrium calculations for a shocked air flow. Constrained equilibrium calculations are performed constraining the mass fraction of O.

shock case:



Reactions 3.37 - 3.39 are written such that the net production rate is always in the forwards direction, and the net production switches from being forwards to reverse midway through the system for 3.40. Reaction 3.37 is the original source of O radicals, as originally no O and only O₂ is present in the shocked mixture. Reaction 3.38 results in the production of one O radical, while reaction 3.39 results in the destruction of one O radical. However, the net forwards production rate from reaction 3.39 is always greater than that of reaction 3.38 in this example, which results in a net destruction of O radicals from these two reactions. As the production rate of O from reaction 3.37 decreases, the destruction of O from the combination of reaction 3.38 and reaction 3.39, and the destruction of O in reaction 3.40, causes the mass fraction of O to decrease after a relative maximum is reached. However, the production of NO from reaction 3.38 and reaction 3.39 is larger than the consumption of NO in reaction 3.40, which causes the mass fraction of NO to increase monotonically through the system, as shown in Fig. 3.9.

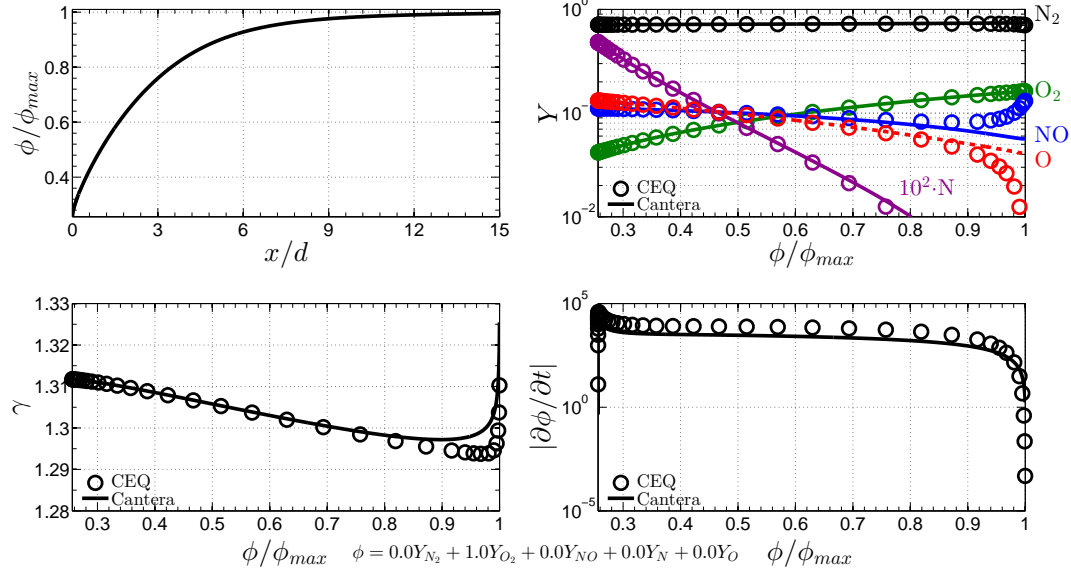


Figure 3.11: Finite rate chemistry and constrained equilibrium calculations for an expanding air flow. Constrained equilibrium calculations are performed constraining the mass fraction of O_2 .

Figure 3.11 shows the results for the nozzle test case, choosing the mass fraction of O_2 as a constraint. As the gas mixture starts in a highly dissociated state, recombination reactions dominate as the flow expands through the nozzle, and the mass fraction of O_2 increases as the flow travels downstream. Similar results are observed when N_2 is chosen as the constraint (Fig. 3.12).

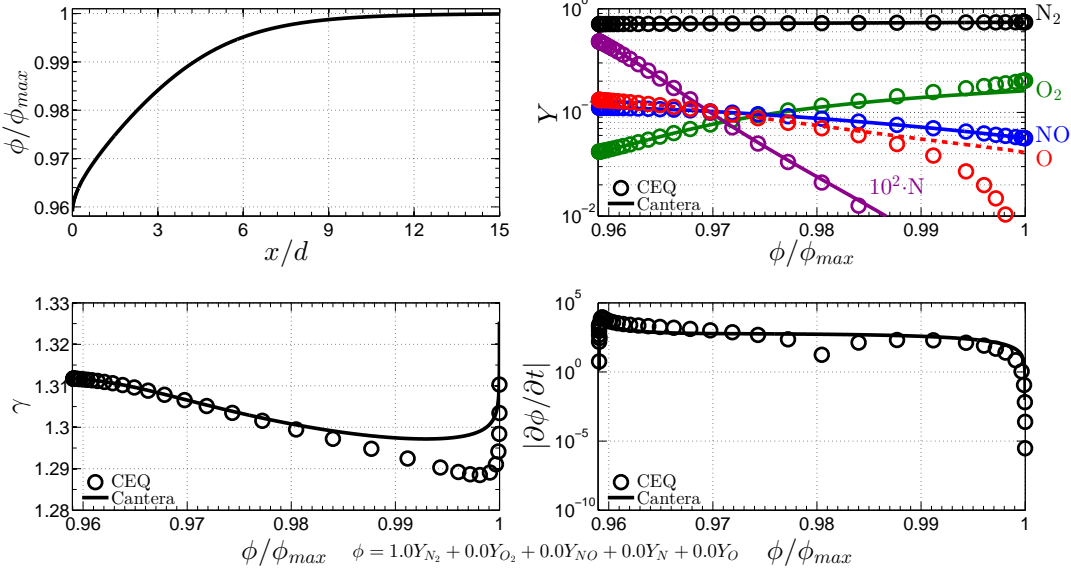


Figure 3.12: Finite rate chemistry and constrained equilibrium calculations for an expanding air flow. Constrained equilibrium calculations are performed constraining the mass fraction of N_2 .

Figures 3.13 and 3.14 show results for O and NO , respectively. These values decrease monoton-

ically through the system, and reach a constant value when the temperature and pressure are low enough that the composition of the flow is “frozen” in the nozzle. The constraint on NO performs better than the constraint placed on O. Although the reconstructed species composition for the O constraint (Fig. 3.13) visually appears to be very accurate, errors are seen in the reconstructed source term. This sensitivity to small errors in mass fractions will be discussed in a later section for a similar example.

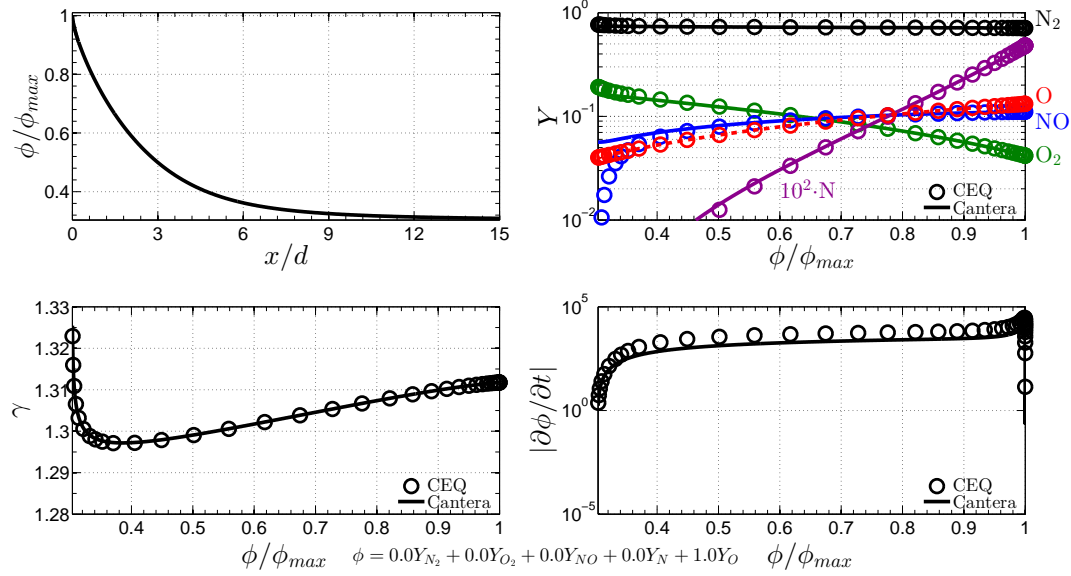


Figure 3.13: Finite rate chemistry and constrained equilibrium calculations for an expanding air flow. Constrained equilibrium calculations are performed constraining the mass fraction of O.

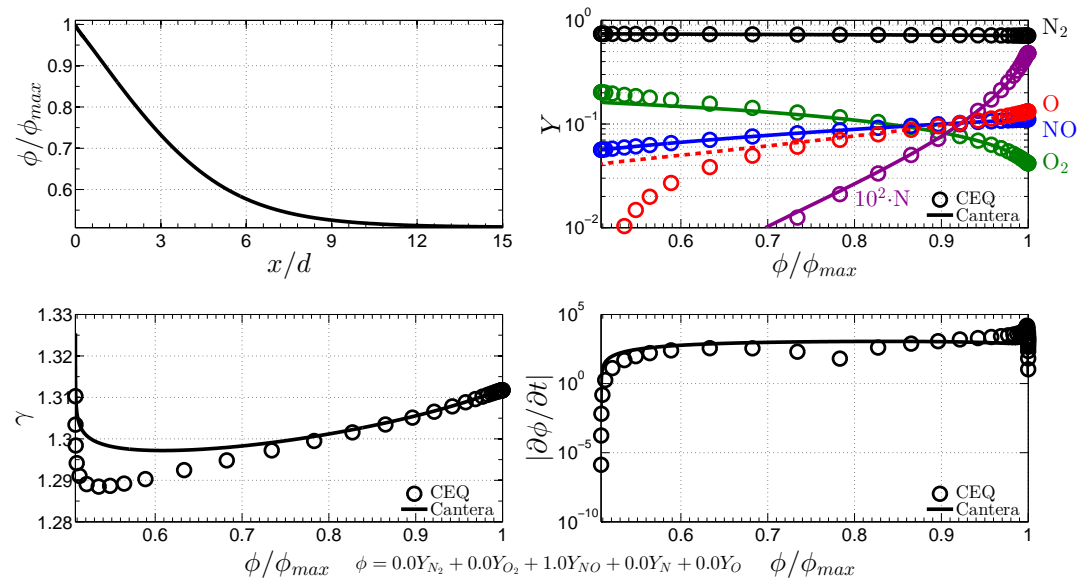


Figure 3.14: Finite rate chemistry and constrained equilibrium calculations for an expanding air flow. Constrained equilibrium calculations are performed constraining the mass fraction of NO.

3.8.3 Constraint: Major and Radical Species

It is also possible to keep the sum of the mass fractions of different species constant through a constrained equilibrium calculations. Major species and radical species are some of the original sums suggested by Keck [70]. The major species make up the majority of the mixture (by mass or mole), while the radical species represent the most reactive components of the mixture, and are generally associated with fast reacting time scales. In the shocked case, the mass fraction of major species decreases through the system (Fig. 3.15), while the mass fraction of radical species increases (Fig. 3.16), as expected. Both constraints visually do a good job of reconstructing the system.

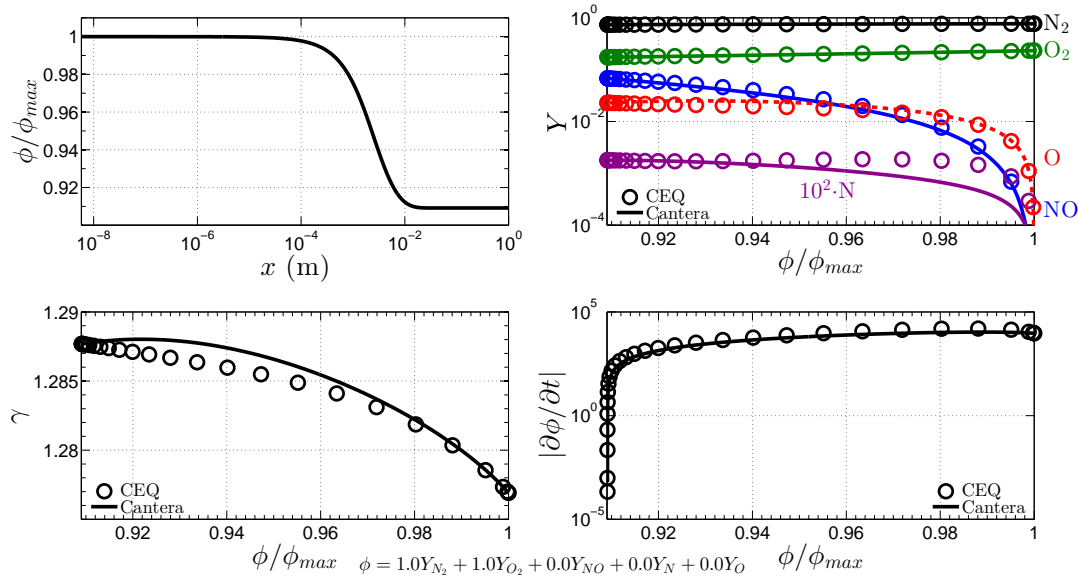


Figure 3.15: Finite rate chemistry and constrained equilibrium calculations for a shocked air flow. Constrained equilibrium calculations are performed constraining the summation of mass fractions of the major species (O_2 and N_2).

Figures 3.17 and 3.18 show the same two constraints applied to expanding air. The opposite trend is seen in the constraint variable in these two cases, as expected. ϕ monotonically increases for the major species, while ϕ monotonically decreases for the radical species.

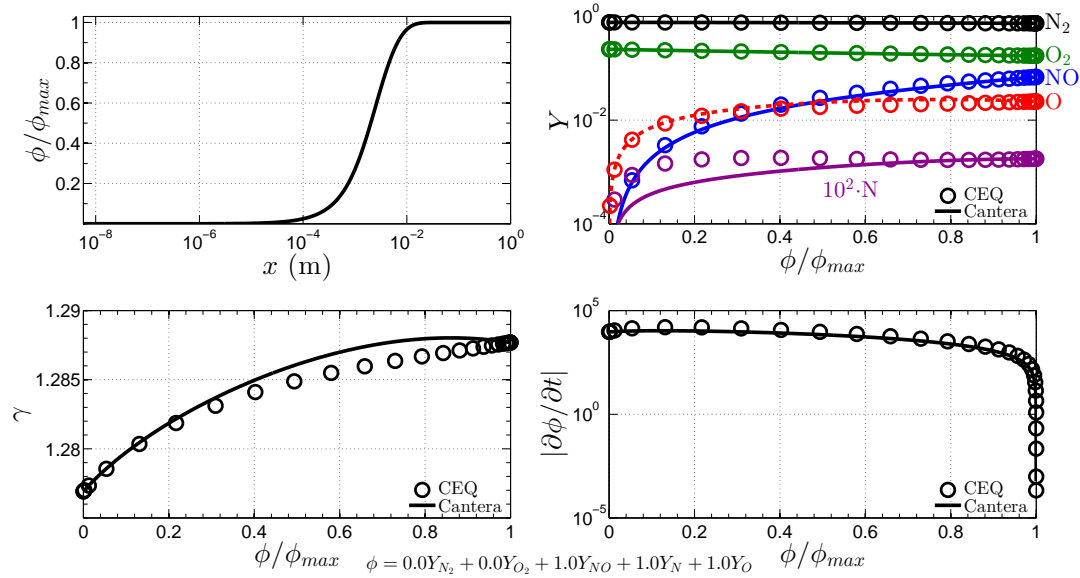


Figure 3.16: Finite rate chemistry and constrained equilibrium calculations for a shocked air flow. Constrained equilibrium calculations are performed constraining the summation of mass fractions of the radical species (NO, N and O).

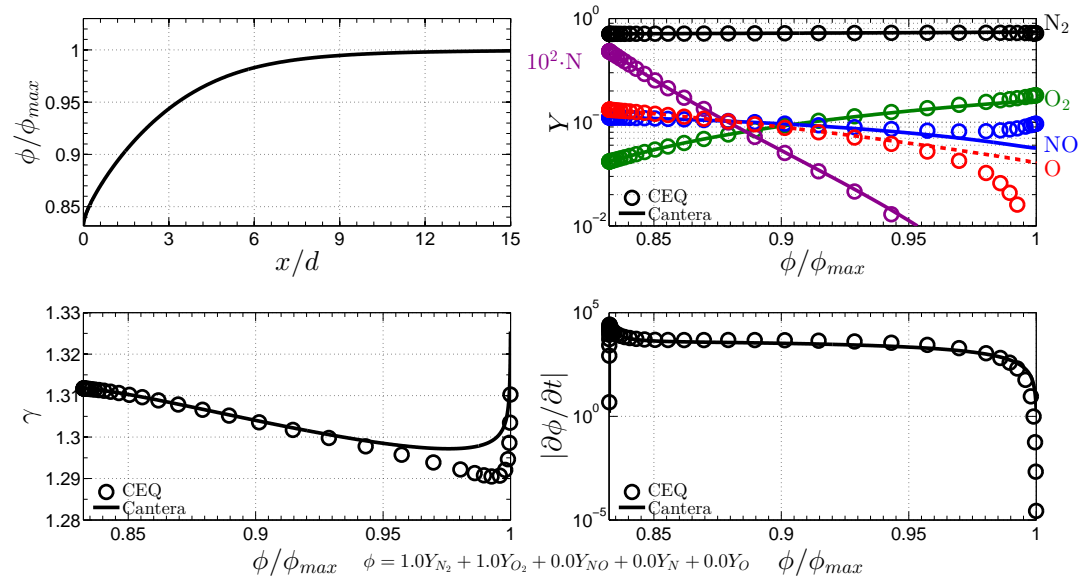


Figure 3.17: Finite rate chemistry and constrained equilibrium calculations for an expanding air flow. Constrained equilibrium calculations are performed constraining the summation of mass fractions of the major species (O_2 and N_2).

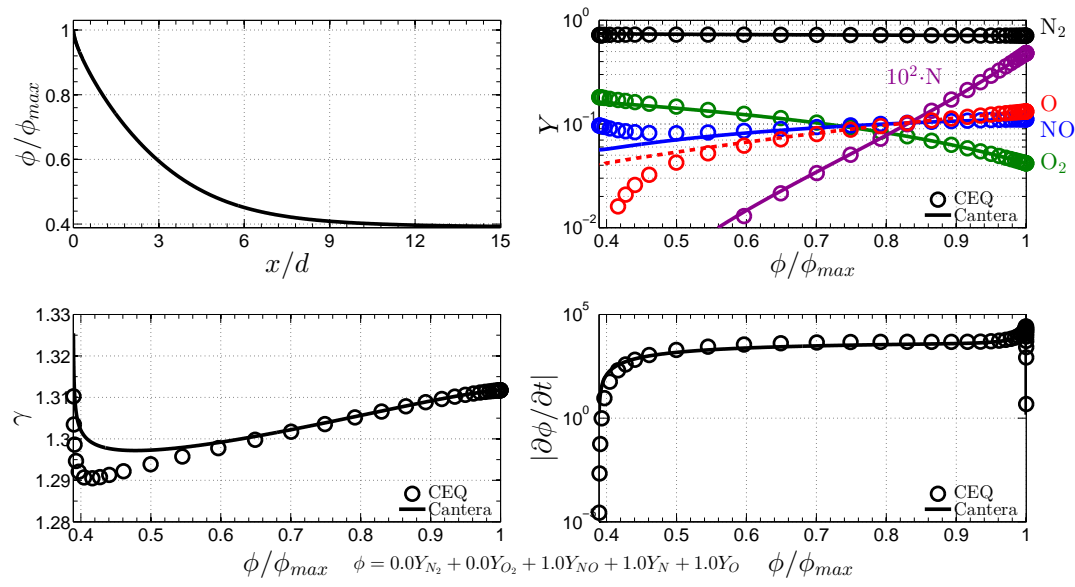


Figure 3.18: Finite rate chemistry and constrained equilibrium calculations for an expanding air flow. Constrained equilibrium calculations are performed constraining the summation of mass fractions of the radical species (NO, N and O).

3.8.4 Constraint: Global Quantities

As mentioned previously, the two global quantities investigated include the inverse of the molecular weight of the mixture, and the standard enthalpy of formation (by mass). There is an extremely small variation in molecular weight throughout the shock system ($\sim 1\%$), and this variation is not monotonic, as shown in Fig. 3.19. To investigate whether this apparent multi-value is a problem, Fig. 3.1 (Sec. 3.4) shows the value of ϕ as a function of T and P . This figure illustrates that even though the same value for molecular weight is reached twice in the system, due to the varying temperature and pressure at each point where this occurs, the evolution of the system is uniquely valued when taking T and P into account. In other words, the mixture composition is still unique for a given set of ϕ , T , and P values.

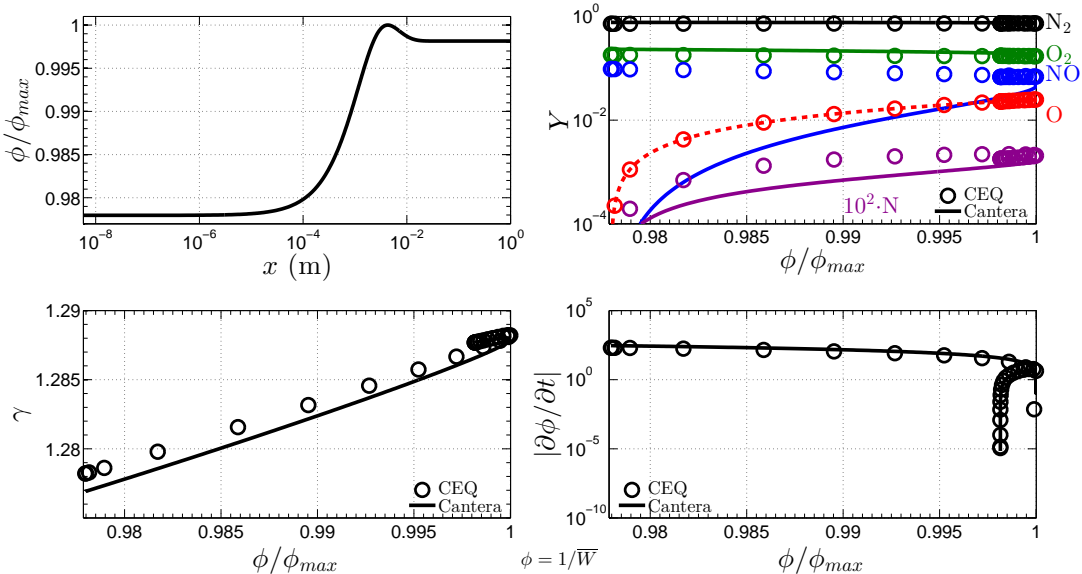


Figure 3.19: Finite rate chemistry and constrained equilibrium calculations for a shocked air flow. Constrained equilibrium calculations are performed by holding the inverse of the molecular weight of the mixture constant.

While there are significant errors made in the reconstructed mass fractions of O_2 , NO , and N , the bulk properties (γ and $|\partial\phi/\partial t|$) are reproduced accurately. For an ideal gas at standard conditions, γ is related to the degrees of freedom of the molecule, f , by $\gamma = 1 + \frac{2}{f}$. For a monoatomic molecule which has 3 translational degrees of freedom, this yields the familiar result that $\gamma = \frac{5}{3}$. For a diatomic molecule at standard conditions, there are 3 translational degrees of freedom and 2 rotational degrees of freedom (the vibrational degree of freedom does not contribute at room temperature), which yields $\gamma = \frac{7}{5}$. In general, a monoatomic molecule has 3 degrees of freedom (3 translational), a diatomic molecule has 6 degrees of freedom (3 translational, 2 rotational, and 1 vibrational), and a non-linear

molecule containing N atoms, where $N > 2$, has $3N$ degrees of freedom (3 translational, 3 rotational, and $3N - 6$ vibrational). Depending on the relative sizes of the atoms present in a system, higher molecular weight molecules are generally associated with a larger number of degrees of freedom. In the air system considered, since N and O have similar molecular weights, the molecular weight of the mixture is an indication of the ratio of monoatomic to diatomic molecules present. Interpreting the molecular weight of a mixture as being related to a weighted average of the number of degrees of freedom of the molecules present in the mixture explains why this constraint accurately reproduces the mixture averaged ratio of specific heats, γ . This is done while simultaneously making significant errors on the individual mass fractions.

The enthalpy of formation (Δh_f°) of a compound is the change in enthalpy due to the formation of the compound from its constituent elements at standard conditions. As O_2 and N_2 exist as diatomic gases at room temperature and atmospheric pressure, this constraint becomes a weighted sum of the mass fractions of the radical species. As will be shown in Sec. 3.8.6, this constraint performs as well and generally better than a simple summation of the radical mass fractions.

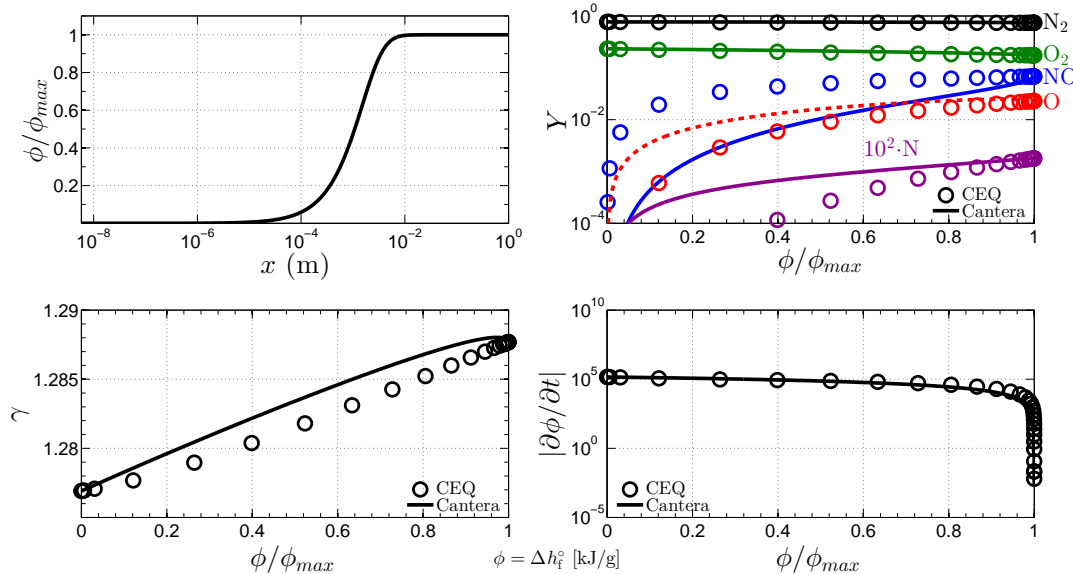


Figure 3.20: Finite rate chemistry and constrained equilibrium calculations for a shocked air flow. Constrained equilibrium calculations are performed by holding the enthalpy of formation (by mass) of the mixture constant.

Similar trends are observed when these two constraints are applied to the nozzle test case (Fig. 3.21 and Fig. 3.22). In both instances, ϕ decreases monotonically as the air expands through the nozzle. However, a difference is seen in how accurately each constraint reproduces the value of $|\partial\phi/\partial t|$. While visually in Fig. 3.22 the mass fractions seem to be very well-represented by the

constrained equilibrium calculations (relative difference $< 1\%$), there is still a large error observed in $|\partial\phi/\partial t|$. The small errors in mass fractions compared to the large error in the source term is shown in Table 3.6. These values are taken at an instantaneous location for when $\phi = 1.82 \text{ kJ/g}$ ($\phi/\phi_{max} = 0.719$).

Table 3.6: Sensitivity of $|\partial\phi/\partial t|$ for the nozzle using the enthalpy of formation as a constraint. Comparisons are made at $\phi = 1.82 \text{ kJ/g}$ ($\phi/\phi_{max} = 0.719$).

	Finite-Rate Kinetics	CEQ	Relative Difference
Y_{N2}	0.7197	0.7196	0.01%
Y_{O2}	0.08281	0.08277	0.05%
Y_{NO}	0.09984	0.1000	0.2%
Y_N	0.0007589	0.0007657	0.9%
Y_O	0.09687	0.09683	0.04%
$ \partial\phi/\partial t $	$4.245 \cdot 10^4$	$8.247 \cdot 10^4$	100%

The high sensitivity to mass fractions stems from the fact that two reactions are close to being in a partial equilibrium throughout the nozzle. Earlier in Sec. 3.7.3, Fig. 3.6b showed that the forwards and backwards reaction rates for $\text{NO} + \text{O} \rightleftharpoons \text{O}_2 + \text{N}$ and $\text{NO} + \text{N} \rightleftharpoons \text{N}_2 + \text{O}$ are close to equal throughout the entire expansion. Minor changes in species concentrations can therefore have a large effect on the net rate of progress ($r^+ - r^-$) for each reaction. This is shown in Table 3.7. The largest discrepancies are seen where the reaction rate depends on the concentration of nitrogen: r^- for $\text{NO} + \text{O} \rightleftharpoons \text{O}_2 + \text{N}$, and r^+ for $\text{NO} + \text{N} \rightleftharpoons \text{N}_2 + \text{O}$. The reaction rates differ by $\sim 1\%$ in each case, which is the same order of magnitude error as the discrepancy in mass fraction of N shown in Table 3.6. However, as the net rate of progress requires the subtraction of the forwards and backwards reaction rates, these small errors produce large discrepancies (Table 3.7). It is important to be aware of this sensitivity when characterizing the performance of the chosen constraints.

Table 3.7: Sensitivity of reaction rates due to small discrepancies in mass fractions. All values are given in $\text{kmol}/(\text{m}^3\text{s})$, and are taken at $\phi = 1.82 \text{ kJ/g}$ ($\phi/\phi_{max} = 0.719$).

Reaction	Finite-Rate Kinetics			CEQ		
	r^+	r^-	$r^+ - r^-$	r^+	r^-	$r^+ - r^-$
$\text{NO} + \text{O} \rightleftharpoons \text{O}_2 + \text{N}$	$3.576 \cdot 10^4$	$3.570 \cdot 10^4$	$0.5668 \cdot 10^2$	$3.5802 \cdot 10^4$	$3.601 \cdot 10^4$	$-2.074 \cdot 10^2$
$\text{NO} + \text{N} \rightleftharpoons \text{N}_2 + \text{O}$	$2.432 \cdot 10^4$	$2.426 \cdot 10^4$	$0.6318 \cdot 10^2$	$2.458 \cdot 10^4$	$2.425 \cdot 10^4$	$3.311 \cdot 10^2$

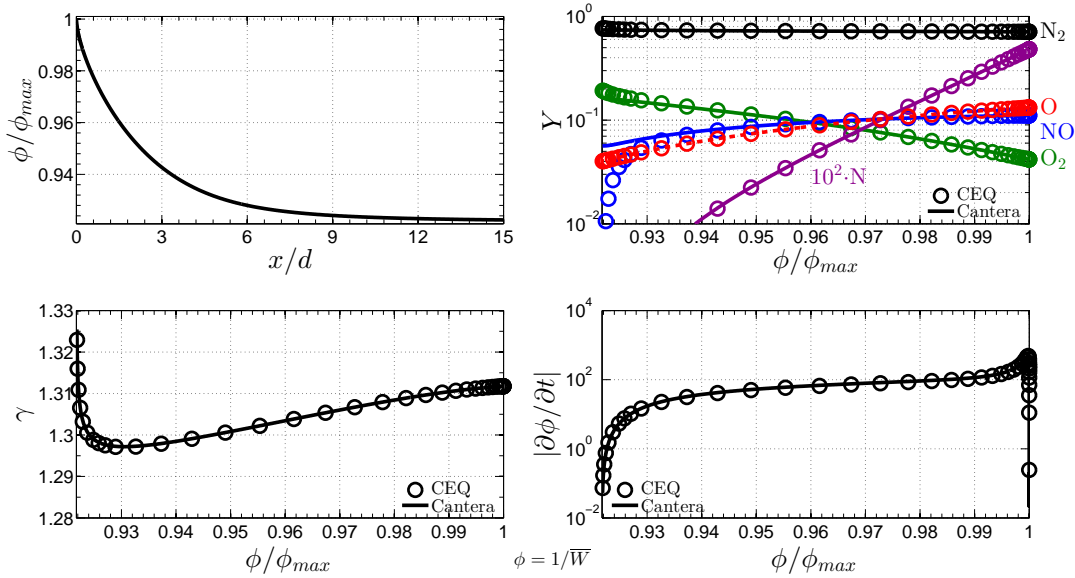


Figure 3.21: Finite rate chemistry and constrained equilibrium calculations for an expanding air flow. Constrained equilibrium calculations are performed by holding the inverse of the molecular weight of the mixture constant.

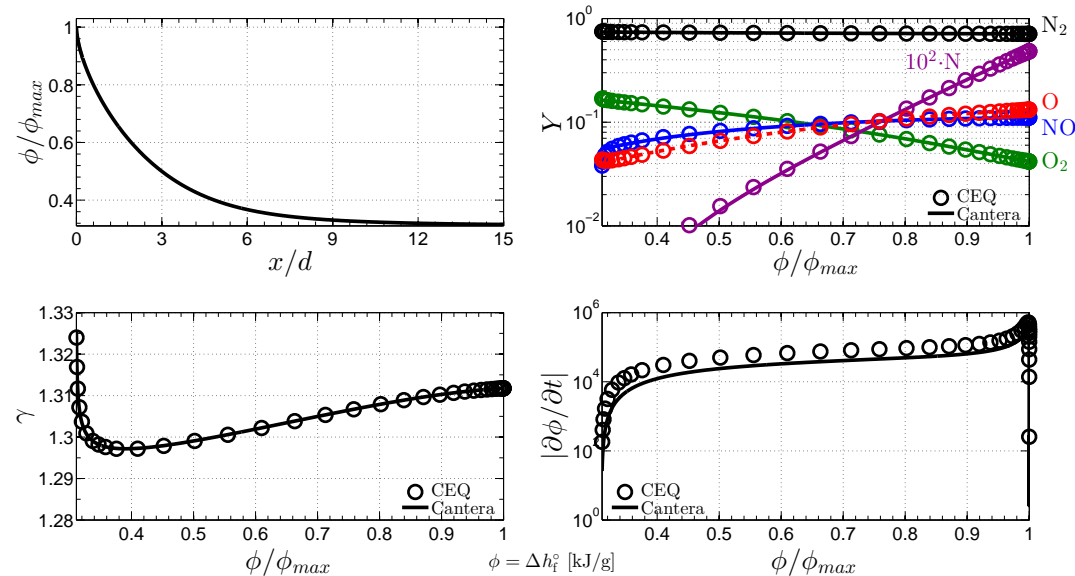


Figure 3.22: Finite rate chemistry and constrained equilibrium calculations for an expanding air flow. Constrained equilibrium calculations are performed by holding the enthalpy of formation (by mass) of the mixture constant.

3.8.5 Constraint: Timescale Analysis and *DOD*

Results from using constraints based on the fast reaction mode in each system and the degree of disequilibrium analysis previously performed are shown in Figs. 3.23—3.26. These constraints work to varying degrees of success when used to reconstruct the system. One of the largest fundamental issues with these constraints is that they are not consistent between the two test cases. The reaction modes (timescale analysis) and individual reactions that are close to being in equilibrium (*DOD*) are not the same for the two test cases due to the fundamental differences in the two flows (dissociation dominated *vs.* recombination dominated, in the shock and nozzle flows, respectively). This implies that it would not be possible to use a single constraint in a flow around a re-entry vehicle, as after the ambient gas is processed by a strong bowshock, it expands around the corner of the vehicle. Only if a single application is required, then these constraints can be efficient, as shown previously for reacting nozzle flow [64].

Figures 3.24 and 3.26 use different choices for the free parameters associated with the *DOD* constraint, as previously shown in Table 3.5. These choices *are* arbitrary, though it is possible to try to incorporate some intuition about the physical system considered when choosing these constraints. For example, in Table 3.5, X_N is set to 0 for the first *DOD* constraint chosen. This is based on the knowledge that due to the relatively small amounts of N present in the shock test case considered, a species constraint based on N does not perform very well. Later, Sec. 3.8.6 shows that the free parameter choices can have a quantitative effect on the performance of the *DOD* constraint.

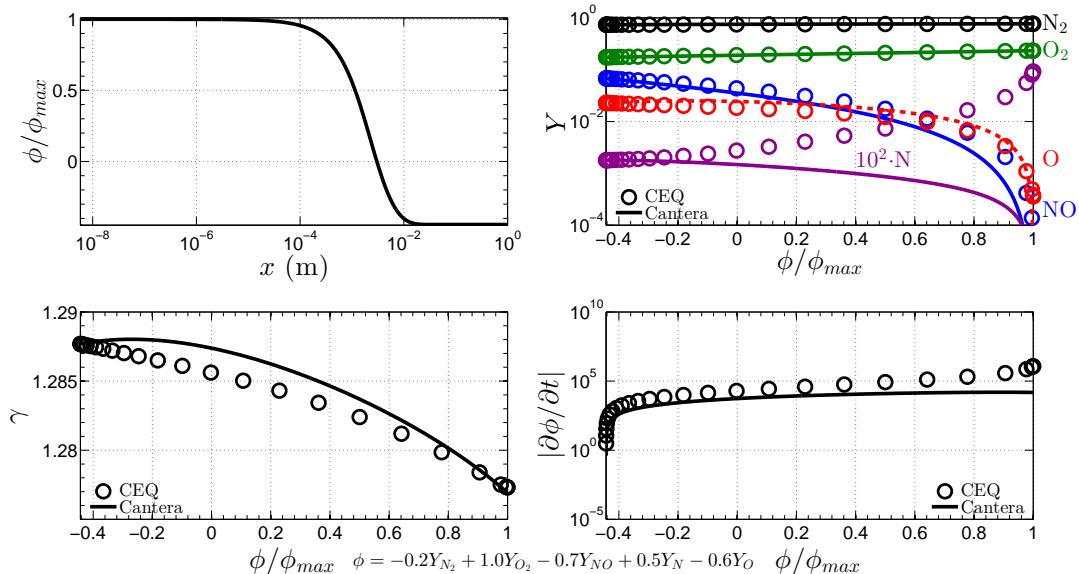


Figure 3.23: Finite rate chemistry and constrained equilibrium calculations for a shocked air flow. Constrained equilibrium calculations are performed using an average of the fastest reaction mode.

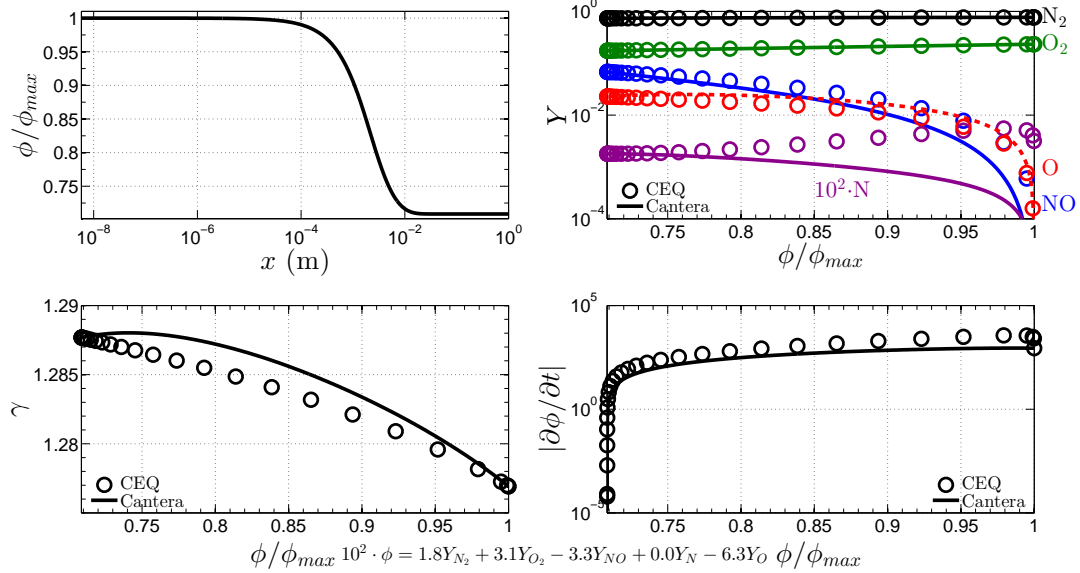


Figure 3.24: Finite rate chemistry and constrained equilibrium calculations for a shocked air flow. Constrained equilibrium calculations are performed by combining degree of disequilibrium analysis and elemental conservation.

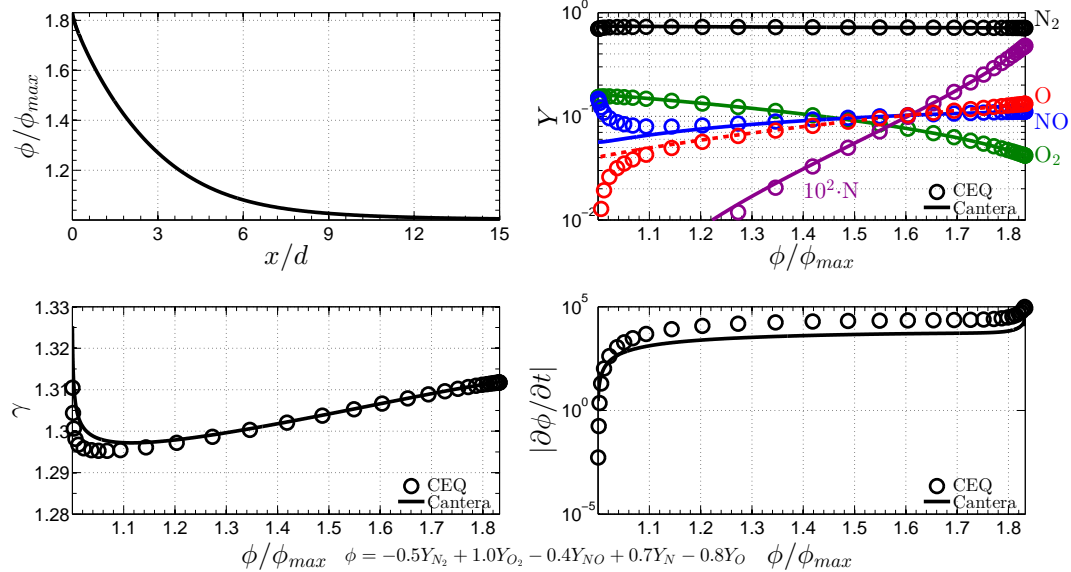


Figure 3.25: Finite rate chemistry and constrained equilibrium calculations for an expanding air flow. Constrained equilibrium calculations are performed using an average of the fastest reaction mode. The fact that ϕ/ϕ_{max} is greater than one indicates that the constraint has a negative value.

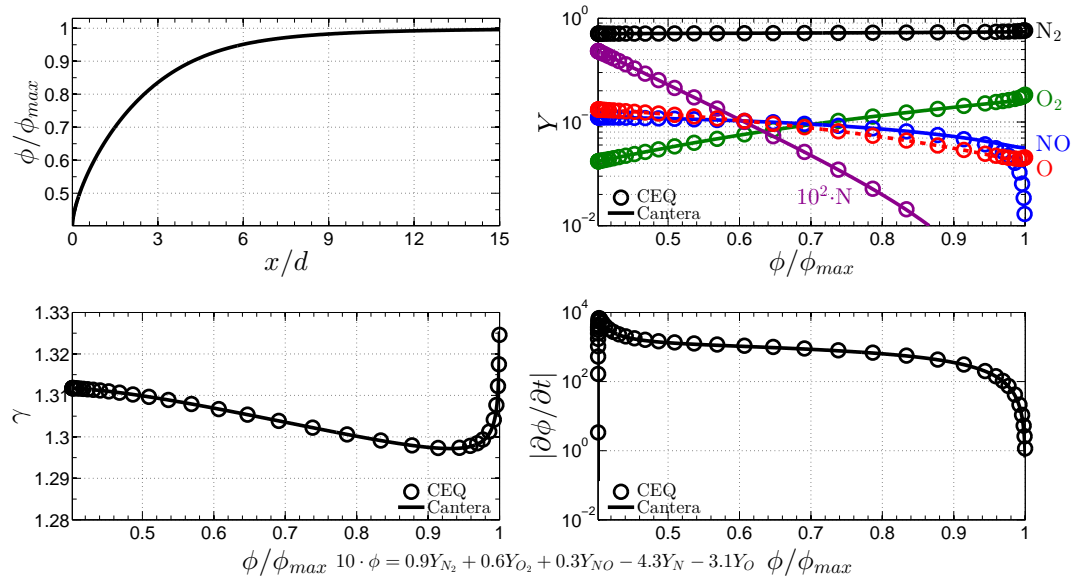


Figure 3.26: Finite rate chemistry and constrained equilibrium calculations for an expanding air flow. Constrained equilibrium calculations are performed by combining degree of disequilibrium analysis and elemental conservation.

3.8.6 Analysis of Constraint Performance

The previous section showed qualitative comparisons evaluating the ability of different constraints to reconstruct the chemical system, based on constrained thermodynamic equilibrium calculations. In this section, quantitative error calculations are presented in order to pick a constraint to be used with an integrated RCCE simulation.

To pick relevant fluid properties to compare between the CEQ calculations and the Cantera calculation, properties that appear in the reacting Euler equations (Eqs. 3.5–3.8) should be considered. In the analysis presented in the previous section, γ , the ratio of specific heats, was used. Although γ does not appear explicitly in Eqs. 3.5–3.8, for an ideal gas, $\gamma = \frac{c_P}{c_p - R}$, where R is the specific gas constant defined by $R = \frac{\mathcal{R}}{W}$. Here \mathcal{R} is the universal gas constant. A γ comparison encompasses errors from both the molecular weight of the mixture, and from the c_p of the mixture. In addition to errors associated with the mixture molecular weight and c_P , comparing γ evaluates errors that are associated with the $\int_{T_o}^T c_{p,i}(T')dT'$ term in the $h_i(T_o)$ calculation previously mentioned (Eq. 3.11).

The reference enthalpy of the mixture ($h(T_o) = \sum_{i=1}^{ns} Y_i h_i(T_o)$) is another logical choice of a bulk property to compare between the two different computational methods, due to the appearance of the h_i terms in Eq. 3.10. The reference enthalpy is used in order to place an emphasis on the error made in mass fractions, and removing any temperature effect that would be apparent if the enthalpy of the mixture were used as a metric for comparison instead. Finally, a comparison of the source term, $\frac{\partial \phi}{\partial t}$ gives an indication of how the system will evolve.

For this work, two different L_2 norms are defined in order to quantitatively compare the different constraints. If an arbitrary fluid property, F , is chosen, the first version of this norm is calculated by

$$L_2^k = \left[\frac{1}{N} \sum_i^N |F(\phi_i^k) - F^{CEQ}(\phi_i^k)|^2 \right]^{1/2}, \quad (3.41)$$

where N is the number of points used in the calculation, i represents a point in the flow, and k corresponds to the specific constraint being compared (see Table 3.3). $F(\phi_i^k)$ (for example, Eq. 3.20) corresponds to a mixture property calculated from detailed chemistry simulations, and $F^{CEQ}(\phi_i^k)$ (for example, Eq. 3.19) corresponds to a mixture property calculated at the same point in the flow, but using constrained equilibrium calculations, for the k th constraint. As discussed, γ , $h(T_o)$, and $\frac{\partial \phi}{\partial t}$ are chosen as the mixture properties to compare (F).

However, the numerical method used to solve Eqs. 3.5–3.8 does not use an equally spaced grid, in either x or ϕ . Points are clustered around strong gradients of ρ , w , P , and \mathbf{Y} . Eq. 3.41 therefore

weights errors associated with regions of higher gradients more heavily than the smoother regions of the flow. This emphasizes the performance of the constraints in these high gradient regions, which is a good indication as to how the constraint performs when there are many chemical reactions present.

In order to remove the effect of a non-uniform grid spacing, a “weighted” L_2 norm is defined to be

$$L_{2,w}^k = \left[\frac{1}{\phi_{max}^k - \phi_{min}^k} \sum_i^N \Delta\phi_i^k |F(\phi_i^k) - F^{CEQ}(\phi_i^k)|^2 \right]^{1/2}, \quad (3.42)$$

where $\Delta\phi_i^k$ is the local grid spacing in ϕ^k ($\Delta\phi_i^k = (\phi_{i+1}^k - \phi_{i-1}^k)/2$), and ϕ_{max}^k and ϕ_{min}^k are the maximum and minimum values of ϕ^k in the domain, respectively. The unweighted error calculations for γ and $h(T_o)$ are shown in Fig. 3.27 and the weighted error calculations for γ and $h(T_o)$ are shown in Fig. 3.28. Weighted and unweighted error comparisons for $|\partial\phi/\partial t|$ are shown in Fig. 3.29.

Figures 3.27 and 3.28 are normalized by the maximum error in each test case, *i.e.*, the maximum error over all k for a specific test case, so that all error calculations range from 0 to 1. Alternatively, each individual data point in Fig. 3.29 is normalized by the local $\max(|\partial\phi/\partial t|)$, *i.e.*, the maximum value of $|\partial\phi/\partial t|$ for a specific k , in order to have an idea of the order of magnitude of error to expect if the source term were to be used to reconstruct the original ϕ profile.

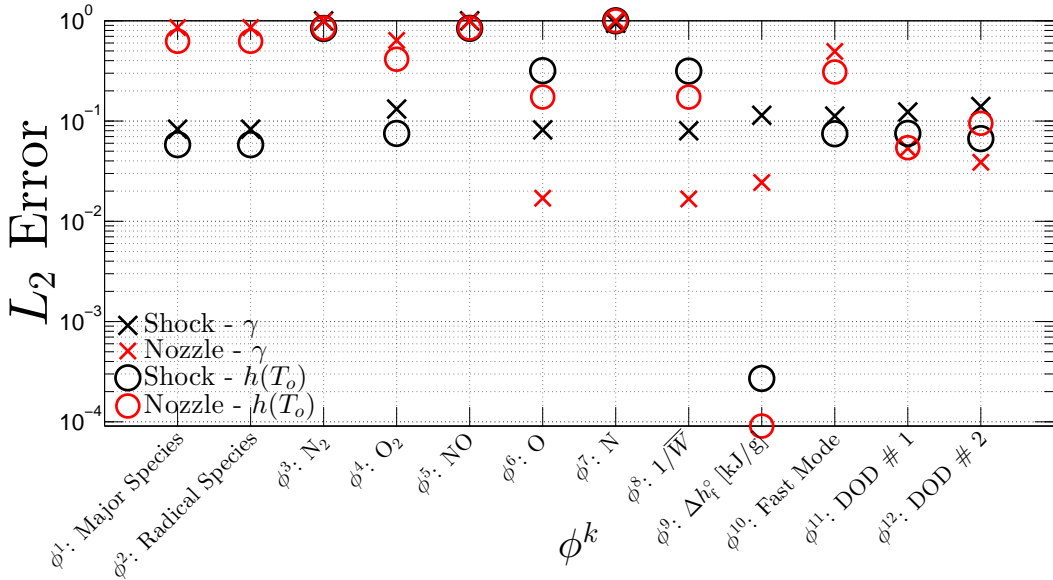


Figure 3.27: L2 Error Plot Air for $h(T_o)$ and γ , calculated from Eq. 3.41. Each data set is normalized by the maximum error from the respective test case. Different constraints are shown on the x-axis (varying k), and their respective norms are plotted vertically.

Figures 3.27—3.29 compare the performance of the different constraints in a quantitative manner. Different constraints are shown on the x-axis (varying k), and their respective norms are plotted

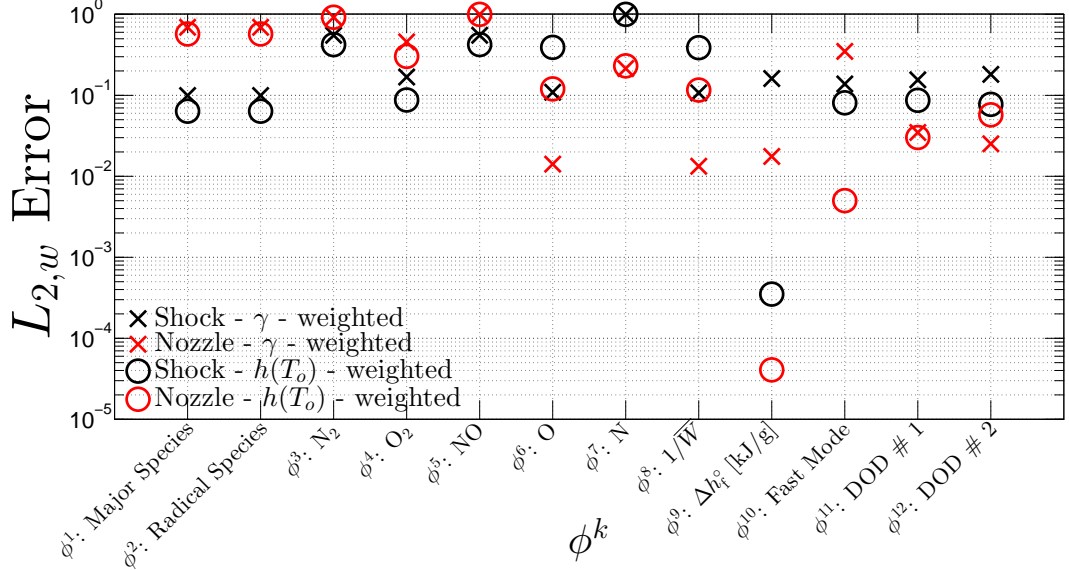


Figure 3.28: L2 Error Plot Air for $h(T_o)$ and γ , calculated from Eq. 3.42. Each data set is normalized by the maximum error from the respective test case. Different constraints are shown on the x-axis (varying k), and their respective norms are plotted vertically.

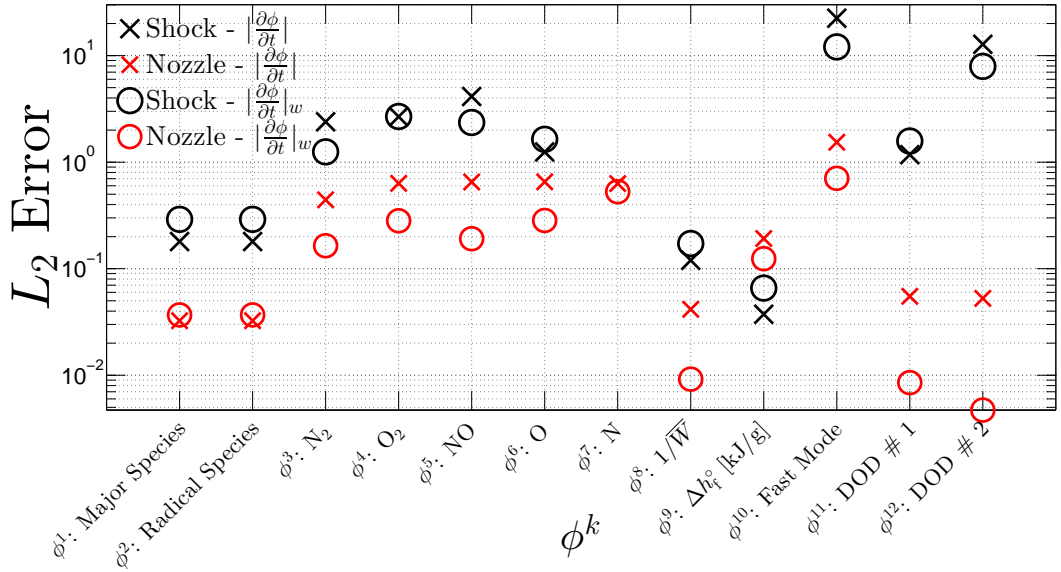


Figure 3.29: L2 Error Plot Air for the source term. $|\partial\phi/\partial t|$ values are calculated from Eq. 3.41, and $|\partial\phi/\partial t|_w$ values are calculated from Eq. 3.42. Calculated errors are individually normalized by $\max(|\partial\phi/\partial t|_{Cantera})$ in each trial, respectively. Different constraints are shown on the x-axis (varying k), and their respective norms are plotted vertically.

vertically. Each vertical column portrays how an individual constraint performs. Symbols closer to the x-axis indicate a smaller norm magnitude, and therefore a smaller error between the CEQ results and the detailed chemistry results. In general, from Fig. 3.27 and Fig. 3.28 it can be seen that

constraining the enthalpy of formation outperforms the other constraints when the errors on γ and $h(T_o)$ are compared. While constraining on the enthalpy of formation is expected to perform well for reproducing the mixture enthalpy, its performance as it pertains to γ is similar (if not better) to any other constraint. In addition, as the enthalpy of formation is a global property of a mixture, this constraint is consistent between the two test cases (shock and nozzle), and no *a priori* knowledge of the underlying chemical model is necessary. It is a constant constraint that can be used both when dissociation or recombination reactions are dominant. In the air system considered, it corresponds to a weighted sum of the radical species present. This constraint performs well because the radical species are associated with fast timescales, which is the fundamental idea of RCCE, and weighting the radicals based on their enthalpy of formations assures that the relevant bulk properties of the mixture is as accurate as possible. This constraint has not received any attention in the literature for previously performed calculations involving RCCE. More variance is seen in the results obtained with the different constraints in Fig. 3.29, when errors on $|\partial\phi/\partial t|$ are compared. Still, the enthalpy of formation constraint performs reasonably well and with similar accuracy for both nozzle and shock cases.

It is apparent that the subjectivity introduced by free parameters in the degree of disequilibrium analysis can lead to varying accuracies of the results. Figure 3.29 also shows that the *DOD* constraints perform much better for the nozzle test case than for the shock test case. This supports the results described in [64], but shows potential issues about applying these constraints to different systems.

To take these results one step further, the evolution of ϕ can be reconstructed, by integrating the $\frac{\partial\phi}{\partial t}$ values calculated in the previous section. This reconstructed value of the constraint will be referred to as ϕ^{RCCEQ} , and will only be calculated for ϕ^9 , the constraint based on the enthalpy of formation. By calculating ϕ^{RCCEQ} in this manner, no feedback from T or P is considered.

From the detailed chemistry calculations performed, the velocity as a function of location (in the shock-fixed frame) is known, as well as the value of the constraint as a function of location. These functions, $U(x)$, and $\phi(x)$ can be used to calculate $\phi(t)$. Knowing $\frac{dx}{dt} = U(x)$, which can be re-arranged to $\int_{t_o}^t dt' = \int_{x_o}^x \frac{dx'}{U(x')}$, numerical integration can be used to solve for $t(x)$. It is convenient to set $t_o = 0$ and $x_o = 0$. Similarly, knowing $\frac{\partial\phi}{\partial t}^{CEQ} = f(\phi)$, where $f(\phi)$ is the function previously plotted, this can be re-arranged to show $\int_{t_o}^t dt' = \int_{\phi_o}^\phi \frac{\partial\phi'^{CEQ}}{f(\phi')}$, and can be integrated numerically to solve for $\phi^{RCCEQ}(t)$. Once again $t_o = 0$ and $\phi_o = \phi(t_o)$. The results of this reconstruction are shown in Fig. 3.30, where ϕ and ϕ^{RCCEQ} are plotted.

As shown in Fig. 3.29, the relative error on $|\partial\phi/\partial t|$ is approximately 0.2 for the nozzle case, and approximately 0.01 for the shock case. For the nozzle case, this corresponds to an average difference of 20% between the source term calculated with CEQ, and with the exact value calculated with Cantera. While the two reconstructions reach the same final value of ϕ , there is approximately a 50% difference around $t \approx 30 \mu\text{s}$ in the nozzle case (Fig. 3.30b). The error is much smaller in the shock case, and the reconstruction is much more accurate, as shown in Fig. 3.30a. This error in the nozzle case could imply that a different state is reached in intermediate locations in the nozzle, which could correspond to discrepancies downstream in the nozzle when nozzle freezing is expected to occur. A fully integrated simulation needs to be run in order to fully evaluate the errors induced in this case.

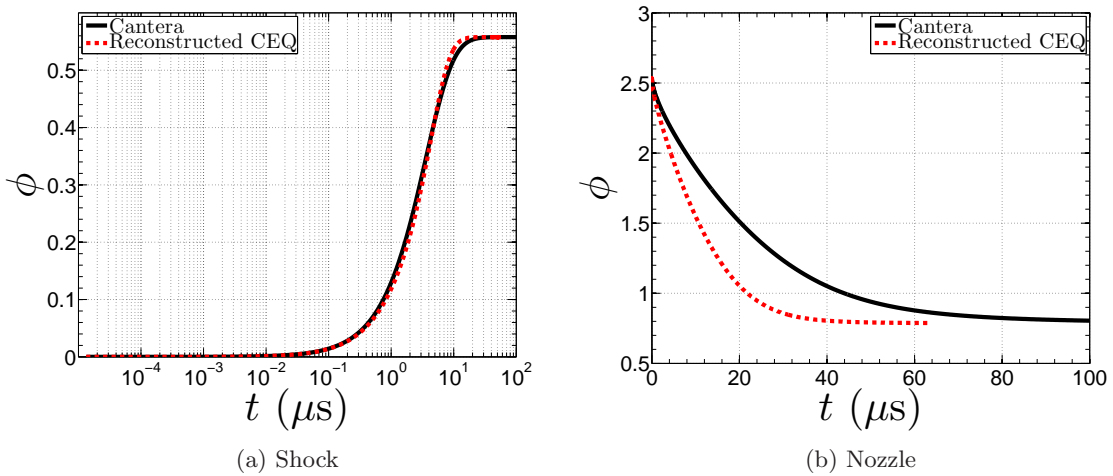


Figure 3.30: Comparison between ϕ^{RCEQ} and ϕ calculated from detailed chemistry simulations, plotted as a function of time for both the nozzle and shock cases. The calculations are performed for ϕ^9 , a constraint based on the enthalpy of formation.

3.9 Integrated RCCE Simulation

In order to confirm that the results shown in Sec. 3.8.6 remain consistent when the full RCCE method is used, an integrated simulation is performed for the shock and nozzle test cases using a single constraint on the enthalpy of formation. Now, feedback from T and P are included in the simulation. To couple the RCCE method with a CFD solver in an efficient manner, a tabulated approach can be used. This is a method that is widely used in computational chemistry (for example, see [130, 139]). Prior to running an integrated CFD simulation, tables can be created that tabulate mass fractions (\mathbf{Y}^{CEQ}) as a function of T , P , and ϕ^9 . The following sections outline how the integrated simulations are performed, and shows the results of these simulations.

3.9.1 Methodology for RCCE Simulations

Knowing that a tabulation method based on temperature and pressure will be used, the 1D reacting Euler equations (Eqs 3.5—3.8) must be re-written in a manner consistent with this choice, and the species equations must be replaced with an equation for ϕ^9 . The superscript 9 will no longer be used with ϕ , as this section only considers ϕ^9 , the constraint based on the enthalpy of formation.

First, Eq. 3.8 is modified such that instead of ns species evolution equations being solved, constraint evolution equation(s) should be solved. With one constraint, an expression for $\frac{d\phi}{dx}$ is required. Properties calculated from the fully integrated RCCE simulation will now take the superscript R . We start with

$$\frac{\partial \phi^R}{\partial t} = \sum_{i=1}^{ns} C_i \frac{\partial Y_i^R}{\partial t} = \sum_{i=1}^{ns} C_i \Omega_i(T^R, P^R, \mathbf{Y}^R) = \frac{\partial \phi^R}{\partial t}(T^R, P^R, \phi^R) = \dot{\phi}^R. \quad (3.43)$$

This simplifies to

$$\frac{d\phi^R}{dx} = \frac{\dot{\phi}^R}{w}, \quad (3.44)$$

which replaces Eq. 3.8. The calculation of Y_i^R will be discussed in Sec. 3.9.2, and is based on a tabulated approach.

In order to keep the system of equations consistent with the tabulation method (as a function of T , P , ϕ) to be used, Eq. 3.5 must be substituted for an evolution equation for temperature. Following the derivations performed in [69], the logarithmic derivative of the ideal gas equation, $P = \rho RT$, can be taken, yielding

$$\frac{dP}{P} = \frac{d\rho}{\rho} + \frac{dR}{R} + \frac{dT}{T}. \quad (3.45)$$

This yields a relationship for the temperature derivative in terms of previously determined quantities except for $\frac{dR}{R}$. It can be shown that

$$\frac{dR}{R} = \sum_{i=1}^{ns} \frac{\bar{W}}{W_i} dY_i. \quad (3.46)$$

Combining Eq. 3.5, Eqs. 3.7—3.10, Eq. 3.45, and Eq. 3.46, yields an equation for the spatial evolution of temperature in the shock fixed frame,

$$\frac{dT}{dx} = \frac{T}{w} \left[(1 - \gamma M^2) \frac{\dot{\sigma}}{\eta} - \sum_{i=1}^{ns} \frac{\bar{W}}{W_i} \dot{\Omega}_i \right]. \quad (3.47)$$

This can be generalized to include an area change if desired, as shown by Kao and Shepherd [69].

All of the equations needed for the RCCE simulation can now be written as:

$$\frac{dw^R}{dx} = \frac{\dot{\sigma}^R}{\eta^R} \quad (3.48)$$

$$\frac{dP^R}{dx} = -\rho^R w^R \frac{\dot{\sigma}^R}{\eta^R} \quad (3.49)$$

$$\frac{dT^R}{dx} = \frac{T^R}{w^R} \left[(1 - \gamma^R (M^R)^2) \frac{\dot{\sigma}^R}{\eta^R} - \sum_{i=1}^{ns} \frac{\bar{W}^R}{W_i} \dot{\Omega}_i^R \right] \quad (3.50)$$

$$\frac{d\phi^R}{dx} = \frac{\dot{\phi}^R}{w}. \quad (3.51)$$

In order to solve Eqs. 3.48—3.51, a method to determine $\mathbf{Y}^R(T^R, P^R, \phi^R)$ is required, as $\dot{\sigma}^R$, η^R , ρ^R , γ^R , \bar{W}^R , $\dot{\Omega}_i^R$, and $\dot{\phi}^R$ are all functions of \mathbf{Y}^R . This is discussed in the next section.

3.9.2 Tabulated Approach

It is possible to calculate $\mathbf{Y}^R(T^R, P^R, \phi^R)$ from constrained thermodynamic equilibrium calculations, assuming that T^R , P^R , and ϕ^R are known (see Sec. 3.4). Instead of having to perform a Gibbs function minimization calculation at every point in the flow, values for $\mathbf{Y}^R(T^R, P^R, \phi^R)$ are tabulated prior to running a simulation. A 3-dimensional table is created, which includes 100 different values for P , T , and ϕ , respectively. The table contains 10^6 points in total. In each respective dimension, the points are linearly spaced between the minimum and maximum values. In order to be able to use the same table for both the shock and nozzle test cases, a relatively large range of temperature, pressure, and ϕ is required. The minimum and maximum values chosen are 39 kPa and 17.5 MPa, 2000 K and 5800 K, and 0 kJ/g and 2.6 kJ/g, for pressure, temperature, and ϕ , respectively. This covers the minimum temperature, pressure, and ϕ range necessary for both the

shock and nozzle test cases. When solving Eqs. 3.48–3.51, after each iteration, $\mathbf{Y}^R(T^R, P^R, \phi^R)$ is taken from the table, using a simple tri-linear interpolation method to interpolate values inside of the table. Appendix B shows that the results for the test cases were fairly insensitive to the table resolution, and all results presented in the next section use the table with 10^6 points.

3.9.3 Integrated Simulation Results - Shock

Results are shown for the mass fraction evolution and the value of the constraint for the shock test case in Fig. 3.31 and Fig. 3.32, respectively. The evolution of ϕ (Fig. 3.32), which includes feedback from T and P , is very similar to the earlier results shown in Fig. 3.30a, where no T and P feedback was considered. This is to be expected, as the variation in temperature and pressure behind the shock is relatively small. Figure 3.31 shows that initially some errors are made on the radical species (over prediction of NO, and an under prediction of O and N), but both the RCCE solution and the detailed chemistry solution tend to an extremely similar equilibrium value. Only minor variations are observed between the detailed chemistry results and the RCCE results; a difference of ~ 100 Pa, ~ 3 K, and ~ 0.002 kJ/g, is observed at $x = 1$ m, for pressure, temperature, and ϕ , respectively. The maximum error in mass fractions at $x = 1$ m is made on Y_{O_2} , and is ~ 0.002 . Only very small errors are expected, as the RCCE method is based heavily on thermodynamics, and should be accurate for flows reaching thermodynamic equilibrium. The final discrepancies are most likely caused by errors induced through tabulation, and from deviations of the RCCE solution and the detailed chemistry solution behind the shock.

The accuracy of this method for the shocked flow is limited by the difficulty in using a constrained thermodynamic equilibrium calculation to reconstruct a mixture that is far from thermodynamic equilibrium. This was illustrated previously in Fig. 3.20. From the original investigation of how the enthalpy of formation constraint performs for a shock flow, it was seen that errors were made on individual species when using constrained equilibrium calculations, but the source term was predicted fairly accurately. These are the same effects that are seen in the full RCCE simulation; the evolution of ϕ is accurate, but errors are made on individual mass fractions. Therefore, it might be possible to increase the accuracy of this method for the shock flow by using more than one constraint for the constrained thermodynamic equilibrium calculations, though this would also increase the number of equations that would need to be solved in the RCCE simulation, and it would also increase the complexity of the tabulation process.

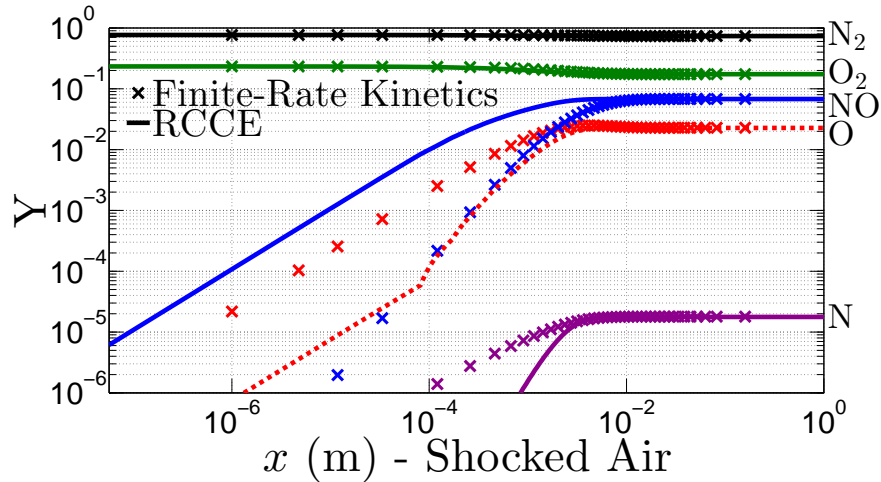


Figure 3.31: Results for a fully integrated simulation using the RCCE method for the shock test case, constraining on enthalpy of formation.

3.9.4 Integrated Simulation Results - Nozzle

Results are shown for the mass fraction evolution and the value of the constraint for the nozzle test case in Fig. 3.33, and Fig. 3.34, respectively. As expected, due to the over-estimation of the source term seen in Fig. 3.30a, the RCCE simulation reaches a slightly different final composition before freezing occurs in the nozzle. Overall, there is good agreement between the two simulations, and the results compare well to the expected results based on the prior reconstruction method performed. At $x/d = 15$, errors of ~ 150 K, ~ 720 Pa, and ~ 0.2 kJ/g are made on temperature, pressure, and ϕ , respectively, between the two simulations. The largest discrepancy in mass fractions at $x/d = 15$ is found to occur on Y_{O_2} , with a value of ~ 0.02 .

When comparing Fig. 3.34 to Fig. 3.30b, it is interesting to see that the fully integrated RCCE simulation actually compares better to the original simulation performed with finite-rate kinetics, than the reconstructed solution calculated in Sec. 3.8.6. It is postulated that this “self-healing” solution can be explained by considering the basic physics involved with reacting nozzle flow. As the flow travels downstream in the nozzle from the throat to the nozzle exit, the pressure and temperature of the flow decreases, while the Mach number increases. As temperature and pressure decrease, the formation of major species (fewer radical species) is favored from a thermodynamic point of view. These recombination reactions are exothermic, and add heat to the flow. Therefore, at the end of the nozzle, a gas mixture assumed to be constantly in local thermodynamic equilibrium will be at a higher temperature than a gas mixture with the same original composition, but is assumed to be in a frozen state throughout the nozzle nozzle. Equilibrium and frozen flow act as limiting cases, and

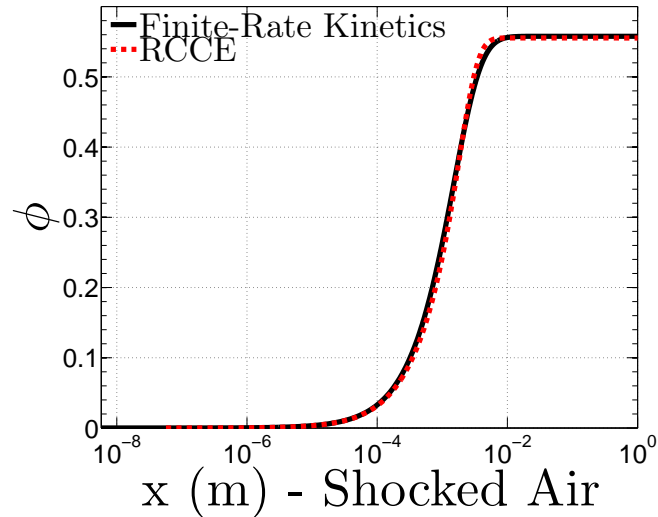


Figure 3.32: Evolution of the constraint variable for a fully integrated simulation using the RCCE method for the shock test case, constraining on enthalpy of formation.

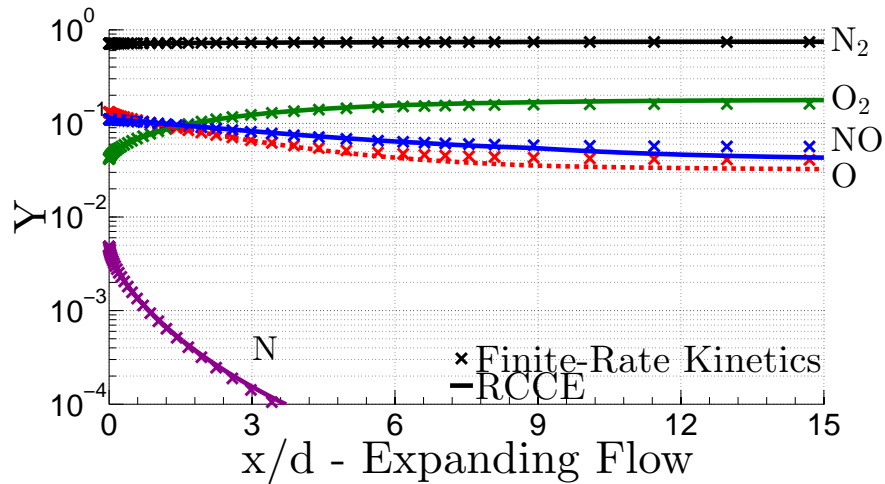


Figure 3.33: Results for a fully integrated simulation using the RCCE method for the nozzle test case, constraining on enthalpy of formation.

reacting flows with finite-rate kinetics lie somewhere in between these two extremes.

In Fig. 3.30b, ϕ^{RCCEQ} is predicted to decrease too quickly as the flow travels through nozzle when compared to the detailed chemistry solution. For the enthalpy of formation constraint used, ϕ^{RCCEQ} is equal to a weighted sum of the mass fractions of the radical species present. Therefore, if ϕ^{RCCEQ} is predicted to decrease too quickly, this corresponds to an over prediction of recombination reactions for the RCCE simulation, when compared to the detailed chemistry results. However, as the recombination reactions are exothermic, an over-prediction in recombination reactions corresponds to an over prediction in the amount of heat added to the flow, and therefore the temperature of

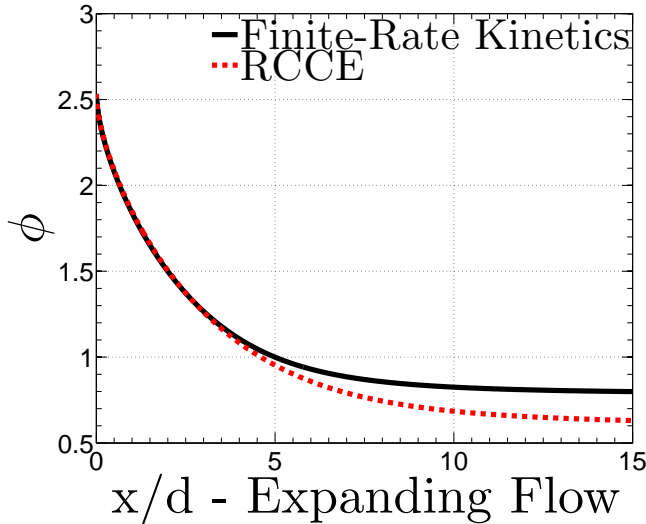


Figure 3.34: Evolution of the constraint variable for a fully integrated simulation using the RCCE method for the nozzle test case, constraining on enthalpy of formation.

the gas mixture is also over-predicted. At this point, the results from the fully integrated RCCE simulation diverge from the reconstructed results, as the RCCE simulation incorporates feedback from temperature and pressure.

For the reconstructed test case, $\mathbf{Y}^{\text{RCEQ}} = \mathbf{Y}^{\text{RCEQ}}(T, P, \phi^{\text{RCEQ}})$, where T and P are the results from the detailed chemistry simulation. For the fully integrated RCCE simulation, even if it is assumed that $\phi^R = \phi^{\text{RCEQ}}$, then $T^R \neq T$, $P^R \neq P$. The most important difference is that $T^R > T$ (as the temperature has the largest effect on the species composition calculated from a constrained thermodynamic equilibrium). This implies that $\mathbf{Y}^{\mathbf{R}}(T^R, P^R, \phi^{\text{RCEQ}})$ will have a higher radical composition than $\mathbf{Y}^{\text{RCEQ}}(T, P, \phi^{\text{RCEQ}})$, as a higher temperature favors the formation of radical species from thermodynamic considerations. This feedback slows down the production of major species, and drives the RCCE solution back towards the detailed chemistry solution.

3.9.5 Integrated Simulation Results - Discussion

In order to evaluate whether or not this method is desirable for a more detailed simulation (potentially 2D or 3D), some consideration should be given to the desired application of the RCCE method. In situations where it is not a priority to perfectly resolve a mixture composition, the RCCE method is advantageous. For the shock case, the RCCE method captures some of the non-equilibrium effects of the flow occurring, tends towards the correct final equilibrium state, and only adds a minimal amount of additional complexity when compared to a non-reacting flow simulation. On the other

hand, for applications where the composition of the flow must be known immediately downstream of a shock (perhaps if there is an extremely small stand-off distance of a bow shock in front of a body), then the errors observed in Fig. 3.31 may become significant. In the nozzle case, Fig. 3.33 shows that the RCCE method was more accurate closer to the nozzle throat, where the flow was closer to being in a state of local equilibrium, and larger errors were observed farther downstream, when the flow moved farther from a local thermodynamic equilibrium state.

It might be possible to increase the accuracy of this method by reducing interpolation errors associated with a tabulated approach through the use of more refined tables, or a higher-order interpolation method. This is especially the case because the mass fractions span several orders of magnitude for individual species, so small errors due to the interpolation method may have a large effect on the final results. Other works have tried to improve on this by tabulating and interpolating the logarithmic values of certain quantities [35], and this could be tested in the future for this method as well. However, no significant difference in the results were noticed for the air test cases if the table resolution was decreased by a factor of two in each dimension, to 50 by 50 by 50, as shown in Appendix B.

With the minor errors observed for the integrated RCCE simulations for both the nozzle and shock cases, these results suggest that one constraint can be used for simulations where both shocks and expansion occur (2D/3D flows). Once again, this relies on the assumption that small errors on individual species concentrations can be tolerated. Care should be taken when constructing a table for a complicated simulation, as the expected pressure, temperature, and ϕ range needs to be considered before creating the table and running the simulation. In addition, if a more accurate description of the mixture composition is needed at all points in the flow, the effect of using more constraints to increase the accuracy of the RCCE method should be investigated.

3.10 Extension to the Martian Atmosphere

In order to evaluate whether or not these constraints can be extended to different systems, a gas mixture characteristic of the Martian atmosphere is tested using the same test problems previously described. A 9 species gas model is used, containing Ar, C, CO, CO₂, N, N₂, NO, O, and O₂. The previous five reactions used for the air system (Eqs. 3.23—3.27) are still used, and in addition, the

following reactions are included:



These additional reactions and reaction rates are taken from GRI-Mech 3.0 [157]. An initial mixture composition of 96.00% CO₂, 1.93% Ar, 1.89% N₂, 0.14% O₂ and 0.04% CO (by volume) is used [93].

A similar analysis is performed as described in the previous sections for the air system, but only constraints consistent between the shock and nozzle conditions are compared for this new investigation. Figures 3.35 and 3.36 show the evolution of mass fractions through the shock test case and the nozzle test case, respectively. The same initial conditions are used in the shock gas as the previous air calculations (20 kPa and 297 K), but the post-shock conditions are now different based on the properties of the new gas mixture.

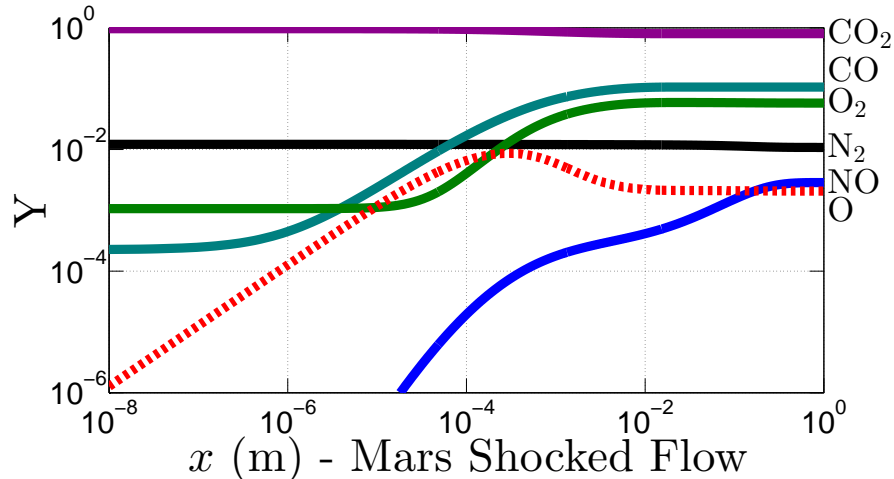


Figure 3.35: Evolution of mass fractions for a gas mixture characteristic of the Martian atmosphere at 20 kPa and 297 K processed by a 3 km/s ($M = 11.1$) normal shock.

Figures 3.37 and 3.38 show comparisons between the constrained equilibrium calculations and finite-rate kinetics simulations using the enthalpy of formation as a constraint. In this case, the enthalpy of formation constraint is no longer a weighted sum of just the radical mass fractions, as non-radical species may have non-zero enthalpies of formation (for example, CO). Similar results

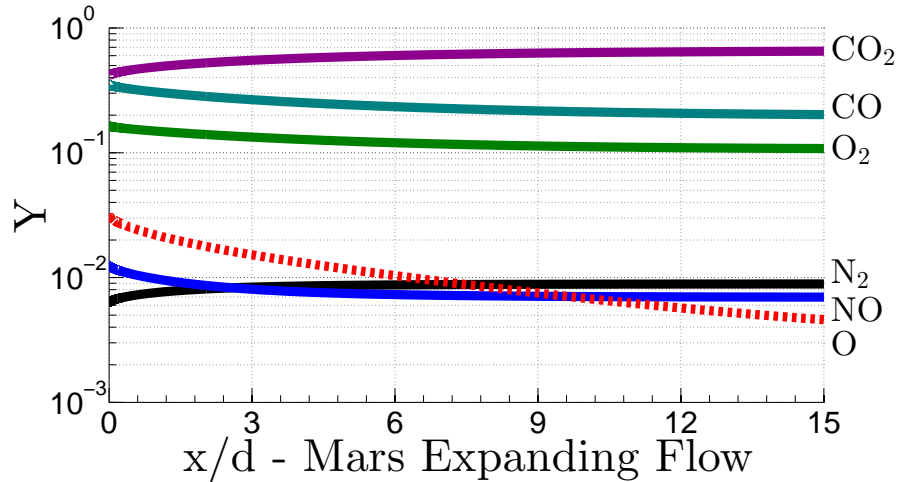


Figure 3.36: Evolution of mass fractions for gas mixture characteristic of the Martian Atmosphere in thermodynamic equilibrium at 4467 K and 45.2 MPa undergoing a steady expansion.

are observed for the Martian atmosphere that were observed for air previously. In the shock case, even though errors are made on the mass fractions of minor species, γ and $|\frac{\partial \phi}{\partial t}|$ are accurately reconstructed. In the expansion case, even though the mass fractions of individual species are well-represented, significant errors are made reconstructing the source term. Once again, the source term is extremely sensitive to small fluctuations in mass fractions, which can be attributed to reactions shown in Eq. 3.26, Eq. 3.52, and Eq. 3.53. These reactions have large forwards and backwards reactions rates which are similar in magnitude, and result in net production/destruction rates that are highly sensitive to small changes in species mass fractions. This is a similar phenomenon to that which was previously described for the air system.

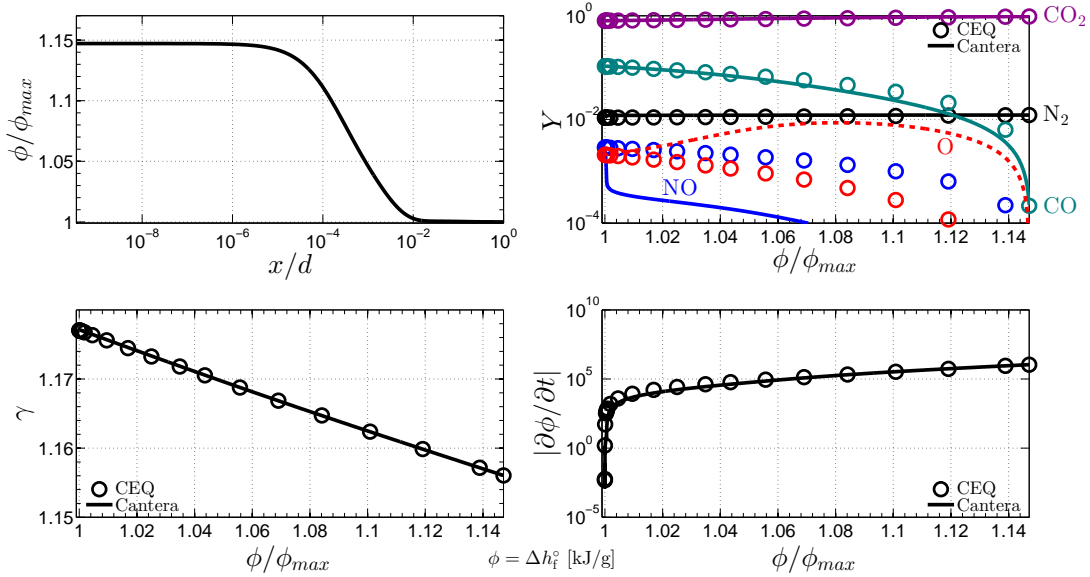


Figure 3.37: Finite rate chemistry and constrained equilibrium calculations for a shocked Martian atmosphere flow. Constrained equilibrium calculations are performed by holding the enthalpy of formation (by mass) of the mixture constant. The fact that ϕ/ϕ_{max} is greater than 1 indicates that the constraint has a negative value.

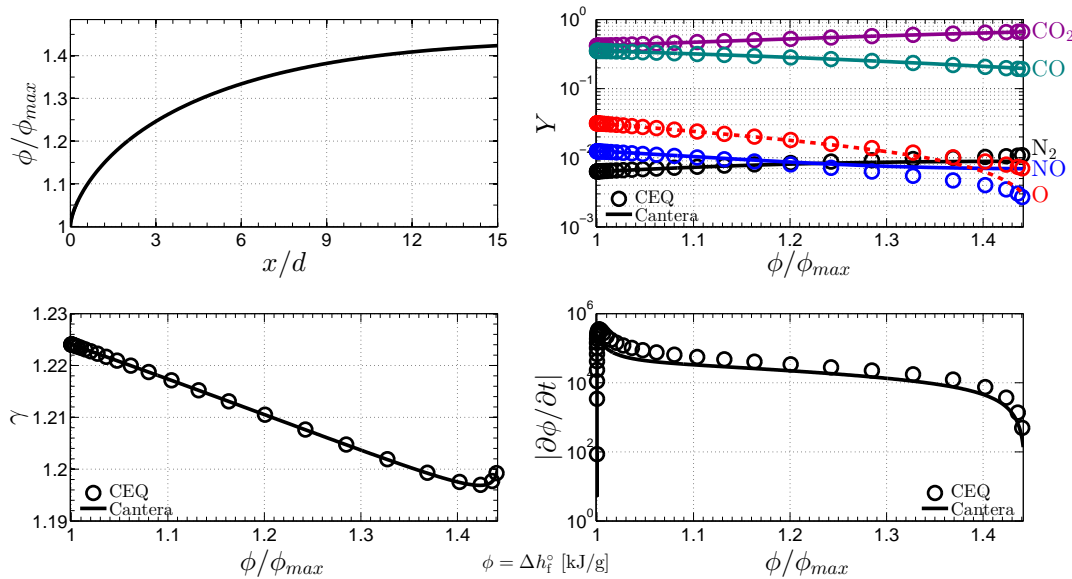


Figure 3.38: Finite rate chemistry and constrained equilibrium calculations for an expanding Martian atmosphere flow. Constrained equilibrium calculations are performed by holding the enthalpy of formation (by mass) of the mixture constant. The fact that ϕ/ϕ_{max} is greater than 1 indicates that the constraint has a negative value.

Quantitative error calculations for the selected set of constraints, $k = 1, 2, 8, 9, 13$, are shown in Fig. 3.39. The values for the C_i^k coefficients are altered from Table 3.3 to remain consistent with the new CO₂ mixture. $k = 13$ is chosen to represent a species constraint on CO₂, where $C_{i=\text{CO}_2}^{13} = 1$, and $C_{i \neq \text{CO}_2}^{13} = 0$. All of the C_i^k coefficients used in this section are consistent between the shock and nozzle cases, for a given k . It is not surprising to note that CO₂ performs well as an individual species constraint, due to the large concentration of CO₂ present in the flow. The enthalpy of formation constraint performs the best overall once again, except when looking at the error on $|\frac{\partial\phi}{\partial t}|$ for the nozzle case.

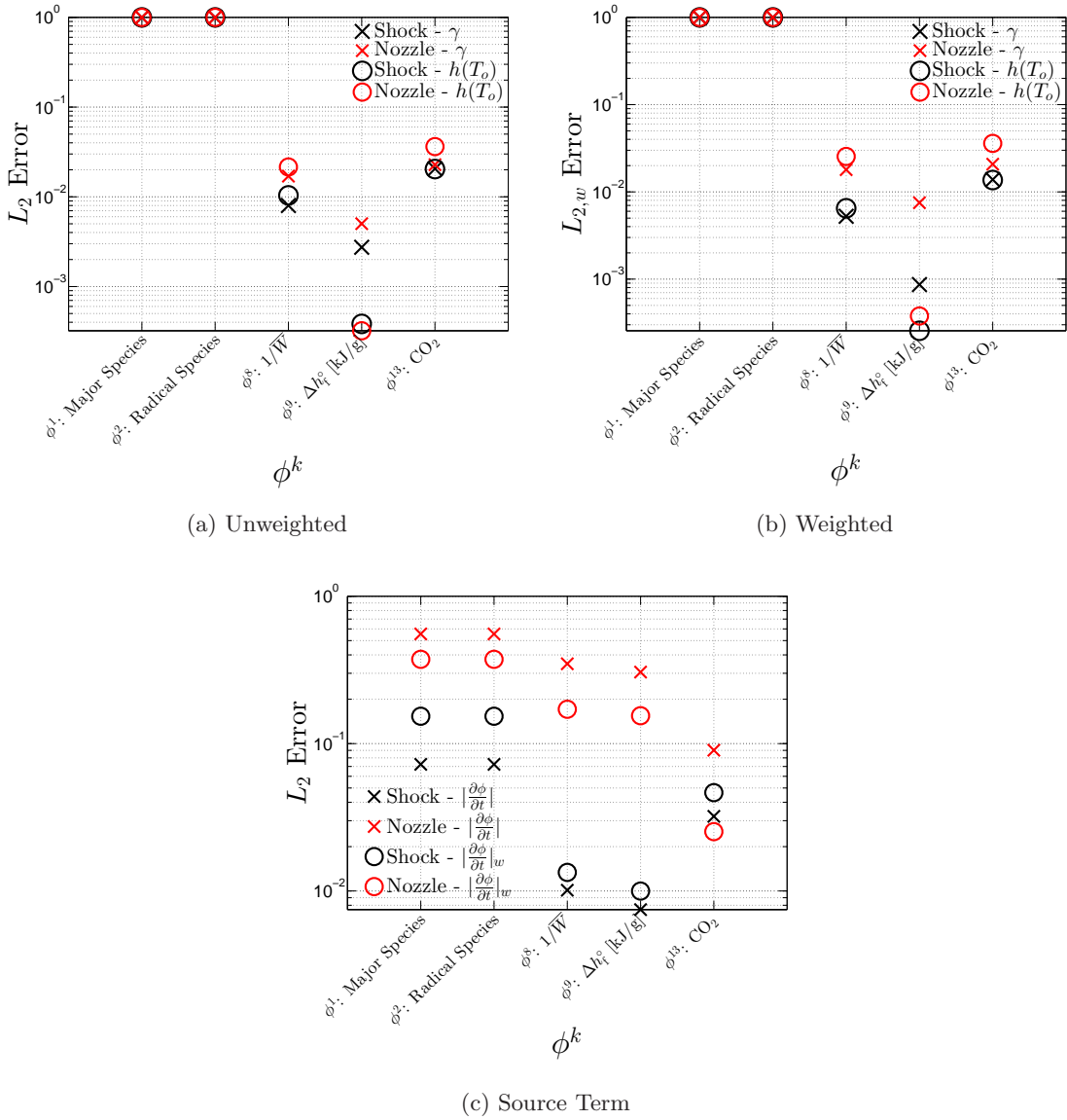


Figure 3.39: L2 Norm comparisons for different properties with a Martian gas mixture.

Using the method outlined in Sec. 3.8.6, ϕ^{RCEQ} is again reconstructed from the calculated

CEQ data, and compared to the data from detailed chemistry simulations. Larger errors are again observed in the nozzle case than the shock case, but the errors are smaller in the Martian mixture than they were in the air investigation. For the air system, the relative error on $\frac{\partial \phi}{\partial t}$ was $\approx 20\%$; while it is only $\approx 5\%$ for the Martian atmosphere.

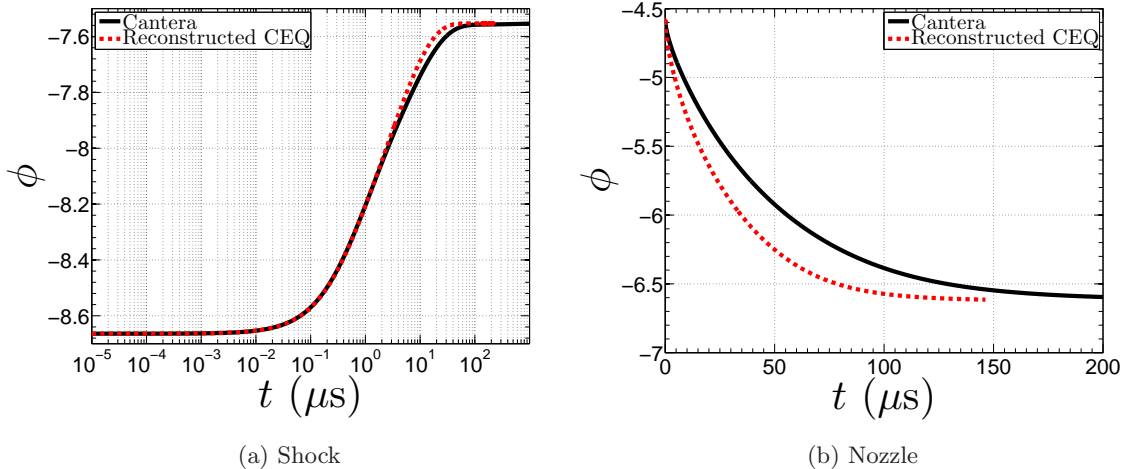


Figure 3.40: Reconstructing the evolution of ϕ as a function of time for both the nozzle and shock cases, assuming a gas mixture characteristic of the Martian atmosphere, constraining the enthalpy of formation.

Finally, a fully integrated RCCE simulation is run for the shock and nozzle test cases using the method outlined in Sec. 3.9. A table is constructed for this simulation with 100 points for pressure, temperature, and ϕ , respectively. The minimum and maximum values chosen are 100 kPa and 45.3 MPa, 2600 K and 4800 K, and -8.7 kJ/g and -4.5 kJ/g, for pressure, temperature, and ϕ , respectively, in order to cover the range of values expected for the two test cases. A tri-linear interpolation method is used to interpolate values within the table again.

Figure 3.41 shows a comparison for the evolution of mass fractions, and Fig. 3.42 shows a comparison of the constraint evolution, for the shock test case. Similar to the air test case, some errors are made on the mass fractions directly behind the shock, and the solutions agree better farther downstream of the shock. A small difference in the final value of ϕ (0.03 kJ/g) is seen in Fig. 3.42. This difference is once again caused by minor deviations between the solutions behind the shock, and potentially by errors induced through interpolation. The differences in mass fractions between the final solution reached by the RCCE method and the detailed chemistry method are small, with the largest error in mass fraction observed between the two solutions being 0.004 for Y_{CO_2} at $x = 1$ m. Minor discrepancies are also seen in the final temperature and pressure states, with the error being ~ 10 K, and ~ 20 Pa, for temperature and pressure, respectively.

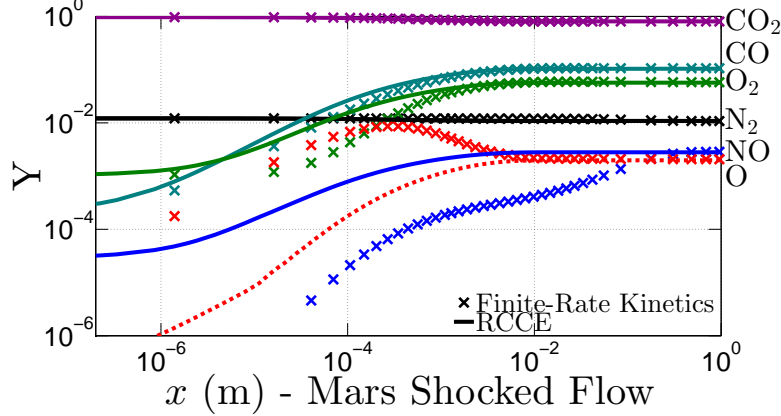


Figure 3.41: Results for a fully integrated simulation using the RCCE method for the shock test case with a composition characteristic of the Martian atmosphere, constraining on enthalpy of formation.

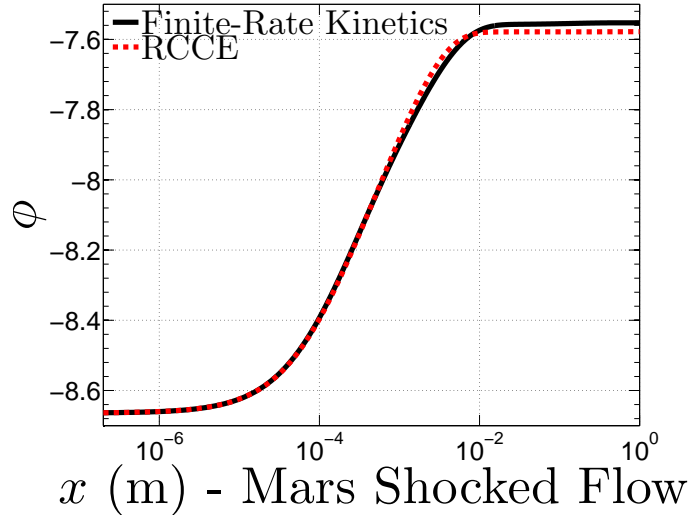


Figure 3.42: Evolution of the constraint variable for a fully integrated simulation using the RCCE method for the shock test case with a composition characteristic of the Martian atmosphere, constraining on enthalpy of formation.

Figure 3.43 shows a comparison for the evolution of mass fractions, and Fig. 3.44 shows a comparison of the constraint evolution for the nozzle test case. Mass fractions of CO_2 , CO , and O_2 are reproduced well, and minor errors are made on N_2 , NO , and O . Figure 3.44 actually shows that the constraint does better than originally predicted in Fig. 3.40b. This is another example of a “self-healing” solution previously described (see Sec. 3.9.4). For the two cases considered, the simple reconstructed ϕ profiles do a very good job at predicting the performance of the corresponding fully integrated RCCE simulations.

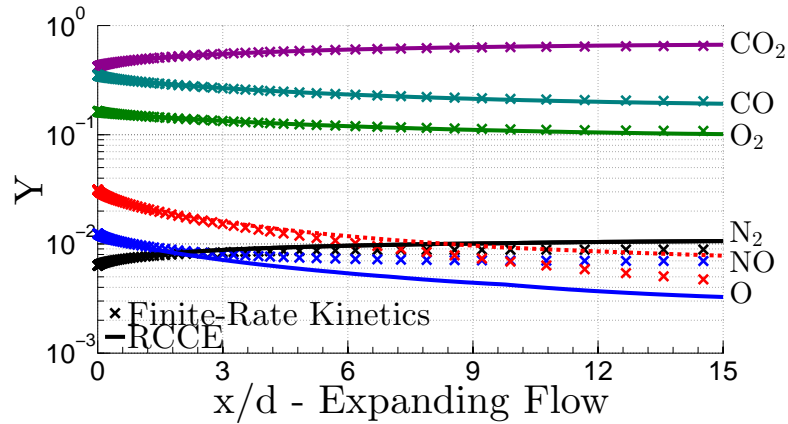


Figure 3.43: Results for a fully integrated simulation using the RCCE method for the nozzle test case with a composition characteristic of the Martian atmosphere, constraining on enthalpy of formation.

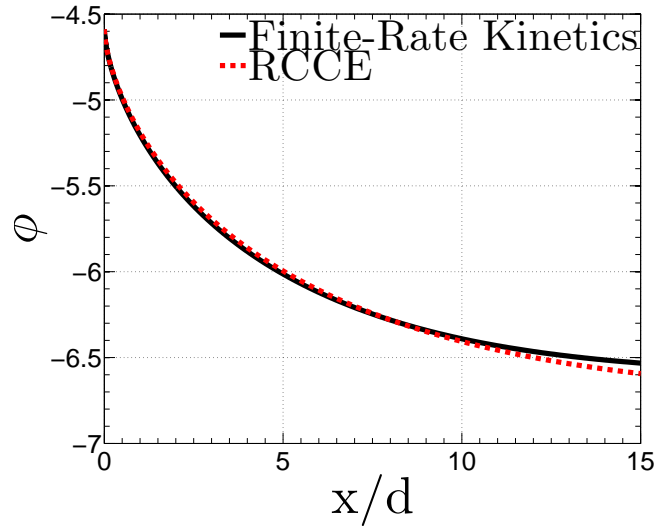


Figure 3.44: Evolution of the constraint variable for a fully integrated simulation using the RCCE method for the nozzle test case with a composition characteristic of the Martian atmosphere, constraining on enthalpy of formation.

3.11 Discussion

There are three main benefits from the RCCE method that will be discussed in this section: 1) the reduction in number of equations that need to be solved to model a reacting flow; 2) the reduction in stiffness of the system of equations that needs to be solved; and 3) the ability to tabulate chemical properties as a function of a constraint once, prior to running a simulation, along with the ability to use the same table for a wide range of simulations.

Both of the mixtures considered in this chapter involve fairly simple reaction mechanisms (5 species and 5 reactions for air, and 9 species and 10 reactions for Mars). Those reaction mechanisms had already been reduced; some chemical species were not included (such as NO₂, N₂O, NCO, CN), and only the major reactions were considered. Nevertheless, the ability to use one constraint has significantly reduced the computational complexity of the problem. With detailed, finite-rate chemistry, 5 species transport equations need to be solved in addition to the flow variables (T , P , w in 1D) for a total of 8 equations for air. For the Martian atmosphere, the total number of equations is 13. The number of equations solved is greatly reduced for the fully integrated RCCE simulations. These simulations need only solve 4 equations simultaneously, regardless of the mixture considered. The reduction in computational cost would be even greater for larger chemical models.

The second benefit from the RCCE method is that the stiffness of the system of equations for a fully integrated RCCE simulation has also been reduced. This is shown with a simple time scale estimation. The simulation shown in Fig. 3.33 is considered at a point of $x/d = 2$. This location is chosen such that recombination reactions are still occurring in the nozzle, and the flow has had a finite amount of time to expand and depart from the thermodynamic equilibrium solution. At $x/d = 2$, the characteristic times associated with chemical reactions are $t_1^* \approx 5 \cdot 10^{-9}$ s, $t_2^* \approx 5 \cdot 10^{-7}$ s, and $t_3^* \approx 1.3 \cdot 10^{-6}$ s (Fig. 3.4). At the same point, the time scale associated with the flow itself is $t_{flow}^* \approx 1.5 \cdot 10^{-5}$ s (Sec. 3.7.3). A time scale for the evolution of ϕ can be estimated from $t_\phi^* \approx \frac{\Delta\phi}{\partial\phi/\partial t}$, where $\Delta\phi$ is the change in ϕ throughout the entire nozzle. At $x/d = 2$, $t_\phi^* \approx 5.4 \cdot 10^{-5}$ s. The time scale associated with the rate of change of ϕ is now on the same order of the relevant fluid mechanical time scales. Due to the fact that $\frac{\partial\phi}{\partial t} = \sum_{i=1}^{ns} C_i \Omega_i$ includes a summation, the slowest timescales associated with the chemical reactions govern the stiffness of the evolution equation for ϕ . By reducing the stiffness of the system of equations, they can be integrated in a more efficient manner, and the computational complexity of the problem is reduced.

Finally, implementing RCCE based on tabulation allows a table to be created *once* before running simulations. In fact, since the tabulation of the constraint is based solely on constrained thermody-

namic equilibrium calculations, the same table can be used for a variety of different problems. This was shown by using the same table for both the shock and nozzle test cases for air, and similarly for the Mars atmosphere test cases.

As was discussed previously, there are limitations associated with the RCCE method. Some errors are made predicting species concentrations for all of the cases considered. For the shock test cases, it was observed that errors seen in the RCCE simulations can largely be attributed to the difficulties in reconstructing the composition of a mixture far from thermodynamic equilibrium using a constrained thermodynamic equilibrium calculation. For the nozzle test cases, where the flows started in thermodynamic equilibrium, it was found that the accuracy of the RCCE method was limited by discrepancies in ϕ between the detailed chemistry results and the RCCE results. $\frac{\partial\phi}{\partial t}$ for the enthalpy of formation constraint was sensitive to small differences in mass fractions, and these errors led to different final properties being predicted for the gas downstream in the nozzle simulations.

If necessary, one way to reduce these errors is to use more than one constraint to describe a system. This increases the computational complexity of the problem, but as more constraints are used, the solution from the RCCE method will tend towards the solution from detailed chemistry simulations. In addition, a simple tabulation method was implemented in this work, with a basic tri-linear interpolation algorithm to interpolate within the tables used. No attempts were made to locally refine the tables created, or to use higher-order interpolation methods. For example, Tang and Pope [163] implemented a method named “*in situ* adaptive tabulation-rate-controlled constrained equilibrium (ISAT-RCCE)”. Tabulation was performed *in situ* during the combustion calculations, and the method was found to be computationally efficient for simulating non-premixed methane/air combustion in a statistically homogeneous turbulent reactor, using RCCE. Solution mapping using polynomial approximation (PRISM) [166] is another example of a method where only the accessed thermochemical state space is computed during the simulation, and stored in a table for use again later, similar to ISAT. These methods are most likely overly-complex for the simple gas models considered in this work, but for more complicated gas mixtures, these advanced tabulation methods could be beneficial. The sensitivity of the obtained results with respect to the tabulation and interpolation method is something that could be investigated in future work.

Chapter 4

Pyrolysis Gas Composition in PICA Heatshields¹

4.1 Motivation

Ablative heatshields, like the one recently used on the successful Mars Science Laboratory (MSL) mission, are designed to dissipate the high heat fluxes experienced during atmospheric entry through material degradation. The heatshield is designed to undergo a phase change such that the thermal energy is dissipated by the ablation of specific components in the heatshield. This translates into a heatshield that is designed to recess upon entry into an atmosphere at hypervelocity speeds. A variety of lightweight ceramic ablators (LCAs) were invented at the NASA Ames Research Center in the 1990s specifically designed for this purpose. These materials are made of a carbon fiber pre-form impregnated with a phenolic resin. Some examples of these materials designed for high speed atmospheric entry include phenolic impregnated carbon ablator (PICA, developed at AMES in the 1990s and first used as the material for the Stardust forebody heat shield, launched in 1999) [117, 167, 168], ASTERM (a PICA like material under development by Astrium through ESA, starting in the early 2000s) [141, 142], and PICA-X² (a PICA like material developed by SpaceX in conjunction with NASA). Sharpe and Wright [152] provide a review of materials used for applications in extreme environments from the 1960s until the present.

Being able to accurately characterize and model these materials in simulations is necessary to safely design a heatshield for a mission. Although this has been an active field of research since

¹The work in this chapter has been presented in large part in Rabinovitch, J., Marx, V. M., and Blanquart, G. Pyrolysis Gas Composition for a Phenolic-Impregnated Carbon Ablator Heatshield. In *Proceedings of the 11th AIAA/ASME Joint Thermophysics and Heat Transfer Conference*. AIAA, Atlanta, Georgia, 2014.

²SpaceX Manufactured Heat Shield Material Passes High Temperature Tests Simulating, <http://www.spacex.com/press/2012/12/19/spacex-manufactured-heat-shield-material-passes-high-temperature-tests-simulating>, accessed 02/03/2014.

the 1960s [28, 46, 72, 83, 98, 134, 133, 135, 138, 162], the state of the art modeling tools used for high-enthalpy aerothermodynamic predictions leave room for improvement. Prediction uncertainty is as high as 60% for laminar convective heating [20, 21, 59, 183]. This in turn necessitates the heatshield to be over-designed and more massive than needed, which takes away mass that could be used towards other mission components, such as additional science payloads.

The goal of this chapter is to perform a detailed investigation into the pyrolysis gases produced by a PICA heatshield. Improving our understanding of the pyrolysis gas composition and the evolution of the pyrolysis gases will aid in accurately modeling the performance of a PICA heatshield. The endothermic phase change from solid to gas is designed to dissipate the high heat loads; modeling this effect is critical. In the ablation community, there is currently a large disconnect between the physical properties of solid PICA, and the pyrolysis gases that are created when PICA starts to undergo a thermal decomposition. For example, there is little discussion in the published literature pertaining to the choice of elemental composition for the pyrolysis gas mixture in numerical simulations, and why the elemental composition of the pyrolysis gas mixture is assumed to be constant [26, 96, 106, 108, 117, 122]. In addition, a constant elemental composition has been used to describe gas mixtures at unrealistically high temperatures, as was shown in Fig. 1.4. This is in direct contrast to experimental data that shows that the elemental composition of the pyrolysis gas mixture varies with temperature [162, 169]. It should be noted that much of the numerical work performed by NASA (for example, see [21, 26, 94, 106, 107, 108]) for modeling the thermal response of PICA uses the fully implicit ablation and thermal response code (FIATv3) [105]. Material properties of high-performance ablators are subject to export-control restrictions, and therefore the ablation and thermal property model used in FIATv3 is only available in the appropriate NASA technical report, available to qualified U.S. persons.³ No information from NASA/TM-2009-215377 is used in this chapter. Unfortunately, because of these restrictions, it is unclear as to which physical phenomena are included in FIATv3, and why certain values are used (for example, the elemental composition of the pyrolysis gas mixture, and why it is assumed to be constant).

Only recently have the numerical capabilities been developed to incorporate a reacting, non-constant elemental pyrolysis gas mixture, with a full thermal response code [78]. To the author's best knowledge, the work performed by Lachaud and Mansour [78] is the only published study that accounts for non-constant elemental composition of the pyrolysis gas mixture, while also accounting for the complicated porous flow field internal to the heatshield. Despite these advances, a simplified

³Milos, F.S., and Chen, Y.-K., "Ablation and Thermal Property Model for Phenolic Impregnated Carbon Ablator (PICA)," NASA/TM-2009-215377, Jan. 2009.

chemistry model is used in [78] for the computation to be feasible. On the contrary, this chapter focuses on the thermodynamic and kinetic processes related to the pyrolysis gas mixture, and simplifying assumptions are made for the fluid mechanics relating to the flow of the pyrolysis gases. The focus is placed on better understanding the complicated chemical processes occurring in the reacting pyrolysis gas mixture.

This chapter links solid PICA to the pyrolysis gases that form at high temperatures by compiling published physical properties of PICA, and by explaining the fundamental processes that are involved with phenolic resin synthesis and the thermal decomposition of the resin. This provides a necessary link between the composition of the resin as a solid, the composition of the pyrolysis gases, and their evolution through the pyrolysis layer. When modeling the pyrolysis gas mixture computationally, certain species must be chosen to create a gas model. The inclusion or emission of species has a large effect on the pyrolysis gas composition, yet there is a lack of literature explaining why certain species are chosen, and why others are neglected in previous studies. The effects of choosing a specific gas species composition are quantitatively shown in this chapter, emphasizing the importance of choosing an accurate model for the pyrolysis gas mixture. Specifically, the need to include large aromatic species in the gas mixture is emphasized, and physical phenomena associated with aromatic species, such as solid carbon deposition, are investigated. The kinetic evolution of the pyrolysis gas mixture is also investigated, and the assumption of thermodynamic equilibrium *vs.* finite-rate kinetics is evaluated. This investigation into a reacting pyrolysis gas mixture allows a much needed consistent and detailed description, of many of the physical phenomena occurring in a PICA heatshield, and their implications, to be formulated. To begin, the following section outlines the many physical processes that occur during ablation.

4.2 Ablation Overview

The multi-component nature of ablation has been described previously in great detail, and many of the modeling issues and uncertainties that are associated with it have been reviewed in previous works [78, 105, 106, 108, 120, 121, 122, 182]. Figure 4.1 shows a schematic overview of the physical phenomena occurring for an ablating heatshield. While the scope of this work is limited to a detailed investigation of the pyrolysis gases formed through the thermal decomposition of a phenolic resin (the type of resin used in PICA heatshields), it is still necessary to be aware of all of the processes occurring during ablation. For example, certain species radiate more than others at high temperatures, influencing the heat transfer to the heatshield. As a result, even though making an

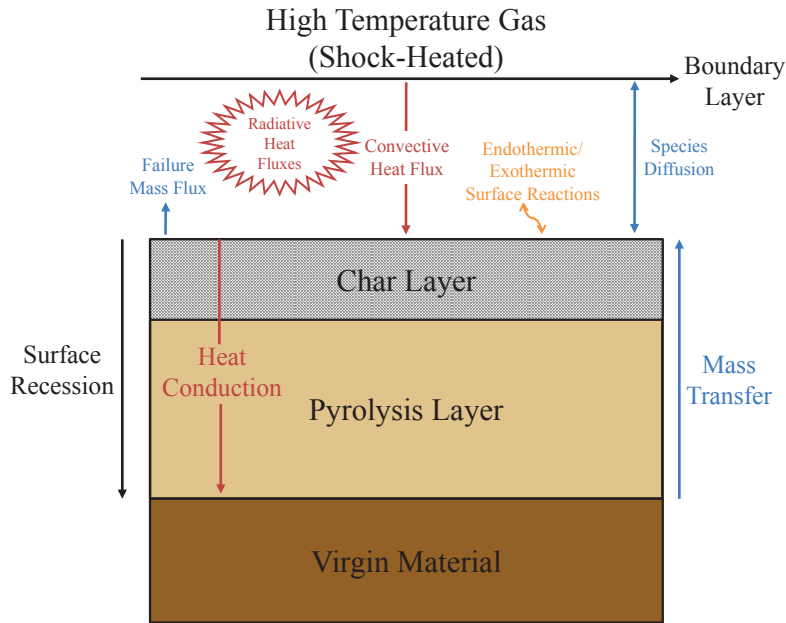


Figure 4.1: Schematic diagram (not to scale) outlining the many physical phenomena occurring for an ablative heatshield. Red arrows refer to heat fluxes, while blue arrows refer to mass fluxes. Surface reactions can involve both heat and mass fluxes, and are shown in orange.

error in the amount of strong radiators (C , CO , C_2 , C_3 , C_5 , C_2H , H , CN)⁴ may not affect the global properties of the gas mixture, the radiative heat flux would no longer be correct.

The virgin material of the heatshield consists of temperature resistant carbon fibers impregnated with a phenolic resin. The resin is composed primarily of carbon, hydrogen, and oxygen, and potentially small amounts of nitrogen and other contaminants (based on the resin type and manufacturing process). As the material is heated, the resin begins to decompose and vaporize. Many small gas bubbles are formed in the material, and once the bubbles become connected, porous flow ensues. The gases produced are referred to as pyrolysis gases, and are generated throughout the entire pyrolysis layer. As the temperature rises, the pressure in the heatshield continues to rise, and the pyrolysis gases flow into the boundary layer. Some of the thermal energy of the external flow is dissipated through this endothermic phase change. A “blowing” phenomenon at the heatshield surface also adds a cooling effect to the flow, as the boundary layer is at a higher temperature than the pyrolysis gases. Furthermore, the addition of the pyrolysis gases into the flow affects many properties of the flowfield, including radiative properties, heat conductivity, flow field dynamics, etc.

Another reason why phenolic resins have been found to be effective for these applications is due to the carbonaceous residue that results from the thermal decomposition of the resin. This solid

⁴Private communications with Professor Alexandre Martin, University of Kentucky.

residue is generally referred to as char. The solid char either adheres to the fibers inside of the heatshield (as shown in Fig. 4.1), or is advected away through the boundary layer. The char layer (Fig. 4.1) refers to the area where all pyrolysis reactions have come to completion, and the carbon fibers closest to the heat shield have been covered (to some degree) with solid char. This highly emissive char can help radiate heat outwards, thermally insulate the interior of the vehicle, and add to the structural stability of the heatshield itself [137]. Reinforcing the original carbon fibers with this char material can also aid in reducing the amount of spallation that occurs during atmospheric entry. It is possible for the fibers/char to ablate and enter the boundary layer in a gaseous form, and it is also possible for spallation to occur, which adds solid carbon to the boundary layer. The spallation effect is generally referred to as a failure flux, and is labeled in Fig. 4.1. A more detailed description of PICA itself will be presented in the next section.

4.3 PICA Composition

Phenolic impregnated carbon ablators, as previously described, are a composite material that consist of rigid, lightweight carbon fibers infused with a phenolic resin. A wide range of physical properties are reported for PICA, and it is the goal of this section to compile previously reported values, in order to understand the range of possible properties for this material. In addition, there is often a large disconnect between the physical properties of PICA, and the pyrolysis gases produced from PICA at high temperatures. Without a proper understanding of the composition of solid PICA, it is not possible to explain the composition of the pyrolysis gases which are produced when PICA starts to undergo a thermal decomposition.

Phenolic resins are not limited to the aerospace industry, and are used for a wide variety of applications: from coatings, to adhesives, to carbon-less copy paper. In the year 2000, worldwide consumption of phenolic resins exceeded $4 \cdot 10^6$ t [75]. Due to this demand, there is a large quantity of literature available concerning phenolic resins, and phenolic composite materials (like PICA), from a pure chemistry or industrial background. This work combines publicly available data from the aerospace community on PICA, as well as knowledge from the chemistry community on resin synthesis/decomposition and reacting mixtures. Combining knowledge from both of these fields allows a full picture of the thermal decomposition of PICA, and the subsequent generation and evolution of pyrolysis gases to be formed.

Shifting back to aerospace, Tran *et al.* [168] report densities for PICA ranging from 14 to 17 lbm/ft³ (224 kg/m³ - 272 kg/m³). If surface densification is performed on the material, then the

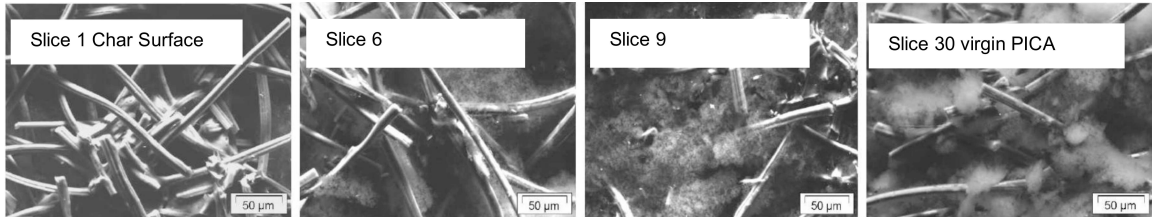


Figure 4.2: Micro-graphs taken at different depths for the Stardust PICA heatshield. Depth increases from left to right, where Slice 1 is close to the heatshield surface, Slice 6 is located ~ 5 mm below the surface, Slice 9 is located ~ 9 mm below the surface, and Slice 30 shows the virgin PICA material. Image reproduced from [159].

density can be increased to 18 - 23 lbm/ft³ (288 kg/m³ - 368 kg/m³). In comparison, Avcoat-5026, the material used for the ablative heat shields in the Apollo capsules, is a heavier material with a density of 32 lbm/ft³ (513 kg/m³). Finally, Helber *et al.* [54] report that densities of ASTERM, an ESA material similar to PICA, range from 240 to 550 kg/m³. Figure 4.2, reproduced from Stackpoole *et al.* [159], shows micro-graphs of samples taken from the Stardust heatshield. These images show the complicated microscopic structure of PICA, and how the amount of resin still bonded to the fibers decreases from the virgin material (Slice 30) to the char layer (Slice 1). Slice 6 and Slice 9 are taken from inside the pyrolysis layer.

The following sections outline the expected physical properties for each individual component of PICA: the carbon fibers, the phenolic resin, and the carbonaceous char that is created when the resin is heated to high enough temperatures.

4.3.1 Expected Fiber Properties

PICA, as outlined by NASA, uses a fibrous ceramic substrate called Fiberform® (manufactured by Fibermaterials Inc.), which consists of rigid, lightweight carbon fibers, designed to be resistant to high temperatures in vacuum [168]. This material is then impregnated with a phenolic resin. Tran *et al.* [168] report that the fibers used have a diameter of 14-16 μm , and that the material (Fiberform®, fibers only) has a density ranging from 8.5 to 11 lbm/ft³ (136 - 176 kg/m³). Information listed about Fiberform® Rigid Insulation is publicly available,⁵ and a density range of 150 kg/m³ to 230 kg/m³ is noted, which is similar to what Tran *et al.* report in [168]. A room temperature porosity range of 80.2%–94.2% is also given.⁵

Helber *et al.* [54] have recently reported results on material response from ablation studies performed in the von Karman Institute for Fluid Dynamics (VKI) Plasmatron [22]. A detailed study

⁵Fiberform®Rigid Insulation, <http://www.fibermaterialsinc.com/product/fiberform-rigid-insulation/> [accessed January 24, 2014].

was performed on ASTERM and other similar materials used by ESA. Properties for a material (carbon fiber pre-form manufactured by Mersen Scotland Ltd.) similar to the pre-form used in ASTERM are given in the report [54]. The fiber diameter is reported to be $d \sim 6.5 \mu\text{m}$, the fiber length is $l \sim 650 \mu\text{m}$, density of the virgin material is $\rho \sim 180 \text{ kg/m}^3$, porosity is $\sim 90 \%$, and the specific surface area is $\sim 3.24 \cdot 10^6 \text{ m}^3/\text{m}^2$, or $18000 \text{ m}^2/\text{kg}$. Visual images presented taken with a scanning electron microscope show the same random nature of the fiber alignments, and the potential for non-uniformity inside of the carbon pre-form as for PICA (Fig. 4.2).

Tran *et al.* [168] also report on the mechanical and thermal performance of the carbon fibers. The fibers themselves are an anisotropic material, with different properties along the fiber length direction (strong direction) than along the fiber diameter (weak direction). In a heatshield, it is useful for the ablative surface to be perpendicular to the weak direction of the fibers as the thermal conductivity in the strong direction is 2.4 times that of the weak direction. In addition, the thermal conductivity is reported by the manufacturer to be 0.21 W/mK at 530 K and 1.24 W/mK at 2500 K in the strong direction.⁵ Tran *et al.* [168] measured the thermal conductivity yielding similar results, and also observed that the thermal conductivity is strongly dependent on the temperature of the fibers.

4.3.2 Expected Resin Properties

The phenolic resin used in PICA is a product of a polycondensation reaction between phenol ($\text{C}_6\text{H}_5\text{OH}$) and formaldehyde (CH_2O) in the presence of a catalyst [152]. The method used to make the resin depends on the original ratio of formaldehyde to phenol (F/P). This process is outlined in other sources [75, 128, 152, 168], and is elaborated on in Appendix C. The chemical processes outlined in Appendix C show how these phenolic resins are synthesized, and how the manufacturing process can affect the final resin composition and its mechanical and thermal properties. The SC-1008 (made by MomentiveTM) phenolic infiltrant is specifically mentioned in NASA reports [168], but other commercial phenolic resins are available (for example, Plenco Phenolic Resins⁶).

4.3.2.1 Types and Production

Phenolic resins can be broadly classified into two groups: novolac resins and resole resins. With an initial molar excess of formaldehyde to phenol ($\text{F}/\text{P} > 1$), a resole resin is produced. The formaldehyde and phenol are mixed, heated, and begin to cross-link (link one polymer chain to another) on their

⁶Plenco - Plastics Engineering Company, <http://www.plenco.com/phenolic-novolac-resol-resins.htm> [accessed October 21, 2013].

Table 4.1: Summary of starting reagent and reaction conditions for novolac and resole resins. Specific ratios are taken from [75].

Type of Resin	F:P	Catalyst Used	Crosslinking Agent Required?
Resole	1.2:1.0 - 3.0:1.0	Basic (Alkaline)	No
Novolac	0.5:1.0 - 0.8:1.0	Acidic	Yes

own. The procedure is performed in the presence of a basic (alkaline) catalyst. With an initial molar excess of phenol to formaldehyde ($F/P < 1$), a novolac resin is produced. Once again, the formaldehyde and phenol are mixed and heated, but do not begin to cross-link until a cross-linking agent is added to the mixture. This procedure is performed in the presence of an acidic catalyst. By changing the original ratio of phenol to formaldehyde, pH, catalyst, reaction temperature, reaction time, and distillation amount, it is possible to generate a variety of resin structures, which in turn have a range of physical properties. The initial conditions for these two types of resins are summarized in Table 4.1.

As an example, let us consider the Durite SC-1008 phenolic resin (data taken from the Momentive website⁷). It is a resole type phenolic resin, and is listed as having a specific gravity of 1.07-1.10 (pre-cure). This is equivalent to a pre-cure density of 1.07 - 1.10 g/cm³. A post-cure density of 1.25 g/cm³ is often used as the density for the resin in many molecular dynamics studies performed [33, 68, 112, 137, 165].

Given the manufacturing process described above and in Appendix C, most resins are composed of carbon, hydrogen and oxygen elements, and potentially leftover components from the manufacturing process. These are the same elements that will be present in the pyrolysis gases. An idealized linear polymer (no cross-linking) is shown in Fig. 4.3, and the composition used for the resin in this thesis will be taken to be the repeating unit, n , in this figure ($C:H:O = 0.500:0.429:0.071$ by mole). The repeating unit, which corresponds to C_7H_6O , has a molecular composition close to that of a single phenol molecule, C_6H_6O . Due to this similarity, pure phenol may be used as a representative “surrogate” for the initial composition of the pyrolysis gases or resin, when a simplified model is required. As an aside, if an idealized, fully cross-linked phenol molecule (3 cross-links per molecule, similar to Fig. C.3) is used to calculate the composition of the resin, then a value of $C:H:O = 0.517:0.414:0.069$ is obtained. This composition and the composition of the repeating unit in Fig. 4.3 will act as limiting idealized cases for the elemental compositions of the resin. Actual phenolic resins are not expected to be 100% cross-linked, but are also not expected to be linear polymers; some finite amount of cross-linking is expected depending on the resin type and synthesis process (see

⁷Momentive, <http://www.momentive.com/Products/TechnicalDataSheet.aspx?id=5652>, accessed December 17, 2013.

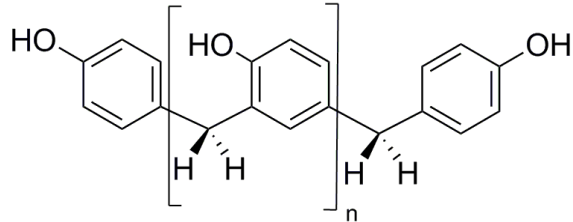


Figure 4.3: Linear polymer representing an idealized cured resin structure for a phenolic resin.

Appendix C). Only minor discrepancies are noted when either of these compositions are used in calculations, as the elemental compositions are extremely similar between the limiting cases.

4.3.2.2 Curing and Thermal Decomposition

The composition of a resin can also be modified post-polymerization by the application of a subsequent curing step. A more detailed explanation of this process and the expected thermal decomposition of the resin is found in Sec. C.2. The present summary is based on results and explanations presented in [75, 128, 162, 169], and more recently in [182].

In the curing step, excess formaldehyde (or a formaldehyde source), sufficient heat (typically $\sim 150^{\circ}\text{C}$), and/or an acid or base catalyst is applied in order to promote the cross-linking of any remaining unjoined or open sites in the polymer. This promotes the formation of methylene bridges, potentially eliminating other types of linkages that may have formed previously (Fig. C.2). This was explicitly noted by Sykes [162], where it was found that the amount of water produced during pyrolysis at relatively low temperatures was greatly affected by the cure time of the sample.

The decomposition of the resin, and pyrolysis gases produced, can generally be broken down into three different temperature ranges. At approximately 300°C , any remaining ether and nitrogen linkages begin to break, forming aldehydes, cresols, and azomethines. Furthermore, at this stage, any small molecules that were trapped from the manufacturing process are released, such as excess phenol, water, formaldehyde, ammonia etc. A large percentage of the pyrolysis gases are found to be H_2O in this temperature range [162, 182]. At approximately 600°C , substantial shrinkage of the polymer occurs as a result of the formation of carbon-carbon bonds between aromatic rings, resulting in the formation of a polyaromatic char. Substantial quantities of pyrolysis gases are liberated, composed mainly of hydrogen, but also methane, volatile aromatic compounds (such as phenol or benzene), water, carbon monoxide, and carbon dioxide. At temperatures above this, ($\sim 900^{\circ}\text{C}$) any non-carbon species continue to be evolved, and the pyrolysis gas consists mainly of H_2 [162, 182].

The expected pyrolysis gas products are a strong function of the temperature at which pyrolysis is occurring. Knowing this, it follows that the elemental composition of the pyrolysis gas products is not expected to be constant, and will also be a strong function of temperature. The fact that the elemental composition of the pyrolysis gases is not constant over a temperature range is very important, and will be discussed in more detail in later sections.

4.3.2.3 Presence of Impurities

Due to the complicated synthesis and curing process that is required to create phenolic resins, it is possible for a phenolic resin to contain small amounts of impurities, which will affect the overall properties of the resin.

The Apollo capsules used Avcoat 5026-39 HC/G as the resin in their ablative heatshields, which is a novolac resin [29]. Hexamethylenetetramine, $(\text{CH}_2)_6\text{N}_4$, is typically used as the cross-linking agent during the production of this resin. As a result, a small amount of leftover nitrogen is often assumed to be present when calculating the composition of the pyrolysis gas from Avcoat, as done by Park *et. al.* [122]. More recent carbon phenolic heatshields use a resole resin where no catalyst is needed in the cross-linking process. In some studies, nitrogen is not included when calculating the composition of the pyrolysis gas [122], whereas in other studies [108], small amounts of nitrogen are included for PICA heat shields. Other contaminants, such as Si, can be included in the pyrolysis gas composition as well [108].

Experimental measurements performed in [162] on a novolac resin (Union Carbide Corporation BRP 5549) showed the post-cure content of the resin to be 75.6% C, 6.12% H, 2.35% N, and 15.93% O by mass ($\text{C:H:N:O} = 0.465:0.449:0.012:0.074$ by mole), extremely close to the expected value of $\text{C:H:O} = 0.500:0.429:0.071$, if a phenol linked with CH_2 (n in Fig. 4.3), is assumed to be the primary component of the resin. The novolac resin used in [162] was premixed with hexamethylenetetramine, and then cured by the authors. The experiments were performed on a neat resin sample, not the composite material.

It is important to note than any nitrogen present in the final resin is generally leftover from the synthesis process, and can be found in two general forms. It is possible that the nitrogen is physically trapped in the resin, not chemically bound to other molecules. It is also possible that the nitrogen is chemically bound in the resin structure (see o in Fig. C.1). Sykes [162] attributes the relatively high nitrogen content in the resin to trapped ammonia (NH_3), as ammonia is a product of the decomposition of hexamethylenetetramine. If it is assumed that all of nitrogen content observed by

Sykes [162] is trapped ammonia, removing this ammonia from the resin results in a new elemental ratio of C:H:O = 0.488:0.434:0.078. This is even closer to the expected composition previously described, further validating the use of the idealized resin structure shown in Fig. 4.3.

4.3.3 Expected Char Composition

Char refers to the solid carbonaceous residue that is created when the resin is heated to high enough temperatures. This is the solid that is left behind as the resin undergoes a thermal decomposition. Some of the initial resin is converted into pyrolysis gases, while some of the resin stays in the solid phase, and evolves into char. The chemical pathways and timescales associated with the solid char formation are still subjects that are under investigation [66, 169, 170].

In general, the amount of polycyclic aromatic char that is expected to form from a virgin resin is approximately 60% by mass of the original virgin resin [75]. This assumes that after a full thermal decomposition of the resin has occurred, 40% of the original mass present was converted into pyrolysis gases, and 60% of the original mass present remained as a solid, and evolved into char. This is close to the value of 54% observed experimentally by Sykes [162].

Sykes [162] analyzed the char composition of a neat, cured novolac resin, through elemental analysis. It was observed that the char present at 850° C contained 92.6% C, 0.9% H, and 6.5% O by mass (C:H:O = 0.856:0.099:0.045 by mole). Tran *et al.* [168] tested a composite material (cured resole resin and fibers) sample in an arc-jet at 1065 Btu/ft²-s (1210 W/cm²), 0.34 atm stagnation pressure, for a total heat load of 26,625 Btu/ft² (30,235 J/cm²). The composition of the char was then measured using X-ray photoelectron spectroscopy. The elemental composition (by mole) of the char was found to be 98% C, 1.7% O, 0.3% Si (Si noted as an error due to the sample processing technique). This discrepancy in char composition between different experimental studies should be addressed in more detail in future works.

The char, which has been observed to be primarily composed of carbon, may also have other elements bound inside of it. For example, Syke's [162] hypothesized that through oxidation reactions it would be possible for oxygen to be present in the solid char. These elements could also be evidence of incomplete pyrolysis, or contamination of the experimental samples.

It is also believed that some parallels can be drawn between soot that traditionally forms in flames, and char. Both char and soot are solids consisting primarily of carbon atoms that are formed at high temperatures, through reactions involving aromatic hydrocarbons. A dehydrogenation process has been observed in combustion with soot formation. As time progresses, or as the

soot matures, the H/C ratio of soot decreases [67, 148]. This type of phenomena should affect the carbon char as well, and may help explain the discrepancies observed in experimentally measured char compositions.

In addition, the char composition reported by Tran *et. al* [168] was taken from an actual PICA sample after arc-jet testing. The PICA sample was subjected to a very high heat load, and was heated for a longer time than the samples in Sykes' [162] work. It is likely that the sample tested by Tran *et. al* [168] was fully pyrolyzed, which could explain the very high carbon content measured in the char. Based on the above discussion, for the rest of this thesis, when an idealized char material is needed, it will be assumed to be composed uniquely of carbon. A similar assumption is made in other works [78].

This section has provided an overview of the physical components of PICA, and a basic explanation of the synthesis of phenolic resins and the expected decomposition products of a phenolic resin at high temperatures. With this understanding of the components that make up PICA, and investigation into the pyrolysis gas composition can now be performed.

4.4 Pyrolysis Gas Composition

Due to the formation of a solid carbonaceous residue (char), it is clear that the elemental composition of the pyrolysis gases injected into the boundary layer is not that of the original resin. Experiments performed on a phenolic resin have confirmed that the pyrolysis gases differ in composition significantly from the original resin [177]. This has large implications for modeling efforts, as the elemental composition of the pyrolysis gas is an additional unknown. Not only is it desired to have an accurate description of the gas that is injected into the boundary layer, but the gas flowing internally in the heat shield must also be modeled correctly in order to accurately predict the full thermal response of the heatshield.

Many experimental works (for example, Sykes [162], Wong *et al.* [182]) show that the elemental composition of the pyrolysis gas mixture produced is not constant over a large temperature range. Very recently, Lachaud and Mansour [78], and Wong *et al.* [182] reported a decomposition model for the solid resin based on experimental results. In this model, the gas mixture does not have a constant elemental composition. The work by Lachaud and Mansour [78] is the first computational work, to the author's knowledge, to report results using a non-constant elemental composition for the pyrolysis gas mixture. This differs significantly from all previous computational works that use an average composition for the pyrolysis gas mixture (for example, see Milos and Chen [108]). A

review of existing thermal response codes is provided by Lachaud *et al.* [77], and a summary of the varying degree of complexity that is included in these codes, *i.e.*, frozen chemistry, equilibrium chemistry, or fine-rate kinetics, is provided by Lachaud and Mansour [78].

In order to understand how these different composition assumptions affect the pyrolysis gas, the following sections investigate the effects of various gas models used, the chosen elemental composition of the pyrolysis gas, and the equilibrium *vs.* non-equilibrium assumption on the mixture enthalpy of the pyrolysis gases.

4.4.1 Equilibrium Pyrolysis Gas Composition

Internal to the heatshield, the pyrolysis gas flows at relatively low speeds. The complicated nature of this porous flow is outside the scope of this work, but has received attention in the literature elsewhere [8, 78]. It has previously been proposed that as the pyrolysis gases flow through the porous medium internal to the heatshield, the gas speed is on the order of 10 m/s [8]. Based on the rather slow motion of the gases inside of the heatshield, previous works have assumed that the pyrolysis gases are in thermodynamic equilibrium at the local temperature and pressure. The current work begins with this assumption.

As described previously, when the phenolic resin starts to degrade, many small gas bubbles are formed in the material, and a porous flow begins once the bubbles become connected. As the flow gets closer to the surface of the heatshield, the temperature increases. A range of temperatures for when the resin starts to decompose can be found in the literature. In [168], 150°C is given (fibers impregnated with resole resin), 250°C is given in [170] (fibers impregnated with resole resin), 300°C is given in [75] (neat resole resin), and 350°C is given in [162] (neat novolac resin), for example. It is expected that different phenolic resins have different physical properties, which helps explain this range of temperatures found in the literature. Given these uncertainties, an average temperature of 230°C is used in this work as a starting point for resin decomposition. This temperature should be understood as the temperature at the edge between the virgin material and the pyrolysis layer (Fig. 4.1), and is similar to what is used in other works [182].

4.4.1.1 Gas Model

Through a collaborative effort with the von Karman Institute (VKI), a reduced 55 species thermodynamic model has been developed to represent the pyrolysis gases produced from a typical PICA heatshield. This model only includes thermodynamic properties for the different species chosen, and

no information pertaining to chemical reactions. Therefore, this model can only be used for thermodynamic equilibrium calculations, and not for calculations that would require a set of chemical reactions and reaction rates (finite-rate chemistry).

To create the model, 193 species were taken from the Chemical Equilibrium with Applications (CEA) database [99]. Species characteristic of a typical carbon phenolic decomposition (species with C/H/O) were originally chosen, and then species containing N were also added. This accounts for mixing between an atmosphere that may be partially composed of nitrogen, and the ablation products from a heatshield. In addition, thermodynamic properties for 8 additional species ($C_{24}H_{12}$, $C_{16}H_{10}$, C_3H , 1C_3H_2 , 3C_3H_2 , C_4H , C_5H , and C_5H_5) were recomputed, and added to the 193 species set, creating a full model with 201 species.

Next, a model reduction was performed by calculating different thermodynamic equilibrium compositions at constant temperature, and pressure, for the full 201 species model. The temperature was varied from 25°C to 5800°C, and pressure was varied from 1 kPa to 10 MPa. At each respective temperature and pressure condition, 1000 different elemental compositions were chosen (uniformly varying in the ratio of C:H:N:O), and thermodynamic equilibrium calculations were performed. If a mole fraction of a specific species was consistently (for all P , T , and C:H:N:O values tested) below 10^{-4} , the species was removed from the gas model. It was found that trying more than 1000 different elemental compositions at every temperature and pressure did not change the final reduced species model.

This reduced the original 201 species model to a 55 species model. A comparison was then made between the 55 species model, and the 201 species model, to calculate relative errors made by the reduced species model on the bulk properties of the mixture. Comparisons were performed at all values of T , P , and C:H:N:O ratios considered for the model reduction. It was found that for c_p , h , s (entropy), and $X_{radiators}$ (see Sec. 4.2), the errors between the 55 species model and the full 201 species model were always less than 1%. The maximum percentage error made on mole fractions of strong radiators present is approximately 0.1%.

The 55 species model was deemed acceptable for this chapter due to the relatively small discrepancies with the full model. Detailed information about the gas species model reduction will be the subject of a forthcoming publication [12]. The full list of species used can be found in Appendix D, along with the sources used for thermodynamic properties. Thermodynamic data is also provided for individual species that were recomputed for this gas model. This 55 species gas model is used for the rest of this chapter.

4.4.1.2 Elemental Composition of Pyrolysis Gases

In order to perform thermodynamic equilibrium calculations, an elemental composition must be specified. Three different elemental compositions are chosen, in order to understand the effect that elemental composition has on the pyrolysis gases. The first composition has a C:H:O ratio of 0.500:0.429:0.071 by mole, which is the expected composition of the pure resin (see Sec. 4.3.2). It is understood that this is more carbon-rich than the expected pyrolysis gas composition, as this gas composition assumes that no char is formed from the resin, but it serves as a limiting test case. The second composition has a C:H:O ratio of 0.358:0.550:0.092 by mole, which is calculated by taking the original resin composition and then assuming that 35% of the mixture, by mass, will turn into a solid char comprised purely of carbon (see Sec. 4.3.1). This mass of carbon is then removed from the mixture (35% char yield). This composition is more characteristic of the pyrolysis gas products for mid-range temperatures during the decomposition process. The 35% char yield assumption yields an elemental composition for the pyrolysis gases that is very close to the experimentally measured composition of the pyrolysis gases at 500°C [162]. The third composition has a C:H:O ratio of 0.195:0.690:0.115 by mole, which corresponds to a 60% char yield by mass (Sec. 4.3.3). These three chosen compositions are summarized by the first three lines of Table 4.2.

In a recently published work, the species blowing rates for the pyrolysis gas were calculated for a PICA material using the FIATv3 [105] thermal response code for a chosen trajectory [108]. During heating, the surface temperature varies from $\sim 200^\circ\text{C}$ to $\sim 3000^\circ\text{C}$ (not monotonically) as a function of time. Milos and Chen [108] show results where the C:H:O ratio of the injected pyrolysis gas remains essentially constant at 0.18:0.68:0.12. The missing 2% from the gas mixture is attributed to 1.4% N, and then trace amounts of Si. The elemental composition used in the numerical simulations by Milos and Chen [108] was taken from experiments, and the nitrogen content can be attributed to impurities in the resin (potentially from synthesis), and it is unclear as to why Si is observed experimentally.⁸

Finally, in an earlier work by Park *et al.* [122], the elemental composition of the pyrolysis gases entering the boundary layer was C:H:O=0.229:0.661:0.110 by mole. Using the simplified resin composition discussed (see Sec. 4.3.2.1), the values used by Park *et al.* [122] correspond to approximately a 56% char yield, and the values used by Milos and Chen [108] correspond to a char yield of roughly 65% (neglecting impurities). All pyrolysis gas compositions are summarized in Table. 4.2.

⁸Private communication with Dr. Frank Milos, NASA-Ames.

Table 4.2: Summary of different pyrolysis gas compositions.

Mixture Description	Elements Included	Composition (by mole)
Pure Resin	C:H:O	0.500:0.429:0.071
35% Char Yield	C:H:O	0.358:0.550:0.092
60% Char Yield	C:H:O	0.195:0.690:0.115
Park <i>et al.</i> [122]	C:H:O	0.229:0.661:0.110
Milos and Chen [108]	C:H:N:O:Si	0.18:0.68:0.014:0.12:0.006

4.4.1.3 Equilibrium Results—Polycyclic-Aromatic Hydrocarbon (PAH) Species

This section shows results for the previously discussed elemental compositions assuming thermodynamic equilibrium. All thermodynamic equilibrium calculations are performed using Cantera [47], and are performed holding temperature and pressure constant. First, the elemental composition of the virgin resin is used, and calculations are performed at different temperatures while keeping the pressure constant at 50 kPa (see Sec. 4.5.1). Fig. 4.4a shows the major species present using the reduced 55 species model. The most pertinent observation is that large quantities of coronene ($C_{24}H_{12}$, Fig. 4.5), are predicted for all temperatures below $\sim 1700^{\circ}\text{C}$. At 1180°C , the mixture is predicted to be 70% coronene by mass, which shows the importance of including this molecule if thermodynamic equilibrium calculations are going to be performed in this temperature range.

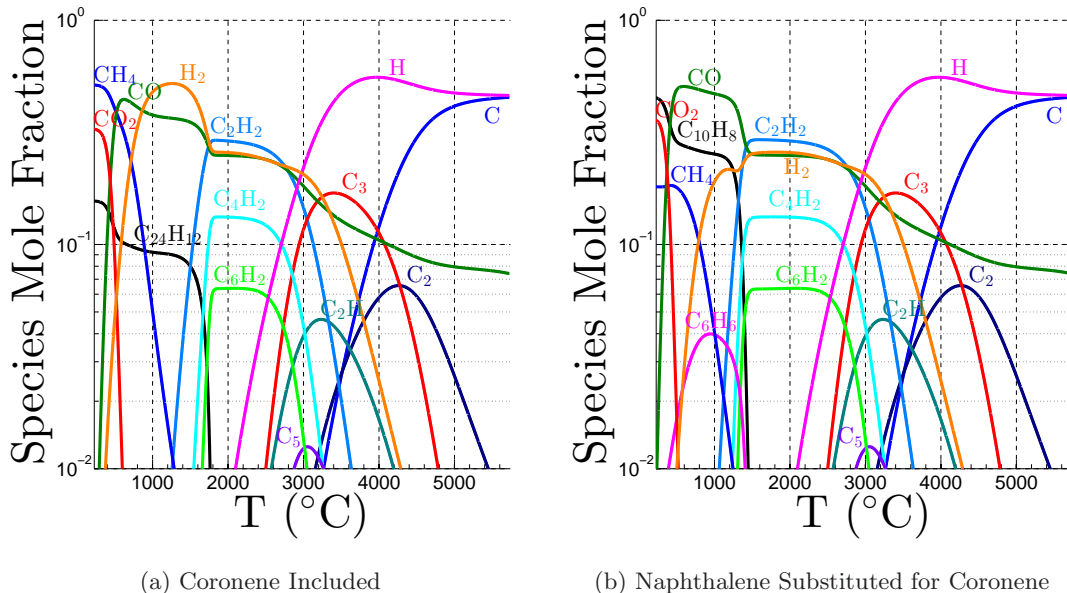


Figure 4.4: Thermodynamic equilibrium composition of the pyrolysis gas mixture assuming an initial resin composition of C:H:O = 0.500:0.429:0.071 by mole, at 50 kPa. Species with mole fractions $> 10^{-2}$ are shown in both plots. (a) includes coronene in the gas model, while (b) substitutes naphthalene for coronene.

In Fig. 4.4b, coronene ($C_{24}H_{12}$) is removed from the list of species included and is replaced by

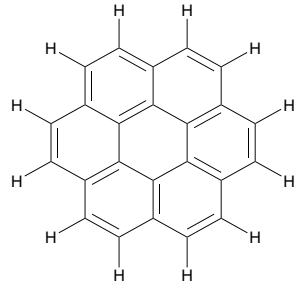


Figure 4.5: Coronene molecule, $C_{24}H_{12}$.

naphthalene ($C_{10}H_8$). Once again, significant quantities of naphthalene are observed at temperatures below ~ 1700 K. In fact, if both coronene ($C_{24}H_{12}$) and naphthalene ($C_{10}H_8$) are included in the species model, the predicted yield of naphthalene is essentially zero, and the results shown in Fig. 4.4a are obtained again. All of the mass goes into the PAH species with the smallest H/C ratio. For naphthalene, H/C = 0.8, and for coronene, H/C = 0.5. As illustrated, from a thermodynamic standpoint, these large hydrocarbon species are likely to form, and only recently have our collaborators started to use these in their models based on our suggestions [78]. High concentrations of these polycyclic-aromatic hydrocarbon (PAH) molecules can also have a large effect on the global properties of the gas mixture, such as the value of the specific heat for the mixture, and the mixture enthalpy. It should be noted that at the conditions considered in this section, while the formation of $C_{24}H_{12}$ is favored from a thermodynamic standpoint, the validity of this assumption from a kinetic standpoint has not been addressed yet, and will be considered in the next section. Above roughly 2000°C, both Fig. 4.4a and Fig. 4.4b show the same mixture compositions. At these high temperatures, PAH species are no longer favored from a thermodynamic stand point, and the inclusion of $C_{24}H_{12}$ or $C_{10}H_8$ has no effect on the mixture composition.

4.4.1.4 Equilibrium Results—Varying Mixture Composition

Figure 4.6 shows the mixture composition assuming different elemental pyrolysis gas compositions resulting from different assumed char yields, namely; 35% char yield in Fig. 4.6a and 60% char yield in Fig. 4.6b. Assuming a 35% char yield results in a maximum value of 50% $C_{24}H_{12}$ by mass at 1190°C, and assuming a 60% char yield results in a maximum of 17% $C_{24}H_{12}$ by mass at 1210°C. Obviously, as the overall carbon content in the pyrolysis gas mixture decreases, the amount of $C_{24}H_{12}$ that forms from a thermodynamic equilibrium calculation decreases.

It is difficult to notice meaningful differences between complicated gas mixtures by looking solely at species concentrations. From an engineering stand point, the question can be raised as to whether

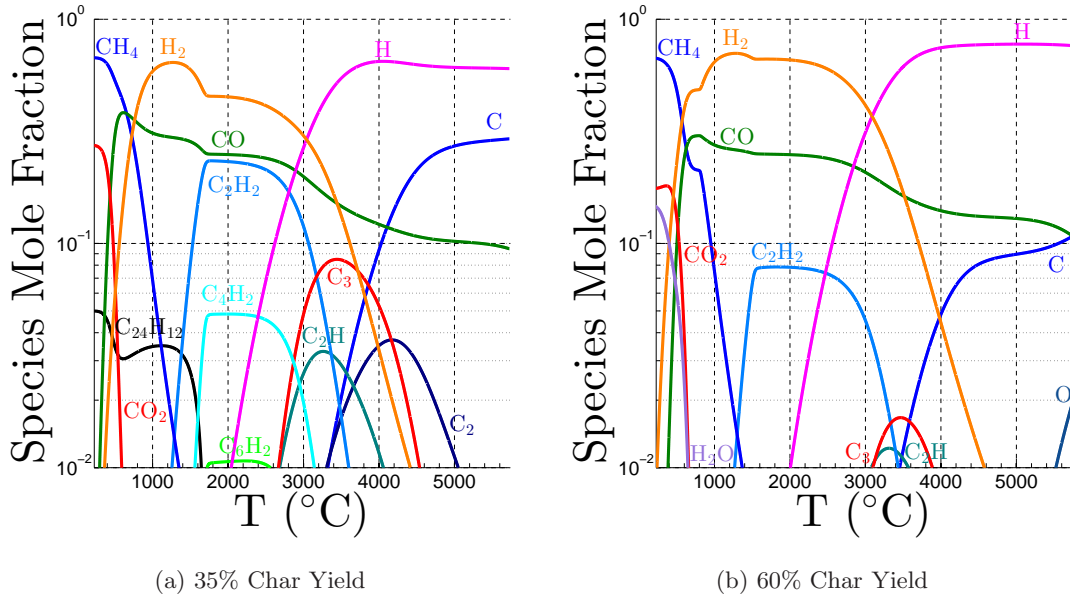


Figure 4.6: Thermodynamic equilibrium composition of the pyrolysis gas mixture assuming two different char yields at 50 kPa. Species with mole fractions $> 10^{-2}$ are shown in both plots. (a) corresponds to a 35% char yield ($\text{C:H:O} = 0.358:0.550:0.092$) and (b) corresponds to a 60% char yield ($\text{C:H:O} = 0.195:0.690:0.11$).

or not it is necessary to know the concentration of every single species in such a complicated mixture.

In this chapter, the mass specific mixture enthalpy is chosen as a relevant property to compare between different mixtures. The mass specific mixture enthalpy gives a measure of the amount of energy contained in the gas mixture, as was discussed previously in Sec. 3.3. For an ablative heatshield to be effective, the endothermic decomposition of the resin and creation of pyrolysis gases should absorb as much of the thermal energy of the external flow as possible. The enthalpy of the mixture relates to the efficiency of the pyrolysis gases in creating a cooling effect. Other quantities, such as c_p , could also be compared, but generally show similar trends as enthalpy, and changes in c_p will also be reflected in the mixture enthalpy. If one were to consider the injection of the pyrolysis gas mixture into the boundary layer of the heatshield, then other properties should be chosen to compare as well, as the injection of the pyrolysis gases into the boundary layer will affect the properties of the flow external to the heatshield. Although the boundary layer flow is not the focus of this work, if this part of the flow were to be considered, one relevant choice would be to compare γ between the different mixtures.

Figure 4.7 shows the quantitative effect of changing the elemental composition of the mixture by plotting the mass specific enthalpy of the mixture over a temperature range characteristic of what would be experienced inside of the heatshield. Figure 4.7 shows that the mixture enthalpy

decreases as the char yield increases. Once again, the lower the char yield, the higher the carbon content in the pyrolysis gas mixture, which means that there is more C₂₄H₁₂ present in the mixture (Figs. 4.4 and 4.6). Figure 4.7 quantitatively shows that changing the elemental composition of the gas mixture, while keeping the species model constant, has a large effect on the overall mass specific mixture enthalpy especially at lower temperatures ($T < 600^{\circ}\text{C}$). Interestingly, the specific enthalpy at higher temperatures ($T \sim 1500^{\circ}\text{C}$) is virtually independent from the char yield, when the reduced 55 species model is used. These two observations are important as the difference in enthalpies is related to how much heat is extracted by gaseous mixture.

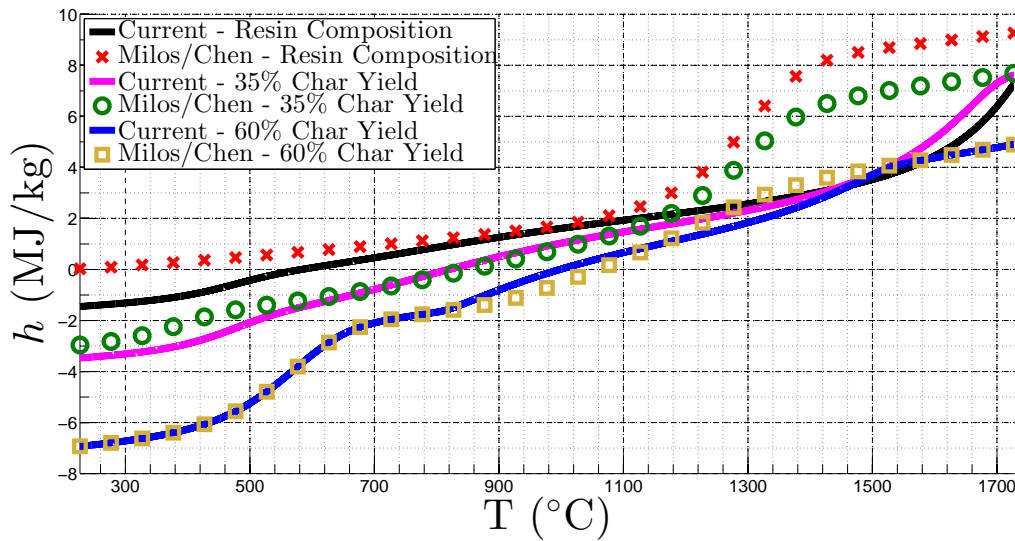


Figure 4.7: Enthalpy comparison for different gas models and elemental compositions. All mixtures are in thermodynamic equilibrium over a range of temperatures and at a pressure of 50 kPa.

In addition to showing the effect of elemental composition on mixture enthalpy, Fig. 4.7 shows the effect that the chosen gas model can have. In a recent study, Milos and Chen [108] used a 23 species gas mixture (including C, H, N, O, and Si) for the pyrolysis gases injected into the boundary layer, where the largest species included is C₆H₆. The gas mixture was calculated using FIATv3 [105].

Elemental compositions corresponding to a 0%, 35%, and 60% char yield are again used, and the current 55 species gas model is replaced by Milos and Chen's 23 species model [108]. Figure 4.7 shows differences in mixture enthalpy between the two different gas models. Figure 4.7 isolates two important phenomena: 1) the effect of elemental composition on the mixture enthalpy and 2) the effect of the chosen gas species model on mixture enthalpy. When performing thermodynamic equilibrium calculations to calculate the composition of the pyrolysis gas mixture, the species model *and* the elemental composition of the mixture must be chosen with care.

4.4.1.5 Equilibrium Results—Discussion

To emphasize the effect that the elemental composition has on the overall composition of the pyrolysis gas mixture, it is necessary to know how carbon rich a gas mixture must be in order to form C₂₄H₁₂ from a thermodynamic standpoint. This is done by varying the char yield from 0% (carbon rich gas mixture) to 70% (carbon lean gas mixture). For a given char yield, the maximum value of mass fraction of C₂₄H₁₂ is calculated for equilibrium mixtures spanning a temperature range from 230°C to 1800°C.

Figure 4.8 shows that for carbon rich gas mixtures, the maximum mass fraction of C₂₄H₁₂ is very high (up to ~ 70%). A smooth decrease in the maximum mass fraction of C₂₄H₁₂ is observed as the % char yield is increased. At a char yield of ~ 65%, no significant amount of C₂₄H₁₂ is predicted to form. This corresponds to a C:H:O elemental composition of 0.152:0.727:0.121 by mole. Figure 4.8 also shows that the decrease in $\max(Y_{C_{24}H_{12}})$ is almost entirely pressure independent. It is found that the temperature associated with the maximum mass fraction of C₂₄H₁₂ occurs for $T > 1150^\circ\text{C}$ (with $P = 50 \text{ kPa}$) for the range of elemental compositions considered when there is a significant amount of C₂₄H₁₂ present. However, as seen in Fig. 4.4a, there is a large quantity of C₂₄H₁₂ (mole fraction) that is predicted to form at temperatures near 230°C. At these relatively low temperatures, the prediction that gaseous coronene will form is most likely not valid. The melting point and boiling point of coronene are 438°C and 525°C respectively, at standard conditions. Even though the pressure considered in the calculations performed in this section is lower than atmospheric conditions (50 kPa *vs.* 101 kPa), at low temperatures, the effect of possible phase changes (condensation or solidification) should be considered. More investigation needs to be performed into this low temperature regime, and this could help explain the point of inflection in mole fraction of C₂₄H₁₂ in Fig. 4.6a. It is possible that temperatures lower than the point of inflection seen in the mole fraction of C₂₄H₁₂ in Fig. 4.6a correspond to unphysical predictions of C₂₄H₁₂, and temperatures higher than this point of inflection are physically accurate, but more work is needed to verify this hypothesis.

The % char yield range shown in Fig. 4.8 covers a wide range of elemental compositions, and shows that the presence of C₂₄H₁₂ is significant over a wide range of mixture compositions. If Park *et al.*'s [122] elemental composition is used (Table 4.2), up to ~ 25% by mass of the equilibrium mixture is predicted to be C₂₄H₁₂ at ~ 1200°C, and if a composition similar to the one used by Milos and Chen (neglecting Si) [108] is used (Table 4.2), then up to ~ 10% by mass of the equilibrium mixture is predicted to be C₂₄H₁₂ by mass at ~ 1200°C; neither of the species models in these two

studies included any large PAH molecules. To the author's best knowledge, no previous published works have included PAH species in pyrolysis gas mixture when modeling PICA heatshields. In order to understand the overall effect of including PAH species in the pyrolysis gas mixture on the performance of a PICA heatshield, full simulations incorporating PAH species into a thermal response code would have to be performed.

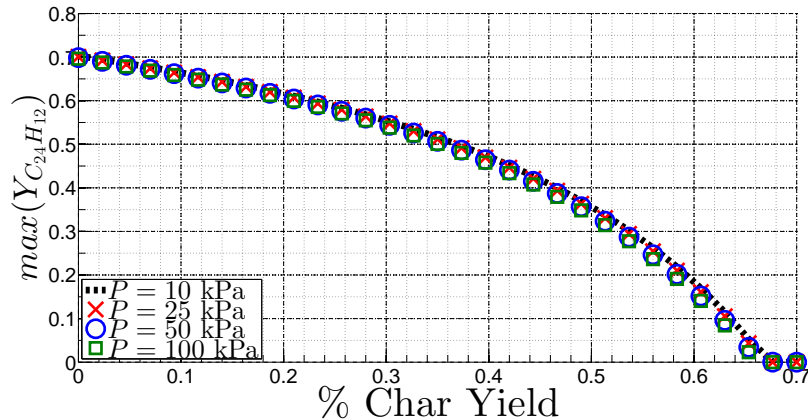


Figure 4.8: Maximum mass fraction observed of $C_{24}H_{12}$ over a temperature range from 230°C to 1800°C , varying the elemental composition. The calculation is performed for four different pressures to show the pressure independence of the plotted values.

4.4.2 Kinetic Evolution of Pyrolysis Gas Composition

The previous section did not take into account the finite amount of time it takes to form the large PAH molecules. Although the formation of molecules such as $C_{24}H_{12}$ and other large aromatic species is favorable from a thermodynamic standpoint, the residence time of the pyrolysis gas inside of the heatshield might be too short for these molecules to actually form. In order to understand the characteristic timescales involved in this process, several simplifying assumptions are made.

Based on results from MSL [21, 94], a characteristic length of 1 cm is chosen for the distance that the pyrolysis gas will flow before leaving the heatshield. This represents the thickness of the pyrolysis and char layers shown in Fig. 4.1. A speed of 10 m/s is chosen to be characteristic of the speed of the gases traveling internal to the heatshield, based on the analysis performed by Ahn *et al.* [8]. Once again, the temperature at the bottom of the pyrolysis layer is assumed to be 230°C , and the temperature at the surface of the heatshield is assumed to be 1800°C . To isolate the effect of finite-rate kinetics, a simple Lagrangian approach is adopted. It is assumed that a packet of gas travels at a constant speed of 10 m/s from the bottom of the pyrolysis layer to the surface of the heatshield, at a constant pressure of 50 kPa. This ignores the complicated flow features associated with porous

flow, and the effect that the changing density, temperature, and pressure of the fluid would have on the velocity profile of the pyrolysis gases in an actual heat shield. Simulations accounting for these effects, but using simplified chemistry models, can be found in [78]. As the packet of fluid travels from the bottom of the pyrolysis layer to the surface of the heatshield, the temperature of the gas increases. Therefore, the temperature ($^{\circ}\text{C}$), can be written as a function of time, and for the rest of this work, a linear temperature profile of

$$T = 230^{\circ}\text{C} + 1.57^{\circ}\text{C} \cdot t, \quad (4.1)$$

is used, where t is given in μs . Prescribing a temperature rise also assumes that the heat release from the individual reactions occurring does not affect the temperature gradient imposed by the high temperature gas external to a heatshield. An initial composition of 100% gaseous phenol (A_1OH) is chosen in order to represent the initial composition of the pyrolysis gases. This acts as a “surrogate” for the phenolic solid resin (Sec. 4.3.2.1). Species diffusion is also neglected for these calculations. All of the previous assumptions are made in order to simplify the complicated reacting flow occurring inside of a heatshield, keeping in mind that the goal of these calculations is to find characteristic times associated with PAH formation.

The combustion database of Blanquart [17, 18, 19, 114] is used for the homogeneous reactions involved with the pyrolysis gas mixture (this mechanism is available for public use⁹). This mechanism contains 172 species and 1878 reactions (forwards and reverse reactions counted separately). While this mechanism is geared towards combustion applications, it contains all major pathways for PAH formation, and is useful for understanding timescales associated with PAH formation in the pyrolysis gas mixture. The largest hydrocarbon species included is $\text{C}_{18}\text{H}_{10}$, as the pathways and rates for the formation of larger species, such as $\text{C}_{24}\text{H}_{12}$, are largely unknown at this time. Chemical abbreviations used in this mechanism include: A_1 (benzene, C_6H_6), A_1OH (phenol, $\text{C}_6\text{H}_6\text{O}$), $\text{A}_1\text{C}_2\text{H}$ (ethynylbenzene, C_8H_6), A_2 (naphthalene, C_{10}H_8), $\text{A}_2\text{R5}$ (acenaphthylene, C_{12}H_8), $\text{A}_2\text{C}_2\text{HB}$ (2-ethynylnaphthalene, C_{12}H_8), $\text{A}_2\text{R5C}_2\text{H}$ (1-ethynylacenaphthylene, C_{14}H_8) and FLTN (fluoranthene, $\text{C}_{16}\text{H}_{10}$).

Simulations are performed using packages from the CHEMKIN 2 library [143]. A constant pressure homogeneous reactor is used with a prescribed temperature rise as a function of time (Eq. 4.1), that corresponds to $\sim 1500^{\circ}\text{C}/\text{cm}$ for a fluid moving with a constant speed of 10 m/s. Figure 4.9 shows the decomposition of phenol and the kinetic evolution of the gases produced under

⁹Mechanism available at <http://www.theforce.caltech.edu/resources/>

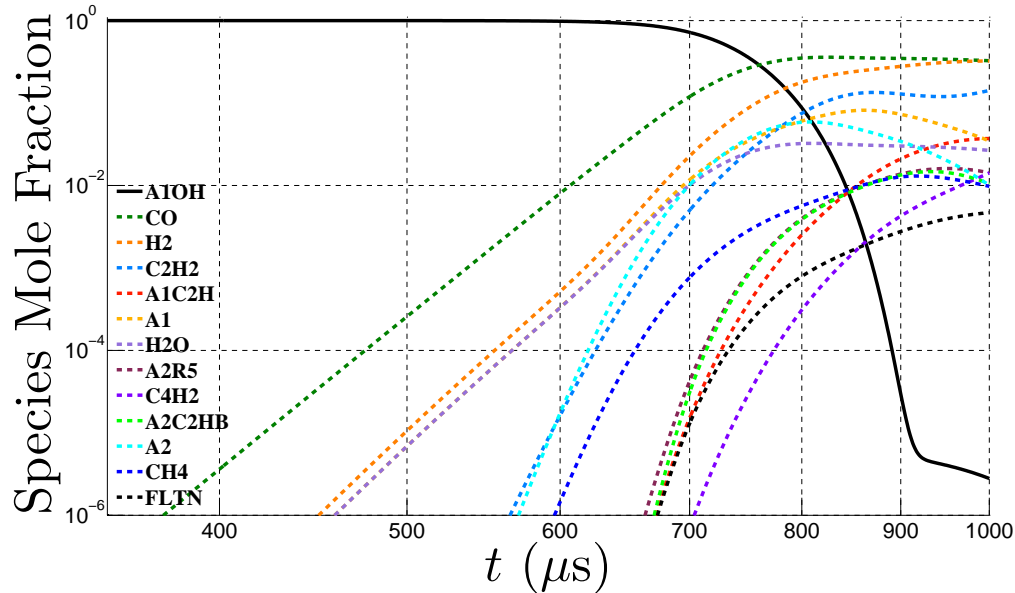


Figure 4.9: Kinetic evolution of pyrolysis gases with an imposed temperature and pressure profile. A time of $1000 \mu\text{s}$ corresponds to the gas traveling a distance of 1 cm at a speed of 10 m/s. $T = 230^\circ\text{C} + 1.57^\circ\text{C} \cdot t$, where T is in $^\circ\text{C}$, and t is in μs . $P = 50 \text{ kPa}$.

constant pressure and a prescribed temperature profile. It is clear that significant concentrations of varying PAH molecules are formed by the end of the simulation ($1000 \mu\text{s}$). To contrast this, Fig. 4.10 shows the composition of the gas mixture if a thermodynamic equilibrium is assumed, with the same C:H:O elemental composition as pure phenol. It is clear that there is a large discrepancy between the two mixtures, as the PAH molecules take time to form in Fig. 4.9. A maximum amount of $\text{C}_{18}\text{H}_{10}$ is found at 1300°C (8% by mole, 55% by mass) when a thermodynamic equilibrium is assumed. A quantitative comparison between the two mixtures is shown in Fig. 4.11, comparing the mixture enthalpies by mass between the two cases. Extremely large discrepancies are noted, showing that the bulk properties of the mixture are greatly affected by a thermodynamic equilibrium assumption.

Figures 4.9—4.11 isolate the effect of assuming that the pyrolysis gas mixture is in thermodynamic equilibrium *vs.* allowing the pyrolysis gas mixture to evolve kinetically. The same elemental composition (that of phenol) was used for both the equilibrium and finite-rate kinetics calculations, and the same species model was used for both of these calculations. Not only is the enthalpy of a mixture in thermodynamic equilibrium largely effected by the largest hydrocarbon molecule included, but the finite amount of time it takes the PAH species to form based on kinetics also has a great effect on the mixture enthalpy. It should be noted that the chemical mechanism used in this section was not directly designed for these conditions. Nevertheless, the results show that significant

quantities of PAH species will form in a relatively small amount of time and this will have significant effects on modeling efforts for these composite ablative materials.

To summarize this entire section, three different effects have been isolated: 1) the effect of elemental composition on the pyrolysis gas mixture; 2) the effect of the gas species model chosen on the pyrolysis gas mixture; and 3) the effect of assuming thermodynamic equilibrium *vs.* finite-rate kinetics on the pyrolysis gas mixture. The large discrepancies shown between all of these assumptions must be known and accounted for when determining what models to use in a thermal response code.

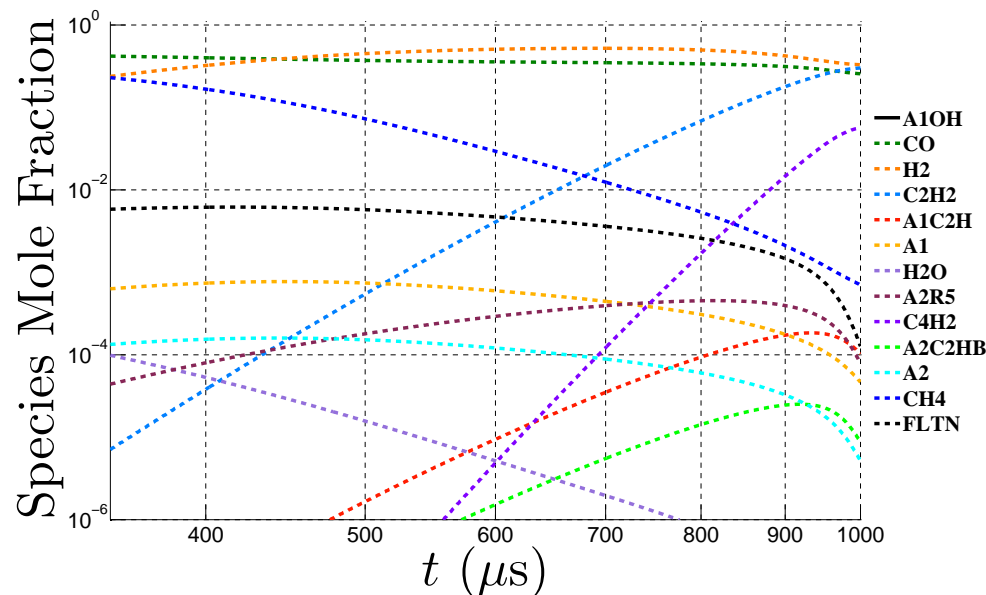


Figure 4.10: Equilibrium composition of pyrolysis gases with the same imposed temperature and pressure profile. $T = 230^\circ\text{C} + 1.57^\circ\text{C} \cdot t$, where T is in $^\circ\text{C}$, and t is in μs . $P = 50$ kPa.

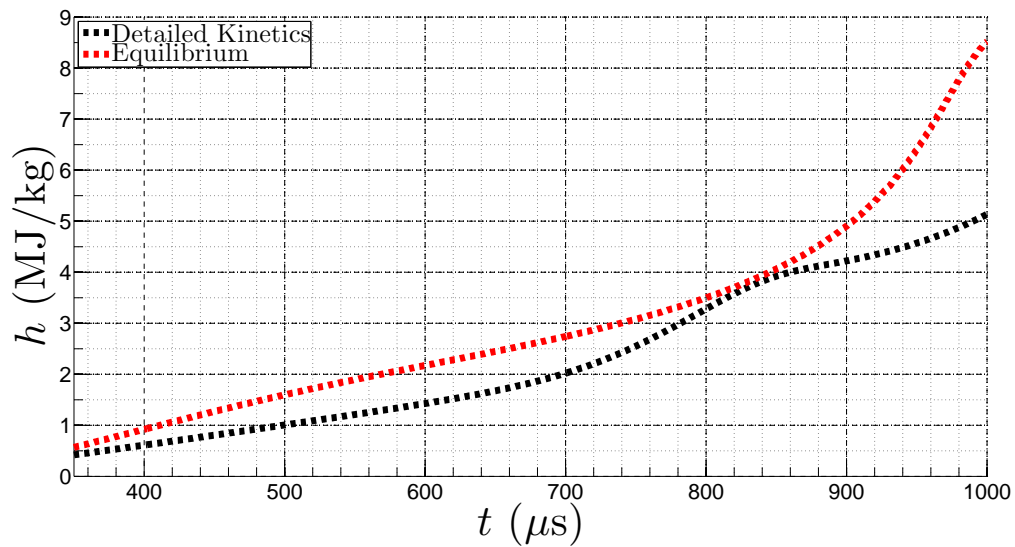


Figure 4.11: Enthalpy comparison between the gas mixtures assuming detailed kinetics (black) and thermodynamic equilibrium (red). $T = 230^\circ\text{C} + 1.57^\circ\text{C} \cdot t$, where T is in $^\circ\text{C}$, and t is in μs . $P = 50 \text{ kPa}$.

4.5 Pyrolysis Gas Flow Regime

The previous analysis was performed assuming a standard continuum flow regime. In order to validate this assumption for the flow of the pyrolysis gases internal to a heatshield, relevant length scales must be compared. In this section, conditions characteristic of what MSL experienced on entry into the Martian atmosphere are used to estimate the flow regime of the pyrolysis gas inside of an ablative heatshield. By using flight data reported by Bose *et al.* [21] and Mahzari *et al.* [94], a mean free path of the pyrolysis gas can be estimated, and this can be compared to the relevant length scales in the heatshield itself (size of the pyrolysis layer, diameter of the fibers in the virgin PICA material, and the average fiber separation).

4.5.1 Continuum Flow Assumption

The mean free path (λ) can be calculated from

$$\lambda = \frac{k_B T}{\sqrt{2\pi}\sigma^2 P}, \quad (4.2)$$

where k_B is the Boltzmann constant (J/K), T is the temperature (K), σ is the collision diameter of the gas molecules (m), and P is the pressure of the gas (Pa). The MISPR reconstructed temperature data shows that the thermocouples installed in the MSL heatshield experienced a wide range of temperatures, depending on the location of the thermocouple in the heatshield, the time during flight, and how deep below the heatshield surface the thermocouple was installed (1.2). 1000 K is taken as a characteristic temperature for these calculations, which is based on the temperature range that the thermocouple closest to the heatshield surface (~ 0.25 cm) experienced.

Surface pressure CFD predictions were made by Bose *et al.* [21], and over the time that corresponds to a heatshield temperature close to 1000 K, surface pressure predictions range from ~ 15 kPa to ~ 30 kPa. These measurements were confirmed by flight data taken by the Mars Entry Atmospheric Data System (MEADS) [88]. Calculations performed by Ahn *et al.* [8] for the Pioneer Venus Small Probe (Day) showed that the pressure of the pyrolysis gas inside the heatshield can be a factor of two or higher than the surface pressure. Taking these facts into consideration, a value of 50 kPa is chosen to be a characteristic pressure inside of the heatshield for this calculation. The same pressure was used for the results presented in the previous section.

To evaluate the collision diameter, the gas mixture is assumed to have the same elemental composition as a cured phenolic resin. Assuming thermal equilibrium, the main constituents of the

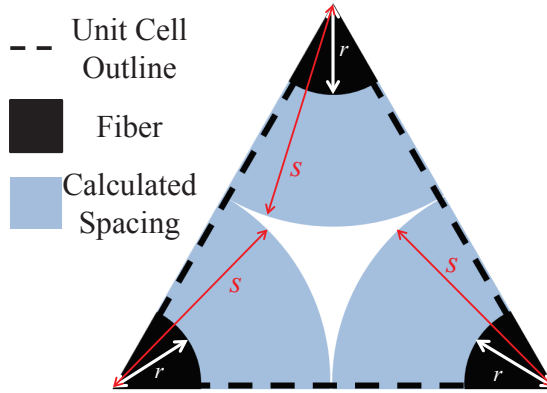


Figure 4.12: Schematic showing the simplified packing assumption for the carbon fibers. r is the fiber radius, and s is a calculated length to give the measured porosity.

mixture by volume are CO (43%), H₂ (25%), CH₄ (22%), and C₂₄H₁₂ (10%) at 1000 K and 50 kPa. For simplicity, as this is an order of magnitude calculation, the diameter of CO ($3.65 \cdot 10^{-10}$ m) is used in this calculation.

The Knudsen number, which is the ratio of the mean free path to a characteristic length scale ($Kn = \lambda/l$), allows one to determine if the flow is in a continuum regime. From Eq. 4.2, the mean free path is evaluated to be approximately $\lambda \approx 6 \cdot 10^{-7}$ m. If this is compared to a characteristic length of 1 cm associated with the pyrolysis layer, then $Kn \ll 1$, and the pyrolysis gas is in a continuum regime. While this Knudsen number shows that on a global scale the flow is in a continuum regime, the potential for collisions between the gas molecules and the carbon fibers must also be taken into account in order to estimate the importance of heterogeneous interactions [78, 182].

A Knudsen number calculation based on a fiber diameter of 10 μm (Sec. 4.3.1) yields $Kn \sim 0.05$. Alternatively, the mean free path can be compared to an estimation of the average separation distance between the fibers in the char layer. The mean distance is calculated by making the simplifying assumption that the cylinders are arranged into a triangular unit cell, and are infinitely long. Assuming a porosity of 90% (Sec. 4.3.1) allows a mean separation to be estimated. A schematic of this arrangement is shown in Fig. 4.12, where r is the fiber radius, and s is a calculated distance to give the desired porosity. Using the properties of ASTERM given in Sec. 4.3.1, a mean distance between the fibers can be estimated to be 10 μm , which results again in $Kn \sim 0.05$. Similar values for Kn were calculated for the PICA heatshield used on the Stardust mission, when different conditions along the Stardust re-entry trajectory were used [76].

A $Kn \sim 0.05$ is low enough that the flow can be considered to be in a continuum regime, but it is also large enough to imply that heterogeneous reactions between the pyrolysis gas and the solid

carbon fibers cannot be ignored. This is the “coking zone” proposed by Lachaud and Mansour [78], and Wong *et al.* [182], where it is possible for the gaseous carbon to form a solid residue on the fibers, and other heterogeneous reactions to occur. In addition, it is possible for solid carbon molecules to be formed through gaseous collisions, similar to soot being formed in a flame. These phenomena remove additional carbon concentration from the pyrolysis gas mixture, and effect the elemental composition of the gas. More details on these phenomena are provided in the following two sections.

4.5.2 PAH Collisions

In previous studies, soot formation is primarily discussed with respect to flames, and a summary of the formation of condensed-phased materials in flames was recently written by Wang [178]. While there are competing theories on soot nucleation and growth, in general, models start from vapor-phase nucleation. Particle growth then occurs through coalescence, coagulation, surface reactions, and condensation of vapor species [110, 178]. Nevertheless, a common trend among these theories is that collisions between PAH species are believed to form pre-cursors species for larger soot particles [178]. Early models used PAH-PAH sticking coefficients on the order of 0.2-0.4 [103], while more recent work looks into great detail of the interactions between two PAH species [155].

The frequency of PAH-PAH collisions can be calculated in order to determine whether or not “sooting” is expected to occur internal to the heatshield. Following the derivation by Vincenti and Kruger [176] for collision rates, the number of free paths terminated for a molecule of type *A*, by a molecule of type *Y*, per unit time is

$$\Theta_{AY} = n_Y \sigma_{AY}^2 \left(\frac{8\pi kT}{m_{AY}^*} \right)^{1/2}, \quad (4.3)$$

where Θ_{AY} is the number of paths terminated per unit time, n_Y is the number of *Y* molecules per unit volume, σ_{AY} is the collision diameter of *A* and *Y*, and m_{AY}^* is the reduced mass for *A* and *Y*. As collisions between two of the same molecules, for instance $C_{24}H_{12}$, are being considered for soot nucleation, the reduced mass is $m_{C_{24}H_{12}}/2$, and the collision diameter is the diameter of a coronene molecule. The collision diameter of $C_{24}H_{12}$ is approximated to be $9.2 \cdot 10^{-10}$ m through a simple MM2 [40] energy minimization calculation. n_Y is a function of both *T* and the partial pressure of $C_{24}H_{12}$. Θ_{AY} represents a collision frequency, and in order to estimate the number of collisions expected, this value is multiplied by a characteristic time. Once again, a speed of 10 m/s is assumed over a length of 1 cm which results in a time of 1 ms. Writing Eq. 4.3 in terms of $P_{C_{24}H_{12}}$, *T* and

multiplying by 1 ms yields

$$\kappa \approx \frac{2300[\kappa \frac{\text{K}^{1/2} \text{ m s}^2}{\text{kg}}] P_{\text{C}_{24}\text{H}_{12}}}{T^{1/2}}, \quad (4.4)$$

where κ is the number of collisions one coronene molecule is expected to undergo with another coronene molecule before it is injected into the boundary layer. From Fig. 4.9, mole fractions for PAH species are observed to be on the order of 1%. Equilibrium mixture calculations previously shown show a range in concentrations of $\text{C}_{24}\text{H}_{12}$, with maximum values corresponding to approximately a 10% mole fraction of coronene. Assuming a mixture pressure of 50 kPa, and a temperature of 1000 K results in a range of approximately 36,000 ($X_{\text{C}_{24}\text{H}_{12}} = 0.01$) collisions to 360,000 ($X_{\text{C}_{24}\text{H}_{12}} = 0.1$) collisions expected.

If every collision between two PAH molecules were to lead to soot pre-cursors, and the removal of the two PAH molecules from the flow, then $\frac{dn_{PAH}}{dt} = -2kn_{PAH}^2$, where k is a rate constant. Relating this expression to Eq. 4.3 yields $\Theta_{PAH,PAH} = kn_{PAH}$. In addition, sooting models generally include a sticking efficiency, which takes into account that for every collision between two molecules, most molecules may not stick to each other, but instead “bounce off” of each other. A value of 0.3 is used for this sticking efficiency [103]. Considering $\text{C}_{24}\text{H}_{12}$ as the PAH molecule results in

$$\frac{dn_{\text{C}_{24}\text{H}_{12}}}{dt} = -2 \cdot 0.3 \cdot \sigma_{\text{C}_{24}\text{H}_{12},\text{C}_{24}\text{H}_{12}}^2 \left(\frac{8\pi kT}{m_{\text{C}_{24}\text{H}_{12},\text{C}_{24}\text{H}_{12}}^*} \right)^{1/2} n_{\text{C}_{24}\text{H}_{12}}^2. \quad (4.5)$$

The solution to this ODE is

$$n_{\text{C}_{24}\text{H}_{12}}(t) = \frac{n_{\text{C}_{24}\text{H}_{12}}^\circ}{1 + 2 \cdot 0.3 \sigma_{\text{C}_{24}\text{H}_{12},\text{C}_{24}\text{H}_{12}}^2 n_{\text{C}_{24}\text{H}_{12}}^\circ t \left(\frac{8\pi kT}{m_{\text{C}_{24}\text{H}_{12},\text{C}_{24}\text{H}_{12}}^*} \right)^{1/2}}, \quad (4.6)$$

where $n_{\text{C}_{24}\text{H}_{12}}^\circ = n_{\text{C}_{24}\text{H}_{12}}(t = 0)$, the initial number of $\text{C}_{24}\text{H}_{12}$ molecules per unit volume.

Evaluating Eq. 4.6 at $t = 0.001$ s (corresponding to the surface of the heatshield), $T = 1000$ K, $P = 50$ kPa, and $X_{\text{C}_{24}\text{H}_{12}} = 0.01$ or $X_{\text{C}_{24}\text{H}_{12}} = 0.1$, results in 99.5% and 99.95%, respectively, of the $\text{C}_{24}\text{H}_{12}$ being removed from the flow. Even if the sticking coefficient is decreased by a factor of 1000, and $X_{\text{C}_{24}\text{H}_{12}} = 0.01$, 95.6% of the $\text{C}_{24}\text{H}_{12}$ is predicted to be removed from the flow, showing that this sooting prediction is relatively insensitive to the chosen sticking efficiency. These calculations imply that it is likely that soot will be formed from any PAH molecules. Once “soot” particles are formed, it would also be possible for these particles to collide with and deposit on the fibers. These calculations, while estimates, show that the removal of PAH species from the flow due to soot formation needs to be taken into account when considering the evolution of the pyrolysis gases.

4.5.3 PAH and Fiber Collisions

Not only must collisions between PAH molecules be considered, but collisions between PAH molecules and the carbon fibers will also occur in a heatshield. Originally, when deriving Eq. 4.2 for the mean free path in a gas mixture, it is standard to assume that one molecule is in motion, and all other molecules are stationary. Following this derivation, once again performed by Vincenti and Kruger [176], the number of collisions per unit time for a single molecule with another molecule of the same type is found to be

$$\Theta = \pi\sigma^2\bar{C}n. \quad (4.7)$$

\bar{C} is the mean molecular speed, σ is a collision diameter (based on a sphere of influence calculation), and n is the number of molecules per unit volume of the gas. This expression must now be altered in order to estimate how many times a single PAH molecule will collide with a stationary carbon fiber, as Eq. 4.7 is only valid for spherical particles impacting other spherical particles. Internal to a heatshield, it is assumed that spherical coronene particles are colliding with infinitely long cylindrical carbon fibers (Fig. 4.12). To simplify this calculation, it is assumed that coronene molecules are traveling perpendicular to the length of fibers, and all of the fibers are parallel to one another, as shown by the infinitely repeating unit cell shown in Fig. 4.12. The $\pi\sigma^2\bar{C}$ product from Eq. 4.7 represents a cylindrical volume carved out by a moving particle. Due to the assumption that cylindrical fibers are all parallel, and that the coronene particles move perpendicular to the fiber length, this term is now modified so that only an in plane area is considered, and becomes $\sigma\bar{C}$. However, a new area of influence must be calculated. The diameter of this “circle” of influence is given by $\sigma_{C_{24}H_{12}} + d_f$, where d_f is the fiber diameter. A 2D schematic of this arrangement is shown in Fig. 4.13. As $d_f \gg \sigma_{C_{24}H_{12}}$, this can be approximated by d_f . A modified n is now calculated such that it refers to a number density (per unit area) of carbon fiber centers.

Combining this information results in

$$\Theta = d_f\bar{C}n^*, \quad (4.8)$$

where n^* is the number of fiber centers per given area. Assuming a Boltzmann distribution, $\bar{C} = \left(\frac{8kT}{\pi m_{C_{24}H_{12}}}\right)^{1/2}$. Multiplying the collision frequency by the same characteristic time as before, results in $\kappa \approx 160[\kappa T^{-0.5}]T^{0.5}$. Assuming a reference temperature of 1000 K, this calculation shows that a single coronene molecule will collide with a carbon fiber approximately 5200 times before leaving the heatshield.

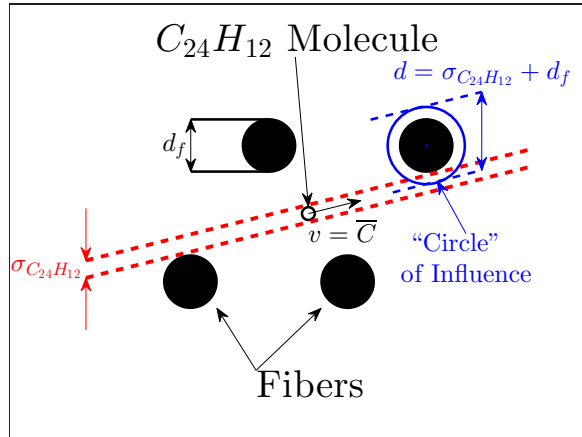


Figure 4.13: 2D schematic outlining the geometrical assumptions for $C_{24}H_{12}$ colliding with a carbon fiber. This figure represents a top-down view of a plane intersected by the fibers (fibers are assumed to be infinitely long in/out of the page). The “circle” of influence outlines an area that needs to be considered for collisions between $C_{24}H_{12}$ molecules and the stationary carbon fibers.

This corresponds to an estimate for an upper bound on the number collisions between PAH molecules and fibers in a heatshield. In the opposite extreme, no collisions would occur if the particles were all traveling parallel to the carbon fibers. This is an unrealistic assumption, as the length of the carbon fibers is expected to be on the order of $650 \mu\text{m}$ (Sec. 4.3.1), which is much smaller than the expected size of the pyrolysis layer ($\sim 1 \text{ cm}$). Furthermore, the mean free path of the molecules was estimated to be less than $1 \mu\text{m}$. Under these conditions, the molecules are not expected to remain parallel to the fibers. As was previously shown in Fig. 4.2, the fibers are expected to be aligned in a random manner. Because of this random structure, and the random motion of the molecules (due to Brownian collisions), a more advanced model would be required to more accurately estimate for the number of collisions between PAH molecules and fibers. Some work has been done investigating the microscopic structure of PICA through the use of numerical simulations [76], though this is outside the scope of this work.

It is interesting to note that the collision rate, Θ , is no longer a function of $n_{C_{24}H_{12}}$, but is constant because n^* is constant. If every collision between a PAH molecule and a carbon fiber were to result with the PAH molecule being deposited on the carbon fiber, then

$$\frac{dn_{PAH}}{dt} = -kn_{PAH}, \quad (4.9)$$

where k is once again a rate constant. Unlike Eq. 4.5, Eq. 4.9 is linear in $n_{C_{24}H_{12}}$, since only collisions between PAH molecules and fibers, and not collisions between PAH molecules and other

PAH molecules are being considered. Combing Eq. 4.8 and Eq. 4.9 gives

$$\frac{dn_{C_{24}H_{12}}}{dt} = -d_f \bar{C} n^* n_{C_{24}H_{12}}. \quad (4.10)$$

The solution to this ODE is

$$n_{C_{24}H_{12}}(t) = n_{C_{24}H_{12}}^0 e^{-d_f \bar{C} n^* t}, \quad (4.11)$$

where $n_{C_{24}H_{12}}^0 = n_{C_{24}H_{12}}(t = 0)$, the initial number of C₂₄H₁₂ molecules per unit volume. Evaluating Eq. 4.11 with $T = 1000$ K, $P = 50$ kPa, and $X_{C_{24}H_{12}} = 0.01$ or $X_{C_{24}H_{12}} = 0.1$, at $t = 0.001$ s, results in essentially none of the original PAH molecules remaining. Even if the right hand side of Eq. 4.9 is divided by 1000, and assuming $X_{C_{24}H_{12}} = 0.01$, Eq. 4.11 predicts that 99% of the PAH species will be removed at $t = 0.001$ s. This results is very similar to the PAH-PAH collision results; the carbon deposition prediction is relatively insensitive to the assumptions that went into the collision model. These calculations once again imply that it is likely that carbon deposition on the fibers will occur.

Primarily, it is challenging to estimate a sticking efficiency for what percentage of collisions between a coronene molecule and a fiber will remove a C₂₄H₁₂ molecule from the gas mixture. More work needs to be put into quantifying how much mass deposition will occur on the solid fibers due to heterogeneous reactions. In the future, it might be possible to experimentally measure a sticking efficiency for the PAH molecules and fibers, similar to what is done for soot formation. Even though it is hard to draw quantitative conclusions from this analysis, the results suggest that heterogeneous collisions will affect the overall evolution of the pyrolysis gas mixture.

4.6 Effect of Carbon Deposition

When the pyrolysis gas flows through a porous medium consisting of carbon fibers, the previous sections showed that a large number of PAH-PAH and PAH-fiber collisions are expected. Preliminary calculations also showed that soot formation, and surface deposition reactions are highly probable. Surface reactions will also likely be encouraged due to the relatively large size of the carbon fibers (μm), compared to the PAH molecules (\AA), and soot nuclei (nm). Heterogeneous reaction rates are still widely unknown, and previous works have only focused on oxidation reactions with respect to the fibers [119]. The potential for solid carbon deposition, through “soot” or PAH/fiber collisions, and the effect that this has on the pyrolysis gas mixture is a topic that has not received much attention previously. In order to determine whether or not solid carbon deposition on the fibers will

affect the bulk properties of the pyrolysis gas, the following models are proposed.

4.6.1 Model #1

To mimic the porous flow of increasing temperature towards the surface of the heat shield, we propose the following model, based on thermodynamic equilibrium calculations. At every temperature considered, any coronene present in the gaseous mixture is removed (due to the high number of collisions predicted in Sec. 4.5.3), and then the enthalpy of the remaining mixture is re-evaluated. The calculations are performed over a temperature range between 230°C and 1800°C. 1800°C is a good approximation of the temperature that the surface of a heat shield would experience during atmospheric entry.

This simple model assumes that any carbon predicted to be in a large PAH molecule is likely to form a solid carbon substance. This assumption accounts for gas-phase nucleation of soot particles, which are then deposited inside of the heatshield, as well as heterogeneous reactions between a PAH molecule and a carbon fiber that result in a PAH molecule “sticking” to a carbon fiber. A slight variant of this model is also proposed such that any hydrogen content from coronene is added back into the overall gaseous species composition. This accounts for the dehydrogenation effect previously mentioned [67, 148]. This method is referred to as Model #1, and is outlined by the following equations:

$$\mathbf{Y}^*(T, P) = \mathbf{Y}^{EQ}(T, P, \mathbf{Y}^\circ) \quad (4.12)$$

$$Y_{i \neq C_{24}H_{12}}^{M1}(T, P) = Y_i^*(T, P) \quad (4.13)$$

$$Y_{C_{24}H_{12}}^{M1}(T, P) = 0 \quad (4.14)$$

$$h^{M1}(T, P) = \sum_{i=1}^{ns} h_i(T) Y_i^{M1*}(T, P) \quad (4.15)$$

where the superscript $M1$ refers to Model #1, and Eq. 4.12 is a thermodynamic equilibrium calculation holding T and P constant, for a chosen constant initial elemental composition (\mathbf{Y}°) of the pyrolysis gas mixture. The mass fractions, \mathbf{Y}^{M1} , are normalized before Eq. 4.15 so that $\sum_{i=1}^{ns} Y_i^{M1*}(T, P) = 1$. P is held constant at 50 kPa, and T is varied. A slight variation to this

model where H is added back into the mixture is outlined by:

$$\mathbf{Y}^*(T, P) = \mathbf{Y}^{\text{EQ}}(T, P, \mathbf{Y}^\circ) \quad (4.16)$$

$$Y_{i \neq \text{C}_{24}\text{H}_{12}, i \neq \text{H}_2}^{M1H}(T, P) = Y_i^*(T, P) \quad (4.17)$$

$$Y_{\text{H}_2}^{M1H}(T, P) = Y_{\text{H}_2}^*(T, P) + 6 \frac{W_{\text{H}_2}}{W_{\text{C}_{24}\text{H}_{12}}} Y_{\text{C}_{24}\text{H}_{12}}^*(T, P) \quad (4.18)$$

$$Y_{\text{C}_{24}\text{H}_{12}}^{M1H}(T, P) = 0 \quad (4.19)$$

$$h^{M1H}(T, P) = \sum_{i=1}^{ns} h_i(T) Y_i^{M1H*}(T, P) \quad (4.20)$$

where the superscript $M1H$ refers to Model #1 - Add H, and Eq. 4.16 is once again a thermodynamic equilibrium calculation holding T and P constant, for a chosen initial elemental composition (\mathbf{Y}°) of the pyrolysis gas mixture. The mass fractions, \mathbf{Y}^{M1H} , are again normalized before Eq. 4.20, so that $\sum_{i=1}^{ns} Y_i^{M1H*}(T, P) = 1$. For both variants of Model #1, no changes in h^{M1} or h^{M1H} are observed if another thermodynamic equilibrium calculation is performed on the modified mixtures ($\mathbf{Y}^{\text{M1}*}$ and $\mathbf{Y}^{\text{M1H}*}$).

4.6.2 Model #2

Model #2 accounts for the fact that Model #1 does not consider the time history of the pyrolysis gas flowing through the porous layer. As the pyrolysis gas travels towards the surface of the heat shield, the local temperature increases, and carbon may be deposited at various locations in the heatshield. In order to take the flow history into account, a simple integration through the pyrolysis/char layer is performed using temperature as the integration variable. This approach once again assumes that the time scale associated with removing the carbon char from the flow is small compared to the time scale associated with the convection of the pyrolysis gases through the heatshield. This method is referred to as Model #2 ($M2$), and it is outlined by the following equations:

$$\mathbf{Y}^*(j) = \mathbf{Y}^{\text{EQ}}(T(j), P, \mathbf{Y}^{\text{M2}*}(j-1)) \quad (4.21)$$

$$Y_{i \neq \text{C}_{24}\text{H}_{12}}^{M2}(j) = Y_i^*(j) \quad (4.22)$$

$$Y_{\text{C}_{24}\text{H}_{12}}^{M2}(j) = 0 \quad (4.23)$$

$$h^{M2}(j) = \sum_{i=1}^{ns} h_i(T(j)) Y_i^{M2*}(j) \quad (4.24)$$

where Eq. 4.21 corresponds to a thermodynamic equilibrium calculation at the specified temperature and pressure, based on the elemental composition from the previous iteration. The mass fractions, $\mathbf{Y}^{\mathbf{M2}}(j)$, are normalized before Eq. 4.24 so that $\sum_{i=1}^{ns} Y_i^{M2*}(j) = 1$. j corresponds to the index of an array, where $j = 1, 2, \dots, 1000$. $\mathbf{Y}^{\mathbf{M2}*}(0)$, the initial condition, is defined to be the thermodynamic equilibrium composition at 230°C, 50 kPa, and a chosen composition of \mathbf{Y}° . As $\mathbf{Y}^{\mathbf{M2}}(j)$ is now a function of $\mathbf{Y}^{\mathbf{M2}}(j - 1)$, any carbon that is removed from the mixture at lower temperatures is no longer present in the mixture at higher temperatures. A temperature array is defined to be $T(j) = 230^\circ\text{C} + j \cdot 1.57^\circ\text{C}$, in order to use 1000 points through the desired temperature range. A large number of temperature iterations are used in order to mimic thermodynamic quasi-equilibrium throughout the heat shield. Increasing the number of points used had no effect on the resulting enthalpy calculations.

Again, a slight variant of this model is also proposed ($M2H$) such that any hydrogen content from coronene is added back into the overall gaseous species composition, and is outlined by:

$$\mathbf{Y}^*(j) = \mathbf{Y}^{\mathbf{EQ}}(T(j), P, \mathbf{Y}^{\mathbf{M2H}*}(j - 1)) \quad (4.25)$$

$$Y_{i \neq \text{C}_{24}\text{H}_{12}, \neq \text{H}_2}^{M2H}(j) = Y_i^*(j) \quad (4.26)$$

$$Y_{\text{H}_2}^{M2H}(j) = Y_{\text{H}_2}^*(j) + 6 \frac{W_{\text{H}_2}}{W_{\text{C}_{24}\text{H}_{12}}} Y_{\text{C}_{24}\text{H}_{12}}^*(j) \quad (4.27)$$

$$Y_{\text{C}_{24}\text{H}_{12}}^{M2H}(j) = 0 \quad (4.28)$$

$$h^{M2H}(j) = \sum_{i=1}^{ns} h_i(T(j)) Y_i^{M2H*}(j), \quad (4.29)$$

where Eq. 4.25 corresponds to a thermodynamic equilibrium calculation at the specified temperature and pressure, based on the elemental composition from the previous iteration. The mass fractions, $\mathbf{Y}^{\mathbf{M2H}}(j)$, are again normalized before Eq. 4.29 so that $\sum_{i=1}^{ns} Y_i^{M2H*}(j) = 1$

4.6.3 Results

The enthalpy of the mixtures are plotted in Fig. 4.14, Fig. 4.15 and Fig. 4.16, for original elemental compositions (\mathbf{Y}°) of 0%, 35%, and 60% char yield, respectively. The enthalpy of the mixture calculated with a standard thermodynamic equilibrium calculation at constant temperature and pressure (no removal of carbon) is also shown.

As expected, a larger discrepancy is seen between the carbon deposition models and the thermodynamic equilibrium calculations for the compositions that initially include more carbon (0% char

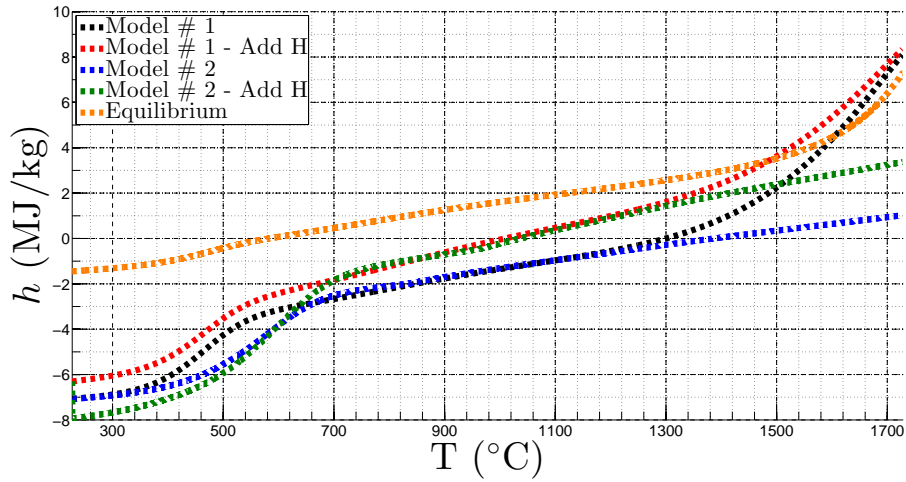


Figure 4.14: Enthalpy comparison using different models to account for solid char deposition. The original elemental composition corresponds to a 0% char yield.

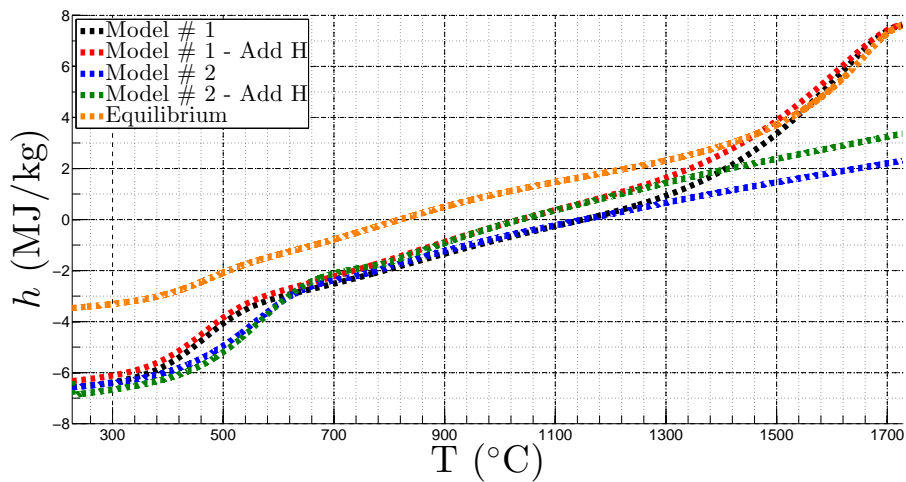


Figure 4.15: Enthalpy comparison using different models to account for solid char deposition. The original elemental composition corresponds to a 35% char yield.

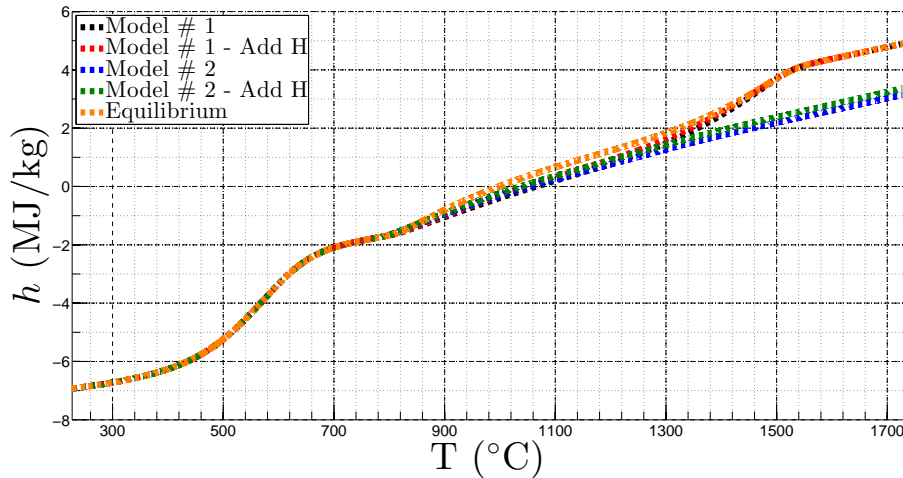


Figure 4.16: Enthalpy comparison using different models to account for solid char deposition. The original elemental composition corresponds to a 60% char yield.

yield). This is because the high carbon content in these mixtures favors the formation of coronene. The main discrepancy between Model # 1 and Model # 2 is seen at higher temperatures. This is due to the constant removal of carbon from the mixture as the temperature is increased for Model #2. Once a significant quantity of carbon is removed from the gas mixture, the formation of PAH molecules is no longer encouraged, and a relatively linear increase in enthalpy is seen as temperature increases. This is attributed to a relatively constant c_p value in this temperature range. These plots indicate that for regions in the pyrolysis layer where there is a high concentration of carbon present in the gaseous phase, solid carbon deposition will greatly influence the enthalpy of the mixture. Finally, the differences between Model #1 and Model #2 at higher temperatures indicate that taking into account the history of the pyrolysis gas flow is important. Where soot formation, or solid carbon deposition occurs in the heat shield will effect where the elemental composition of the pyrolysis gas changes. The species composition and elemental composition of the pyrolysis gas will continue to change as the gas flows from the pyrolysis layer, through the char layer, and into the boundary layer, and should be accounted for in material response models.

4.7 Analysis of Experimental Results

All of the previous sections have quantitatively shown the effect that different modeling assumptions (*i.e.*, equilibrium *vs.* finite-rate kinetics) have on the pyrolysis gas mixture. In order to investigate the validity of some the assumptions previously made, a detailed analysis of available experimental data is performed in order to determine whether or not experimentally measured pyrolysis gases are

in a state of thermodynamic equilibrium, and to investigate the range of elemental compositions observed in previous studies.

In 1967, Sykes [162] produced the first detailed report in the aerospace community on the composition of the pyrolysis gases produced by the thermal decomposition of a phenolic resin. A commercially available novolac-type resin (Union Carbide Corporation - BRP 5549) premixed with hexamethylenetetramine was used in this study. The resin was cured, and ~ 7 mg samples were tested. These specimens were placed in a pyrolyzer attached to a gas chromatograph [113]. The samples were heated to a desired temperature for 10 seconds, and then the temperature was quenched. Temperatures from 100°C to 1000°C were analyzed at 50°C intervals. A detailed explanation of the experimental set-up can be found in [160].

The experimental data collected by Sykes [162] are shown in Fig. 4.17 and are compared to equilibrium calculations with the same H:C:O composition. The elemental composition of the pyrolysis gas measured by Sykes [162] varies at each temperature (Table 4.3), and was used in the equilibrium calculations shown in Fig. 4.17. The gas mixture contains the same 55 species used throughout this chapter, and includes additional species measured by Sykes (toluene - C₇H₈, phenol - C₆H₅OH and xylenol - (CH₃)₂C₆H₃OH). References for the thermodynamic data for the added species can be found in Appendix D. Results comparing the experimental measurements and numerical calculations are shown in Fig. 4.17. It is clear that the experimentally-measured gas mixture is not in thermodynamic equilibrium, and the greatest relative discrepancy is seen in the amount of C₇H₈, C₆H₅OH and (CH₃)₂C₆H₃OH present around 500°C. At 500°C and 550°C, the equilibrium calculations predict $X_{C_{24}H_{12}} \approx 0.04$ and $X_{C_{24}H_{12}} \approx 0.02$ at the two temperatures, respectively. This corresponds to $Y_{C_{24}H_{12}} \approx 0.4$ at 500°C and $Y_{C_{24}H_{12}} \approx 0.2$ at 550°C. Again, the species with the largest C/H ratio is favored from a thermodynamic standpoint. As discussed in Sec. 4.4.1.5, at these relatively low temperatures, not accounting for gas condensation/solidification may effect the thermodynamic equilibrium calculations performed.

Under these experimental conditions, the kinetics of the decomposition of the resin, specifically the finite time needed for the observed large hydrocarbon molecules to break down, plays a large role in accurately predicting the composition of the pyrolysis gases. In summary, an equilibrium assumption does not accurately predict the composition of the gas mixture (Fig. 4.17).

Trick *et al.* [169] performed a similar experiment to Sykes [162], except that a composite material (fibers and resin) was used, unlike the neat resin analyzed previously. A Fiberite Inc. commercially available carbon phenolic composite material was used, designated SC1008/T300. This material has

Table 4.3: Calculated elemental composition of measured pyrolysis gases over a large temperature range measured by Sykes [162].

Temperature (°C)	C (molar)	H (molar)	O (molar)
100	0.000	0.667	0.333
150	0.000	0.667	0.333
200	0.000	0.667	0.333
250	0.000	0.667	0.333
300	0.000	0.667	0.333
350	0.000	0.667	0.333
400	0.202	0.586	0.212
450	0.211	0.594	0.195
500	0.368	0.534	0.098
550	0.319	0.573	0.108
600	0.273	0.644	0.083
650	0.225	0.690	0.085
700	0.164	0.769	0.067
750	0.103	0.849	0.048
800	0.044	0.929	0.027
850	0.030	0.954	0.015
900	0.009	0.991	0.000
950	0.000	1.00	0.000
1000	0.000	1.00	0.000

Amoco heat-treated T300 carbon fibers impregnated with a resole resin [170]. The samples were pyrolyzed in a thermogravimetric balance, and a constant heating rate of 1°C/min was used. Fourier transform infrared spectroscopy (FTIR) was used to analyze the experiments. These measurements were combined with pyrolysis gas composition measurements performed in other studies [74, 118], and this data has been converted to elemental mole fractions in Table 4.4. The experiments did not distinguish between phenol C₆H₆O and cresol (C₇H₈O, and referred to the combination of the two as “low molecular weight substances (LMS)”. They also provided different compositions over three different characteristic temperature ranges. In Table 4.4, the first two lines represent the same experimental measurement, with the first line assuming that all of the LMS observed can be attributed to phenol, and the second line assumes that all of the LMS observed can be attributed to cresol. The results are similar for each assumption, and bound the possible composition range. The results show a large change in the elemental composition of the pyrolysis gases over the different temperature ranges (consistent with the results from Sykes [162]).

Combining the previous experimental data for the elemental composition of the pyrolysis gases produced from a phenolic resin, over a large range of temperatures, results in a large range of values, as shown in Fig. 4.18. This plot contains values for temperatures above 300°C so that the results are not affected by the resin cure time [162]. The shading for Trick *et al.*’s [170] data at low temperatures represents the range previously described due to measuring a combined fraction of cresol and phenol.

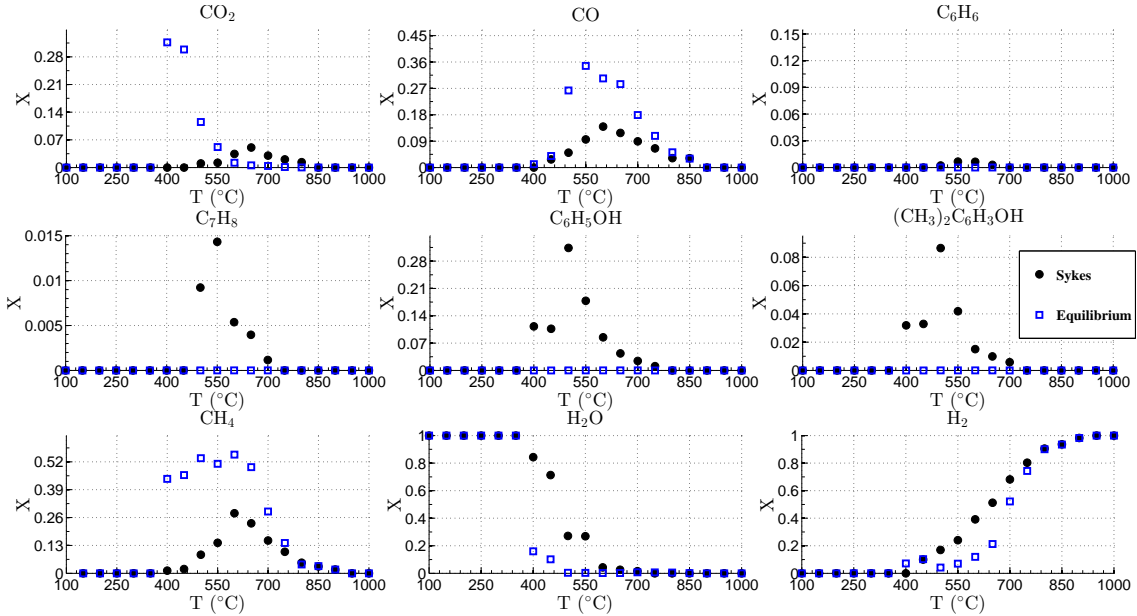


Figure 4.17: Experimental data reported in Table 1 of [162] compared to thermodynamic equilibrium calculations.

Table 4.4: Calculated molar elemental composition of the pyrolysis gases reported by Trick *et al.* (Table 2 in [169]).

Temperature Range (°C)	C (molar)	H (molar)	O (molar)
300-550 (100% Phenol)	0.400	0.466	0.133
300-550 (100% Cresol)	0.389	0.500	0.111
400-800	0.108	0.792	0.010
560-900	0.071	0.788	0.141

It is hard to quantitatively estimate the error associated with the experimental measurements, as there is a contribution both from experimental error, and errors associated with not all mass of gaseous species being accounted for. Ongoing work by Wong *et al.* [182] should rectify potential conservation of mass issues. In addition, as outlined in Sec. 4.3.3, a range of char compositions has been observed experimentally. Figure 4.18 shows that the constant gas compositions used in previous numerical studies represents a simple average composition over a large temperature range. As shown in the previous sections, this over-simplification of the pyrolysis gas elemental composition has significant effects on the pyrolysis gas composition and properties.

When comparing data reported by Trick *et al.* [170] to the data reported by Sykes [162], the effect of measuring gas species over a large temperature range must be accounted for. The data reported by Trick *et al.* [170] represents an integration of the pyrolysis gas products over a temperature range. However, neither the elemental composition nor the volume of pyrolysis gas evolved is constant with temperature. For proper comparison, the data set reported by Sykes [162] must be integrated over

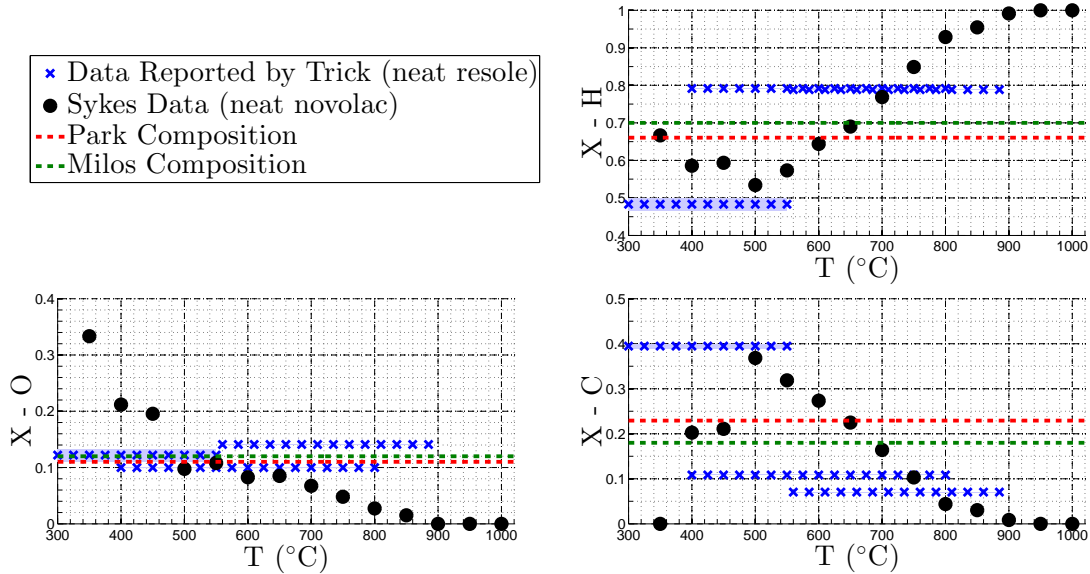


Figure 4.18: Comparison of pyrolysis gas elemental compositions from experimental studies and computational studies. Shaded areas represent the range in Trick *et al.*'s [170] data from the phenol/cresol combination. Values taken from Milos and Chen [108] are approximate, as the original composition also includes some N and Si. Values taken from Park *et. al.* [122] correspond to a pyrolysis gas mixture for a PICA heatshield (Fig. 1.4).

temperature in a manner similar to the data set reported by Trick *et al.* [170]. Figure 4.19 shows the resulting comparison with Sykes' [162] data. Discrepancies are still observed between the two studies, and further experimental investigations are required to describe the observed differences.

4.8 Constrained Equilibrium Calculations

While the pyrolysis gas mixture measured by Sykes [162] is not in thermodynamic equilibrium (as shown in Sec. 4.7), intuition gained from Chapter 3 suggests that it may still be possible for the pyrolysis gases to be in a state of constrained thermodynamic equilibrium. This section is geared towards investigating the feasibility of using constrained equilibrium calculations to represent the pyrolysis gas mixture.

Again, all constrained equilibrium calculations are performed using the CEQ program using mass fractions, and include 58 species (55 species model + 3 additional species measured experimentally by Sykes [162]) [129, 132]. Many constraints were experimented with, including general linear constraints (summation of mass fractions of multiple species) and individual species constraints. As is shown in Fig. 4.20, it was found that the experimental data could be well represented if individual species constraints were put on CO_2 , C_7H_8 , $\text{C}_6\text{H}_5\text{OH}$ and $(\text{CH}_3)_2\text{C}_6\text{H}_3\text{OH}$.

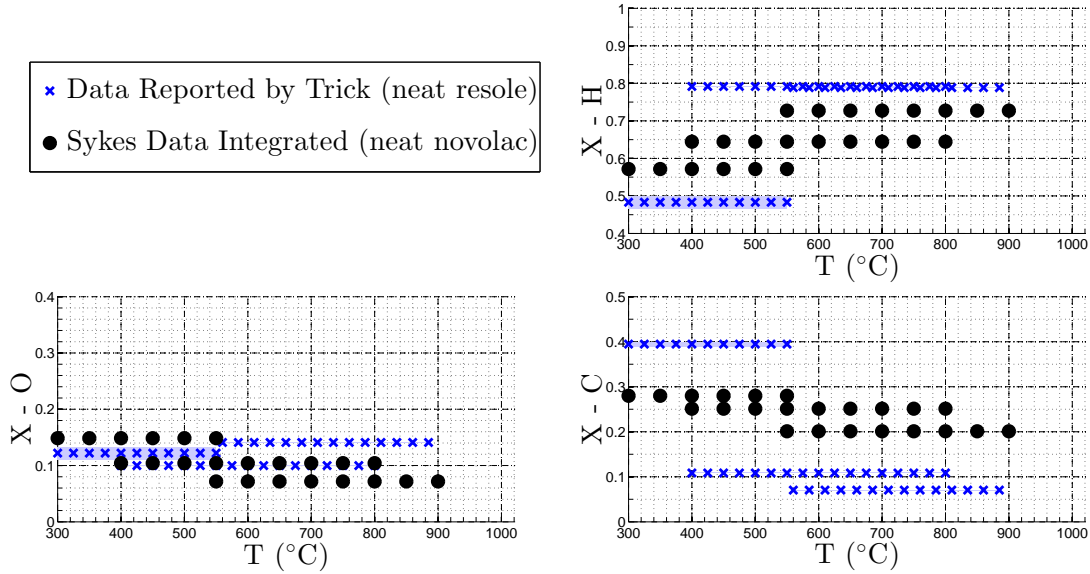


Figure 4.19: Comparison of pyrolysis gas elemental composition from the work of Trick *et al.* [170] and Sykes [162]. Shaded areas represent the range in Trick *et al.*'s [170] data from the phenol/cresol combination. Data from Sykes has been integrated over the temperature ranges that Trick reports.

From Fig. 4.20 several conclusions can be drawn. While the measured gases are not in thermodynamic equilibrium at each temperature, the mixture composition is well-represented by a constrained equilibrium calculation. The aromatic species measured are only present in a temperature range from ~ 400 °C to ~ 700 °C. Above this temperature, these species are no longer pyrolysis gas products. Below this temperature these species have not yet been formed (*i.e.* they have not yet been liberated from the resin). A more detailed explanation of the resin decomposition is given in Sec. C.2. C_7H_8 , C_6H_5OH and $(CH_3)_2C_6H_3OH$ represent direct products from the decomposition of the resin, and this is why they are observed experimentally.

A comparison of mass specific mixture enthalpy is shown in Fig. 4.21 for the three different gas compositions discussed (Sykes' [162] data, an equilibrium mixture, and a constrained equilibrium mixture). While the mixture composition changes drastically, the calculated enthalpies are still surprisingly similar. The largest (albeit small) discrepancies are observed when there is a strong concentration of aromatic species (mid-temperature range). These results are consistent with the computational results previously shown in Fig. 4.7. This figure shows that for temperatures between ~ 500 °C and ~ 800 °C, the mixture enthalpy is fairly independent of the gas species model used; but it is largely dependent on the elemental composition of the gas considered. This is the same effect that is shown in Fig. 4.21. For temperatures ~ 500 °C, the equilibrium calculations do not predict the mixture composition well, but the enthalpy is well re-produced. At higher temperatures, the

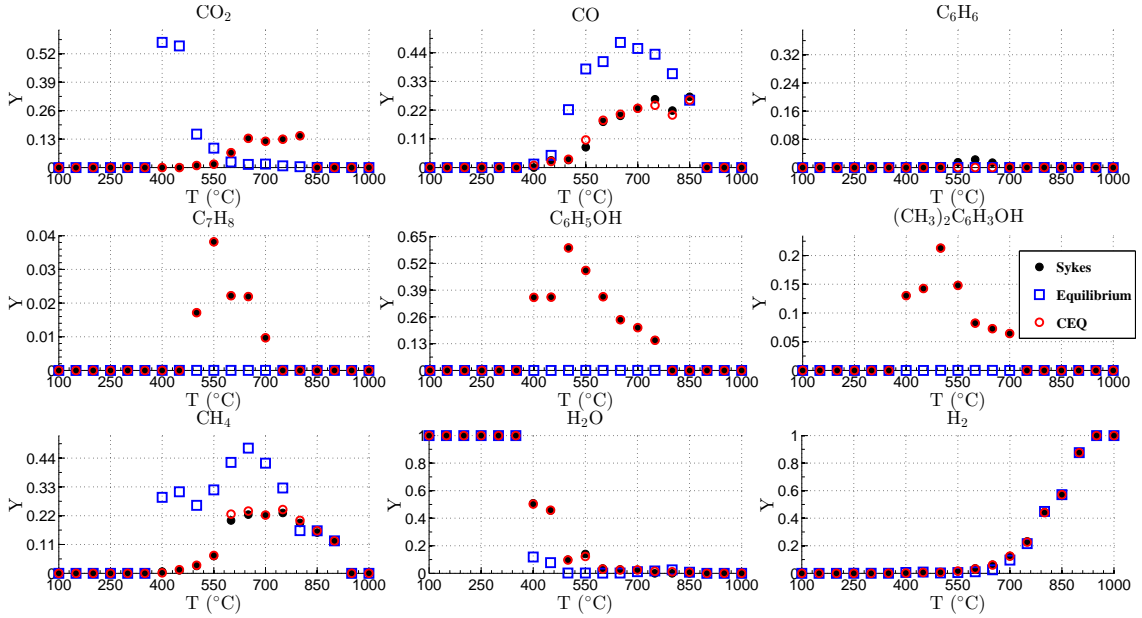


Figure 4.20: Experimental data reported in Table 1 in [162], converted to mass fractions, and compared to constrained equilibrium calculations.

mixture composition measured by Sykes [162] is mainly hydrogen, so it is not surprising that the mixture compositions and enthalpies are matched in this regime.

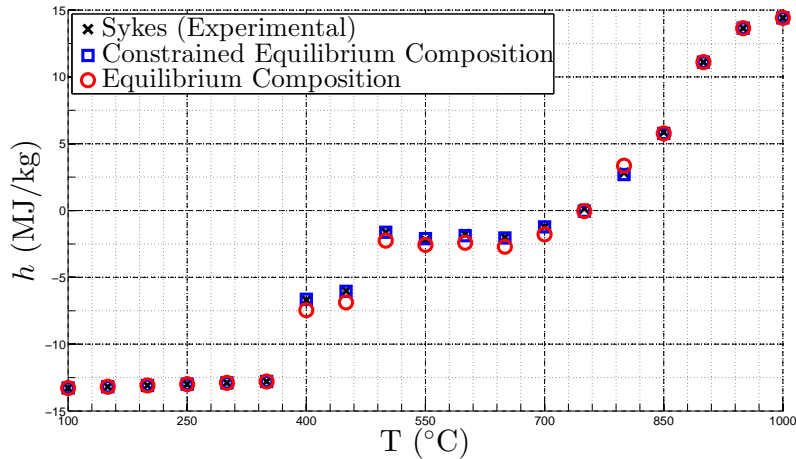


Figure 4.21: Comparison of mixture enthalpies based on experimental data reported in Table 1 in [162].

The same constrained thermodynamic equilibrium method is applied to the more complicated mixture described in Sec. 4.4.2. Due to the large number of species present, the constraint previously used on enthalpy of formation (Chapter 3) does not perform well. Constraints placed on individual species perform better, and two sample plots showing the mixture reconstruction are shown

in Fig. 4.22 and Fig. 4.23. A constraint is always placed on phenol (A_1OH), as the simulations performed in Sec. 4.4.2 assumed an initial composition of 100% phenol. The kinetic decomposition of phenol therefore plays a very important role in the evolution of the gas mixture, and is a logical choice for a species constraint. In addition, due to the important role that PAH molecules play in pyrolysis gas mixtures, constraints are also placed on the PAH species present. As illustrated in Fig. 4.22 and Fig. 4.23, when more constraints are used, the mixture composition is more accurately represented. The order of species constrained is: A_1OH , A_1C_2H , A_1 , A_2R5 , A_2C_2HB , A_2R5C_2H , A_2 , and $FLTN$, which is based on the predicted mass fractions present of these species at $t = 1000 \mu s$. In Fig. 4.22, Fig. 4.23, and Fig. 4.24, the molecule CO is reconstructed accurately, even though it is not a constrained species. This is important as it has been previously identified as a strong radiator (Sec. 4.2).

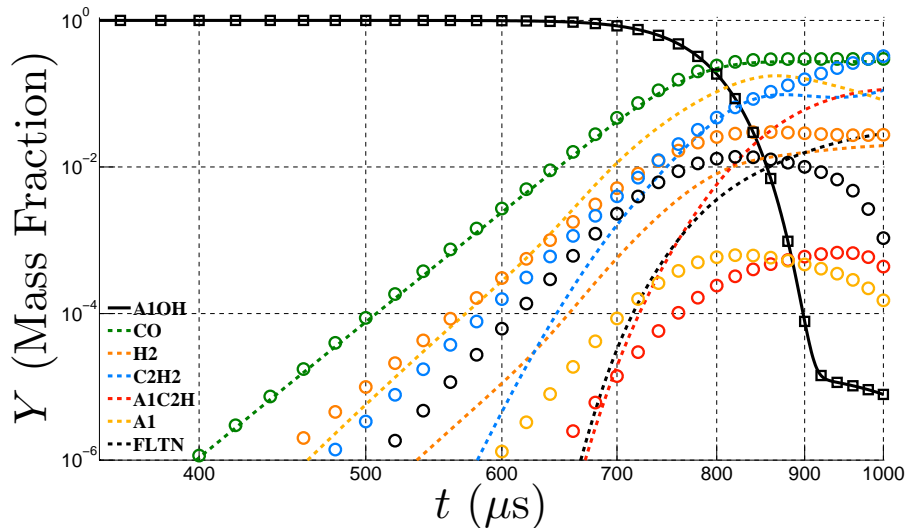


Figure 4.22: Comparison of mixture composition for finite-rate chemistry results and constrained equilibrium calculations constraining on A_1OH . Lines represent finite-rate chemistry results, and symbols represent constrained equilibrium calculations. $T = 230^\circ C + 1.57^\circ C \cdot t$, where T is in $^\circ C$, and t is in μs . $P = 50$ kPa.

Alternatively, a sum of the mass fractions of A_1C_2H , A_1 , A_2R5 , A_2C_2HB , A_2R5C_2H , A_2 , and $FLTN$, is used as a constraint, in conjunction with a species constraint placed on A_1OH . These results are shown in Fig. 4.24. While visually it appears as this constraint does not do a good job at representing the mixture composition, the enthalpy plot shown in Fig. 4.25 illustrates how the mass specific enthalpy of the mixture is well-represented with this constraint. Unsurprisingly, as this idealized mixture starts entirely as phenol, Fig. 4.25 shows that a large benefit is initially gained by constraining the mass fraction of phenol. At times $\gtrsim 700 \mu s$, when significant amounts of the original

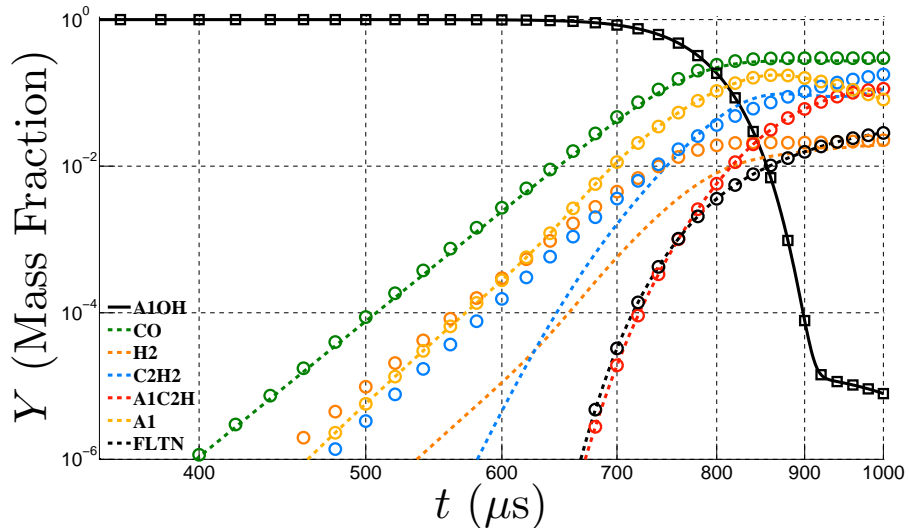


Figure 4.23: Comparison of mixture composition for finite-rate chemistry results and constrained equilibrium calculations constraining on 8 species. Lines represent finite-rate chemistry results, and symbols represent constrained equilibrium calculations. $T = 230^\circ\text{C} + 1.57^\circ\text{C} \cdot t$, where T is in $^\circ\text{C}$, and t is in μs . $P = 50$ kPa.

phenol start to react, discrepancies are seen between the different constraint selections. In general, the more constraints that are used, the closer the enthalpy is to that of the mixture calculated using finite-rate kinetics. However, the constraint based on the sum of the aforementioned PAH species, while over predicting the concentration of the largest PAH species included (FLTN, Fig. 4.24), the enthalpy of the mixture is better represented than constraining on 7 other species individually. This highlights the importance of PAH species in these types of gas mixtures, and shows that choosing the appropriate constraint when performing constrained equilibrium calculations can yield significant benefits.

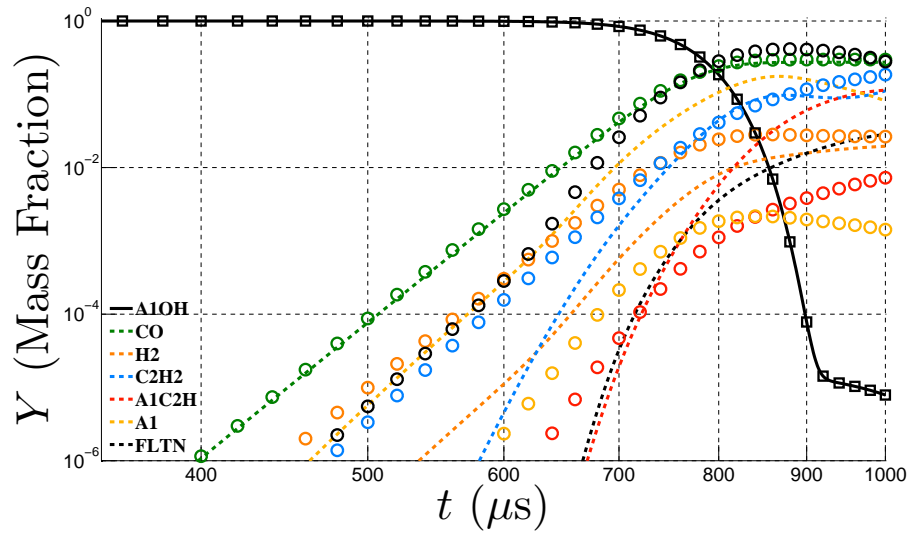


Figure 4.24: Comparison of mixture composition for finite-rate chemistry results and constrained equilibrium calculations constraining on AlOH and the summation of mass fractions of A_1C_2H , A_1 , A_2R5 , A_2C_2HB , A_2R5C_2H , A_2 , and FLTN. Lines represent finite-rate chemistry results, and symbols represent constrained equilibrium calculations. $T = 230^\circ\text{C} + 1.57^\circ\text{C} \cdot t$, where T is in $^\circ\text{C}$, and t is in μs . $P = 50 \text{ kPa}$.

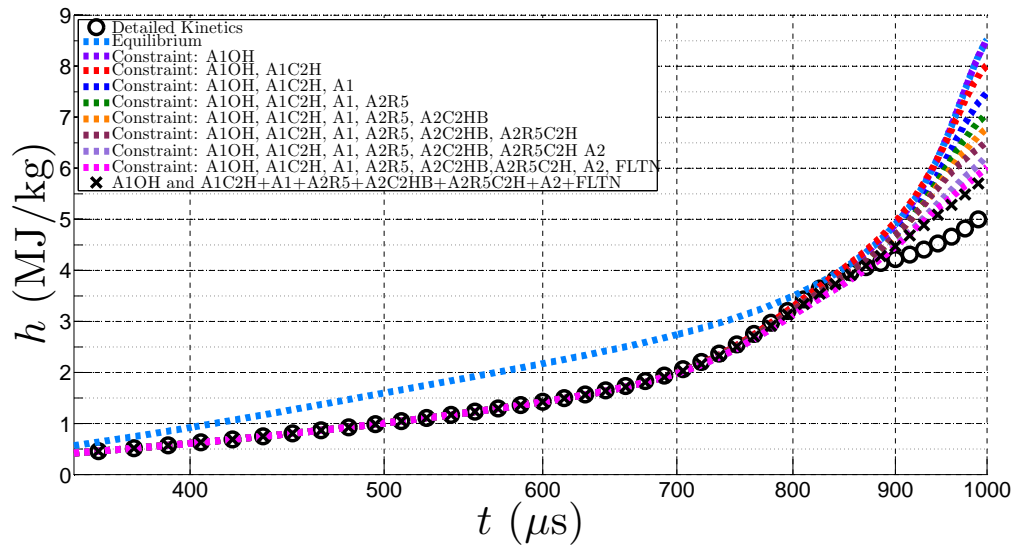


Figure 4.25: Evolution of mixture enthalpy for the different gas mixtures calculated through constrained equilibrium calculations. $T = 230^\circ\text{C} + 1.57^\circ\text{C} \cdot t$, where T is in $^\circ\text{C}$, and t is in μs . $P = 50 \text{ kPa}$.

4.9 Summary and Discussion

Current kinetic models are not advanced enough to capture all aspects of the phenolic resin decomposition, including phase transition from solid to gaseous species, decomposition products, heterogeneous reactions, soot formation, etc. On a more basic level, despite the continued investigation of the decomposition of phenol (which is a major component of the resin), there is still a debate about the primary mechanism for this decomposition, and the primary products that are created [23, 31, 73, 89, 95, 147, 151, 184, 185]. A review of previous work on phenol decomposition can be found in [151], which illustrates a long debate over the primary reaction involved in the thermal decomposition of phenol. Due to the complicated nature of this system, it is clear that reduced “engineering” models are needed for design purposes.

Based on the detailed investigation performed in this chapter, it is now possible to create a fuller, more consistent description of many of the physical phenomena, and their implications, occurring in an ablative heatshield.

- The solid constituents of phenolic resin are known (see Sec. 4.3.2 and Appendix C). Any minor variations in resin composition, possibly due to cross-linking density or impurities, will not be a leading source of error for modeling efforts. An elemental composition of C:H:O = 0.500:0.429:0.071 by mole is believed to be a good choice for the resin composition.
- A mass-loss model used to determine the mass and composition of pyrolysis gas produced [78] currently appears (in the author’s opinion) to be the most viable method to approach the initial decomposition of the solid resin, *i.e.*, solid→gas phase transformation. The model is consistent with charring; not all of the solid resin undergoes a phase transformation, and some mass remains behind as char.
- The mass-loss model [78] does *not* assume that the pyrolysis gases produced have a constant elemental composition over time and temperature. The model was derived to be consistent with experimentally observed pyrolysis gas products (see Sec. 4.7). The temperature varies as a function of depth in the heatshield; therefore different pyrolysis products will be produced at different depths in the heatshield.
- The gaseous pyrolysis products must now be modeled. To predict the correct species composition of the gas mixture initially formed from the resin decomposition, constrained equilibrium calculations can be used. Constraints should be placed on the large aromatic species that are the direct products of the decomposition of the resin (Fig 4.20).

- As the pyrolysis gases continue to evolve, *if* the correct elemental composition is used for $500^{\circ}\text{C} \lesssim T \lesssim 800^{\circ}\text{C}$, the mass specific enthalpy of the mixture can be well represented (Fig. 4.7 and Fig. 4.21) by a thermodynamic equilibrium calculation. For $T \gtrsim 1200^{\circ}\text{C}$, the mass specific mixture enthalpy depends largely on the gas model used (Fig. 4.7). For a gas model to be accurate over a large range of temperatures, *both* the mixture elemental composition must be known, and an accurate gas species model must be used that includes PAH species (Fig. 4.4 and Fig. 4.6).
- The formation of PAH species at higher temperatures through gas phase reactions is supported both by thermodynamic equilibrium calculations (Fig. 4.4 and Fig. 4.6) *and* calculations based on finite-rate kinetics (Fig. 4.9).
- Once the PAH species are formed, they are expected to be deposited on the fibers; particle growth through vapor phase nucleation (see Sec. 4.5.2) and heterogeneous reactions with the carbon fibers (see Sec. 4.5.3) will remove carbon from the gas mixture.
- This solid carbon deposition changes the elemental composition (C:H:O) ratio of the gas mixture, therefore changing the bulk properties of the gas mixture (Fig. 4.14, Fig. 4.15, and Fig. 4.16).
- Due to the slow time scales involved with PAH formation, a thermodynamic equilibrium approach *should not* be used (Fig. 4.9 and Fig. 4.10).
- Preliminary constrained equilibrium calculations show that with an intelligent choice of constraint based on PAH species, the mixture properties can be well approximated *if* the slow time scale associated with PAH formation were to be known (Fig. 4.25).

Further experiments and investigations are still needed to accurately measure/simulate the evolution of PAH species in conditions relevant to pyrolysis in ablative heatshields. Once these time scale are known with more certainty, it will be possible to model the pyrolysis gas mixture with more accuracy. In addition, the effects of diffusion have been neglected in this work. Mass diffusion will likely play a role internal to the heatshield itself, and near the surface of the heatshield in the char layer. Near the surface of the heatshield it is possible for atmospheric gas from the boundary layer to diffuse into the char layer. Some authors have investigated this effect [76], though this is still an open research topic. In addition, species diffusion will occur inside of pyrolysis layer, when porous flow is occurring. State of the art computations [78] have not been able to account for species diffusion with detailed kinetic models, and this is also a topic for future work.

Chapter 5

Conclusions and Future Work

Guided by the NASA Space Technology Roadmaps and Priorities report, and motivated by recent MSL flight data, this work has contributed to the advancement of EDL technologies for future space missions. Through the use of computational fluid mechanics and computational chemistry methods, significant contributions have been made to advancing ground testing facilities, computational methods for reacting flows, and ablation modeling. These contributions will help further entry, descent and landing technologies for future space missions, and will allow more advanced and ambitious missions to take place in the future.

5.1 Vertical Expansion Tunnel

Due to the difficulties in performing flight tests in the hypervelocity regime, a new ground testing facility called the vertical expansion tunnel was proposed. The adverse effects from secondary diaphragm rupture in an expansion tunnel may be reduced or eliminated by orienting the tunnel vertically, matching the test gas pressure and the accelerator gas pressure, and initially separating the test gas from the accelerator gas by density stratification. Two benefits are: 1) the removal of the diaphragm particulates in the test gas after its rupture and 2) the elimination of the wave system that is a result of a real secondary diaphragm having a finite mass and thickness. An inviscid perfect-gas analysis and quasi-1D Euler computations were performed to find the available reservoir conditions (pressure and mass specific enthalpy), and the useful test time in a VET. The VET was compared to a conventional expansion tunnel and a reflected shock tunnel. The maximum reservoir conditions of the VET were found to be higher than the RST, but lower than the ET. The useful test time in the VET is slightly longer than the ET, but shorter than the RST. If some sacrifice of the reservoir conditions could be made, the VET could be utilized in hypervelocity ground testing, without the problems associated with secondary diaphragm rupture.

To validate the VET concept, a bench top facility should be constructed. This will allow the

efficacy of the proposed design to be investigated experimentally. All sizing calculations performed in Chapter 2 were specifically geared towards facilitating the construction a small prototype facility. Additional design possibilities include constructing a facility with a variable location for the secondary diaphragm. If the intermediate and accelerator lengths can be varied for a standard ET, or a VET, test times can be optimized for a variety of fill conditions. If the VET design were to be validated for a bench-top size facility experimentally, additional theoretical and numerical calculations could be performed to evaluate the possibility to extend the VET concept to even higher enthalpies; for example, the feasibility of a free-piston driven VET could be investigated.

5.2 Rate-Controlled Constrained-Equilibrium

A fundamental investigation into the performance of different constraints for the Rate-Controlled Constrained-Equilibrium method was performed for reacting supersonic flows. Simple gas mixtures were used, and the effectiveness of different constraints was isolated by performing a point-wise comparison to detailed chemistry results. Formal time scale analysis techniques were combined with RCCE in order to determine possible new constraints. However, due to subjectivity involved with the numerical implementation of these constraints, and an inconsistent performance across simulations that involved both shocks and expansions, a new constraint based on the enthalpy of formation was proposed. This constraint worked well for both the nozzle and shock test cases used, though small errors in mass fractions were seen for both test cases. In addition, this constraint worked well both for the air mixture considered, and for a gas mixture consisting primarily of CO₂ (which is characteristic of the Martian atmosphere). Detailed analyses were performed in order to predict the performance of a specific constraint when used in a fully integrated RCCE simulation. The predictions matched well with the results of the RCCE simulations. Three main benefits from the RCCE method were determined: 1) the reduction in number of equations that need to be solved to model a reacting flow; 2) the reduction in stiffness of the system of equations needed to be solved; and 3) the ability to tabulate chemical properties as a function of a constraint once, prior to running a simulation, along with the ability to use the same table for multiple simulations.

Future work related to the RCCE method could be to extend this method to other atmospheres relevant to potential future NASA missions. For example, the atmosphere of Titan (the largest moon of Saturn), consists primarily of nitrogen, with some methane content as well. This chemical mixture would require a much larger mechanism than the ones used in this thesis for air and CO₂. While the potential for computational savings is much higher with this more complicated system, it

is unclear as to how many constraints would be needed to model a system like the Titan atmosphere.

5.3 Pyrolysis Gas Composition in PICA Heatshields

The final chapter of this work performed a detailed investigation into the pyrolysis gases produced by a PICA heatshield. Published physical properties of PICA were compiled, and the fundamental processes that go into phenolic resin synthesis were explained, providing a needed link between the physical properties of solid PICA, and the pyrolysis gases that are created when PICA starts to undergo a thermal decomposition. The implications of including or excluding certain species in the gas model were illustrated, and an emphasis was specifically placed on the need to include PAH species in the gas mixture. The effect of solid carbon deposition, a phenomena associated with the presence of PAH species, was predicted to have an effect on the elemental composition of the gas mixture, and on the bulk properties of the mixture. The kinetic evolution of the pyrolysis gas mixture was also investigated, and the assumption of thermodynamic equilibrium *vs.* finite-rate kinetics was evaluated. In order to model the pyrolysis gas mixture in a consistent and accurate way, an equilibrium approach is inadequate, and a method to account for the finite time scale associated with PAH formation should be used. Constrained equilibrium calculations were shown to reproduce the mass specific mixture enthalpy of the pyrolysis gases well, if a time scale associated with PAH formation were to be known.

Future work should focus on two of the unknowns identified in this work; the rate of solid carbon deposition, and a timescale associated with PAH formation under conditions relevant to pyrolysis. Once an accurate timescale for PAH formation can be determined, combined with the RCCE method, it is believed that an engineering model could be developed to accurately track the kinetic evolution of the pyrolysis gases inside of the heatshield. Additionally, experimentally quantifying the effects of solid carbon deposition could validate the previously proposed sooting and collision models accounting for this effect. Finally, effect of mass diffusion inside of the heatshield could be investigated in the future as well.

The detailed investigation into reacting pyrolysis gas mixture in Chapter 4 allowed consistent, and more detailed description of many of the physical phenomena occurring in a PICA heatshield, and their implications, to be created. Knowing that Fig. 1.4 is an oversimplification of the problem, we now have a better understanding of the problem at hand, and have advanced modeling techniques for ablative heatshields.

Bibliography

- [1] Caltech News December 1986. http://caltechcampuspubs.library.caltech.edu/2419/1/1986_12_20_06.pdf [retrieved 21 April 2014]. 2
- [2] Mars Exploration Rover Landings (Press Kit January 2004). <http://marsrovers.jpl.nasa.gov/newsroom/merlandings.pdf> [retrieved 21 April 2014]. 3
- [3] Mars Pathfinder Landing (Press Kit July 1997). <http://www2.jpl.nasa.gov/files//misc/mpfland.pdf> [retrieved 21 April 2014]. 3
- [4] Mars Science Laboratory Landing (Press Kit July 2012). <http://mars.jpl.nasa.gov/msl/news/pdfs/MSLLanding.pdf> [retrieved 21 April 2014]. 3, 4
- [5] Phoenix Landing (Press Kit May 2008). http://www.jpl.nasa.gov/news/press_kits/phoenix-landing.pdf [retrieved 21 April 2014]. 3
- [6] Viking (February 1975). <http://mars.jpl.nasa.gov/mro/newsroom/presskits/viking.pdf> [retrieved 21 April 2014]. 3
- [7] R. Abgrall and S. Karni. Computations of compressible multifluids. *Journal of Computational Physics*, 169(2):594–623, 2001. 25
- [8] H. K. Ahn, C. Park, and K. Sawada. Dynamics of pyrolysis gas in charring materials ablation. In *36th AIAA Aerospace Sciences Meeting and Exhibit*. AIAA, 1998. 111, 119, 124
- [9] M. H. Anderson, B. P. Puranik, J. G. Oakley, P. W. Brooks, and R. Bonazza. Shock tube investigation of hydrodynamic issues related to inertial confinement fusion. *Shock Waves*, 10(5):377–387, 2000. 36
- [10] R. J. Bakos and R. G. Morgan. Chemical recombination in an expansion tube. *AIAA Journal*, 32(6):1316–1319, 1994. 15

- [11] S. P. M. Bane, J. L. Ziegler, and J. E. Shepherd. Development of one-step chemistry models for flame and ignition simulation. GALCIT Report GALCITFM:2010.002, 2010. [10](#)
- [12] B. Barros-Fernandez, J. B. Scoggins, J. Rabinovitch, G. Blanquart, A. Martin, , R. L. Jaffe, N. N. Mansour, and T. Magin. Thermodynamic properties in equilibrium composition of carbon phenolic mixtures. *In Preparation.* [112](#), [182](#), [183](#)
- [13] A. Ben-Yakar and R. K. Hanson. Characterization of expansion tube flows for hypervelocity combustion studies. *Journal of Propulsion and Power*, 18(4):943–952, 2002. [7](#), [15](#), [35](#)
- [14] G. P. Beretta, J. C. Keck, M. Janbozorgi, and H. Metghalchi. The rate-controlled constrained-equilibrium approach to far-from-local-equilibrium thermodynamics. *Entropy*, 14(2):92–130, 2012. [40](#), [45](#)
- [15] J. J. Bertin and R. M. Cummings. Fifty years of hypersonics: where we've been, where we're going. *Progress in Aerospace Sciences*, 39(67):511–536, 2003. [3](#)
- [16] P. S. Bishnu, D. Hamiroune, M. Metghalchi, and J. C. Keck. Constrained-equilibrium calculations for chemical systems subject to generalized linear constraints using the NASA and STANJAN equilibrium programs. *Combustion Theory and Modelling*, 1(3):295–312, 1997. [168](#)
- [17] G. Blanquart and P. Pepiot. Detailed chemical mechanism and surrogate formulations for engine fuels. In *Proceedings of 7th US Combustion Meeting, Atlanta, Georgia*, pages 9–12, 2011. [120](#)
- [18] G. Blanquart, P. Pepiot-Desjardins, and H. Pitsch. Chemical mechanism for high temperature combustion of engine relevant fuels with emphasis on soot precursors. *Combustion and Flame*, 156(3):588–607, 2009. [120](#)
- [19] G. Blanquart and H. Pitsch. Thermochemical properties of polycyclic aromatic hydrocarbons (PAH) from G3MP2B3 calculations. *The Journal of Physical Chemistry A*, 111(28):6510–6520, 2007. [120](#), [183](#)
- [20] D. Bose, J. L. Brown, D. K. Prabhu, P. Gnoffo, C. O. Johnston, and B. Hollis. Uncertainty assessment of hypersonic aerothermodynamics prediction capability. *Journal of Spacecraft and Rockets*, 50(1):12–18, 2013. [100](#)
- [21] D. Bose, T. White, J. Santos, J. Feldman, M. Mahzari, M. Olson, and B. Laub. Initial assessment of Mars Science Laboratory heatshield instrumentation and flight data. In *51st AIAA*

Aerospace Sciences Meeting including the New Horizons Forum and Aerospace Exposition.
AIAA, 2013. [4](#), [6](#), [11](#), [12](#), [100](#), [119](#), [124](#)

- [22] B. Bottin, O. Chazot, M. Carbonaro, V. van der Haegen, and S. Paris. The VKI plasmatron characteristics and performance. DTIC Document, 2000. [104](#)
- [23] K. Brezinsky, M. Pecullan, and I. Glassman. Pyrolysis and oxidation of phenol. *The Journal of Physical Chemistry A*, 102(44):8614–8619, 1998. [145](#)
- [24] M. Brouillette and B. Sturtevant. Growth induced by multiple shock waves normally incident on plane gaseous interfaces. *Physica D: Nonlinear Phenomena*, 37:248–263, 1989. [36](#)
- [25] S. Browne, J. Ziegler, and J. E. Shepherd. Numerical solution methods for shock and detonation jump conditions. GALCIT - FM2006-006, 2006. [18](#), [19](#), [42](#), [51](#), [52](#)
- [26] Y.-K. Chen and F. S. Milos. Ablation and thermal response program for spacecraft heatshield analysis. *Journal of Spacecraft and Rockets*, 36(3):475–483, 1999. [11](#), [100](#)
- [27] R. S. M. Chue, R. J. Bakos, C.-Y. Tsai, and A. Betti. Design of a shock-free expansion tunnel nozzle in HYPULSE. *Shock Waves*, 13(4):261–270, 2003. [35](#)
- [28] B. T. F. Chung and J.S. Hsiao. Heat transfer with ablation in a finite slab subjected to time-variant heat fluxes. *AIAA Journal*, 23(1):145–150, 1985. [100](#)
- [29] R. K. Crouch and G. D. Walberg. An investigation of ablation behavior of Avcoat 5026/39M over a wide range of thermal environments. NASA TM X-1778, 1969. [108](#)
- [30] R. S. Crowder and J. D. Moote. Apollo entry aerodynamics. *Journal of Spacecraft and Rockets*, 6(3):302–307, 1969. [3](#), [4](#)
- [31] R. Cypres and B. Bettens. Mecanismes de fragmentation pyrolytique du phenol et des cresols. *Tetrahedron*, 30(10):1253 – 1260, 1974. [145](#)
- [32] L. Davies and J. L. Wilson. Influence of reflected shock and boundary-layer interaction on shock-tube flows. *Physics of Fluids*, 12(5):I37, 1969. [19](#)
- [33] T. G. Desai, J. W. Lawson, and P. Kebinski. Modeling initial stage of phenolic pyrolysis: Graphitic precursor formation and interfacial effects. *Polymer*, 52(2):577 – 585, 2011. [106](#)

- [34] A. Dufrene, M. Sharma, and J. M. Austin. Design and characterization of a hypervelocity expansion tube facility. *Journal of Spacecraft and Rockets*, 23(6):1185–1193, 2007. [14](#), [15](#), [16](#), [19](#), [34](#), [35](#)
- [35] C. A. Eckett. *Numerical and Analytical Studies of the Dynamics of Gaseous Detonations*. PhD thesis, California Institute of Technology, 2000. [10](#), [47](#), [89](#)
- [36] K. T. Edquist, A. A. Dyakonov, M. J. Wright, and C. Y Tang. Aerothermodynamic design of the Mars Science Laboratory heatshield. In *41st Thermophysics Conference*. AIAA, 2009. [4](#)
- [37] K. T. Edquist, B. R. Hollis, A. A. Dyakonov, B. Laub, M. J. Wright, T. P. Rivellini, E. M. Slimko, and W. H. Willcockson. Mars Science Laboratory entry capsule aerothermodynamics and thermal protection system. In *Aerospace Conference, 2007 IEEE*, pages 1–13, March 2007. [3](#)
- [38] J. I. Erdos, R. J. Bakos, A. Castrogiovanni, and R. C. Rodgers. Dual mode shock-expansion/reflected-shock tunnel. In *Proceedings of the 35th Aerospace Sciences Meeting and Exhibit*, Reno, Nevada, 1997. AIAA. [15](#)
- [39] Steering Committee for NASA Technology Roadmaps; National Research Council of the National Academies. *NASA Space Technology Roadmaps and Priorities: Restoring NASA’s Technological Edge and Paving the Way for a New Era in Space*. The National Academies Press, 2012. [1](#), [2](#)
- [40] M. J. Frisch, G. W. Trucks, H. B. Schlegel, G. E. Scuseria, M. A. Robb, J. R. Cheeseman, J. A. Montgomery, Jr., T. Vreven, K. N. Kudin, J. C. Burant, J. M. Millam, S. S. Iyengar, J. Tomasi, V. Barone, B. Mennucci, M. Cossi, G. Scalmani, N. Rega, G. A. Petersson, H. Nakatsuji, M. Hada, M. Ehara, K. Toyota, R. Fukuda, J. Hasegawa, M. Ishida, T. Nakajima, Y. Honda, O. Kitao, H. Nakai, M. Klene, X. Li, J. E. Knox, H. P. Hratchian, J. B. Cross, V. Bakken, C. Adamo, J. Jaramillo, R. Gomperts, R. E. Stratmann, O. Yazyev, A. J. Austin, R. Cammi, C. Pomelli, J. W. Ochterski, P. Y. Ayala, K. Morokuma, G. A. Voth, P. Salvador, J. J. Dannenberg, V. G. Zakrzewski, S. Dapprich, A. D. Daniels, M. C. Strain, O. Farkas, D. K. Malick, A. D. Rabuck, K. Raghavachari, J. B. Foresman, J. V. Ortiz, Q. Cui, A. G. Baboul, S. Clifford, J. Cioslowski, B. B. Stefanov, G. Liu, A. Liashenko, P. Piskorz, I. Komaromi, R. L. Martin, D. J. Fox, T. Keith, M. A. Al-Laham, C. Y. Peng, A. Nanayakkara, M. Challacombe, P. M. W. Gill, B. Johnson, W. Chen, M. W. Wong, C. Gonzalez, and J. A. Pople. Gaussian 03, Revision C.02. Gaussian, Inc., Wallingford, CT, 2004. [126](#)

- [41] T. Furukawa, T. Aochi, and A. Sasoh. Expansion tube operation with thin secondary diaphragm. *AIAA Journal*, 45(1):214–217, 2007. [15](#)
- [42] A. G. Gaydon and I. R. Hurel. *The Shock Tube in High-Temperature Chemical Physics*. Reinhold Publishing Corporation, First edition, 1963. [15](#)
- [43] M. J. Gazarik, M. J. Wright, A. Little, F. M. Cheatwood, J. A. Herath, M. M. Munk, F. J. Novak, and E. R. Martinez. Overview of the MEDLI project. In *Aerospace Conference, 2008 IEEE*, pages 1–12, 2008. [5](#)
- [44] O. Gicquel, N. Darabiha, and D. Thévenin. Laminar premixed hydrogen/air counterflow flame simulations using flame prolongation of ildm with differential diffusion. *Proceedings of the Combustion Institute*, 28(2):1901–1908, 2000. [9](#)
- [45] P. Glaister. Flux difference splitting for the Euler equations in one spatial coordinate with area variation. *International Journal for Numerical Methods in Fluids*, 8:97–119, 1988. [20](#), [21](#)
- [46] T. R. Goodman. Application of integral methods to transient nonlinear heat. *Advances in Heat Transfer*, 1:51–122, 1964. [100](#)
- [47] D. G. Goodwin. An open-source, extensible software suite for CVD process simulation. *Electrochemical Society*, pages 155–162, 2003. [18](#), [19](#), [34](#), [51](#), [114](#), [183](#)
- [48] S. Gordon and B. J. McBride. Computer program for calculation of complex equilibrium composition, rocket performance, incident and reflected shocks and Chapman-Jouguet detonations. NASA SP-273, 1971. [168](#)
- [49] S. Gordon and B. J. McBride. Computer program for calculation of complex chemical equilibrium compositions and applications. I. Analysis. NASA RP-1311, 1994. [183](#)
- [50] S. Gordon and B. J. McBride. Thermodynamic data to 20000 K for monatomic gases. NASA TP-1999-208523, 1999. [18](#), [51](#)
- [51] X. Gou, W. Sun, Z. Chen, and Y. Ju. A dynamic multi-timescale method for combustion modeling with detailed and reduced chemical kinetic mechanisms. *Combustion and Flame*, 157(6):1111–1121, 2010. [47](#)
- [52] D. A. Goussis and S. H. Lam. A study of homogeneous methanol oxidation kinetics using CSP. *Symposium (International) on Combustion*, 24(1):113–120, 1992. [38](#), [47](#)

- [53] R. N. Gupta, J. M. Yos, R. A. Thompson, and K. P. Lee. A review of reaction rates and thermodynamic and transport properties for an 11-species air model for chemical and thermal nonequilibrium calculations to 30000 K. NASA-RP-1232, 1990. [9](#), [18](#), [51](#)
- [54] B. Helber, O. Chazot, T. Magin, and A. Hubin. Ablation of carbon preform in the VKI plasmatron. In *43rd AIAA Thermophysics Conference*. AIAA, 2012. [104](#), [105](#)
- [55] W. N. Heltsley, J. A. Snyder, A. J. Houle, D. F. Davidson, M. G. Mungal, and R. K. Hanson. Design and characterization of the Stanford 6 inch expansion tube. In *42nd AIAA/ASME/SAE/ASEE Joint Propulsion Conference and Exhibit*. AIAA, 2006. [7](#), [15](#)
- [56] V. Hiremath, Z. Ren, and S. B. Pope. A greedy algorithm for species selection in dimension reduction of combustion chemistry. *Combustion Theory and Modelling*, 14(5):619–652, 2010. [10](#), [39](#), [40](#)
- [57] J. O. Hirschfelder, C. F. Curtiss, and R. B. Bird. *Molecular Theory of Gases and Liquids*. John Wiley and Sons, 1954. [34](#)
- [58] M. S. Holden, T. P. Wadhams, and G. V. Candler. Experimental studies in the LENS shock tunnel and expansion tunnel to examine real-gas effects in hypervelocity flows. In *Proceedings of the 42nd AIAA Aerospace Sciences Meeting and Exhibit*, Reno, Nevada, 2004. AIAA. [15](#)
- [59] B. R. Hollis and D. K. Prabhu. Assessment of laminar, convective aeroheating prediction uncertainties for Mars-entry vehicles. *Journal of Spacecraft and Rockets*, 50(1):56–68, 2013. [100](#)
- [60] H.G. Hornung. Experimental hypervelocity flow simulation, needs, achievements and limitations. In *Proceedings of the 1st Pacific International Conference on Aero Sc. and Tech.*, Taiwan, 1993. [7](#), [8](#), [9](#), [15](#), [16](#), [19](#), [37](#)
- [61] P. Hung. *Algorithms for Reaction Mechanism Reduction and Numerical Simulation of Detonations Initiated by Projectiles*. PhD thesis, California Institute of Technology, 2003. [10](#), [47](#)
- [62] P.A. Jacobs. Numerical simulation of transient hypervelocity flow in an expansion tube. *Computers and Fluids*, 23(1):77–101, 1994. [14](#)

- [63] M. Janbozorgi and H. Metghalchi. Rate-controlled constrained-equilibrium theory applied to the expansion of combustion products in the power stroke of an internal combustion engine. *International Journal of Thermodynamics*, 12(1), 2009. [10](#), [39](#), [40](#)
- [64] M. Janbozorgi and H. Metghalchi. Rate-controlled constrained-equilibrium modeling of H/O reacting nozzle flow. *Journal of Propulsion and Power*, 28(4):677–684, 2012. [40](#), [49](#), [75](#), [81](#)
- [65] M. Janbozorgi, S. Ugarte, H. Metghalchi, and J. C. Keck. Combustion modeling of mono-carbon fuels using the rate-controlled constrained-equilibrium method. *Combustion and Flame*, 156(10):1871 – 1885, 2009. [10](#), [39](#), [40](#)
- [66] G. M. Jenkins, K. Kawamura, and L. L. Ban. Formation and structure of polymeric carbons. *Proceedings of the Royal Society of London. Series A, Mathematical and Physical Sciences*, 327(1571):pp. 501–517, 1972. [109](#)
- [67] K. A. Jensen, J. M. Suo-Anttila, and L. G. Blevins. Measurement of soot morphology, chemistry, and optical properties in the visible and near-infrared spectrum in the flame zone and overfire region of large JP-8 pool fires. *Combustion Science and Technology*, 179(12):2453–2487, 2007. [110](#), [131](#)
- [68] D.-e. Jiang, A. C. T. van Duin, W. A. Goddard, and S. Dai. Simulating the initial stage of phenolic resin carbonization via the reaxff reactive force field. *The Journal of Physical Chemistry A*, 113(25):6891–6894, 2009. [106](#)
- [69] S. Kao and J. E. Shepherd. Numerical solution methods for control volume explosions and ZND detonation structure. FM2006-007, 2006. [18](#), [42](#), [83](#), [84](#)
- [70] J. C. Keck. Rate-controlled constrained-equilibrium theory of chemical reactions in complex systems. *Progress in Energy and Combustion Science*, 16:125–154, 1990. [10](#), [38](#), [39](#), [40](#), [43](#), [44](#), [46](#), [49](#), [55](#), [68](#)
- [71] J. C. Keck and D. Gillespie. Rate-controlled partial-equilibrium method for treating reacting gas mixtures. *Combustion and Flame*, 17(2):237 – 241, 1971. [10](#), [39](#)
- [72] R. M. Kendall, R. A. Rindal, and E. P. Bartlett. Thermochemical ablation. *AIAA Paper*, 642:13–15, 1965. [100](#)

- [73] L. Khachatryan, J. Adounkpe, and B. Dellinger. Formation of phenoxy and cyclopentadienyl radicals from the gas-phase pyrolysis of phenol. *The Journal of Physical Chemistry A*, 112(3):481–487, 2008. [145](#)
- [74] K. Kobayashi, S. Sugawara, S. Toyoda, and H. Honda. An X-ray diffraction study of phenol-formaldehyde resin carbons. *Carbon*, 6(3):359–363, 1968. [137](#)
- [75] P. W. Kopf. *Phenolic Resins*, volume 7. John Wiley & Sons, Inc., 2002. [103](#), [105](#), [106](#), [107](#), [109](#), [111](#), [172](#)
- [76] J. Lachaud, I. Cozmuta, and N. N. Mansour. Multiscale approach to ablation modeling of phenolic impregnated carbon ablators. *Journal of Spacecraft and Rockets*, 47(6):910–921, 2010. [125](#), [129](#), [146](#)
- [77] J. Lachaud, T. E. Magin, I. Cozmuta, and N. N. Mansour. A short review of ablative material response models and simulation tools. In *7th European Symposium on the Aerothermodynamics*, pages 9–12, 2011. [111](#)
- [78] J. Lachaud and N. N. Mansour. Porous-material analysis toolbox based on OpenFOAM and applications. *Journal of Thermophysics and Heat Transfer*, pages 1–12, 2014. [100](#), [101](#), [110](#), [111](#), [115](#), [120](#), [125](#), [126](#), [145](#), [146](#)
- [79] C. K. Law. *Combustion Physics*. Cambridge University Press, 2006. [47](#)
- [80] R. Law, M. Metghalchi, and J. C. Keck. Rate-controlled constrained equilibrium calculation of ignition delay times in hydrogen-oxygen mixtures. *Symposium (International) on Combustion*, 22(1):1705 – 1713, 1989. [10](#), [39](#), [40](#)
- [81] P. D. Lax and X.-D. Liu. Solution of two-dimensional Riemann problems of gas dynamics by positive schemes. *SIAM Journal on Scientific Computing*, 2(2):319–340, 1998. [27](#)
- [82] L. Lees. Laminar heat transfer over blunt-nosed bodies at hypersonic flight speeds. *Journal of Jet Propulsion*, 26(4):259–269, 1956. [3](#)
- [83] S. A. Leone, R. L. Potts, and A. L. Laganelli. Enhancements to integral solutions to ablation and charring. *Journal of Spacecraft and Rockets*, 32(2):210–216, 1995. [100](#)
- [84] R. J. Leveque. *Finite Volume Methods for Hyperbolic Problems*. Cambridge Texts in Applied Mathematics, 2007. [26](#)

- [85] D. H. Lieberman. *Detonation Interaction with Sharp and Diffuse Interfaces*. PhD thesis, California Institute of Technology, 2006. [34](#)
- [86] D. H. Lieberman and J. E. Shepherd. Detonation interaction with a diffuse interface and subsequent chemical reaction. *Shock Waves*, 16:421–429, 2007. [34](#)
- [87] H. W. Liepmann and A. Roshko. *Elements of Gasdynamics*. Dover Publications, 1993. [16](#)
- [88] A. Little, D. Bose, C. Karlgaard, M. Munk, C. Kuhl, M. Schoenenberger, C. Antill, R. Verhappen, P. Kutty, and T. White. The Mars Science Laboratory (MSL) entry, descent and landing instrumentation (MEDLI): Hardware performance and data reconstruction. In *36th AAS Guidance and Control Conference*, Breckenridge, CO, 1-6 February 2013. [124](#)
- [89] A. B. Lovell, K. Brezinsky, and I. Glassman. The gas phase pyrolysis of phenol. *International Journal of Chemical Kinetics*, 21(7):547–560, 1989. [145](#)
- [90] J. Lukasiewicz. *Experimental Methods of Hypersonics*. Marcel Decker, first edition, 1973. [6](#), [7](#)
- [91] U. Maas and S. B. Pope. Implementation of simplified chemical kinetics based on intrinsic low-dimensional manifolds. *Symposium (International) on Combustion*, 24(1):103–112, 1992. [38](#), [47](#), [48](#)
- [92] U. Maas and S. B. Pope. Simplifying chemical kinetics: Intrinsic low-dimensional manifolds in composition space. *Combustion and Flame*, 88(3-4):239–264, 1992. [38](#), [47](#), [48](#)
- [93] P. R. Mahaffy, C. R. Webster, S. K. Atreya, H. Franz, M. Wong, P. G. Conrad, D. Harpold, J. J. Jones, L. A. Leshin, H. Manning, et al. Abundance and isotopic composition of gases in the Martian atmosphere from the Curiosity rover. *Science*, 341(6143):263–266, 2013. [90](#)
- [94] M. Mahzari, T. White, R. Braun, and D. Bose. Preliminary analysis of the Mars Science Laboratory’s entry aerothermodynamic environment and thermal protection system performance. In *51st AIAA Aerospace Sciences Meeting including the New Horizons Forum and Aerospace Exposition*. AIAA, 2013. [3](#), [5](#), [10](#), [100](#), [119](#), [124](#)
- [95] J. A Manion and R. Louw. Rates, products, and mechanisms in the gas-phase hydrogenolysis of phenol between 922 and 1175 k. *The Journal of Physical Chemistry*, 93(9):3563–3574, 1989. [145](#)

- [96] A. Martin, I. D. Boyd, I. Cozmuta, and M. J. Wright. Chemistry model for ablating carbon-phenolic material during atmospheric re-entry. In *48th AIAA Aerospace Sciences Meeting and Exhibit*. AIAA, 2010. [11](#), [100](#)
- [97] T. J. Martin-Mur, G. L. Kruizingas, P. D. Burkhardt, M. C. Wong, and F. Abilleira. Mars Science Laboratory navigation results. In *23rd International Symposium on Space Flight Dynamics, Pasadena, California*. Jet Propulsion Laboratory, National Aeronautics and Space Administration, 2012. [4](#)
- [98] S. Maruyama, R. Viskanta, and T. Aihara. Active thermal protection system against intense irradiation. *Journal of Thermophysics and Heat Transfer*, 3(4):389–394, 1989. [100](#)
- [99] B. J. McBride and S. Gordon. Chemical equilibrium with applications. <http://www.grc.nasa.gov/WWW/CEAWeb/>. [112](#), [183](#)
- [100] B. J. McBride, M. J. Zehe, and S. Gordon. NASA Glenn coefficients for calculating thermodynamic properties of individual species. NASA TP-2002-211556, 2002. [18](#), [51](#), [182](#), [183](#)
- [101] M. McGilvray, J. M. Austin, M. Sharma, P. A. Jacobs, and R. G. Morgan. Diagnostic modelling of an expansion tube operating condition. *Shock Waves*, 19(1):59–66, 2009. [35](#)
- [102] C. G. Miller. Operational experience in the Langley expansion tube with various gases. NASA TM-78637, 1977. [14](#)
- [103] J. H. Miller. The kinetics of polynuclear aromatic hydrocarbon agglomeration in flames. In *Symposium (International) on Combustion*, volume 23, pages 91–98. Elsevier, 1991. [126](#), [127](#)
- [104] V. A. Miller, M. Gamba, M. G. Mungal, and R. K. Hanson. Secondary diaphragm thickness effects and improved pressure measurements in an expansion tube. *AIAA Journal*, pages 1–5, 2014. [7](#), [8](#), [15](#)
- [105] F. S. Milos and Y.-K. Chen. Comprehensive model for multicomponent ablation thermochemistry. In *35th Aerospace Sciences Meeting and Exhibit*. AIAA, 1997. [100](#), [101](#), [113](#), [117](#)
- [106] F. S. Milos and Y.-K. Chen. Ablation and thermal response property model validation for phenolic impregnated carbon ablator. *Journal of Spacecraft and Rockets*, 47(5):786–805, 2010. [11](#), [100](#), [101](#)

- [107] F. S. Milos and Y.-K. Chen. Ablation predictions for carbonaceous materials using two databases for species thermodynamics. *Journal of Spacecraft and Rockets*, 50(2):245–255, 2013. [100](#)
- [108] F. S. Milos and Y.-K. Chen. Ablation, thermal response, and chemistry program for analysis of thermal protection systems. *Journal of Spacecraft and Rockets*, 50(1):137–149, 2013. [11](#), [12](#), [100](#), [101](#), [108](#), [110](#), [113](#), [114](#), [117](#), [118](#), [139](#)
- [109] H. Mirels. Shock tube test time limitation due to turbulent-wall boundary layer. *AIAA Journal*, 2(1):84–93, 1964. [19](#), [34](#)
- [110] P. Mitchell and M. Frenklach. Particle aggregation with simultaneous surface growth. *Phys. Rev. E*, 67:061407, Jun 2003. [126](#)
- [111] A. R. Morr and J. B. Heywood. Partial equilibrium model for predicting concentration of CO in combustion. *Acta Astronautica*, 1(78):949 – 966, 1974. [39](#)
- [112] Farshad Saberi Movahed, Gary Cheng, Balaji Shankar Venkatachari, and Ioana Cozmuta. Atomistic simulation of thermal decomposition of crosslinked and non-crosslinked phenolic resin chains. In *42nd AIAA Thermophysics Conference*. AIAA, 2011. [106](#)
- [113] S. D. N. and R. S. Juvet, Jr. *Gas-Liquid Chromatography. Theory and practice*. Interscience (Wiley), New York, 1962. [136](#)
- [114] K. Narayanaswamy, G. Blanquart, and H. Pitsch. A consistent chemical mechanism for oxidation of substituted aromatic species. *Combustion and Flame*, 157(10):1879–1898, 2010. [120](#), [183](#)
- [115] A. J. Neely and R. G. Morgan. The superorbital expansion tube concept, experiment and analysis. *The Aeronautical Journal*, 98(973):97–105, 1994. [15](#)
- [116] G. D. Norfleet, J. J. Lacey, and J. D. Whitfield. Results of an experimental investigation of the performance of an expansion tube. In *Proceedings of the 4th Hypervelocity Tech. Symp.*, Tullahoma, Tennessee, 1965. [14](#)
- [117] D. Olynick, Y.-K. Chen, and M. E. Tauber. Aerothermodynamics of the Stardust sample return capsule. *Journal of Spacecraft and Rockets*, 36(3):442–462, 1999. [11](#), [99](#), [100](#)
- [118] K. Ouchi and H. Honda. Pyrolysis of coal I: Thermal cracking of phenolformaldehyde resins taken as coal models. *Fuel*, 38(4):429–443, 1959. [137](#)

- [119] F. Panerai, A. Martin, N. N. Mansour, S. A. Sepka, and J. Lachaud. Flow-tube oxidation experiments on the carbon preform of a phenolic-impregnated carbon ablator. *Journal of Thermophysics and Heat Transfer*, pages 1–10, 2014. [130](#)
- [120] C. Park. Review of chemical-kinetic problems of future NASA missions, I: Earth entries. *Journal of Thermophysics and Heat Transfer*, 7(3):385–398, 1993. [3](#), [101](#)
- [121] C. Park, J. T. Howe, R. L. Jaffe, and G. V. Candler. Review of chemical-kinetic problems of future NASA missions, II: Mars entries. *Journal of Thermophysics and Heat Transfer*, 8(1):9–23, 1994. [101](#)
- [122] C. Park, R. L. Jaffe, and H. Partridge. Chemical-kinetic parameters of hyperbolic earth entry. *Journal of Thermophysics and Heat Transfer*, 15(1):76–90, 2001. [11](#), [100](#), [101](#), [108](#), [113](#), [114](#), [118](#), [139](#)
- [123] N. J. Parziale. *Slender-Body Hypervelocity Boundary-Layer Instability*. PhD thesis, California Institute of Technology, 2013. [52](#)
- [124] A. Paull and R. J. Stalker. The effect on an acoustic wave as it traverses an unsteady expansion. *Physics of Fluids*, 3(4):717–719, 1991. [14](#)
- [125] A. Paull and R. J. Stalker. Test flow disturbances in an expansion tube. *Journal of Fluid Mechanics*, 245:493–521, 1992. [14](#), [16](#)
- [126] W. Payman and W. C. F. Shepherd. Explosion waves and shock waves VI. The disturbance produced by bursting diaphragms with compressed air. *Proceedings of the Royal Society of London Series A: Mathematical and Physical Sciences*, 186(1006):293–321, 1946. [15](#)
- [127] N. Peters. Laminar diffusion flamelet models in non-premixed turbulent combustion. *Progress in energy and combustion science*, 10(3):319–339, 1984. [9](#)
- [128] L. Pilato. *Phenolic resins: a century of progress*. Springer, 2010. [105](#), [107](#), [172](#)
- [129] S. B. Pope. Gibbs function continuation for the stable computation of chemical equilibrium. *Combustion and Flame*, 139(3):222 – 226, 2004. [45](#), [139](#), [168](#)
- [130] S.B. Pope. Computationally efficient implementation of combustion chemistry using in situ adaptive tabulation. *Combustion Theory and Modelling*, 1(1):41–63, 1997. [83](#)

- [131] S.B. Pope. CEQ: A Fortran library to compute equilibrium compositions using Gibbs function continuation. <http://eccentric.mae.cornell.edu/~pope/ceq>, 2003. [45](#)
- [132] S.B. Pope. The computation of constrained and unconstrained equilibrium compositions of ideal gas mixtures using Gibbs function continuation. Cornell University Report FDA 03-02, 2003. [45](#), [139](#), [168](#)
- [133] R. L. Potts. An integral method theorem for heat conduction. *AIAA Journal*, 21(4):630–631, 1983. [100](#)
- [134] R. L. Potts. Hybrid integral/quasi-steady solution of charring ablation. In *5th Joint Thermo-physics and Heat Transfer Conference*. AIAA, 1990. [100](#)
- [135] R. L. Potts. Application of integral methods to ablation charring erosion - a review. *Journal of Spacecraft and Rockets*, 32(2):200–209, 1995. [100](#)
- [136] R. J. Purser and L. M. Leslie. An efficient interpolation procedure for high-order three-dimensional semi-Lagrangian models. *Monthly Weather Review*, 119(10):2492–2498, 1991. [26](#)
- [137] T. Qi, C. W. Bauschlicher, Jr., J. W. Lawson, T. G. Desai, and E. J. Reed. Comparison of ReaxFF, DFTB, and DFT for phenolic pyrolysis. 1. Molecular dynamics simulations. *The Journal of Physical Chemistry A*, 117(44):11115–11125, 2013. [103](#), [106](#)
- [138] V. Quan. Integral solution for erosion heat transfer. *AIAA Journal*, 8(8):1512–1514, 1970. [100](#)
- [139] J. D. Regele, E. Knudsen, H. Pitsch, and G. Blanquart. A two-equation model for non-unity Lewis number differential diffusion in lean premixed laminar flames. *Combustion and Flame*, 160(2):240 – 250, 2013. [83](#)
- [140] W. C. Reynolds. The element potential method for chemical equilibrium analysis: Implementation in the interactive program STANJAN, version 3. Stanford University Report ME 270 HO no. 7, 1986. [168](#)
- [141] H. Ritter, O. Bayle, Y. Mignot, E. Boulier, P. Portela, J-M. Bouilly, and R. Sharda. On-going European developments on entry heatshields and TPS materials. In *8th International Planetary Probe Workshop*, Portsmouth, Virginia, 2011. [99](#)
- [142] H. Ritter, P. Portela, K. Keller, J.-M. Bouilly, and S. Burnage. Development of a European ablative material for heatshields of sample return missions. In *6th European Workshop on Thermal Protection Systems and Hot Structures*, Stuttgart, Germany, 2009. [99](#)

- [143] J. Robert. Chemkin-II: A Fortran chemical kinetics package for the analysis of gas-phase chemical kinetics. *Sandia National Laboratories Report SAND89-8009B*, 1989. [120](#)
- [144] G. T. Roberts, R. G. Morgan, and R. J. Stalker. Influence of secondary diaphragm on flow quality in expansion tubes. In *Proceedings of the 19th International Symposium on Shock Waves*, pages 203–208, Pasadena, CA, 1995. Springer-Verlag. [15](#)
- [145] P. L. Roe. Approximate Riemann solvers, parameter vectors, and difference schemes. *Journal of Computational Physics*, 43(2):357–372, 1981. [23](#)
- [146] E. M. Rothkopf and W. Low. Diaphragm opening process in shock tubes. *Physics of Fluids*, 17(6):1169–1173, 1974. [15](#)
- [147] K. Roy, C. Horn, P. Frank, V. G. Slutsky, and T. Just. High-temperature investigations on the pyrolysis of cyclopentadiene. *Symposium (International) on Combustion*, 27(1):329 – 336, 1998. [145](#)
- [148] C. Russo, M. Alfè, J.-N. Rouzaud, F. Stanzone, A. Tregrossi, and A. Ciajolo. Probing structures of soot formed in premixed flames of methane, ethylene and benzene. *Proceedings of the Combustion Institute*, 34(1):1885 – 1892, 2013. [110](#), [131](#)
- [149] R. Sanders, E. Morano, and M.-C. Druget. Multidimensional dissipation for upwind schemes: Stability and applications to gas dynamics. *Journal of Computational Physics*, 145:511–537, 1998. [27](#)
- [150] A. Sasoh, Y. Ohnishi, D. Ramjaun, K. Takayama, H. Otsu, and T. Abe. Effective test time evaluation in high-enthalpy expansion tube. *AIAA Journal*, 39(11):2141–2147, 2001. [15](#)
- [151] A. M. Scheer, C. Mukarakate, D. J. Robichaud, M. R. Nimlos, H.-H. Carstensen, and G. B. Ellison. Unimolecular thermal decomposition of phenol and d5-phenol: Direct observation of cyclopentadiene formation via cyclohexadienone. *The Journal of Chemical Physics*, 136:044309, 2012. [145](#)
- [152] R. J. Sharpe and M. D. Wright. NASA materials research for extreme conditions. NASA TM-2009-215901, 2009. [99](#), [105](#)
- [153] J. L. Shinn and C. G. Miller. Experimental perfect-gas study of expansion-tube flow characteristics. NASA TP-1317, 1978. [14](#)

- [154] C. J. Simpson, T. R. Chandler, and K. B. Bridgman. Effect on shock trajectory of the opening time of diaphragms in a shock tube. *Physics of Fluids*, 10(9):1894–1897, 1967. [15](#)
- [155] M. O. Sinnokrot and C. D. Sherrill. Highly accurate coupled cluster potential energy curves for the benzene dimer: sandwich, T-shaped, and parallel-displaced configurations. *The Journal of Physical Chemistry A*, 108(46):10200–10207, 2004. [126](#)
- [156] C. E. Smith. The starting process in a hypersonic nozzle. *Journal of Fluid Mechanics*, 24:625–640, 1966. [19](#), [32](#)
- [157] G. P. Smith, D. M. Golden, M. Frenklach, N. W. Moriarty, B. Eiteneer, M. Goldenberg, C. T. Bowman, R. K. Hanson, S. Song, W. C. Gardiner, V. V. Lissianski, and Z. Qin. GRI-Mech 3.0. Available: http://www.me.berkeley.edu/gri_mech/, 1999. Accessed: 04/03/2014. [9](#), [90](#)
- [158] J. H. Spurk. Design, operation and preliminary results of the BRL expansion tube. In *Proceedings of the 4th Hypervelocity Tech. Symp.*, Tullahoma, Tennessee, 1965. [14](#)
- [159] M. Stackpoole, S. Sepka, I. Cozmuta, and D. Kontinos. Post-flight evaluation of stardust sample return capsule forebody heatshield material. In *46th Aerospace Sciences Meeting and Exhibit*. AIAA, 2008. [11](#), [104](#)
- [160] R. L. Stone and H. F. Rase. Differential thermal analysis. New technique for testing silica-alumina catalysts. *Analytical Chemistry*, 29(9):1273–1277, 1957. [136](#)
- [161] N. Sudani and H. G. Hornung. Gasdynamical detectors of driver gas contamination in a high-enthalpy shock tunnel. *AIAA Journal*, 36(3):313–319, 1998. [19](#)
- [162] G. F. Sykes Jr. Decomposition characteristics of a char-forming phenolic polymer used for ablative composites. NASA TN D-3810, 1967. [12](#), [100](#), [107](#), [108](#), [109](#), [110](#), [111](#), [113](#), [136](#), [137](#), [138](#), [139](#), [140](#), [141](#), [172](#), [182](#), [183](#)
- [163] Q. Tang and S. B. Pope. Implementation of combustion chemistry by in situ adaptive tabulation of rate-controlled constrained equilibrium manifolds. *Proceedings of the Combustion Institute*, 29(1):1411–1417, 2002. [10](#), [39](#), [40](#), [98](#)
- [164] Q. Tang and S. B. Pope. A more accurate projection in the rate-controlled constrained-equilibrium method for dimension reduction of combustion chemistry. *Combustion Theory and Modelling*, 8(2):255–279, 2004. [10](#), [39](#), [40](#)

- [165] Stephen Till, Andrew Heaton, David Payne, Corinne Stone, and Martin Swan. Computational chemistry studies of phenolic resin. In *51st AIAA Aerospace Sciences Meeting including the New Horizons Forum and Aerospace Exposition*. AIAA, 2013. [106](#)
- [166] S. R. Tonse, N. W. Moriarty, N. J. Brown, and M. Frenklach. Prism: Piecewise reusable implementation of solution mapping. an economical strategy for chemical kinetics. *Israel Journal of Chemistry*, 39(1):97–106, 1999. [98](#)
- [167] H. K. Tran. Development of lightweight ceramic ablators and arc-jet test results. NASA TM-108798, 1994. [99](#)
- [168] H. K. Tran, C. E. Johnson, D. J. Rasky, F. C. L. Hui, M.-T. Hsu, T. Chen, Y. K. Chen, D. Paragas, and L. Kobayashi. Phenolic impregnated carbon ablators (PICA) as thermal protection systems for discovery missions. NASA TM-110440, 1997. [99](#), [103](#), [104](#), [105](#), [109](#), [110](#), [111](#)
- [169] K. A. Trick and T. E. Saliba. Mechanisms of the pyrolysis of phenolic resin in a carbon/phenolic composite. *Carbon*, 33(11):1509 – 1515, 1995. [100](#), [107](#), [109](#), [136](#), [138](#), [172](#)
- [170] K.A. Trick, T.E. Saliba, and S.S. Sandhu. A kinetic model of the pyrolysis of phenolic resin in a carbon/phenolic composite. *Carbon*, 35(3):393 – 401, 1997. [109](#), [111](#), [137](#), [138](#), [139](#), [140](#)
- [171] R. L. Trimpli. A preliminary theoretical study of the expansion tube, a new device for producing high-enthalpy short-duration hypersonic gas flows. NASA TR R-133, 1962. [13](#)
- [172] R. L. Trimpli and L. B. Callis. A perfect-gas analysis of the expansion tunnel, a modification to the expansion tube. NASA TR R-223, 1965. [13](#)
- [173] B. Van Leer. Towards the ultimate conservative difference scheme II. Monotonicity and conservation combined in a second order scheme. *Journal of Computational Physics*, 14(4):361–370, 1974. doi: 10.1016/0021-9991(74)90019-9. [26](#)
- [174] J. A. van Oijen, F. A. Lammers, and L. P. H. de Goey. Modeling of complex premixed burner systems by using flamelet-generated manifolds. *Combustion and Flame*, 127(3):2124–2134, 2001. [9](#)
- [175] R. Vicquelin, B. Fiorina, S. Payet, N. Darabiha, and O. Gicquel. Coupling tabulated chemistry with compressible CFD solvers. *Proceedings of the Combustion Institute*, 33(1):1481–1488, 2011. [9](#)

- [176] W. G. Vincenti and C. H. Kruger. *Introduction to physical gas dynamics*, volume 1. Wiley: New York, 1965. [126](#), [128](#)
- [177] M. Wakefield and W. C. Pitts. Analysis of the heat-shield experiment on the Pioneer-Venus entry probes. *AIAA 1980-1494*, 1980. [110](#)
- [178] H. Wang. Formation of nascent soot and other condensed-phase materials in flames. *Proceedings of the Combustion Institute*, 33(1):41–67, 2011. [126](#)
- [179] M. Wegener, M. Sutcliffe, and R. Morgan. Optical study of a light diaphragm rupture process in an expansion tube. *Shock Waves*, 10:167–178, 2000. [15](#)
- [180] D. R. White. Influence of diaphragm opening time on shock-tube flows. *Journal of Fluid Mechanics*, 4(6):585–599, 1958. [15](#)
- [181] E. Wintenberger, J. M. Austin, M. Cooper, S. Jackson, and J. E. Shepherd. Analytical model for the impulse of single-cycle pulse detonation tube. *Journal of Propulsion and Power*, 19(1):22–38, 2003. [19](#)
- [182] H.-W. Wong, J. Peck, R. Edwards, G. Reinisch, J. Lachaud, and N. N. Mansour. Measurement of pyrolysis products from phenolic polymer thermal decomposition. In *52nd Aerospace Sciences Meeting*. AIAA, 2014. [12](#), [101](#), [107](#), [110](#), [111](#), [125](#), [126](#), [138](#)
- [183] M. Wright, K. Edquist, C. Tang, B. Hollis, P. Krasa, and C. Campbell. A review of aerothermal modeling for Mars entry missions. In *48th AIAA Aerospace Sciences Meeting Including the New Horizons Forum and Aerospace Exposition*. AIAA, 2010. [100](#)
- [184] Z. F. Xu and M. C. Lin. Ab initio kinetics for the unimolecular reaction $C_6H_5OH \rightarrow CO + C_5H_6$. *The Journal of Physical Chemistry A*, 110(4):1672–1677, 2006. [145](#)
- [185] L. Zhu and J. W. Bozzelli. Kinetics and thermochemistry for the gas-phase keto-enol tautomerism of phenol \leftrightarrow 2,4-cyclohexadienone. *The Journal of Physical Chemistry A*, 107(19):3696–3703, 2003. [145](#)

Appendices

Appendix A

Constrained Thermodynamic Equilibrium Calculations

All constrained equilibrium calculations performed in this thesis were made using the CEQ code developed by Professor Stephen B. Pope at Cornell University. CEQ is a Fortran 90 library that implements a Gibbs function continuation method [132] in order to calculate thermodynamic, or constrained thermodynamic gas mixture compositions. The chemical equilibrium composition is calculated either at fixed pressure and temperature, or at fixed pressure and enthalpy. For constrained thermodynamic equilibrium calculations, constraints can be imposed on individual species, or on arbitrary linear combinations of species. The CEQ software may be downloaded at <http://eccentric.mae.cornell.edu/~pope/CEQ>.

A detailed explanation of the full mathematical method used can be found in [132], and an overview of the Gibbs function continuation method for standard thermodynamic equilibrium calculations can be found in [129]. The Gibbs function continuation method uses Lagrange multipliers in order to solve the constrained minimization problem. These Lagrange multipliers are determined from the solution of a set of non-linear equations. It is claimed that the Gibbs function continuation method addresses the fact using Newton's method to solve the non-linear system of equations may fail due to a singular iteration matrix [132]. The CEQ code was developed in order to address issues that Bishnu *et al.* [16] reported - showing that both the NASA code [48] and the STANJAN [140] code, when extended to constrained equilibrium calculations, failed to determine constrained equilibrium compositions in some cases.

Appendix B

RCCE Table Sensitivity

Results for the shock test case for different table resolutions are shown in Fig. B.1 and Fig. B.2, constraining on the enthalpy of formation. Each table uses minimum and maximum values of 39 kPa and 17.5 MPa, 2000 K and 5800 K, and 0 kJ/g and 2.6 kJ/g, for pressure, temperature, and ϕ , respectively. However, one table uses 50 points in each dimension, one 75, and one 100, corresponding to tables with 125000, 421875, and 1000000 points in total, respectively. All quantities are linearly spaced in each dimension. The mass fraction results are observed to be fairly insensitive to the table resolution. The maximum difference over the entire domain between the lowest resolution table and the highest resolution table, for the mass fraction of each species present, is less than $3 \cdot 10^{-4}$, $4 \cdot 10^{-4}$, $6 \cdot 10^{-4}$, $3 \cdot 10^{-4}$, and $4 \cdot 10^{-7}$, for Y_{N_2} , Y_{O_2} , Y_{NO} , Y_O , and Y_N , respectively. Similarly, the maximum difference in ϕ is less than 0.005 kJ/g over the entire domain.

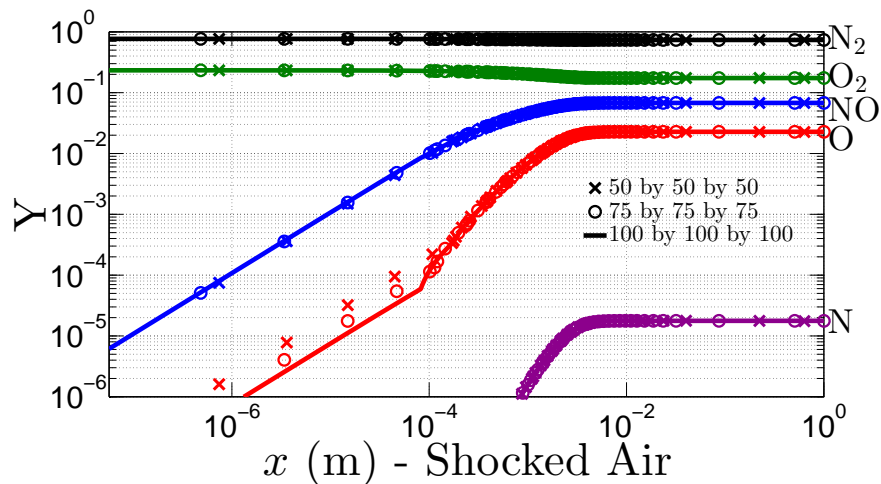


Figure B.1: Sensitivity of RCCE mass fractions results to table resolution for the shock test case.

Similar results for the nozzle test case are shown in Fig. B.3 and Fig. B.4, using the same three tables, and a constraint based on the enthalpy of formation. The maximum difference over the entire

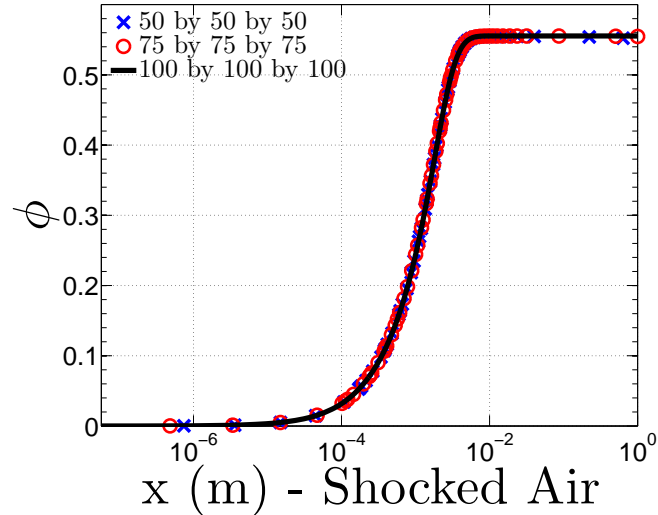


Figure B.2: Sensitivity of RCCE constraint value to table resolution for the shock test case.

domain between the lowest resolution table and the highest resolution table, for the mass fraction of each species present, is less than $4 \cdot 10^{-5}$, $3 \cdot 10^{-4}$, $7 \cdot 10^{-5}$, $2 \cdot 10^{-4}$, and $2 \cdot 10^{-5}$, for Y_{N_2} , Y_{O_2} , Y_{NO} , Y_O , and Y_N , respectively. The maximum difference in ϕ is less than 0.003 kJ/g over the entire domain.

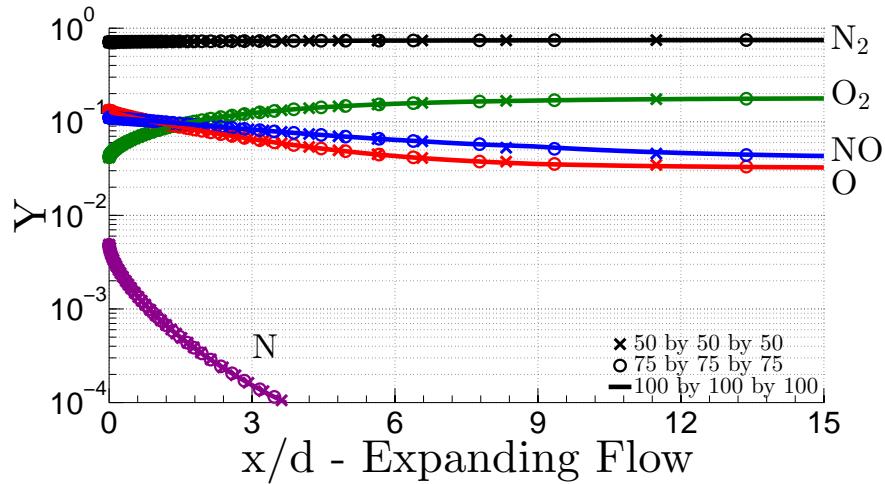


Figure B.3: Sensitivity of RCCE mass fractions results to table resolution for the nozzle test case.

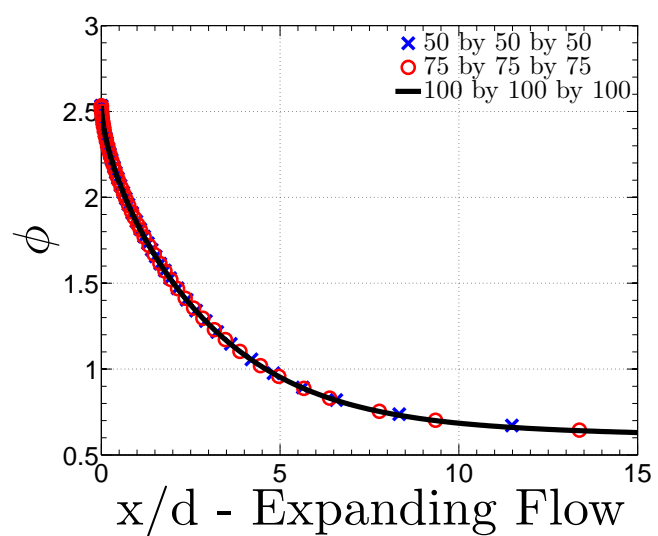


Figure B.4: Sensitivity of RCCE constraint value to table resolution for the nozzle test case.

Appendix C

Resin Synthesis¹

This section is included for completeness, and provides a basic overview of some of the possible synthesis processes used for making phenolic resins. All mechanisms and properties are adapted from [162], [75], [128], and [169], and the references mentioned therein.

C.1 General

Novolac and resole resins are synthetic polymers (**3**), generated via the co-polymerization of phenol (**1**) and formaldehyde (**2**), in the presence of an acid or base catalyst, respectively (Fig. C.1). Although the polymers generated using an acid catalyst (novolac resins) are structurally similar to those generated using a base catalyst (resole resins), their structure and composition often differ. With respect to the simplified polymer structure (**3**) shown in Fig. C.1, these differences include variations in cross-linking density (*n*), amount of 2,2'-methylene (CH_2) linkages (*m*) vs. 2,4'-methylene linkages (*q*), ether linkages (CH_2OCH_2) (*p*), and nitrogen incorporation (CH_2NHCH_2) (*o*). A more detailed discussion regarding the synthesis, and subsequent compositional differences of novolac and resole resins is given in Sec. C.3.

The method employed to synthesize the resin results in compositional differences such as the cross-linking density, as well as the number of nitrogen and oxygen linkages present. This will affect the resulting physical properties of the resin, including hardness as well as chemical and thermal stability. Generally, resins synthesized by acid catalysis (novolacs) comprise a more limited structural range than those synthesized by base catalysis (resoles), and thus resole resins generally result in products with more diverse properties. It is worthy to note that cure times, as well as temperatures,

¹The work in this appendix was performed in collaboration with V. M. Marx, has been presented in large part in Rabinovitch, J., Marx, V. M., and Blanquart, G. Pyrolysis Gas Composition for a Phenolic-Impregnated Carbon Ablator Heatshield. In *Proceedings of the 11th AIAA/ASME Joint Thermophysics and Heat Transfer Conference*. AIAA, Atlanta, Georgia, 2014.

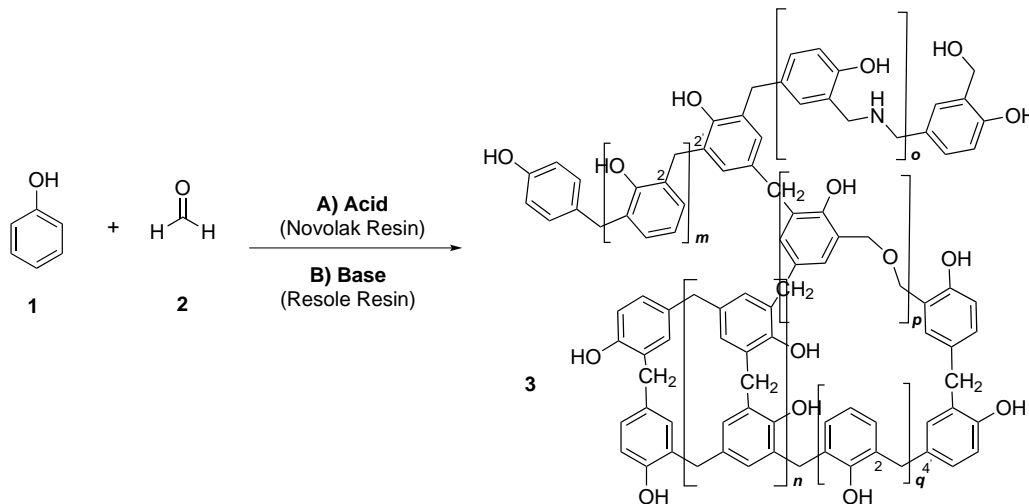


Figure C.1: Synthesis of a phenolic resin by co-polymerization of phenol and formaldehyde under acidic conditions (*i.e.*, novolac resins) or basic conditions (*i.e.*, resole resins).

are dependent upon the structure of the uncured resin following polymerization. Furthermore, the presence of impurities such as residual water, phenol, and acid or base catalysts can also affect the extent of the cure.

C.2 Curing and Decomposition Characteristics

The composition of a resin can also be modified post-polymerization by application of a subsequent curing step. In the curing step, excess formaldehyde (or a formaldehyde source), sufficient heat (typically $\sim 150^\circ\text{C}$), and/or an acid or base catalyst is applied in order to promote the cross-linking of any remaining unjoined or open sites. The high temperatures employed can also result in elimination of the ether and amine linkages (*o* and *p* in **3**) to give methylene linkages (Fig. C.2). For example, pre-cured novolacs containing an increased amount of 2,2'-methylene linkages (e.g., high ortho novolacs, see Sec. C.3.2) cross-link more easily, and cure faster than those predominantly comprised of 2,4'-linkages.

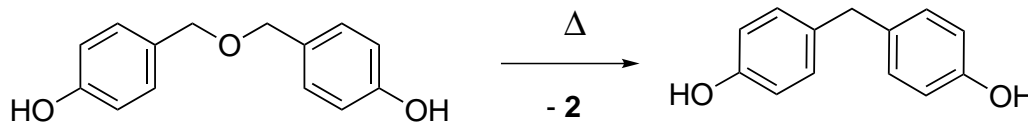


Figure C.2: Conversion of ether to methylene linkages upon curing.

The extent of curing is important as this will also affect the resulting composition and properties of the resin, as well as the pyrolysis gases evolved. At approximately 300°C , any remaining ether (*p*

in **3**) and nitrogen (*o* in **3**) linkages will begin to break forming aldehydes, cresols, and azomethines (which can also cause coloring). Furthermore, at this stage any small molecules that were trapped from the manufacturing process will be released, such as excess phenol, water, formaldehyde, ammonia etc. Substantial decomposition of the resin occurs at approximately 400°C, due to cleavage of the phenolic hydroxyl groups as well as the methylene linkages. These processes generate reactive oxygen species, which can further accelerate the breakdown of the methylene linkages via oxidation to hydroperoxide, ketone, and alcohol intermediates, which rapidly decompose. Volatile byproducts are formed such as water, hydrogen, methane (CH₄), carbon monoxide (CO), carbon dioxide (CO₂), and phenols. Little shrinkage of the resin occurs, because many of the methylene cross-linkages are replaced by carbon-carbon bonds that form between two aromatic rings directly. At approximately 600°C, substantial shrinkage occurs as a result of the formation of additional carbon-carbon bonds between aromatic rings, resulting in a polyaromatic char (typically, approximately 60% of the original resin). Substantial quantities of pyrolysis gases are liberated, composed mainly of hydrogen, but also methane, volatile aromatic compounds (such as phenol or benzene), water, carbon monoxide, and carbon dioxide. Finally, although the char ignites at 900°C, controlled decomposition of phenolic resins in an inert atmosphere in the presence of other forms of carbon (e.g., carbon fibers, coke, synthetic graphite) can be used to yield stable, glassy composites.

C.3 Synthesis of Novolac Resins

Novolac resins are synthesized by acid-catalyzed polymerization of phenol and formaldehyde (Fig. C.3). Typically 0.1% - 2% (by mole) of acid catalyst is used. An acidic medium favors the production of linear polymers (in which repeat units are comprised of di-substituted phenol units). As substitution on phenol (**1**) increases, its reactivity towards formaldehyde decreases. As a result, excess phenol is added in order to achieve a controlled polymerization. This is effective up to molecular weights of ~1000 g/mol, beyond which the concentration of end groups and unreacted phenol becomes too low, and polymer branching (in which repeat units are comprised of tri-substituted phenol units) becomes competitive with linear chain growth. With the addition of a cross-linking agent, the polymer is then cross-linked in a second, subsequent step in which the polymer chains are joined via additional 2,2'- or 2,4'-methylene linkages between open sites (highlighted in Fig. C.3).

In terms of resin composition, it is worth mentioning that because benzylic alcohols (**10**) are unstable in the presence of strong acids, and resins synthesized using strong acid catalysts are generally devoid of ether linkages. However, ether linkages may be produced in small amounts when

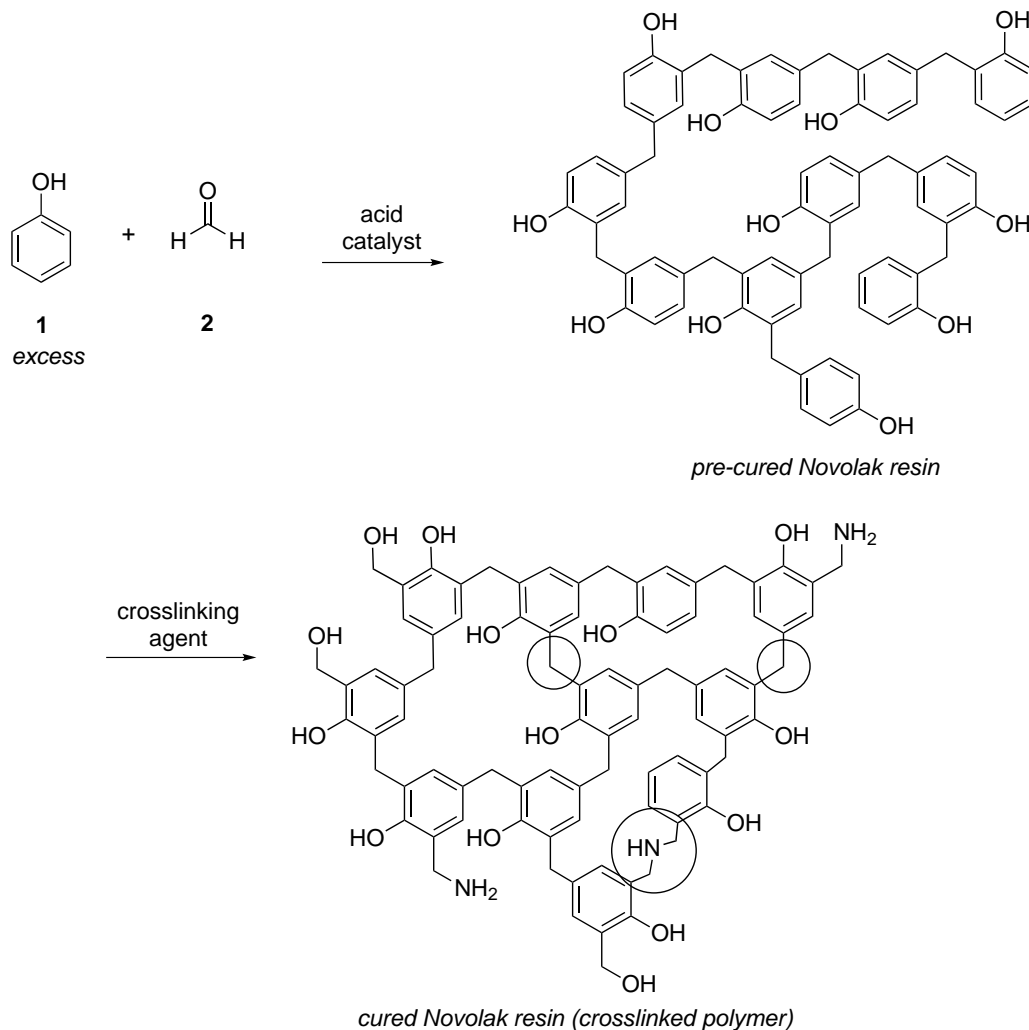


Figure C.3: General synthetic scheme for the production of a novolac resin.

weak acid catalysts (such as oxalic acid) are employed (see Sec. C.5 for a more detailed explanation). In the curing step for these resins, nitrogen-containing compounds, such as hexamethylenetetramine (**4**), are often employed as a source of formaldehyde (**2**). Figure C.4 outlines how **4** serves as a source of **2**. Typically 5% - 15% (by mole) of **4** is utilized; as a result, varying amounts of nitrogen is often incorporated in novolac resins due to competing reactions of phenol (**1**) with imine (**5**).

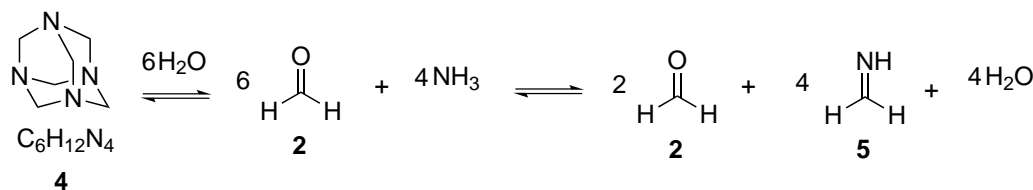


Figure C.4: Hexamethylenetetramine (**4**) as a source of formaldehyde (**2**).

C.3.1 Brønsted Acid Catalysts—Novolac Resins

Figure C.5 gives a generalized mechanism for polymerization under Brønsted acidic conditions. In water, formaldehyde (**2**) exists primarily in its hydrate form (**7**), which is a commercially available as formalin. Compound **7** is protonated in the presence of a Brønsted acid, such as sulfuric acid (**6**), a representative strong acid, generating **8** which expels water to provide protonated formaldehyde **9**. Compound **9** then engages in electrophilic aromatic substitution with phenol (**1**). Although either C2 or C4 of phenol can react, a reaction at C4 is favored. In strong acid, the resulting benzylic alcohol (**10**) has a very short lifetime, and rapidly undergoes proton transfer providing **11**. In weak acid, **11** is in an equilibrium with its unprotonated form (which can yield additional byproducts, discussed in Sec. C.5). Compound **11** then reacts with a second equivalent of phenol (**1**). Again, the reaction preferentially takes place at the C4 position, generating **12** which leads to **13** as the major product (bearing a 4,4'-methylene linkage). Compounds **15** and **19** are generated in an analogous manner as shown.

The major product **13** only has open sites at the C2 position, so formaldehyde (**2**) will next add at the C2 position. The entire pathway described in Fig. C.5 is then repeated with preferential substitution at C4 of phenol (**1**). In the end, this yields a polymer comprised of predominantly 2,4'-methylene linkages (typically ~50%-75%): the remaining linkages are primarily 4,4'-methylene units (~20%), and only small amounts of 2,2'-methylene units are produced (~5%).

C.3.2 Lewis (Neutral) Acid Catalysts—High Ortho Novolac Resins

Figure C.6 gives a plausible mechanism for polymerization under Lewis acid conditions. Initially, phenol (**1**) forms a coordination complex (**21**) from reaction with a divalent metal precursor (**20**) ($M = Zn, Mg, Mn, Cd, Co, Pb, Cu, \text{ or } Ni$). Complex **21** can coordinate formalin (**7**), which directs the initial addition to C2, generating **22**. Compound **22** undergoes proton transfer yielding **23**, which then unselectively reacts with phenol (**1**) at either C4 or C2 to form **15** and **19**, respectively. This entire process is repeated as in Fig. C.6, thus producing a polymer exhibiting a high content of 2,2'-linkages (typically 45% [2,2'], 45% [2,4']). In addition, as benzylic alcohol intermediates are present, ether linkages are also produced as minor byproducts (~10%) (see C.5).

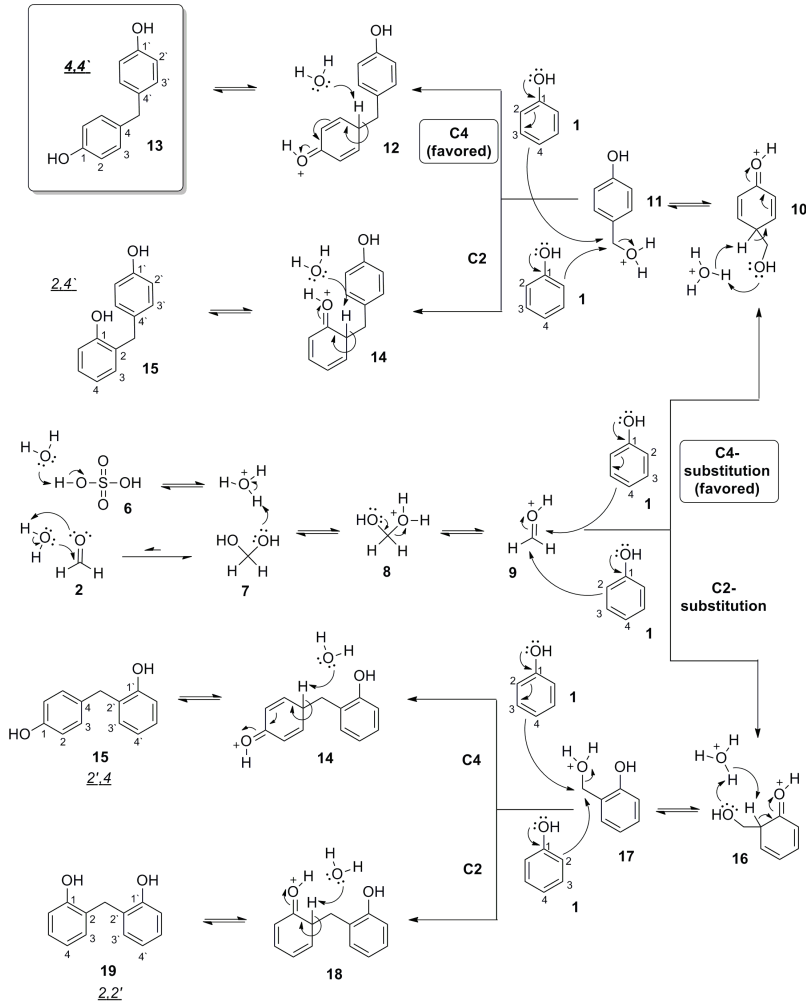


Figure C.5: Brønsted acid-catalyzed reaction of phenol with formaldehyde.

C.4 Synthesis of Resole Resins

Resole resins are synthesized by base-catalyzed polymerization of phenol and formaldehyde (Fig. C.7). Typically $\sim 1\% - 12\%$ (by mole) of base catalyst is used. A basic medium favors the production of branched polymers, because substitution of phenolate ions (generated from **1** under basic conditions) increases reactivity towards formaldehyde. Similarly, these polymers often cross-link under the reaction conditions and thus generally do not require the addition of a cross-linking agent in the curing step. As a result of this polymethylation of phenol, excess formaldehyde is added in order to achieve a controlled polymerization. Regardless, resole resins will still often contain a small amount of unreacted, “trapped” phenol ($\sim 5\% - 15\%$ by mole). As benzylic alcohols are stable in the presence of base, resins synthesized using base catalysts also generally contain a high amount of benzylic ether linkages (**39**) prior to curing (see Sec. C.5). However, these linkages can be converted

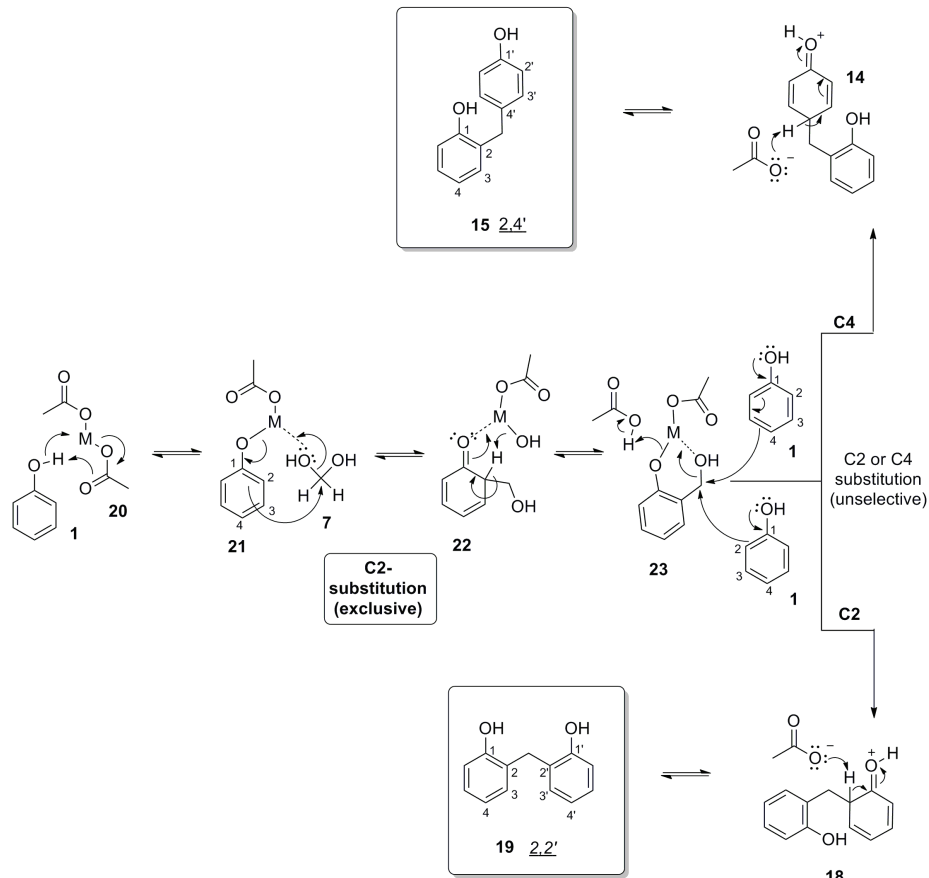


Figure C.6: Lewis acid catalyzed reaction of phenol with formaldehyde.

to the stronger methylene linkages (Fig. C.2) upon heating in the subsequent curing step. Fewer ether linkages are produced if weaker bases such as amine bases are used as catalysts instead of sodium hydroxide (NaOH). However, in these cases a significant amount of nitrogen is incorporated. This occurs as a result of reaction of phenolate ions with imines (**5**), which form from the reaction of formaldehyde (**2**) with the amine catalyst (Fig. C.4). The use of amine bases also typically results in polymers with higher molecular weights, less free phenol, lower water solubility, and a higher glass transition temperature.

As a result of the spontaneous cross-linking of the polymethylol groups that occurs under the reaction conditions for resole resins, the polymerization and curing processes can be conducted in one step; this is in contrast to novolac resins in which polymerization and curing are always conducted in two separate steps.

Figure C.8 gives a generalized mechanism for polymerization under basic conditions. Phenol (**1**) reacts with base to form phenolate ion (**24**), which reacts with formaldehyde (**2**) (generated from formalin (**7**) in the presence of base) to yield **25**. Proton transfer produces mono-substituted

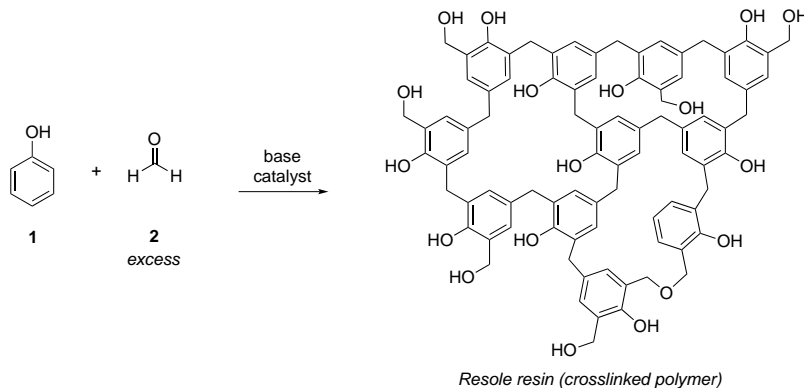


Figure C.7: General synthetic scheme for the production of a resole resin.

phenolate ion (**26**), which reacts with formaldehyde (**2**) analogously to **24**, yielding phenolate (**27**). Substitution increases the reactivity of phenolate ions: thus, reactivity increases in the order of **24 < 26 < 27**. Reaction of phenolate (**27**) with **2** produces compound **28**, which can eliminate hydroxide ion yielding **29**. Reaction of **29** with phenolate ion (**24**) produces **30**. Proton transfer reactions result in **31** and then **32**, which can continue to react with **24** in an analogous fashion to **29**, producing **33**, **34**, and finally fully branched phenol (**35**). Polymerization proceeds via further reaction of **35** and its intermediates until all of the formaldehyde is consumed, generating highly branched polymers. Furthermore, these polymethylolated repeat units can also react with each other, generating a highly cross-linked polymer network.

C.5 Byproducts formed in synthesis of resins

Figure C.9 illustrates representative examples of various byproducts that can be formed in the synthesis of resins. Small (~1% - 2% by mole) benzodioxane (**37**) impurities are found when weak acids (such as oxalic or phosphoric acid) are used, due to the small amounts of benzylic alcohols (**36**) that are produced and react with protonated formaldehyde (**9**). This is not seen when sulfonic or sulfuric acid is used, as benzylic alcohols rapidly decompose under strongly acidic conditions; instead, they remain fully protonated as **17**. However, **37** can liberate formaldehyde upon curing and can be subsequently reincorporated and cross-linked as methylene bridges. Formation of benzylic alcohols (**36**) under weak or neutral acidic conditions, as well as basic conditions, can also result in the production of varying amounts of benzylic ethers (**38**). However, these also generally decompose to formaldehyde and methylene linkages upon curing (Fig. C.2). Formation of **39** can occur under any of the reaction conditions, and **39** can dimerize to produce **40**. It is unlikely that this byproduct will

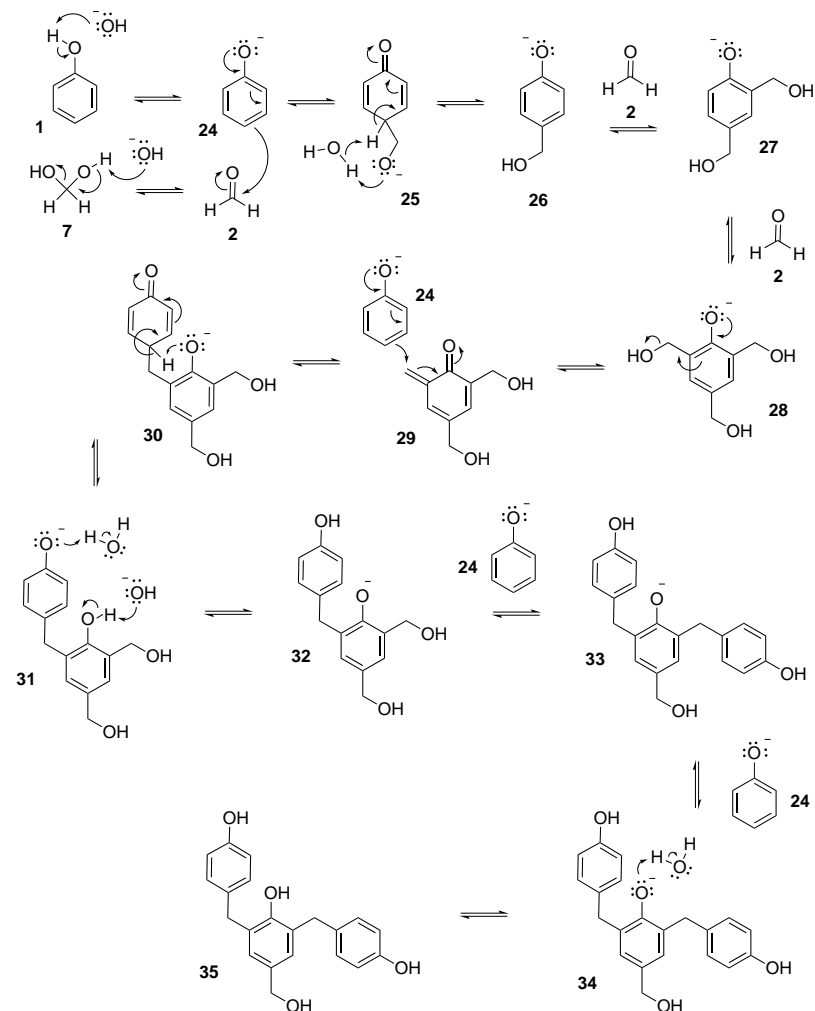


Figure C.8: Base-catalyzed reaction of phenol with formaldehyde.

decompose under the curing conditions. Hence, it might remain trapped in the resin and liberated as a pyrolysis gas at higher temperatures.

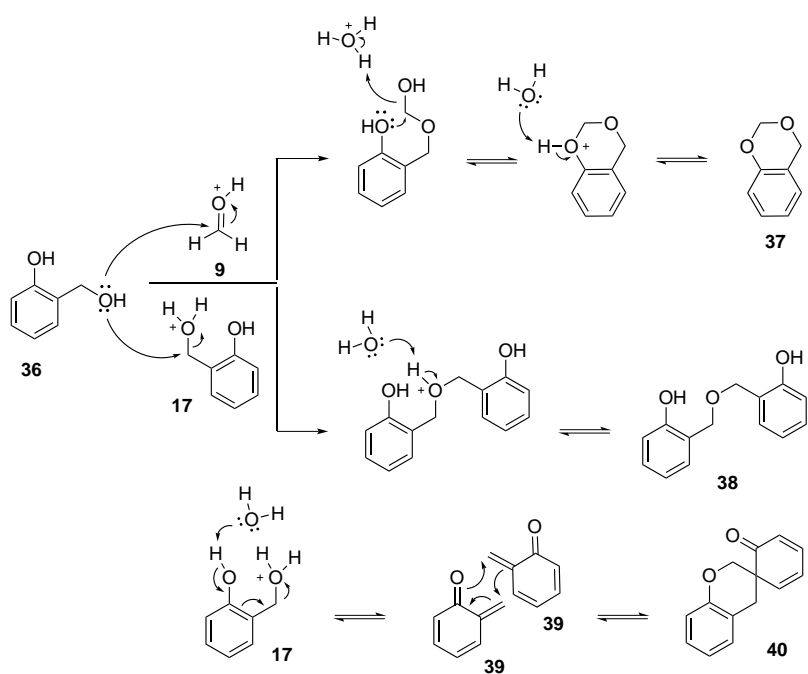


Figure C.9: Byproducts formed in resin synthesis.

Appendix D

Pyrolysis Gas Model

The 55 species used for the pyrolysis gas mixture model are listed in Table D.1. Even though no nitrogen content is assumed in this work, the entire model is included for generality. Only 8 species ($C_{24}H_{12}$, $C_{16}H_{10}$, C_3H, C_3H_2 -triplet, C_4 , C_4H , C_5 , C_5H , and C_3H_2 -singlet) do not use the standard CEA data, and the thermodynamic data used is included at the end of this appendix for completion. The three additional species used to model the work by Sykes [162] are shown in Table D.2.

Table D.1: 55 gas species model used to model the pyrolysis gas mixture.

Species	Reference	Name (if different) in Paper Figures
C	Ref. [100]	
C^+	Ref. [100]	
C_2	Ref. [100]	
$C_{16}H_{10}$	Ref. [12]	
$C_{24}H_{12}$	Ref. [12]	
C_2H	Ref. [100]	
C_2H_2 , acetylene	Ref. [100]	
C_2H_2 , vinylidene	Ref. [100]	C_2H_2
C_2H_4	Ref. [100]	
C_2H_6	Ref. [100]	
C_2N_2	Ref. [100]	
C_2O	Ref. [100]	
C_3	Ref. [100]	
C_3H	Ref. [12]	
C_3H_2 , triplet	Ref. [12]	C_3H_2
C_3H_3 , 2-propynyl	Ref. [100]	
C_3H_4 , allene	Ref. [100]	
C_3H_4 , propyne	Ref. [100]	
C_3O_2	Ref. [100]	
C_4	Ref. [12]	
C_4H	Ref. [12]	
C_4H_2 , butadiyne	Ref. [100]	C_4H_2
C_4N_2	Ref. [100]	
C_5	Ref. [12]	
C_5H	Ref. [12]	
C_6H_2	Ref. [100]	
C_6H_6	Ref. [100]	

CCN	Ref. [100]	
CH	Ref. [100]	
CH ₂	Ref. [100]	
CH ₃	Ref. [100]	
CH ₃ CN	Ref. [100]	
CH ₄	Ref. [100]	
CN	Ref. [100]	
CNC	Ref. [100]	
CO	Ref. [100]	
CO ₂	Ref. [100]	
e ⁻	Ref. [100]	
H	Ref. [100]	
H ⁺	Ref. [100]	
H ₂	Ref. [100]	
H ₂ O	Ref. [100]	
C ₃ H ₂ , singlet	Ref. [12]	HCCCH
HCN	Ref. [100]	
HNC	Ref. [100]	
HO ₂	Ref. [100]	
N	Ref. [100]	
N ₂	Ref. [100]	
NH	Ref. [100]	
NH ₃	Ref. [100]	
NO	Ref. [100]	
NO ⁺	Ref. [100]	
O	Ref. [100]	
O ⁺	Ref. [100]	
O ₂	Ref. [100]	
OH	Ref. [100]	

Table D.2: References for additional 3 species used to model Sykes' data [162].

Species	Reference	Name (if different) in Paper Figures
C ₇ H ₈	Ref. [100]	
C ₆ H ₅ OH	Ref. [100]	
(CH ₃) ₂ C ₆ H ₃ OH	Personal calculations [19, 114]	

Thermodynamic data used in this thesis that is not available from the CEA [99] database is presented below, using constant NASA polynomial fits [49], and shown in the input format for Cantera [47].

```
species(name="C24H12",
atoms = " C:24 H:12 ",
thermo =
NASA9( [ 200.00, 1000.00], [ 1.383880670E+06, -1.053873090E+04, 4.417694380E+00,
2.338931650E-01, -2.612047160E-04, 1.520433220E-07,
-3.635641460E-11, 9.132072210E+04, -5.550829190E+01] ),
NASA9( [ 1000.00, 6000.00], [ 7.917402510E+06, -5.299587210E+04, 1.374419740E+02,
-1.056258770E-02, 2.038212660E-06, -2.098331830E-10,
8.905690460E-15, 3.233839640E+05, -8.591038290E+02] )
),)
```

```

species(name="C10H8",
       atoms = " C:10 H:8 ",
       thermo = (
NASA9( [ 200.00, 1000.00], [-2.602845316E+05, 6.237409570E+03, -5.226095040E+01,
         2.397692776E-01, -2.912244803E-04, 1.854944401E-07,
         -4.816619270E-11, -1.114700880E+04, 2.972139517E+02 ] ),
NASA9( [ 1000.00, 6000.00], [ 5.906172110E+06, -3.163229240E+04, 7.030342030E+01,
         -6.018865540E-03, 1.142052144E-06, -1.161605689E-10,
         4.892844020E-15, 1.962567046E+05, -4.347848950E+02 ] )
       ),)

species(name="C3H",
       atoms = " C:3 H:1 ",
       thermo = (
NASA9( [ 200.00, 1000.00], [ -4.370697870E+04, 3.864188930E+02, 3.768803720E+00,
         8.973917020E-03, -7.419268860E-06, 3.700122010E-09,
         -8.337208180E-13, 8.239066050E+04, 6.490524130E+00 ] ),
NASA9( [ 1000.00, 6000.00], [ 1.061164700E+06, -4.180064720E+03, 1.221115430E+01,
         -6.649242000E-04, 1.156319000E-07, -1.081795820E-11,
         4.209683310E-16, 1.096660270E+05, -4.894138010E+01 ] )
       ), )

species(name="C3H2, singlet",
       atoms = " C:3 H:2 ",
       thermo = (
NASA9( [ 200.00, 1000.00], [ 1.571611930E+05, -1.805718300E+03, 1.144535590E+01,
         -7.207286770E-04, 2.657982850E-06, -1.312447490E-09,
         1.355365380E-13, 7.861045500E+04, -4.025988140E+01 ] ),
NASA9( [ 1000.00, 6000.00], [ 1.797943970E+06, -7.091352330E+03, 1.684099870E+01,
         -1.180921210E-03, 2.096836660E-07, -2.000344190E-11,
         7.927151790E-16, 1.121174950E+05, -8.070969030E+01 ] )
       ), )

species(name="C3H2, triplet",
       atoms = " C:3 H:2 ",
       thermo = (
NASA9( [ 200.00, 1000.00], [ -1.285712600E+04, 7.349430760E+01, 6.468831070E+00,
         8.291493810E-03, -7.554556720E-06, 4.780476460E-09,
         -1.325294590E-12, 6.276309600E+04, -7.594614420E+00 ] ),
NASA9( [ 1000.00, 6000.00], [ 1.974617930E+06, -6.712789200E+03, 1.618225050E+01,
         -8.370312160E-04, 1.237531890E-07, -9.503648200E-12,
         2.896386860E-16, 1.048523410E+05, -7.393045090E+01 ] )
       ), )

species(name="C4H",
       atoms = " C:4 H:1 ",

```

```

thermo = (
    NASA9( [ 200.00, 1000.00], [ 2.387116150E+05, -3.190597560E+03, 1.770049480E+01,
        -1.352198470E-02, 1.904183020E-05, -1.205074560E-08,
        2.926006000E-12, 1.121671410E+05, -7.760462490E+01] ),
    NASA9( [ 1000.00, 6000.00], [ 1.393117560E+06, -6.387192280E+03, 1.709846550E+01,
        -1.154160270E-03, 2.138718680E-07, -2.126358940E-11,
        8.760314590E-16, 1.336746000E+05, -8.229773560E+01] )
),)

atoms = " C:5 H:1 ",
thermo = (
    NASA9( [ 200.00, 1000.00], [ -4.221257120E+04, -2.670627130E+02, 8.727034160E+00,
        1.017403710E-02, -5.707367690E-06, 1.279424970E-09,
        -8.975136370E-15, 1.104880580E+05, -1.971612140E+01] ),
    NASA9( [ 1000.00, 6000.00], [ 1.212530080E+06, -6.103203090E+03, 1.998790840E+01,
        -1.135041710E-03, 2.132642460E-07, -2.147467780E-11,
        8.948595310E-16, 1.448008030E+05, -9.393232520E+01] )
),)

species(name="(CH3)2C6H3OH",
atoms = "C:8 H:10 O:1 ",
thermo = (
    NASA( [ 300.00, 1000.00], [-2.11293458E+00, 7.85176505E-02, -3.77077553E-05,
        -7.65526959E-09, 9.28225883E-12, -2.20903042E+04,
        3.84698808E+01] ),
    NASA( [ 1000.00, 3000.00], [1.46057910E+00, 6.94131778E-02, -4.07352658E-05,
        1.14191146E-08, -1.23365591E-12,
        -2.27678245E+04, 2.06740013E+01] )
),)

```